Investigation and Characterization of Single Hot Spot Laser-Plasma Interactions

By

Ronald J. Focia

B.S., Electrical Engineering with Computer Engineering Option
Michigan State University, East Lansing, MI 1986.

M.S., Electrical Engineering with Concentration in Pulsed Power and Plasma Science
The University of New Mexico, Albuquerque, NM 1996.

Submitted to the Department of Electrical Engineering and
Computer Science in Partial Fulfillment of the
Requirements for the Degree of

Doctor of Philosophy in Electrical Engineering

at the

Massachusetts Institute of Technology

December, 2001

Signature of Author……………………………………………………………………………
Department of Electrical Engineering and Computer Science
December, 2001

Certified by……………………………………………………………………………………
Prof. Abraham Bers
Professor of Electrical Engineering and Computer Science
Thesis Supervisor

Certified by……………………………………………………………………………………
Dr. Juan C. Fernández
Deputy Group Leader of P-24, Los Alamos National Laboratory
Thesis Co-Supervisor

Accepted by…………………………………………………………………………………...
Arthur C. Smith
Chairman, Committee on Graduate Students
Department of Electrical Engineering and Computer Science

Acknowledgment

I am grateful to Professor Abraham Bers for guiding me through the Ph.D. process at MIT and mentoring me. I am especially thankful for his part in setting up the collaboration with the Los Alamos National Laboratory (LANL) which gave me the opportunity to participate in world-class laser-plasma experiments.

I am grateful to Dr. Magdi Shoucri from the Centre Canadien de Fusion Magnétique, IREQ, Varennes, Canada who provided to me the Vlasov code used to support work in this thesis. He did not merely provide the code, but rather, took the time to go over in great detail the numerical methods used in it and also provided countless feedback on its usage.

I am also grateful for receiving funding from LANL and the relief from MIT that made possible my participation in experiments at LANL. Everyone I worked with at LANL was extremely competent and helpful. Special thanks are in order for David Montgomery who is an excellent experimentalist and helped me out immensely, Juan Fernández who is also an experimentalist and acted as my mentor at LANL, and Randy Johnson who is part of and leads an exceptional group of people - the TRIDENT laser operations group.

Biographical Note

Ron Focia was born in Oak Park, Illinois, in September of 1963. When he was eight years old, the Focia family packed up and moved to Albuquerque, New Mexico. After a few years in the Albuquerque area, the Focia family purchased and moved to a 160 acre farm near the small town of Estancia, New Mexico. For those who don't know where Estancia is, it is located between the towns of McIntosh and Willard. Ninety acres of the farm were planted in alfalfa and Ron became the farm hand, repair mechanic, and hay hauler. Ron graduated from Estancia High School in 1981 with a class of 42 people.

In 1986, Ron received the Bachelor of Science degree, with Computer Engineering option, from Michigan State University in East Lansing, Michigan. While interviewing for jobs during his next-to-last quarter at MSU, Ron found the U.S. Navy's Nuclear Submarine Officer program most interesting. He enlisted in the Navy and during his last quarter at MSU was a Nuclear Propulsion Officer Candidate (NUPOC).

After graduating from MSU he proceeded directly to Officer's Candidate School (OCS) in Newport, Rhode Island, for indoctrination into the Navy. After OCS he returned to MSU for 13 weeks of Recruiter duty. The next stop in the nuclear Navy training pipeline was a six month training period at the Nuclear Power School (NPS) in Orlando, Florida, where the theory of nuclear reactors and propulsion was taught. After NPS was another six month training period at the Idaho National Engineering Laboratory (INEL) near Idaho Falls, Idaho, where actual hands-on experience was gained operating nuclear propulsion prototypes. The last stop in the Navy training pipeline was the Submarine Officer School in Groton, Connecticut, where training is given on navigation, warfare tactics, damage control, and other topics essential to the performance of duties onboard a submarine. After the completion of all required training, in July of 1988 Ron finally proceeded to his first tour of duty onboard the USS Sam Houston (SSN 609) stationed in Honolulu, Hawaii. The Sam Houston was a special operations boat equipped to support the missions of a US Navy SEAL team.

Ron spent about four years as a Division Officer onboard the Sam Houston. During this time the USS Sam Houston went on a two month Northern Pacific covert operation, a six month Western Pacific (WESTPAC) tour, and performed various local operations around the Hawaiian Islands. Ron became the senior Division Officer onboard. As the Sam Houston neared the end of its useful service life, Ron performed the last emergency surface, the final reactor shutdown, and saw the submarine through decommissioning at the Puget Sound Naval Shipyard in Bremerton, Washington. Ron decided to stay in the Navy for an additional three year tour of duty as an instructor at the King's Bay Naval Submarine Base Trident Training Facility in King's Bay, Georgia. There, he was the Engineering Department Division Officer and educated senior Naval personnel on advanced reactor plant operations and chemistry and radiological controls. He decided to leave the Navy to pursue graduate education. While on vacation in Key West, Florida, he met his future wife Carmen at Sloppy Joe's Bar.

In the Fall of 1994 Ron started work on a Master of Science Degree at the University of New Mexico in Albuquerque, New Mexico. His thesis work was in the area of pulsed power and plasma science and concentrated on Russian-made fast switching solid-state diodes. He completed all requirements and graduated from UNM in the summer of 1996 with a GPA of 3.98/4.0. At the suggestion of Carmen, Ron applied to Princeton, Cornell, and MIT to pursue the Doctoral degree. He was accepted at all three schools. His true interest was in plasma science and controlled fusion and he decided that MIT would provide the best education in this area.

Investigation and Characterization of Single Hot Spot Laser-Plasma Interactions

By

Ronald J. Focia

Submitted to the Department of Electrical Engineering and Computer Science in Partial Fulfillment of the Requirements for the Degree of Doctor of Philosophy in Electrical Engineering

ABSTRACT

Control of parametric laser-plasma interactions (LPI) is essential to the success of inertial confinement fusion (ICF). Through a research collaboration with the Los Alamos National Laboratory (LANL), we have had the opportunity to participate in world-class laser-plasma experiments. The goal of these experiments was to gain a fundamental understanding of LPI by studying the interaction of a single laser hot spot, or speckle, with a preformed, quasi-homogeneous, long scale-length plasma. Recent single hot spot experiments resulted in a wealth of data and the first definitive observation of two LPIs. Namely, the Langmuir decay instability (LDI) cascade and stimulated scattering off of an acoustic-like electron mode below the usual electron plasma wave frequency.

The LDI is the result of the electron plasma wave (EPW) generated by stimulated Raman scattering (SRS) growing to a sufficient amplitude such that it exceeds a threshold (proportional to the damping of the LDI daughter waves) and undergoes parametric decay into another counter-propagating EPW and a co-propagating ion acoustic wave (IAW). Subsequent EPW decays due to LDI are possible and collectively more than one EPW generated by LDI is called LDI cascade. The LDI cascade can play a role in the saturation of SRS since wave energy from the SRS EPW couples into secondary waves that are non-resonant with the SRS process.

Stimulated scattering from an electrostatic wave at a frequency and phase velocity ($\omega \approx 0.4\omega_{pe}$, $v_\phi \approx 1.4 v_e$) between that of an EPW and IAW was also observed. In this thesis, a Vlasov-Maxwell code is used to numerically predict the time evolution of the electron distribution function for the experimental parameters. The resultant distribution function is then modeled as a bi-Maxwellian (one background and one beaming) to show that it exhibits linear modes that include the observed electron acoustic wave. A quasimode analysis of laser scattering off of this linear mode is presented as one possible explanation of the experimental observation.

Thesis Supervisors:

Prof. Abraham Bers, Professor of Electrical Engineering and Computer Science

Dr. Juan C. Fernández, Deputy Group Leader of P-24, LANL (Co-Supervisor)

Table of Contents

ACKNOWLEDGMENT 2

BIOGRAPHICAL NOTE 3

ABSTRACT 5

TABLE OF CONTENTS 6

LIST OF FIGURES 8

LIST OF TABLES 12

GLOSSARY 13

CHAPTER 1: INTRODUCTION 15

CHAPTER 2: EXPERIMENTAL PROCEDURES 19

2.1 OVERVIEW OF THE TRIDENT LASER AND THE SINGLE HOT SPOT CONFIGURATION 20

2.2 INCIDENT BEAM AND BACKSCATTER DIAGNOSTICS 27

2.3 TRANSMITTED BEAM DIAGNOSTIC 39

2.4 COLLECTIVE THOMSON SCATTERING DIAGNOSTICS 42

CHAPTER 3: OBSERVATION OF LANGMUIR CASCADE 54

3.1 THE THEORY OF SRS AND LDI 55

3.2 OBSERVATION OF LDI CASCADE AND INTERPRETATION OF THE DATA 63

3.3 DATA SORTING AND GENERAL TRENDS 77

3.4 CONCLUSIONS ON THE OBSERVATION OF LDI AND FUTURE WORK NECESSARY 82

CHAPTER 4: OBSERVATION OF STIMULATED ELECTRON ACOUSTIC WAVE SCATTERING 84

4.1 EXPERIMENTAL OBSERVATION OF STIMULATED ELECTRON ACOUSTIC SCATTERING 86

4.2 NUMERICAL SIMULATION OF SRS USING A 1D VLASOV CODE 93

4.3 RESULTS OF NUMERICAL MODELING 99

4.4 DESCRIPTION OF SEAS USING BI-MAXWELLIAN ELECTRON DISTRIBUTION 110

4.5 VLASOV DESCRIPTION FOR STIMULATED SCATTERING OFF OF ELECTRON MODES AND QUASIMODES IN A PLASMA 118

CHAPTER 5: CONCLUSIONS 120

APPENDIX A 122

DERIVATION OF THE DISPERSION RELATION DESCRIBING STIMULATED RAMAN SCATTERING 122

APPENDIX B 133

DERIVATION OF THE DISPERSION RELATION DESCRIBING THE LANGMUIR DECAY INSTABILITY 133

APPENDIX C 143

VLASOV DESCRIPTION FOR STIMULATED SCATTERING OFF OF ELECTROSTATIC MODES AND QUASIMODES IN A PLASMA 143

APPENDIX D 149

ONE-DIMENSIONAL (1D) RELATIVISTIC VLASOV CODE DESCRIPTION 149

APPENDIX E 197

MATHCAD WORKSHEETS USED FOR VARIOUS CALCULATIONS CITED IN THE THESIS 197

REFERENCES 247

List of Figures

Figure 1. Schematic diagram of the single hot spot experiment. 21

Figure 2. Beam intensity versus time for the single hot spot experiments. 22

Figure 3. The experimentally measured (CH plasma at t = 1.0±0.1 ns) electron density and temperature, ion temperature, and transverse flow velocity are in rough agreement with 2D LASNEX simulations. All measured values were determined by analyzing the Thomson scattered data in a manner similar to that described in a later section of this chapter. 23

Figure 4. (a) Actual hot spot intensity pattern at best focus, and (b) lineout of the intensity pattern (data points) compared to the ideal diffraction limit for an f/7 beam. The stray data point in (b) is most likely due to a bad pixel on the CCD camera. For the f/7 527 nm beam, the first Airy minima is expected to occur at a radius of r = $1.22F\lambda = 4.5\ \mu$m. 26

Figure 5. Schematic diagram of the incident interaction beam path. 28

Figure 6. Schematic diagram of the backscatter diagnostic table. 29

Figure 7. Mercury (Hg) lamp calibration images for the SRS spectrometer with 100 gpmm grating. (a) Actual Hg lamp image and 527 nm laser lines with column sum lineout normalized to the peak intensity, and (b) Linear fit to the data. 31

Figure 8. Typical backscattered SRS image. This image shows bifurcation, i.e. splitting of the SRS into two distinct density pockets most likely due to filamentation. The ω_{ES}/ω_o scale predicts the normalized frequency at which the electrostatic wave will appear and is used for correlation with other diagnostics. 32

Figure 9. Calibration curve for the reflected energy photodiode. The slope of the linear fit to the data is 0.582 V/J with a reference filter optical density of 6.88. 37

Figure 10. NBI images showing (a) a high intensity (I = 1.8×10^{16} W/cm^2) shot exhibiting significant backscattered beam deflection, and (b) a low intensity (I = 4.4×10^{15} W/cm^2) shot with little light scattered out of the incident cone. In both figures, the outline of the NBI scatter plate aperture is clearly visible. 38

Figure 11. TBD images showing (a) a low-intensity (I = 2.2×10^{15} W/cm^2) shot with little beam break up, and (b) a high-intensity (I = 2×10^{16} W/cm^2) shot with significant beam break up and deflection. The undeflected beam spot is indicated by the dashed line which appears elliptical since the TBD CCD camera was not oriented normal to the scatter plate. 40

Figure 12. The geometry of a focusing beam is used to determine the angle that the beam cone will span. This depends on the f-number of the optic used. 41

Figure 13. Schematic diagram of the Streaked Thomson diagnostic. 42

Figure 14. Schematic diagram of the Gated Thomson Diagnostic. 43

Figure 15. Streaked Thomson diagnostic wavelength calibration curves and curve fit parameters for (a) 100 grid per millimeter (gpmm), (b) 1200 gpmm, and (c) 1800 gpmm gratings. 45

Figure 16. Gated Thomson diagnostic wavelength calibration curves for (a) 100 gpmm and (b) 1200 gpmm gratings. 45

Figure 17. Mask and CCD image used for angular displacement calibration of the Gated Thomson diagnostic. 46

Figure 18. Scattering diagram for the electron plasma wave resulting from backscattered SRS. 50

Figure 19. (a) Streaked Thomson image from scattering off of thermal levels of ion acoustic waves. (b) Wavelength integrated lineout of data and Gaussian fit showing definitions for early, mid and late time temperatures. 52

Figure 20. Mid-time lineout of IAW Thomson scattering data (solid line) and numerical fit (dashed line) of the Thomson shape factor. The amplitudes of both curves have been normalized to their maximum values and are presented in arbitrary units (A.U.). 53

Figure 21. (a) Diagram showing polarizations of the pump and scattered EMWs for both propagating in the same plane, and (b) 1D frequency and wave vector matching diagram illustrating the maximized SRS interaction. Note that frequencies and wavenumbers are normalized to that of the laser. 57

Figure 22. 1D frequency and wave vector matching diagram illustrating the maximized SRS, LDI and LDI cascade interaction. Note that frequencies and wavenumbers are normalized to that of the laser and for this figure, the IAW phase velocity has been exaggerated to illustrate the LDI cascade process. 61

Figure 23. The SRS spectrum observed on shot number 12805. The normalized frequency scale ω_{ES}/ω_o (ω_o is the angular frequency of the SHS laser) shows the expected electrostatic wave frequency for a given wavelength. 65

Figure 24. (a) Time-resolved Thomson spectrum from shot number 12805 showing the forward propagating EPW from SRS and the second LDI cascade. (b) A horizontal lineout taken where the cascade separation is indicated in (a). 67

Figure 25. Time-integrated Thomson spectrum from shot number 12805 showing the forward propagating EPW from SRS and the second LDI cascade. 71

Figure 26. SRS and 2nd LDI Langmuir wave behavior in *k*-space assuming (a) a constant temperature and decreasing density and (b) a constant density and decreasing temperature. Graphs were generated using linear theory dispersion relations and resonance matching calculation worksheet in Appendix E (Sections 9 and 18). The observed behavior is consistent with graph (b). 73

Figure 27. Streaked Thomson spectrum from shot 12767 showing two independent LDI cascade processes resulting from the bifurcated SRS spectrum shown in Figure 8. For this shot $I_o = 4.35 \times 10^{15}$ W/cm^2, R = 4.46 %, $n_e/n_c = 0.035$, and $k\lambda_{De} = 0.245$. ... 74

Figure 28. Power in the SRS EMW, SRS EPW and the LDI #2 cascade. The power is defined as the wavelength integrated counts on the CCD image for the particular wave per unit time. The LDI cascade EPW is normalized to the peak value of the SRS EPW.. 76

Figure 29. Visualizations of the qualitative data sorting categories and assigned ratings. 78

Figure 30. Qualitative data sorting – plot of the rating versus n_e/n_c. 79

Figure 31. Qualitative data sorting – plot of the rating versus $k\lambda_{De}$. 80

Figure 32. Qualitative data sorting – plot of the rating versus intensity. 80

Figure 33. Qualitative data sorting – plot of the rating versus the product of Intensity and n_e/n_c normalized to 10^{14} W/cm^2. 81

Figure 34. Composite image from two separate shots showing the time-integrated SRS and SEAS signals. The amplitude of the SEAS is seen to be approximately 3000x less than the SRS signal and occurs at a much lower phase velocity. 88

Figure 35. 1D resonance matching diagram showing the SRS and SEAS interactions. The phase velocity of the EAW dispersion has been set to that predicted by the experimental observation.. 89

Figure 36. Hot spot and probe geometry for investigation of plasma waves outside of the SHS. 91

Figure 37. (a) SRS and (b) streaked Thomson spectra from shot 12831 where EPWs were probed outside of the SHS. The broad SRS spectrum does not directly correlate to the numerous spectro-temporal events observed in the streaked Thomson image. These EPWs could be the result of beaming electrons interacting with the plasma. . 92

Figure 38. Spectral content of (a) the electromagnetic and (b) the electrostatic fields in the simulation box when the laser has propagated the simulation box ~1.2x. 102

Figure 39. Snapshot at time $\tau \approx 51.7$ (ω_{pe}^{-1}) of a region in phase space showing the formation of vortices. 103

Figure 40. (a) Spatial average of the electron distribution over one plasma wave wavelength at $\tau \approx 51.7$ (ω_{pe}^{-1}) and x ≈ 8.7 (c/ω_{pe}). (b) The deviation from the initial Maxwellian (normalized to the maximum of the time-evolved distribution) shows a redistribution of particles from lower energies to higher energies. 105

Figure 41. (a) Phase space window from Figure 39 at time $\tau \approx 122.2$ (ω_{pe}^{-1}). (b) Spatial average of the electron distribution over three vortices centered on the vortex at x ≈ 16.6 (c/ω_{pe}). 107

Figure 42. (a) Phase space window from Figure 39 at time $\tau \approx 197.4$ (ω_{pe}^{-1}). (b) Spatial average of the electron distribution over three vortices centered on the vortex at x ≈ 25.1 (c/ω_{pe}). 108

Figure 43. Fourier spectrum of the backward propagating EMW passing the left-hand boundary of the plasma region at time $\tau = 128$ (ω_{pe}^{-1}). 110

Figure 44. (a) Zero contours of the real and imaginary parts of (31) in the complex ω-plane for $k\lambda_{De} = 0.28$. Where these contours intersect is a root of the dispersion relation. (b) dispersion of the first (EPW) and second (EAW) Landau roots for a range of $k\lambda_{De}$ values. Note that in (b) the $k\lambda_{De}$ values do not go to zero due to numerical problems following the EAW root in this region. 113

Figure 45. (a) Zero contours of (31) in the complex ω plane for a bi-Maxwellian plasma with parameters $T_e = 390$, $T_b = 20$, $n_e = .97$, $n_b = 0.03$, $V_b = 7.42$ (~$0.4v_{\phi EPW}$). (b) Dispersion of the electron plasma wave and weakest damped electron acoustic root. 116

Figure 46. Plot of the frequency and damping of the EAW mode versus beam density fraction for the parameters $T_e = 390$, $T_b = 20$, $V_b = 7.42$ (~$0.4v_{\phi EPW}$), and $k\lambda_{De} = 0.28$. 117

Figure 47. Plot of the inverse of the longitudinal permittivity function showing the difference between the Maxwellian and bi-Maxwellian models. For the parameters K = $k\lambda_{De} = 0.28$, $T_e = 390$ eV, $T_i = 100$ eV, $T_b = 20$ eV, $n_e = .97$, $n_b = 0.03$, and $V_b = 7.6$ (~$0.4v_{\phi EPW}$) the bi-Maxwellian model predicts the emergence of the EAW mode where observed experimentally. 119

Figure 48. Geometry for justifying using the fluid approximation for the transverse velocity. 151

Figure 49. (a) Simulation electron density profile and (b) close up of the piecewise parabolic transition from the vacuum to plasma region. 160

List of Tables

Table 1: Calculated parameters used to determine probe and collection angles for T_e = 500 eV. 51

Table 2: Nonlinear coupled mode growth rates for various laser plasma instabilities for the parameters 50/50 CH plasma, n_e/n_c = 0.03, I_o = 2x10^{15} W/cm^2, λ_L = 527 nm, T_e 350 eV, and T_i = 100 eV. The growth rates and thresholds are normalized to the laser frequency and the direction of maximum growth is with respect to the direction of the laser propagation. The convective and absolute thresholds are represented by γ_c and γ_a, respectively. If the growth rate for an interaction is $\gamma_c < \gamma_{max} < \gamma_a$, the spatial growth rate κ_{max} (normalized to the laser wavenumber) is given in parenthesis. Spatial growth rates for filamentation are given in μm^{-1} and for calculating the threshold (i.e. 2KL > 1) L = 75 μm was used. 59

Table 3. Qualitative sorting category ratings and descriptions. 77

Table 4: Summary of SEAS mode observations. Δt is the time duration of the observed spectrum. 90

Glossary

This glossary of terms used throughout the thesis represents to a large extent the language of inertial confinement fusion and laser-plasma experiments and theory. Although the terms are defined in the chapters in which they are presented, this glossary serves as a convenient reference for their definitions.

ICF	Acronym for inertial confinement fusion
I	Laser intensity in watts per centimeter squared (W/cm^2)
SHS	Acronym for single hot spot. This is the interaction volume resulting from focusing a nearly diffraction-limited laser beam into a plasma
n_e	The electron density (cm^{-3})
n_c	The critical electron density above which light does not propagate (cm^{-3}). This is found by setting the laser frequency equal to the electron plasma frequency.
ω_{pe}	The electron plasma frequency defined by $\omega_{pe} = \sqrt{n_e e^2 / \varepsilon_o m_e}$, where e is the electron charge, ε_o is the permittivity of free space, and m_e is the electron mass.
n_e/n_c	The electron density divided by the critical density. Equivalent to the square of the electron plasma frequency to laser frequency, i.e. $(n_e / n_c) = \omega_{pe}^2 / \omega_L^2$
LPI	Acronym for laser plasma interaction (or laser plasma instability)
EMW	Acronym for electromagnetic wave
EPW	Acronym for electron plasma wave
EAW	Acronym for electron acoustic wave
IAW	Acronym for ion acoustic wave
SRS	Acronym for stimulated Raman scattering. This is the decay of the incident laser into an electromagnetic wave and an electron plasma wave.
SBS	Acronym for stimulated Brillouin scattering. This is the decay of the incident laser into an electromagnetic wave and an ion acoustic wave.
SEAS	Acronym for stimulated electron acoustic scattering. This is the decay of the incident laser into an electromagnetic wave and an electron acoustic wave.
TP	Acronym for the two-plasmon interaction. This is the decay of the incident laser into two electron plasma waves.
PP	Acronym for the plasmon-phonon interaction. This is the decay of the incident laser into an electron plasma wave and an ion acoustic wave.

$\boldsymbol{k_B}$	Boltzmann's constant (k_B = 1.3807x10^{-23} J/K)
eV	Electron volt. A unit of energy equal to 1.6022x10^{-19} Joule
$\mathbf{T_e}$	Electron temperature. Usually assumed to be multiplied by k_B and expressed in eV.
RPP	Acronym for random phase plate. This is one method used to smooth the intensity profile of high intensity laser beams. As its name implies the plate has in it many randomly placed elements that introduce a phase shift in the incident wavefront.
$\mathbf{V_{Te}}$	The electron thermal velocity given by $\mathrm{V}_{Te} = \sqrt{k_B T_e / m_e}$
$\boldsymbol{\lambda_{De}}$	The electron Debye length given by $\lambda_{De} = \mathrm{V}_{Te} / \omega_{pe}$

Chapter 1: Introduction

Control of parametric laser-plasma interactions is essential to the success of inertial confinement fusion (ICF) [1,2]. Stimulated Raman scattering (SRS) [3,4] is one such interaction involving the resonant decay of an incident electromagnetic wave (EMW) into a scattered EMW and an electron plasma (or Langmuir) wave (EPW). SRS is undesirable not only because it can cause losses in drive energy and illumination symmetry but also because it can trap and accelerate electrons that could preheat the fusion capsule and thus inhibit its compression. The onset and scaling of SRS has been the subject of much investigation [5].

In quasi-homogeneous ignition-relevant plasmas (i.e. in the context of the indirect drive approach to ICF [2]) the EPW amplitude can be large for moderate SRS reflectivity and saturation by nonlinear mechanisms is expected [6,7,8,9]. One possible source of non-linearity is coupling of SRS to other parametric processes via wave-wave interactions. One such mechanism is the Langmuir decay instability (LDI) [10,11], in which the daughter EPW from SRS decays into an EPW and an ion acoustic wave (IAW). LDI occurs when the amplitude of the primary EPW exceeds a threshold that is proportional to the product of the damping rates for the secondary EPW and IAW. The growth rate for LDI is maximized when the daughter EPW and IAW are propagating anti-parallel and parallel, respectively, to the primary EPW. Subsequent EPW decays due to LDI are possible if their amplitudes exceed the threshold. The terminology used in this thesis is that an EPW generated by LDI is called an LDI cascade step and, collectively, more than one cascade step is called LDI cascade. The LDI cascade can play a role in the saturation of SRS since wave energy from the SRS EPW couples into secondary EPWs and IAWs that are non-resonant with the SRS process. The saturation effect is strongest when the daughter waves are strongly damped, but not so strongly damped that growth rate for the interaction does not exceeded the threshold. Backward propagating EPWs presumed to be from LDI have been observed [12,13,14] and LDI has been observed in ionospheric plasmas [15,16]. Observation of Langmuir turbulence (i.e. the plasma is so strongly excited that a continuous spectrum of frequencies is present) in a laser-produced plasma has been reported recently [17]. However, it could not be established whether strong turbulence or weak LDI cascade was observed in those experiments due to inhomogeneity [18,19]. Additionally, in the French experiments regions in k-space were masked off in order to surmise that LDI was occurring at a specific frequency and wavenumber and thus true structure was not observed. In the single hot spot (SHS) experiments reported on in this thesis, we obtained the first unambiguous observations of multiple LDI cascade steps driven by SRS backscatter [20].

The nonlinear evolution of electrostatic waves in plasmas is prevalent in many aspects of plasma physics. In laser plasma research, intense lasers can couple nonlinearly to weakly damped electrostatic waves in the plasma and produce scattered light waves from these modes. Two small-amplitude plasma modes that have been studied extensively in unmagnetized plasmas are the EPW [21], and the IAW [22]. Both of these modes are weakly damped for a broad range of laser and plasma conditions. Nonlinear coupling of the intense laser field to these modes can result in significant loss of laser energy via SRS and stimulated Brillouin scattering (SBS) [23]. Early researchers [22,24,25], examining the linearized Vlasov electrostatic dispersion relation (which ignores particle-trapping effects) also noted solutions which they termed electron acoustic waves (EAW) due to their acoustic-like dispersion, i.e. the dispersion is linear and $\omega \propto k$. In [24] mode damping was ignored and for regions other than the minimum wavelength the analysis resulted in the dispersion relation for undamped EAWs of $\omega \approx 1.31 k V_{Te}$, where (ω, k) are the electrostatic wave-frequency and wave number, and $V_{Te} = \sqrt{k_B T_e / m_e}$ is the electron thermal velocity (k_B is Boltzmann's constant and T_e and m_e are, respectively, the electron temperature and mass). In [22] and [25] the effects of Landau damping were included and, in the long wavelength limit, the analysis resulted in the dispersion relation for EAWs of $\omega \approx 3.6 k V_{Te}$. These intermediate phase velocity ($v_\phi = \omega/k$) modes were obtained in addition to the weakly damped slow phase velocity IAW ($v_\phi/V_{Te} << 1$), and the high phase velocity EPW ($v_\phi/V_{Te} >> 1$). The EAW solutions were discounted by those early researchers due to their *huge* linear damping with Maxwellian distributions, $-\mathrm{Im}(\omega)/\mathrm{Re}(\omega) \geq 1$ [22,25]. However, other studies of nonlinear Vlasov-Maxwell systems [26,27,28,29,30] found that electrons trapped in the wave electrostatic potential can result in undamped solutions, so-called BGK modes [26], allowing a nonlinear EAW mode to exist. However, the dispersion (obtained by taking a limiting case of the nonlinear problem) produces a lower phase velocity EAW ($\omega \approx 1.31 k V_{Te}$) [27-30] compared to the least-damped (but still heavily damped) linear EAW solution ($\omega \approx 3.6 k V_{Te}$). A fully nonlinear analysis of EPWs gives acoustic-like dispersion for $\omega_{pi} << \omega << \omega_{pe}$ that depend on the EPW field amplitude [31]. In the SHS experiments reported on in this thesis, stimulated scattering from an electrostatic wave was observed at a frequency and phase velocity ($\omega \approx 0.4\omega_{pe}$, $v_{\phi}/V_{Te} \approx 1.4$) between that of an EPW and IAW [32].

The possibility that particles may become trapped in the potential of large amplitude electrostatic wave was mentioned earlier. In theory, these trapped particles are responsible for numerous effects including, a nonlinear frequency shift of EPWs [33,34,35], generation of hot electron tails [36], a reduction in EPW damping [35], and EPW generation due to the beam-plasma or streaming-type interactions [37,38]. In the SHS experiments reported on in this thesis, a few shots were taken to probe the plasma outside of the SHS interaction volume. As will be shown in Chapter 4, fine structure was observed in the Thomson spectra indicating numerous EPWs at distinct frequencies. Additionally, numerous EPW Thomson spectra exhibit a time-dependent broadening in frequency. It is possible that we have made the first experimental observation of the non-linear shift in EPW frequency outlined in [33-35].

In summary, the present SHS laser-plasma experiments have generated a wealth of high-quality data. The work for this dissertation was motivated by the desire to measure and characterize the EPW spectrum driven by SRS in a plasma and see if indeed the distinct daughter waves from the LDI cascade could be observed. The experiments were successful and resulted in various other data such that the dissertation is not simply on one topic. The data shows the first unambiguous observation of LDI cascade and stimulated scattering off of an electron acoustic mode below that of the usual EPW frequency.

The organization of this thesis is as follows. Chapter 2 outlines the laser system, the diagnostics, and discusses in detail the experimental procedures used. Chapter 3 presents the theory and observation of Langmuir cascade. Chapter 4 presents the observation of stimulated electron acoustic scattering (SEAS) and presents one possible model for its explanation. Chapter 5 concludes and summarizes the previous chapters and outlines additional work necessary. Derivations of important equations and results presented in the chapters are provided in several appendices.

Chapter 2: Experimental Procedures

The experiment was conducted at the Los Alamos National Laboratory (LANL) using the TRIDENT laser facility [39]. In the experiment, a preformed plasma is illuminated with a nearly diffraction-limited single hot spot (SHS) laser [40] to drive SRS in a plasma. Although the TRIDENT laser and the SHS experiments are extensively described in the references cited, it is hoped that enough information is provided in this chapter so that the reader need not consult them. Several diagnostics were used to collect data in the experiment. These include

- An absolutely calibrated photodiode to measure the SRS reflectivity levels,
- A streaked SRS backscatter diagnostic to resolve the directly backscattered light in both time and wavelength,
- Energy measurements of the incident heater, interaction, and Thomson probe beams,
- A near backscatter imaging (NBI) diagnostic to assess the amount of light scattered outside of the incident cone,
- A transmitted beam diagnostic (TBD) to observe beam steering and breakup, and
- Collective Thomson scattering diagnostics to diagnose the electron plasma wave (EPW) spectrum driven by SRS or the thermal ion acoustic wave (IAW) spectrum as an indicator of the electron temperature.

In this chapter, these diagnostics are described in detail and any relevant theory of operation is provided. Calibration information for each diagnostic used for interpreting the data presented in subsequent chapters is also provided where appropriate. Plasma characterization measurements are also provided, e.g. determination of electron temperature.

2.1 Overview of the TRIDENT Laser and the Single Hot Spot Configuration

The TRIDENT laser is a Neodymium-Phosphate doped glass (Nd:Glass) system configured in the master oscillator power amplifier (MOPA) architecture. The fundamental harmonic or wavelength of the Nd:Glass laser system is λ = 1054 nm. In laser-plasma interaction (LPI) terminology, the fundamental frequency of a laser system is referred to as 1ω, and the harmonics as 2ω, 3ω, etc. A low energy seed laser is used to form various pulse shapes (e.g. Gaussian or flat-topped) which are then amplified by a series of flash-lamp pumped amplifiers. To mitigate heating effects and prevent optical damage, these amplifiers change initially from smaller diameter rods in the low-energy stages to larger diameter disks in the high-energy stages. Three beams are available at the second harmonic (2ω) wavelength of λ = 527 nm. Two of these beams are high energy (~150 J nominal each) and are usually used for plasma formation and heating. A third, lower energy beam (~1 J nominal) is usually used as the interaction beam and can also be split and frequency converted to provide an additional λ = 351 nm (3ω) or λ = 263.5 nm (4ω) probe beam for use in collective Thomson scattering diagnostics.

A schematic of the experimental setup is shown in Figure 1. The plasma is formed by vaporizing a thin foil target and heating it with a line-focused λ=527 nm laser beam. The targets may be fabricated from any material available in thin foil form. However, parylene (C_8H_8) targets were used primarily in the experiments. The heater beam is defocused so as to create a plasma having density scale lengths transverse and parallel to the interaction laser focal spot of ~200 μm and ~1000 μm, respectively. Thus, the plasma is considered quasi-homogeneous over the entire interaction volume of the SHS (discussed in a later section).

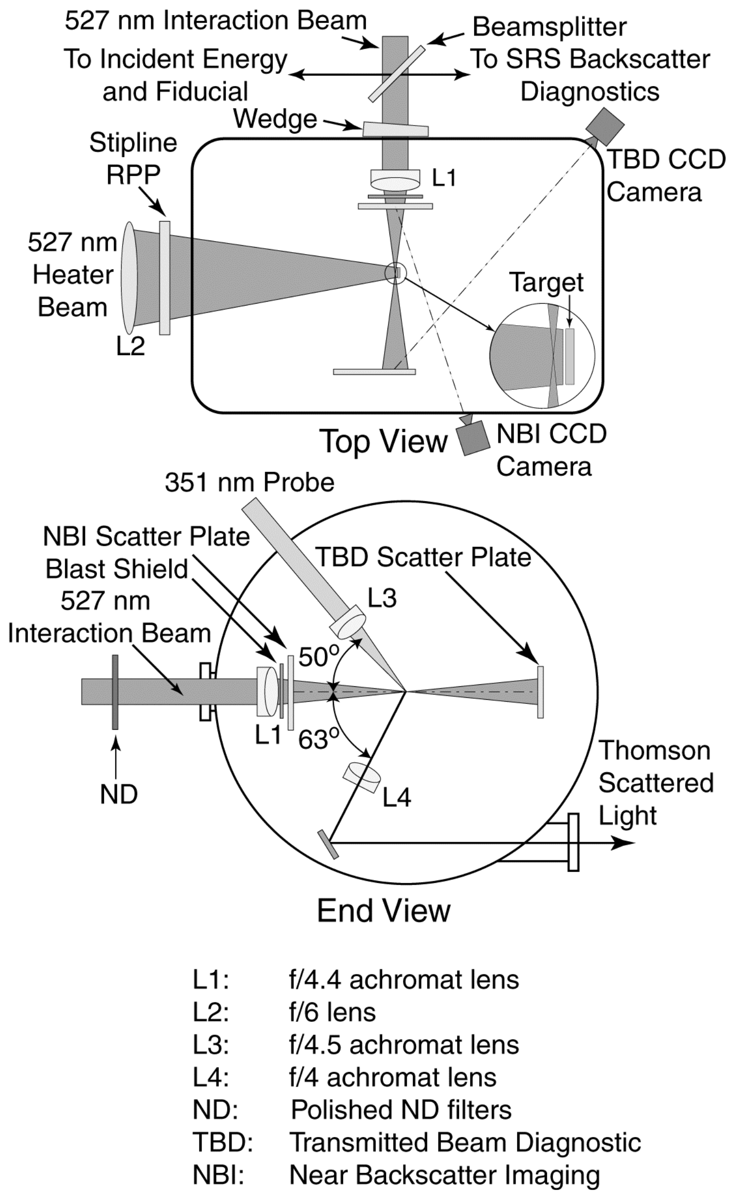

Figure 1. Schematic diagram of the single hot spot experiment.

The relative beam timing is shown in Figure 2. The heater beam has a flat-topped pulse profile with duration of 1.2 ns full-width at half maximum (FWHM). At a time 200 ps after the heater beam is turned off, the interaction beam (λ=527 nm), having a Gaussian pulse shape with a 200±10 ps FWHM, is focused into the plasma through an f/4.4 lens perpendicular to the plasma flow (i.e. parallel to the original surface of the target). The Mach ~2 flow (transverse to the interaction laser beam) has been shown to stabilize self-focusing, and produces nonlinear beam steering [41]. The ultraviolet (λ=351 nm) Thomson probe beam is also a Gaussian pulse with a 200±10 ps FWHM, coincident in time with the interaction beam, and is focused into the plasma through an f/4.5 lens. The Thomson scattered light is collected through the full aperture of the collection optic (f/4). The Thomson scattering diagnostic was set up to look only at the forward propagating EPWs, i.e. those propagating in the same direction as the interaction laser.

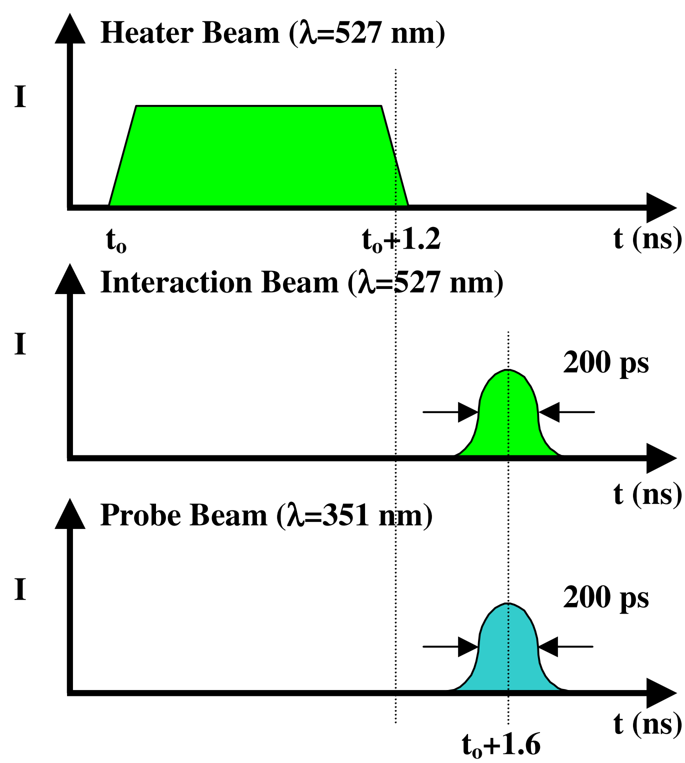

Figure 2. Beam intensity versus time for the single hot spot experiments.

Previous SHS experiments have thoroughly characterized the initial conditions of the plasmas used. Hydrodynamic simulations performed using the computer code LASNEX [42] have also been used to predict the plasma conditions. Data measured on a previous SHS experiment and 2D LASNEX simulation data are combined on one graph for comparison and shown in Figure 3. For the experiments described in this thesis, the location of the SHS was placed at ~400 μm in front of the target, resulting in $n_e/n_c \approx 0.03$-0.032 as inferred from the backscattered SRS data shown later. Here, n_e is the electron density and $n_c \approx 4.02 \times 10^{21}$ cm^{-3} is the critical density above which 527 nm light does not propagate. The definition of the critical density is obtained from the linear dispersion relation for electromagnetic waves (EMW) in a plasma, i.e. $\omega^2 = \omega_{pe}^2 + c^2 k^2$, where

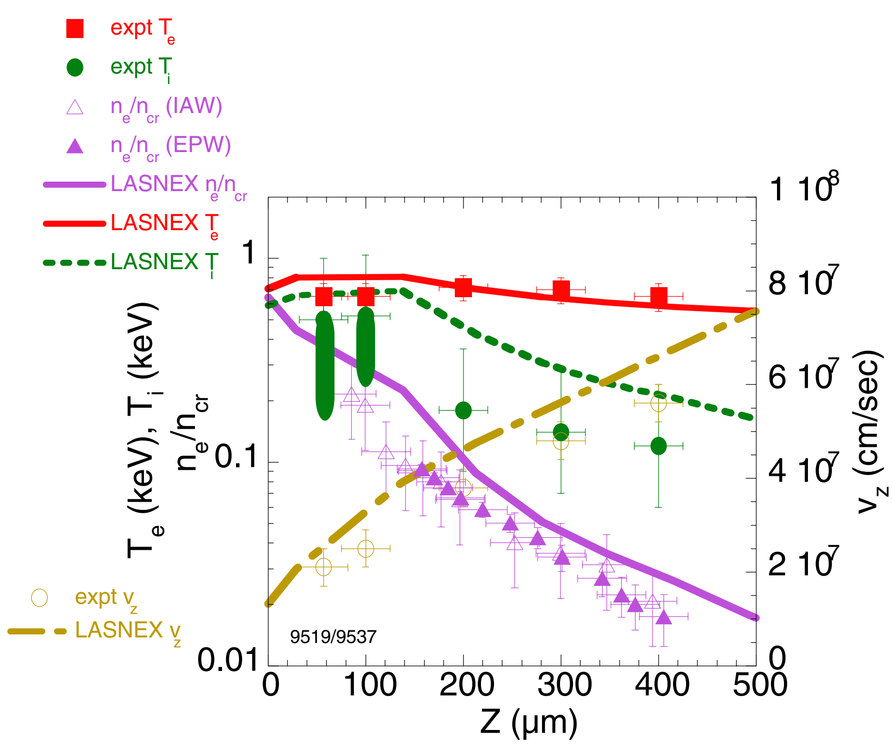

Figure 3. The experimentally measured (CH plasma at t = 1.0±0.1 ns) electron density and temperature, ion temperature, and transverse flow velocity are in rough agreement with 2D LASNEX simulations. All measured values were determined by analyzing the Thomson scattered data in a manner similar to that described in a later section of this chapter.

$\omega_{pe} = \sqrt{n_e e^2 / \varepsilon_o m_e}$ is the electron plasma frequency. When $\omega < \omega_{pe}$ the wavenumber k becomes pure imaginary and the EMW is evanescent. Thus when $\omega = \omega_{pe}$ the EMW ceases to propagate and solving for the critical electron density gives $n_c = \omega_L^2 \varepsilon_o m_e / e^2$, where ω_L is the laser radial frequency The plasma initial conditions are homogeneous on the scale of the laser focal spot volume where the interaction occurs, and enables the observation of fine spectral structure, e.g. that associated with LDI cascade. This removes any ambiguity due to inhomogeneity when interpreting the data.

The targets used were ~1 mm in diameter and ~6.5 μm thick parylene (C_8H_8). Carbon and Aluminum targets were also used in the experiment but provided little data. The carbon targets were first-time prototypes and were prone to severe positioning errors due to their surface roughness and thickness. As a result, no plasma was ever generated at the desired density using the carbon targets. A few thin foil aluminum targets provided some data but their supply was limited. So, the bulk of the data was generated using the parylene targets.

The diffraction theory of light through a circular aperture, predicts that the radial (in r) and longitudinal (in z) intensity profile of the interaction beam at and near focus is given by [43]

$$\mathrm{I}(r) \approx \left(\frac{2J_1(\pi r / \mathrm{F}\lambda_o)}{\pi r / \mathrm{F}\lambda_o} \right)^2 \mathrm{I}_o \text{, and} \qquad \textbf{(1)}$$

$$\mathrm{I}(z) \approx \left(\frac{\sin(\pi z / 8\mathrm{F}^2 \lambda_o)}{\pi z / 8\mathrm{F}^2 \lambda_o} \right)^2 \mathrm{I}_o , \qquad \textbf{(2)}$$

respectively, where λ_o is the laser wavelength (527 nm for the SHS interaction laser) and F is the f-number of the focusing optic. The f-number F = *f*/d is defined as the ratio of the focal length to the optic diameter or actual beam diameter, whichever is less. The f-number is usually specified in shorthand notation as f/#, where # is the calculated f-number. For the present experiments described in this thesis, the interaction laser beam diameter was set at 36 mm using an opaque aperture and thus the full aperture of the focusing lens was not used. The focal length of the focusing lens was 160 mm resulting in an f-number of f/4.4. The actual three-dimensional (3D) intensity distribution near focus is much more complicated than (1) and (2) predict. However, these equations allow one to approximate the extents of the interaction volume of the SHS. The width and length of the SHS at one half of the maximum intensity are obtained from (1) and (2) and given by

$$\mathrm{w} \approx 1.028\mathrm{F}\lambda_o \text{, and} \tag{3}$$

$$\mathrm{L} \approx 7.08\mathrm{F}^2\lambda_o, \tag{4}$$

respectively. Using these relations and the parameters for the SHS experiments, the laser focal spot is characterized by a width of w≈2.4 μm and length of L≈72 μm. The SHS interaction volume is essentially a elliptically-shaped surface of revolution defined by the dimensions of w and L given above. Note that at best focus, the intensity looks like the classic Airy pattern [43]. The radius of the first minima (zero) is found by setting $J_1(\pi r / \mathrm{F}\lambda_o) = 0$. The first minima of the $J_1(x)$ Bessel function occurs at an argument x = 1.22π and thus the diameter of the Airy disk is given by $d = 2.44F\lambda$ [43].

Special care is taken with the interaction beam generation, alignment, and optics in order to produce a wave-front with minimal distortion. This entails such things as using only rod (rather than disk) amplifiers, paying special attention to details like the mounting and alignment of certain optics, minimizing air turbulence throughout the beam path, and limiting the beam diameter to 36 mm in order to use small, high-quality optics [40]. After alignment and prior to the start of full energy shots, the focal spot of the interaction beam is analyzed to see how close it is to the diffraction limit. Figure 4 shows a typical image of the focal spot intensity pattern from a previous experiment. It is seen that the far field contains slightly more energy beyond the first Airy minima compared to

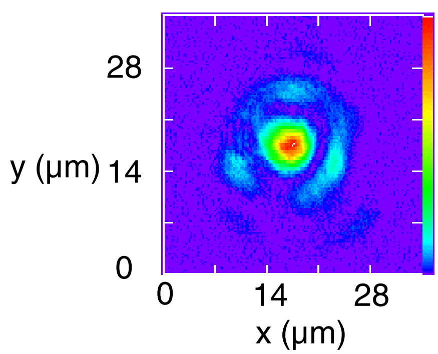

(a)

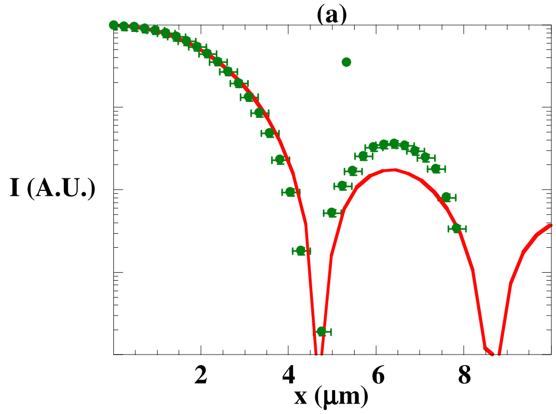

(b)

Figure 4. (a) Actual hot spot intensity pattern at best focus, and (b) lineout of the intensity pattern (data points) compared to the ideal diffraction limit for an f/7 beam. The stray data point in (b) is most likely due to a bad pixel on the CCD camera. For the f/7 527 nm beam, the first Airy minima is expected to occur at a radius of r = 1.22Fλ = 4.5 μm.

the ideal diffraction limit. The performance is very good but not quite perfect and thus we characterize the SHS as the result of a “nearly diffraction limited” beam.

2.2 Incident Beam and Backscatter Diagnostics

Grouped in this section are the incident beam energy calorimeter, the fiducial leg, the streaked SRS diagnostic, the reflected energy photodiode, and the near backscatter imager (NBI). These diagnostics allowed for measurement of the energy incident in the interaction beam, provide an absolute wavelength and time reference, resolution of the directly backscattered light in wavelength versus time, measurement of the energy reflected by stimulated Raman scattering (SRS), and detecting how much, if any, backscattered light did not traverse the incident light cone, respectively.

A schematic diagram of the incident beam path is shown in Figure 5. The interaction beam (C-beam) is guided from a lower optics table using a polarization preserving (i.e. the electric field is not rotated) periscope P_1. Polished and calibrated neutral density (ND) filters can be inserted in the beam path to reduce the incident energy, and thus, the intensity of the interaction beam. Nominally, 500 mJ unfiltered will produce a focal spot intensity of ~1×10^{16} W/cm^2 in the plasma. The interaction beam then passes through a 50/50 beam splitter BS_1. Half of the beam goes to a fiducial time delay leg and an energy measurement pick off and the other half goes to the target chamber. The path length of the fiducial leg is set to produce a time delay of ~1 ns (i.e. ~11.8 inches round trip path difference) from light directly backscattered from the target. This provides an absolute wavelength (λ = 527 nm) and time calibration for all backscattered

SRS measurements. A mirror on a kinematic mount can also be placed in the fiducial path to aid in the alignment of the backscatter diagnostics.

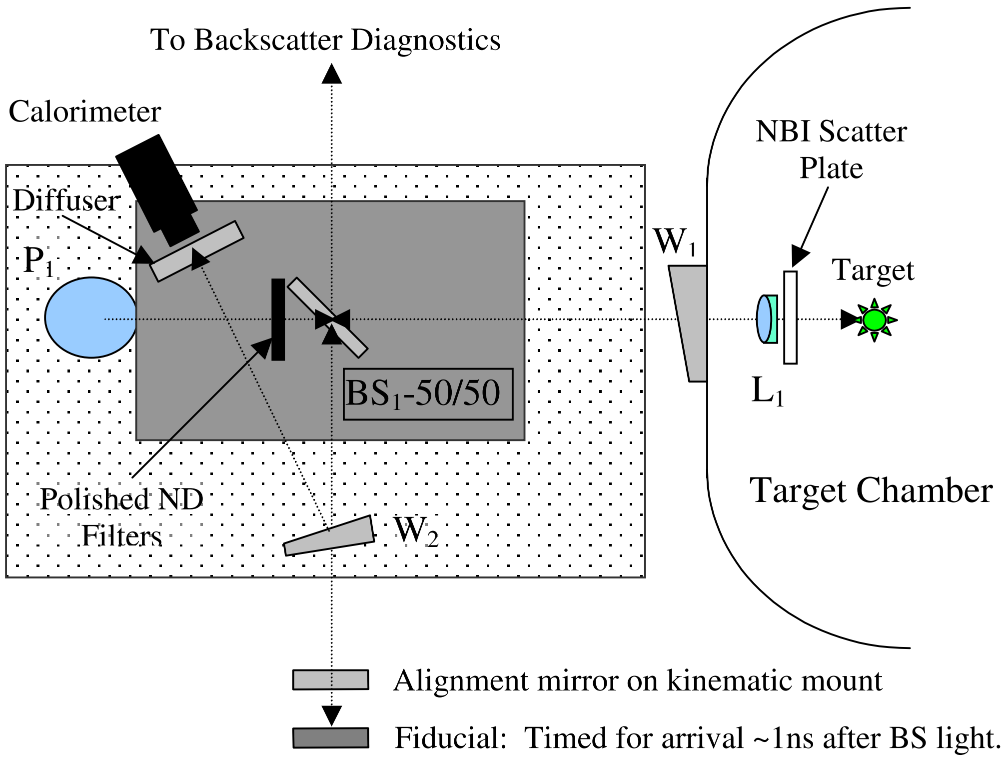

Figure 5. Schematic diagram of the incident interaction beam path.

The incident energy is measured directly with a calorimeter. Prior to the start of experiments, several calibration shots are performed to determine the actual energy that is being measured. This is accomplished with the aid of another temporary calorimeter placed downstream of BS_1 that measures the energy directed into the target chamber. Wedge W_1 directs any reflections of the incident beam out of the path that the backscattered light would follow. The backscattered light is collected using the f/4.4 achromatic focusing optic L_1 and thus follows approximately the same path that the incident beam would. The backscattered light is reflected off of BS_1 and sent to the streaked SRS and photodiode diagnostics.

A schematic of the backscatter diagnostics is shown in Figure 6. Periscope P_2 preserves polarization of the collimated backscattered light beam and lowers it to the level of the spectrometer entrance slit. The backscattered light is split by beam splitter BS_2 so that half goes to the spectrometer and the other half goes to the reflected energy photodiode. Lenses L_2 and L_3 focus the light onto the spectrometer slit and the photodiode diffuser plate, respectively. Neutral density filters are placed in front of L_2 and the photodiode diffuser plate to accommodate the wide range of reflected energies encountered. The ½ meter Chromex spectrometer disperses the backscattered light in wavelength. Thus, what is actually measured is the free space wavelength of the backscattered light. The Hamamatsu streak camera allows for the temporal resolution of

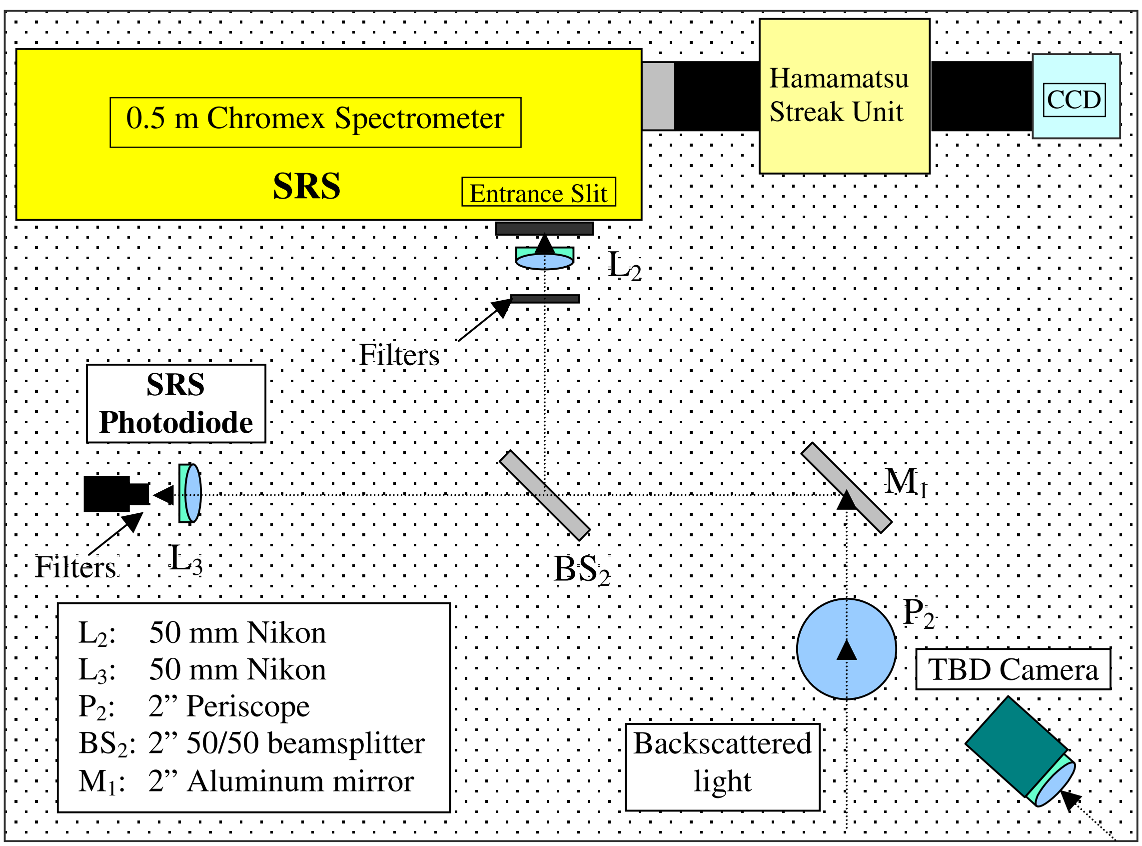

Figure 6. Schematic diagram of the backscatter diagnostic table.

the signal on various time scales. The CCD camera is thermo-electrically and water cooled to provide a low noise background and captures the data image to a binary file.

Prior to data collection, the dispersion of the particular grating that will be used (i.e. wavelength versus pixel on the CCD image) is determined using calibration lamps. Calibration lamps containing different gas mixtures are available and those that provide spectral lines (i.e. transition radiation) in the region of wavelengths that will be measured are used for the calibration. A sample calibration image and lineout are shown in Figure 7(a). A linear fit is made to the known wavelengths and a typical calibration plot is shown in Figure 7(b). The 100 grid-per-millimeter (gpmm) grating was used to collect the majority of the data on the SRS spectrometer and its calibration was 0.577 nm/pixel. On a handful of shots, the SRS spectrometer was used to look for stimulated electron acoustic scattering (SEAS) described in a later chapter. For these shots the 1800 gpmm grating was used and its calibration was 0.03 nm/pixel. The calibration is checked periodically or if the spectrometer grating or optical alignment is changed.

Calibration of the time axis for a particular streak window is performed by observing the number of pixels in the full width at half maximum (FWHM) of the interaction laser pulse. The interaction pulse is known to have a FWHM duration of 200 ps. For the data shots, the SRS streak camera was kept on the 2 ns streak window and the time axis calibration was determined to be 1.77 ps/pixel.

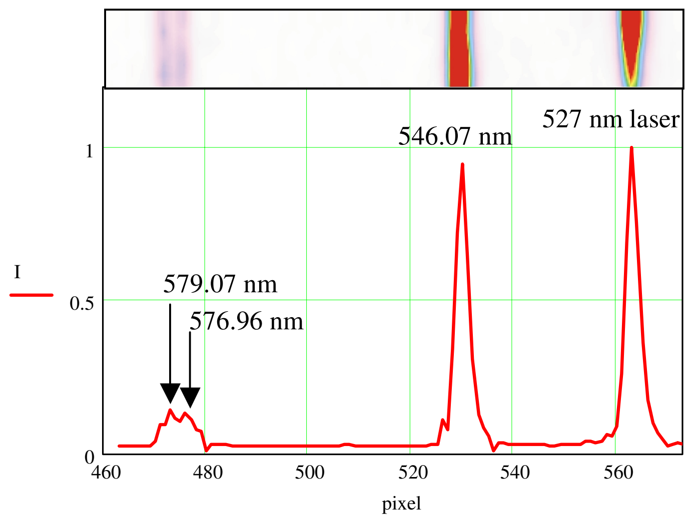

(a)

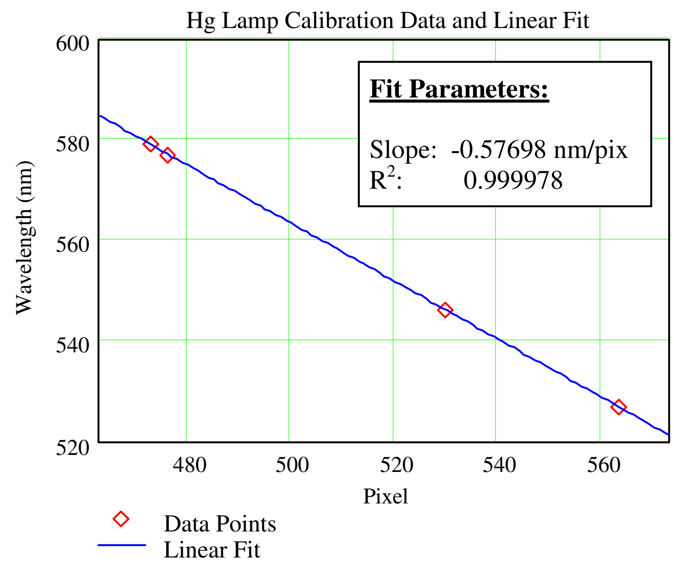

(b)

Figure 7. Mercury (Hg) lamp calibration images for the SRS spectrometer with 100 gpmm grating. (a) Actual Hg lamp image and 527 nm laser lines with column sum lineout normalized to the peak intensity, and (b) Linear fit to the data.

A typical SRS diagnostic image is shown in Figure 8. Knowing the calibration of the diagnostic, as described above, one can determine the free-space wavelength of the backscattered SRS light. In the very homogeneous SHS plasmas, this wavelength is an excellent indicator of the electron density. Since SRS is a resonant process, i.e. energy

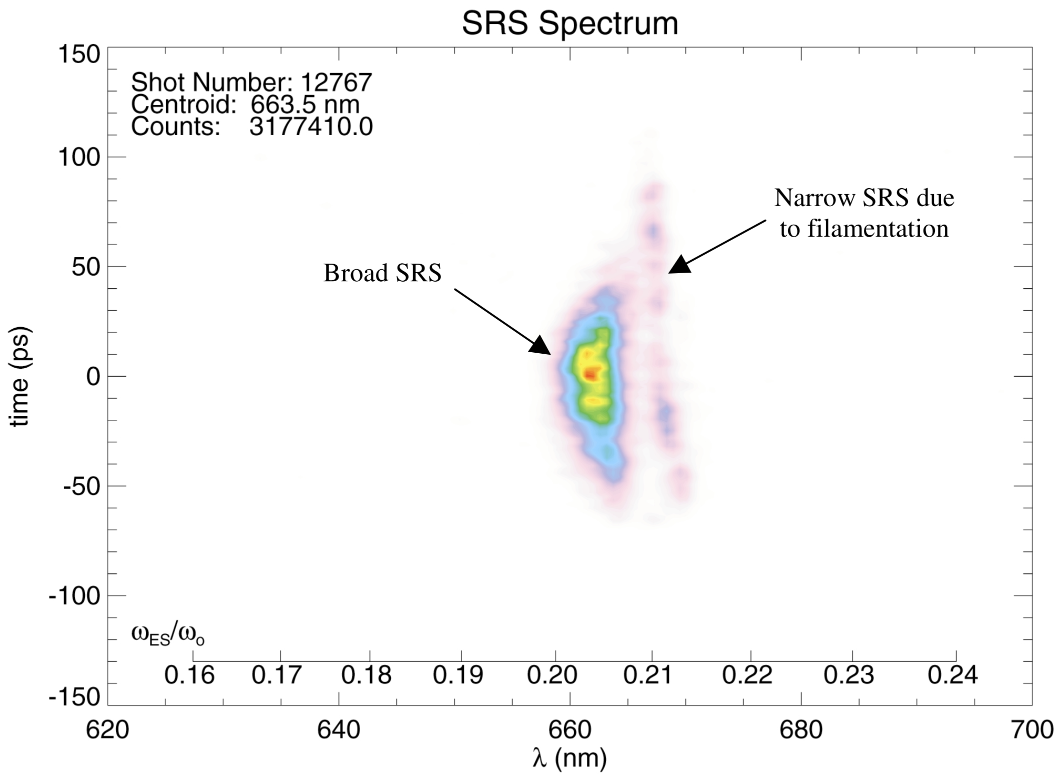

Figure 8. Typical backscattered SRS image. This image shows bifurcation, i.e. splitting of the SRS into two distinct density pockets most likely due to filamentation. The ω_{ES}/ω_o scale predicts the normalized frequency at which the electrostatic wave will appear and is used for correlation with other diagnostics.

and momentum are conserved, a rough estimate of the electron density can be obtained by looking at the frequency matching, condition for the SRS process

$$\omega_L = \omega_S + \omega_{ES}, \qquad \textbf{(5)}$$

where ω_L, ω_S, and ω_{ES} are, respectively, the laser, scattered light, and electrostatic wave frequencies. The electrostatic wave frequency will be approximately equal to the plasma frequency, i.e. $\omega_{ES} \approx \omega_{pe} = \sqrt{e^2 n_e / \varepsilon_o m_e}$. As defined previously, the laser frequency is equal to the plasma frequency at the critical density n_c, thus $(\omega_{pe} / \omega_L) = \sqrt{n_e / n_c}$. Subtracting ω_{ES} from both sides of (5), factoring out the laser frequency, using the definitions and approximations above, and realizing that in free space $\omega_L = 2\pi c / \lambda_L$, (5) can be recast as

$$\lambda_S = \frac{\lambda_L}{\left[1 - \sqrt{\frac{n_e}{n_c}}\right]}, \tag{6}$$

or equivalently solving for the ratio n_e/n_c gives

$$\frac{n_e}{n_c} = \left[1 - \frac{\lambda_L}{\lambda_S}\right]^2. \tag{7}$$

A much better estimate for the electron density is obtained by considering the effect of the finite electron temperature on the electrostatic wave frequency. The linear dispersion relation for an electron plasma wave (EPW) in a plasma is given by

$$\omega_{ES}^2 = \omega_{pe}^2 + 3\mathrm{V}_{Te}^2 k_{ES}^2 = \omega_{pe}^2 (1 + 3k_{ES}^2 \lambda_{De}^2), \tag{8}$$

where $\mathrm{V}_{Te} = \sqrt{k_B T_e / m_e}$ is the electron thermal velocity, k_B is Boltzmann's constant, T_e and m_e are the electron temperature and mass, respectively, k_{ES} is the EPW wave number, and $\lambda_{De} = \mathrm{V}_{Te}/\omega_{pe}$ is the electron Debye length. Usually, the electron temperature is considered to be multiplied by k_B, converted to electron volts (eV) and grouped into one term T_e. So, in actuality the EPW frequency will be greater than the plasma frequency and is dependent on its wave number and the electron temperature. To determine what the EPW frequency will be, one needs to consider that SRS is a three-wave resonant process and solve, simultaneously, the linear dispersion relations for the incident laser and scattered electromagnetic waves (EMW)

$$\omega_L^2 = \omega_{pe}^2 + c^2 k_L^2, \tag{9}$$

$$\omega_S^2 = \omega_{pe}^2 + c^2 k_S^2, \tag{10}$$

and the linear dispersion relation for the EPW (8), the frequency matching condition (5), and the wave number matching (momentum conservation) condition given in one dimension (direct backscatter) by

$$k_L = k_S + k_{ES}\,. \tag{11}$$

Of course, the plasma frequency must first be estimated so solving this system is an iterative process in which one starts with the measured value for T_e, a guess value for the electron density and then refines this value such that the scattered light wavelength matches the observation. An even better estimate for the electron density can be obtained by replacing (8) with the dispersion relation for an EPW derived using kinetic theory

$$D(k,\omega) = 1 - \frac{1}{2k^2\lambda_{De}^2} Z'\left(\frac{\omega/\omega_{pe}}{\sqrt{2}k\lambda_{De}}\right) = 0, \tag{12}$$

where Z' is the derivative of the plasma dispersion function [44] with respect to its argument. . Since (12) has an infinite number of roots, we choose only the one that is weakly damped (i.e. $k^2\lambda_{De}^2 << 1$) and corresponds approximately to (8). This method is also an iterative process and was the one used to arrive at any electron density values stated in this dissertation.

This iterative process of simultaneously solving the linear dispersion relations and resonance matching conditions is referenced many times in the thesis and often referred to as the *ideal calculation*. Given input parameters, this ideal calculation is used to predict numerous quantities, including

- n_e/n_c given the assumed and measured plasma and laser conditions, i.e. T_e, T_i, and λ_L, or vice versa, the expected SRS wavelength given n_e/n_c, T_e, and T_i,
- The Thomson probe and collection angles given a particular EPW frequency and wavenumber determined from resonance matching the SRS-LDI interaction,
- Resonance matching the stimulated electron acoustic interaction outlined in a later chapter,
- Creating plots showing the resonance matching for various laser plasma interactions, and
- Determining instability thresholds and growth rates for various laser plasma interactions.

Mathcad [45], an interactive and integrated environment for performing and communicating math-related work, was used to perform the calculations mentioned above. Rather than try to explain these calculations here, the Mathcad worksheets used for the calculations are presented in their entirety in Appendix E. The worksheets have been commented to hopefully make clear what is going on. In addition to its scratch pad user interface, the benefit of using Mathcad to solve the resonance matching problem is that an arbitrary number of equations can be solved simultaneously for the unknowns in a *solve block* thus making iterative calculations simple.

It is apparent that one must still know the electron temperature to get an accurate value for the electron density. In a later section of this chapter, measurements are described from which the electron temperature is ascertained using collective Thomson scattering off of thermal levels of ion acoustic waves (IAW) in the plasma. These measurements revealed that the electron temperature in these SHS experiments was initially ~480±50 eV and decreased to ~300±50 eV over the duration of the probe pulse. At the mid-point of the interaction pulse T_e ~ 390 eV. Note that one cannot make a direct comparison of these T_e values to those shown in Figure 3 as they are measured at different times in the evolution of the plasma. In Figure 3 the electron temperature is measured at the tail end of the heater pulse (t ~ 1.0 ± 0.1 ns). The Thomson scattering measurement is performed at ~200-400 ps after the heater beam is turned off and the plasma has cooled significantly due to expansion. [46,47] The plasma cooling can be easily understood by considering that the temperature corresponds essentially to an energy density. As the plasma expands, its volume increases. Without a source of energy, e.g. the heater beam, the energy density and thus the temperature of the plasma decreases.

The reflected energy photodiode (see Figure 6) must also be calibrated prior to the start of experiments. This is accomplished during the same calibration shots performed for the incident energy calorimeters by placing a mirror in the fiducial leg. The output of the photodiode is a time-dependent voltage. This voltage signal is sent via a low-loss coaxial transmission line to a Tektronix 7250 fast transient digitizer (~6 GHz bandwidth). Since the response time of the diode is much greater than time duration of the backscattered light pulse, what is seen on the digitizer is actually the diode's impulse response to the applied signal. Thus, the peak of the diode's voltage signal represents the time-integrated reflectivity, or in other words, the total reflected energy. Neutral density filters must be placed in the path of the light sent to the reflected energy photodiode in order to accommodate the wide range of energies encountered without saturating the signal. During the diode energy calibration shots, a reference optical density (OD) must be recorded in order to calculate future reflected energies since the filter OD changes quite frequently. The diode voltage is multiplied by the ratio of actual to reference OD values to provide a voltage which is then divided by the calibration of the diode (in V/J) to obtain the actual reflected energy. Calibration data for the reflected energy photodiode is shown in Figure 9. The slope of the liner fit to the data points is 0.582 V/J with a reference filter OD of 6.88 (attenuation of $10^{-6.88} = 1.32 \times 10^{-7}$).

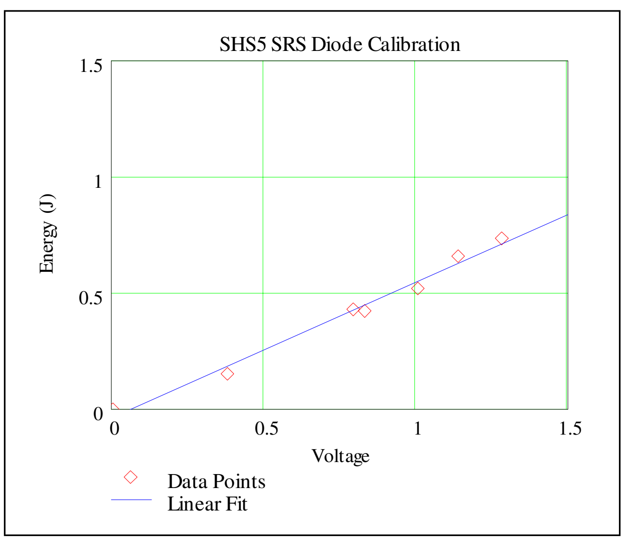

Figure 9. Calibration curve for the reflected energy photodiode. The slope of the linear fit to the data is 0.582 V/J with a reference filter optical density of 6.88.

Nonlinear pondermotive beam steering effects may direct the backscattered light out of the incident light cone [41]. This light is detected using the near backscatter imaging (NBI) diagnostic. The NBI measures the time-integrated light reflected off of a scatter plate placed in front of the interaction beam focusing optic L_1. The scatter plate has an aperture slightly larger than the incident beam diameter. The NBI can be used to estimate the amount of backscattered energy directed outside of the incident light cone, e.g. when trying to reconstruct an abnormally low reflected energy measurement, and also as an indicator of significant nonlinear effects, e.g. beam steering, occurring. Typical NBI images are shown in Figure 10.

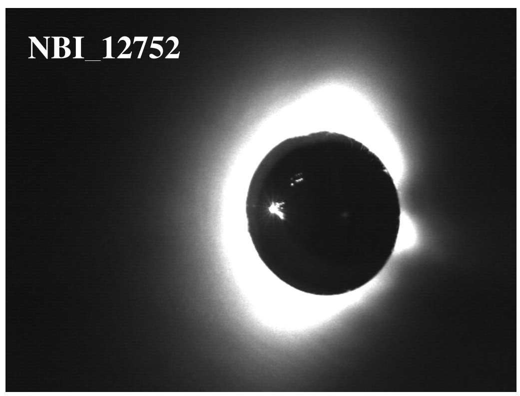

(a)

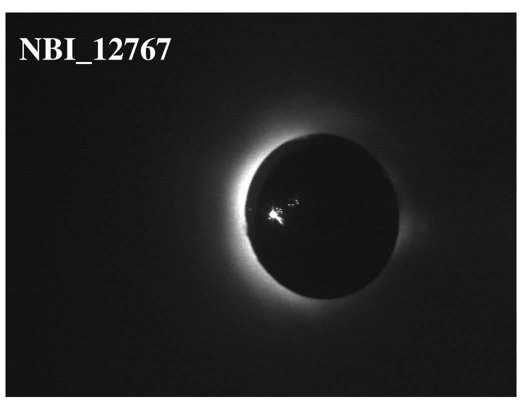

(b)

Figure 10. NBI images showing (a) a high intensity ($I = 1.8 \times 10^{16}$ W/cm^2) shot exhibiting significant backscattered beam deflection, and (b) a low intensity ($I = 4.4 \times 10^{15}$ W/cm^2) shot with little light scattered out of the incident cone. In both figures, the outline of the NBI scatter plate aperture is clearly visible.

2.3 Transmitted Beam Diagnostic

As seen in the measured and simulated plasma conditions shown in Figure 3, the plasma exhibits a density gradient in a direction perpendicular to the interaction beam. This density gradient results in a variation of the index of refraction in the plasma, and thus, refraction of the incident beam is expected in a direction opposite to that of the density gradient, i.e. towards lower densities or slower phase velocities. This can be best described by rearranging the linear dispersion relation for an EMW in a plasma (9) to a form that expresses the index of refraction $n = c / \mathrm{v}_\phi = ck / \omega$ in terms of other known quantities, i.e.

$$n = \frac{ck_L}{\omega_L} = \sqrt{1 - \frac{\omega_{pe}^2}{\omega_L^2}} = \sqrt{1 - \frac{n_e}{n_c}}\,. \qquad \textbf{(13)}$$

For a plasma, the index of refraction is < 1. As the electron density decreases the index of refraction increases towards unity and the phase velocity of the EMW decreases towards the limit of the speed of light. Snell's law [43] tells us that the angle a light ray will make at the interface between media with different indices of refraction n_1 and n_2 is

$$n_1 \sin\theta_1 = n_2 \sin\theta_2 \Rightarrow \sin\theta_2 = \frac{n_1}{n_2} \sin\theta_1\,. \qquad \textbf{(14)}$$

If n_2 is the index at a lower electron density, $n_1/n_2 > 1$ and thus, $\theta_2 > \theta_1$. Stated simply, for a plasma the light ray will refract towards the region having a lower density. Previous experiments [41] and calculations have shown that for the SHS plasmas the maximum expected refraction is ~6.5±0.5^o and that intensity-dependent, nonlinear flow-induced beam steering can act to deflect, or steer, the interaction beam by as much as an additional ~3.5^o. Essentially, this beam steering is due to density depleted regions caused by the pondermotive force being swept away from the target by the plasma flow. The net result is that the beam becomes trapped in these density depleted pockets and is then steered significantly due to a transverse flow. The transmitted beam diagnostic (TBD) measures any combination of beam refraction and steering and is also an indicator of beam break up or filamentation. Thus, if there are significant nonlinear effects such as beam steering or filamentation occurring on a particular shot they will be revealed by the TBD. Additionally, if the TBD shows an undeflected beam this clearly indicates an extremely low density plasma or no plasma at all. Oddly enough, the latter occurred several times during the experiments for various reasons, e.g. heater beam misfire, target falling off of its stalk, etc. Typical TBD images are shown in Figure 11.

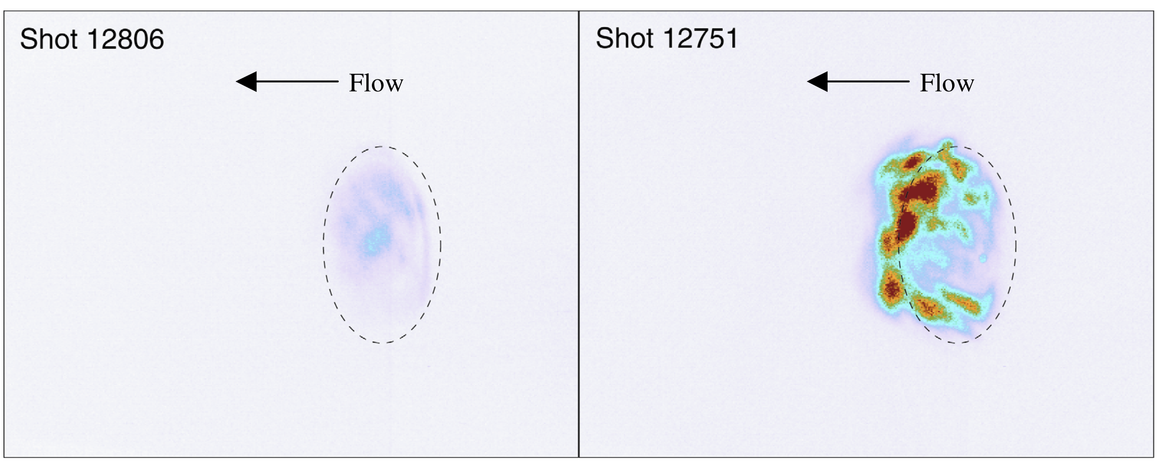

(a) (b)

Figure 11. TBD images showing (a) a low-intensity (I = 2.2×10^{15} W/cm^2) shot with little beam break up, and (b) a high-intensity (I = 2×10^{16} W/cm^2) shot with significant beam break up and deflection. The undeflected beam spot is indicated by the dashed line which appears elliptical since the TBD CCD camera was not oriented normal to the scatter plate.

The amount of beam refraction and deflection can be estimated by knowing the f-number F of the focusing optic and having a reference image of an undeflected beam, i.e. an image taken of the transmitted beam spot when no plasma was present. Via the geometry shown in Figure 12, the total angle that the beam spot will span is given by $\theta = 2\tan^{-1}(1/2\text{F})$. For example, the cone of a laser beam focusing and defocusing through an F/4.4 optic will span ~13$^{\text{o}}$. One can then compare the deflected beam and reference images on the TBD image and determine the degrees of combined refraction and deflection based on the relative deviation from the reference image.

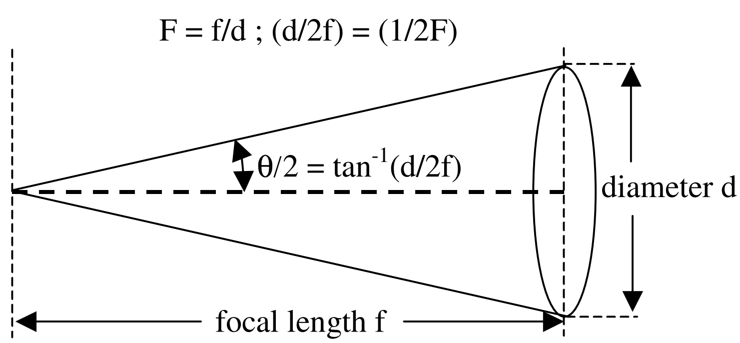

Figure 12. The geometry of a focusing beam is used to determine the angle that the beam cone will span. This depends on the f-number of the optic used.

2.4 Collective Thomson Scattering Diagnostics

Collective Thomson scattering was used to diagnose EPWs driven by SRS and LDI occurring in the plasma. A brief tutorial on Thomson scattering is given later in this section. Half of the scattered light was sent to a diagnostic that resolved the scattered light in wavelength and time while integrating over all wave vectors (Streaked Thomson) and the other half was sent to a diagnostic that resolved the wavelength and angle on the collection optic (effectively giving ω vs. $\vec{k}$) while integrating over the time duration of the probe pulse (Gated Thomson). The latter was accomplished by imaging the collection optic surface rather than its focal plane [48] and will be described in more detail later in this section. The Gated Thomson optical path also served as a useful tool for aligning and verifying the overlap of the interaction and Thomson probe beams. Schematic diagrams of the Streaked and Gated Thomson diagnostics are shown in Figure 13 and Figure 14, respectively. Data obtained using these diagnostics will be presented in the following chapters.

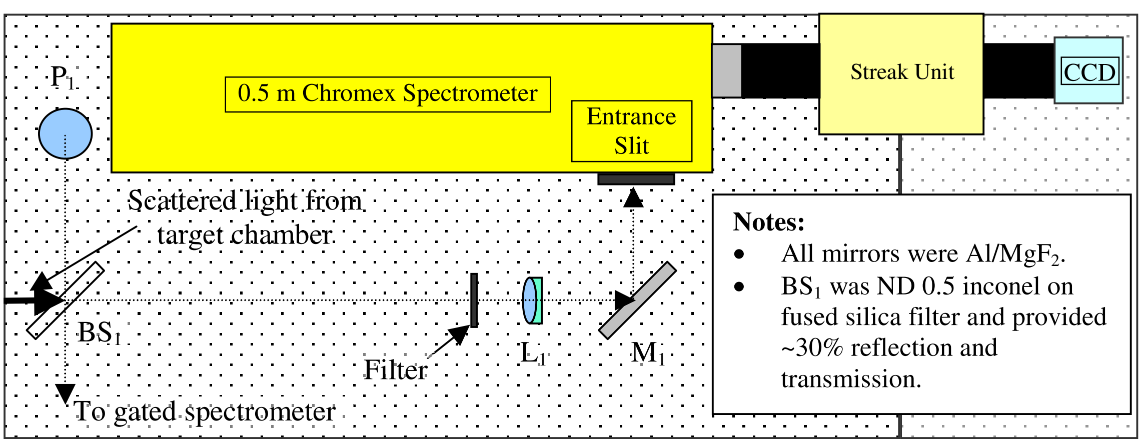

Figure 13. Schematic diagram of the Streaked Thomson diagnostic.

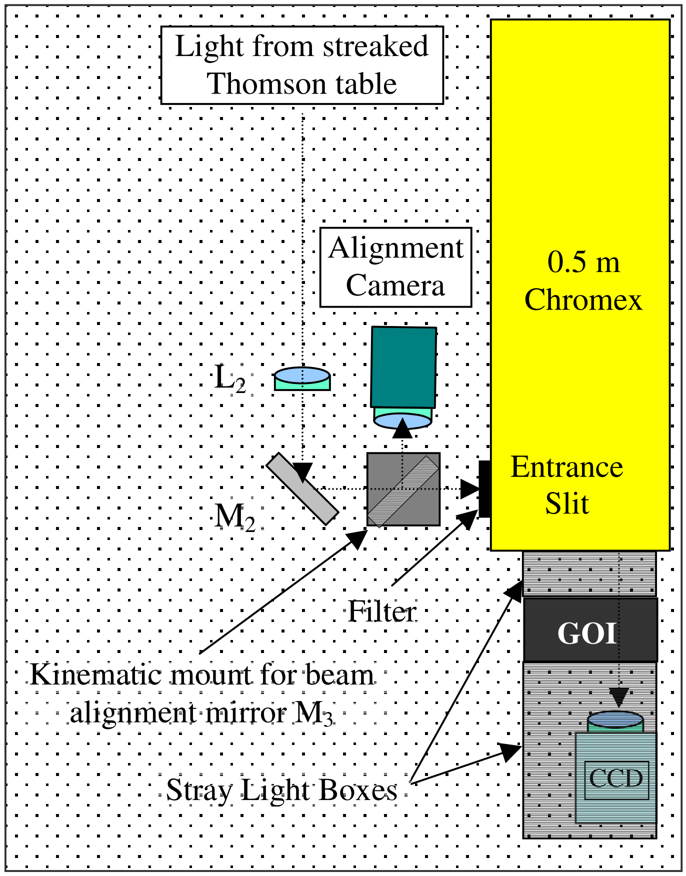

Figure 14. Schematic diagram of the Gated Thomson Diagnostic.

As seen in Figure 1, the ultraviolet (λ=351 nm) Thomson probe beam is focused into the plasma through an f/4.5 lens at a nominal angle of 50^o. The finite beam diameter and focal length of the focusing optic allows for a range of wave vectors at angles of 50±6.3^o to participate in the Thomson scattering process (see Figure 12). The Thomson scattered light is collected at a nominal angle of 63^o through the full aperture of the collection optic (f/4) thus accommodating wave vectors at angles of 63±7.1^o. The collimated scattered light is directed out of the target chamber by a two inch magnesium-fluoride (MgF_2) coated mirror. Coated mirrors are used throughout the Thomson scattering diagnostic beam paths as they offer superior reflectivity over ordinary silvercoated mirrors in the UV range and thus minimize loss of signal. The scattered light is split using BS_1 - an OD = 0.5, 2" square inconel on fused silica filter. This filter was used in place of a wideband UV 50/50 beam splitter as one was not available. It provided ~30% reflection and transmission with the remainder of the signal being absorbed in the filter material. Half of the scattered light propagates through UV filters, lens L_1, and mirror M_1 and is focused onto the slit of the spectrometer. M_1 has x-y tilt adjustments to allow easy alignment on the spectrometer slit. The other half of the scattered light is sent to a polarization-preserving periscope P_1 (also constructed using UV mirrors) which elevates the light to the level of the Gated Thomson optic table. Lens L_2 provided magnification of the image and was positioned to focus the plane of the collection optic on the spectrometer slit. Mirror M_2 also had x-y tilt adjustments to allow easy alignment on the slit. Kinematically mounted mirror M_3 could be placed in the light path to allow looking upstream at the target using a camera and television monitor. The target alignment hole (~100-150 μm in diameter) was used as a reference to align the interaction and probe beam overlap prior to every shot. The gated optical imager (GOI) provided a snapshot of the dispersed light over a time duration of ~120-600 ps. The light path from the output of the spectrometer, through the GOI, and to the CCD camera was enclosed with opaque material to prevent stray light from contaminating the very weak signal.

As with the streaked SRS diagnostic, both the Streaked and Gated Thomson diagnostics must be calibrated in wavelength using the same method as previously described. Calibration curves and curve fit parameters for these diagnostics are provided in Figure 15 and Figure 16. The time axis calibration for the ST spectrometer in the 2 ns window was calculated to be 1.33 ps/pixel.

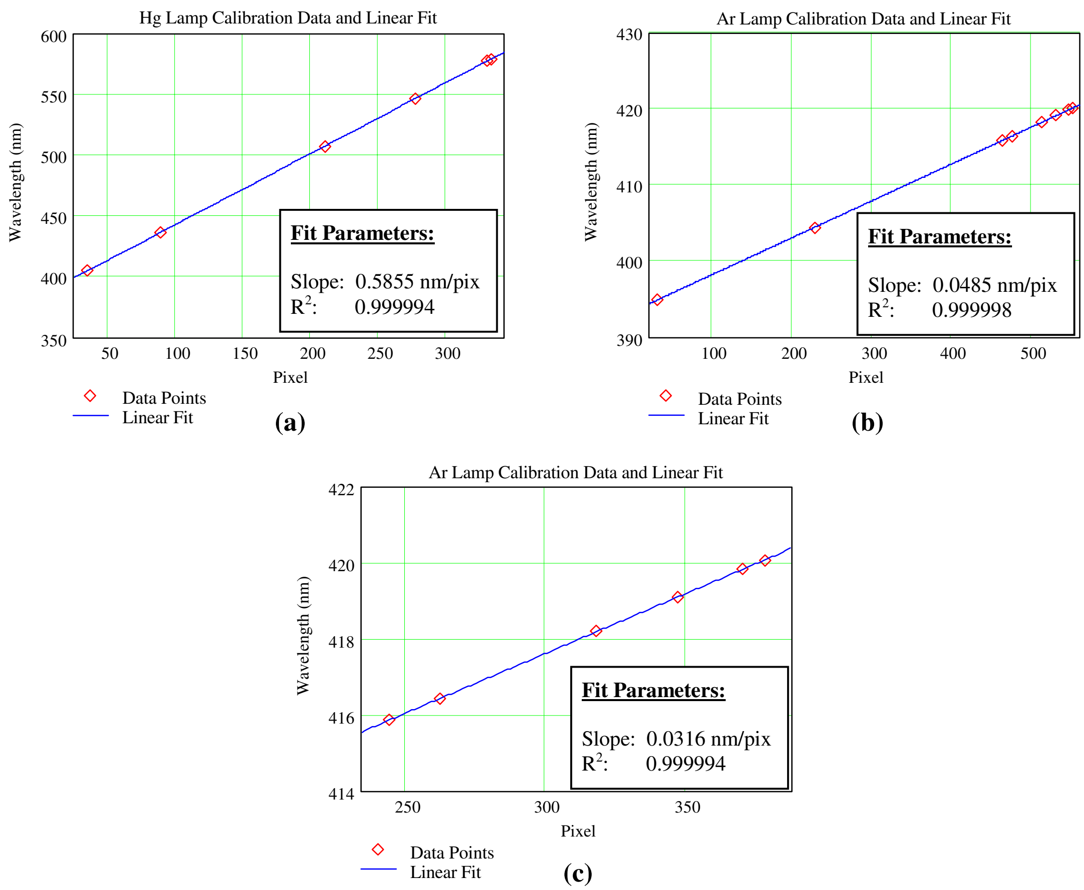

Figure 15. Streaked Thomson diagnostic wavelength calibration curves and curve fit parameters for (a) 100 grid per millimeter (gpmm), (b) 1200 gpmm, and (c) 1800 gpmm gratings.

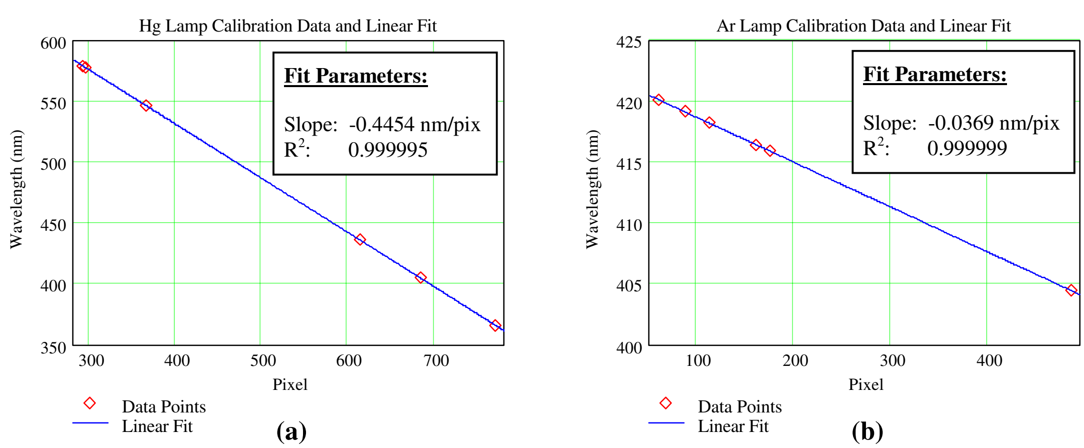

Figure 16. Gated Thomson diagnostic wavelength calibration curves for (a) 100 gpmm and (b) 1200 gpmm gratings.

The Gated Thomson diagnostic required additional calibration so that the angular displacement on the optic surface could be determined. This was accomplished by placing an opaque mask having a notch with known dimensions on the collection optic and then determining the number of pixels that the notch spanned on the CCD image. Knowing a length on the surface of the collection optic and the optic f-number is equivalent to knowing an angular displacement and ultimately this can be translated into a wave vector magnitude for the EPW being diagnosed. For our calibration, we placed an opaque piece of paper with a 1/8 inch notch in it on the surface of the collection optic. A piece of tape (4.44 mm wide) was also placed across the optic for an additional reference dimension. A picture of the calibration mask and the resultant CCD image is shown in Figure 17. The 4.44 mm wide tape was 90 mm from best focus and spanned 39 pixels giving a calibration of 0.072 ^{o}/pixel. To complete the calibration, a Mathcad

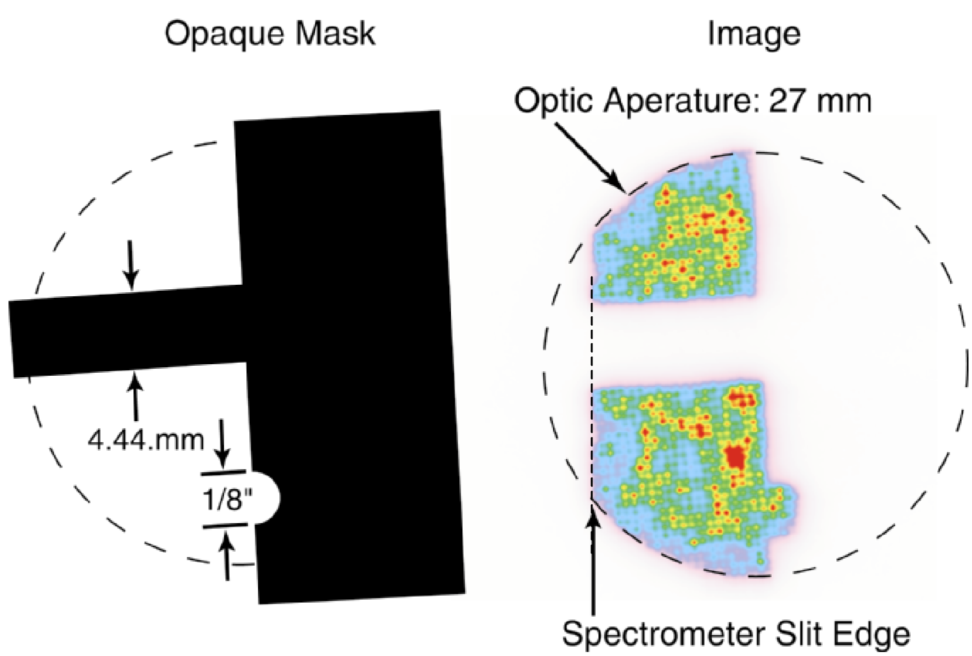

Figure 17. Mask and CCD image used for angular displacement calibration of the Gated Thomson diagnostic.

worksheet was used to determine matching conditions for SRS and LDI and thus calculate the scattered light angle and wave vector magnitude for multiple LDI cascades. The calculated change in EPW wave number normalized to the laser wave number was $\Delta k/k_o = 0.133$ for a change in scattering angle of $\Delta\theta = 4.1^o$. Thus, for a given angular displacement on the collection optic the normalized change in EPW wave vector magnitude is $\Delta k/k_o = \Delta\theta/30.9$. Knowing this and the previous calibration, one can generate an axis calibration that represents the change in EPW wave number normalized to the laser wave number. The resultant calibration was $(\Delta k/k_o) = 0.0023$/pixel.

Thomson scattering was used as a diagnostic tool in the experiments. Rather than providing a detailed derivation of the theory of Thomson scattering, an abbreviated tutorial is presented. For more exhaustive theory and derivations the reader is referred to the literature (c.f. [14], [49], and [50] and references therein). Thomson scattering is a useful diagnostic in plasma experiments and can yield significant information about the plasma, such as the electron temperature and density. The goal of any diagnostic method should be to minimize the perturbation that it will have on the system being measured while at the same time gathering the desired information on the state of the system. Thomson scattering accomplishes these goals.

A much simplified explanation for the scattering of EMWs by a plasma is that the incident fields, e.g. from the probe laser, accelerate free charges (i.e. electrons and ions) in the plasma. These moving and accelerated charges produce currents which in turn are the sources of the scattered radiation. If the electrons and ions participating in the scattering have a thermal velocity spread, the scattered radiation will be broadened due to Doppler shifts. The incident probe EMW causes acceleration of both electrons and ions.

The ions are much heavier than electrons as the mass ratio of a proton ion to electron is $M_i/m_e \approx 1837$. Thus, for the same imposed fields the acceleration of and subsequent radiation generated by ions is considerably less than that from electrons and can often be neglected. Even though the radiation directly from ions can be neglected they will have an effect on the radiation from electrons as the electrons act to shield out the ion charges. The radiation due to uncorrelated electrons and ions in the plasma is called incoherent Thomson scattering.

Collective oscillations, such as the EPW and IAW electrostatic normal modes, may exist in a plasma. When electrons are participating in these collective oscillations, either directly or indirectly due to their shielding effect on the ions, the radiation they emit adds coherently. The radiation due to correlated electron and ion oscillations in the plasma is called collective Thomson scattering. Thus, the total radiation scattered by a plasma will consist of a relatively weaker incoherent component and a stronger coherent (or collective) component exhibiting peaks at the electrostatic normal modes present in the plasma. Instabilities such as SRS and Stimulated Brillouin Scattering (SBS) can develop in the plasma and enhance the level of EPW and IAW fluctuations above thermal levels. This will result in an enhancement of the collective mode peaks in regions of frequency and wavenumber that satisfy the resonance matching conditions for the particular interaction.

The effect of collective modes on the scattered radiation intensity is taken into account by a *shape factor* given by (c.f. [14])

$$S(\mathbf{k},\omega) = \frac{2\pi}{n_e k}\left[\left|1-\frac{\chi_e(\mathbf{k},\omega)}{\varepsilon(\mathbf{k},\omega)}\right|^2 f_{1e}\left(\frac{\omega}{k}\right) + \left|\frac{-\chi_e(\mathbf{k},\omega)}{\varepsilon(\mathbf{k},\omega)}\right|^2 \sum_\alpha Z_\alpha^2 f_{1i\alpha}\left(\frac{\omega}{k}\right)\right], \qquad \mathbf{(15)}$$

where, $\chi_e(\boldsymbol{k},\omega)$ is the electron susceptibility, f_{1e} and f_{1i} are , respectively, the first order electron and ion distribution functions (resulting from the linearization of the electron and ion Vlasov equations), Z is the ion charge number, and the permittivity is given by $\varepsilon(\mathbf{k},\omega) = 1 + \chi_e(\mathbf{k},\omega) + \sum_\alpha \chi_{i\alpha}(\mathbf{k},\omega)$, where the sum is over all ion species present in the plasma. The shape factor is used to numerically fit the experimentally measured Thomson scattered light intensity data in order to determine parameters such as the electron density and temperature. The kinetic equations (i.e. Vlasov equation and plasma dispersion function [44]) are used to evaluate these effects and determine the susceptibility of the individual charge species.

Basically, the permittivity of the plasma will cause the incoherent spectrum to be enhanced at normal modes of the plasma, i.e. electrostatic longitudinal modes such as ion acoustic and electron plasma waves. Like SRS and SBS, scattering off of normal modes in the plasma obeys the frequency and wave vector matching conditions $\omega_P = \omega_S + \omega_{ES}$ and $\vec{k}_P = \vec{k}_S + \vec{k}_{ES}$, where the subscripts P, S, and ES represent the probe, scattered, and electrostatic waves, respectively. In addition to frequency and wave vector matching, all waves involved in the scattering process must also obey their linear dispersion relations. Resonant wave vector matching is illustrated in the scattering diagram shown in Figure 18. For a given orientation and wavenumber of the ES wave, the probe and collection angles must adjust accordingly to satisfy the frequency and wave vector matching conditions and thus coherent peaks in the scattered light intensity will only be observed at the appropriate probe and collection angles.

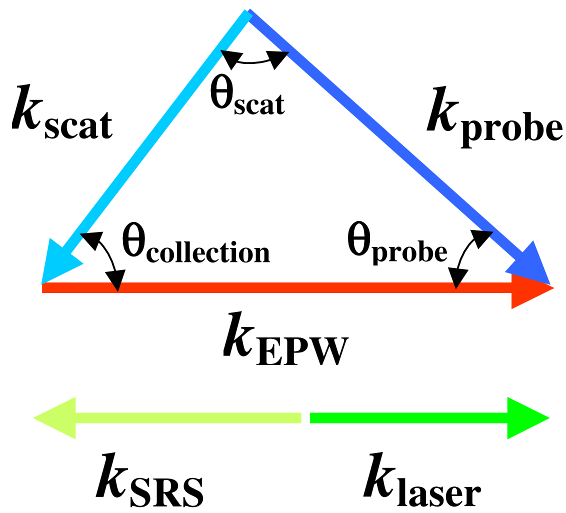

Figure 18. Scattering diagram for the electron plasma wave resulting from backscattered SRS.

The growth rate for the SRS instability (presented in a later chapter) is maximized when the laser, scattered EMW, and EPW are collinear and the scattered EMW is propagating in a direction opposite to that of the laser. This is called backscattered SRS or BSRS for short. Thus, those EPWs driven by SRS that are collinear with the laser wave vector and propagating in the same direction will grow the fastest. The probe and collection angles required to diagnose a particular EPW are determined by frequency and wave vector matching the interaction. The Thomson probe was set up to investigate plasma densities near $n_e/n_c \approx 0.03$ based on previous SHS experiments producing significant SRS in this regime. Calculations of the anticipated probe and collection angles for an electron temperature Te = 500 eV are presented in Table 1. These calculations were performed using the Mathcad worksheet shown in Appendix E (Section 16) and determined the nominal angles of 50 and 63 degrees for the probe and collection optics (scattering angle θ_s = 67^o). The finite f-number of these optics allowed probing waves parallel to k_o (the free space wave number of the SHS laser beam) from $1.34k_o$ to $1.76k_o$. We calculated that our diagnostic would allow resolution of the SRS EPW and up to three EPWs from subsequent forward-propagating LDI cascade steps. As pointed out, the average T_e was somewhat less than 500 eV and this may have affected the total number of cascades that could have been observed. As shown in more detail in a subsequent chapter, for an assumed constant density (a good assumption for the SHS experiments) a decrease in temperature will result in a larger deviation in wavenumber ($\Delta k/k_o$), and thus, larger angle on the collection optic between subsequent cascade steps. If the temperature deviation is large enough, the LDI EPWs will move out of the range of the collection optic.

Table 1: Calculated parameters used to determine probe and collection angles for T_e = 500 eV.

n/n_c	Wave	λ (nm)	k (m^{-1})	λ_s (nm)	k_s (m^{-1})	θ_{probe}	$\theta_{collect}$
0.05							
	SRS EPW	2150.22	202222.17	419.47	147412.3	45.14	58.35
	2nd cascade	2195.9	176458.8	417.78	148029.8	49.51	65.44
	4th cascade	2237.65	150624.76	416.3	148572.12	53.19	72.55
0.03							
	SRS EPW	2598.6	210228.02	405.81	153455.22	45.65	55.95
	2nd cascade	2666.01	190600.25	404.22	154072.04	49.29	61.03
	4th cascade	2731.15	170868.66	402.76	154639.3	52.61	66.01

On several shots, thermal ion acoustic waves were probed in order to monitor the background electron temperature. Since the deviation in pulse shape and energy of the heater beam was negligible and the electron temperature varies little with distance from the target (see Figure 3), monitoring the electron temperature on only a small percentage of the total number of shots is sufficient to provide an indication of electron temperature for all shots in the experiment. Figure 19 shows the Streaked Thomson image for shot number 12809. A horizontal lineout of this image at the peak intensity of the probe pulse is presented in Figure 20 along with a numerical fit to the data generated using the multi-species Thomson scattering form factor (15) corrected for instrument resolution (~1 Å). In general, the one-half of the peak separation is an indicator of the acoustic velocity and

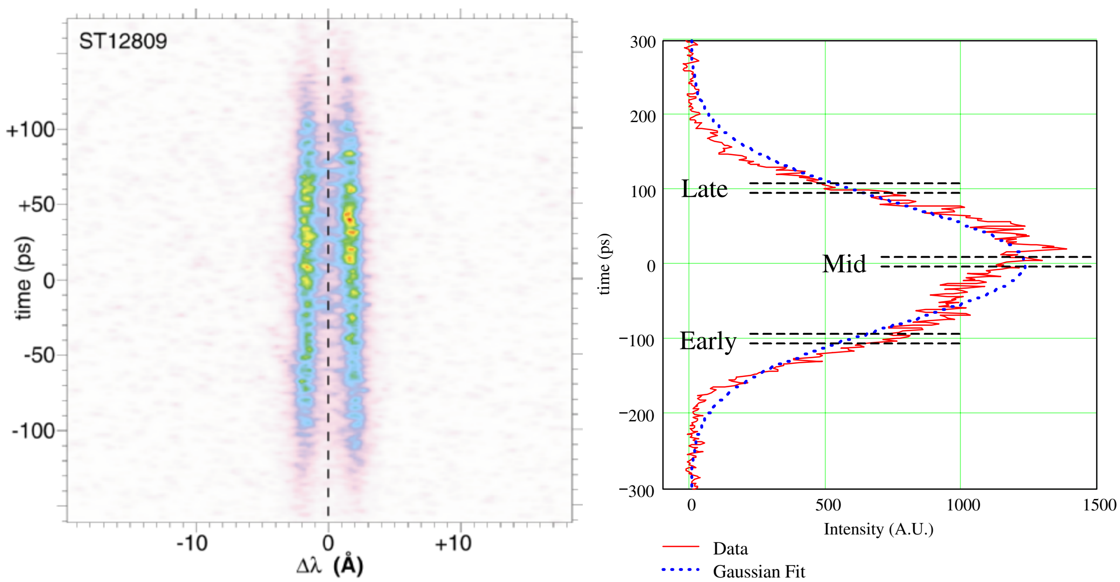

(a) (b)

Figure 19. (a) Streaked Thomson image from scattering off of thermal levels of ion acoustic waves. (b) Wavelength integrated lineout of data and Gaussian fit showing definitions for early, mid and late time temperatures.

thus the electron temperature. A difference in the amplitude of the Stokes (downshifted) and anti-Stokes (up shifted) peaks may appear due to a relative drift between the electrons and ions V_{ei}. The numerical fit underestimates the region between the peaks most likely due to the effects of collisions which are neglected in (15). The early, mid, and late times are defined by looking at the peak and FWHM of a Gaussian fit to the wavelength integrated scattered light intensity (see Figure 19(b)). Thus, mid-time corresponds to the peak intensity of the scattering image, and the early and late times, respectively, correspond to minus and plus one-half of the full width from the mid-time. By numerically fitting the Thomson scattering form factor to the data, the early, mid, and late time T_e, respectively, were determined to be ~480 eV, ~390 eV and ~300 eV (all ±50 eV). As with other calculations, a Mathcad worksheet was used to implement the multi-species Thomson form factor and numerically fit it to the data. This worksheet is provided in Appendix E (Section 21).

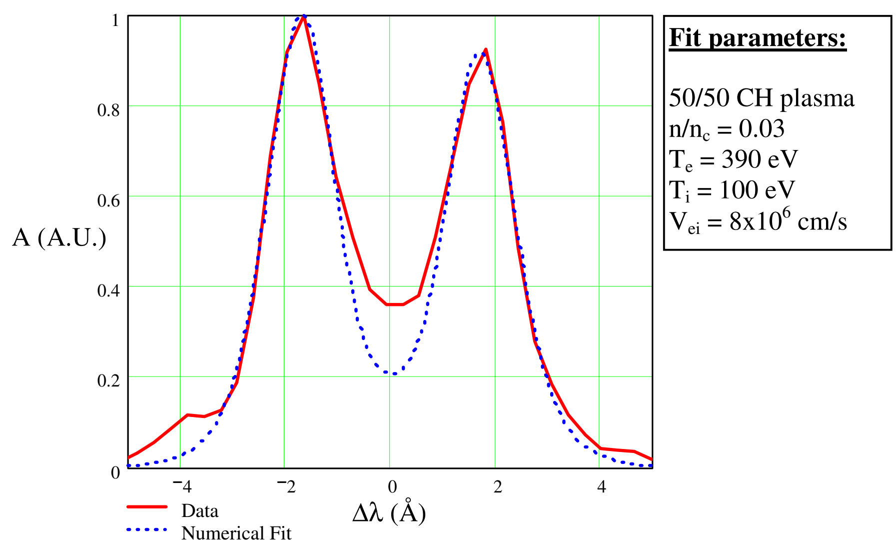

Figure 20. Mid-time lineout of IAW Thomson scattering data (solid line) and numerical fit (dashed line) of the Thomson shape factor. The amplitudes of both curves have been normalized to their maximum values and are presented in arbitrary units (A.U.).

Chapter 3: Observation of Langmuir Cascade

The results presented in this chapter, in my opinion, represent the first unambiguous experimental observation of the Langmuir decay instability (LDI) cascade driven by stimulated Raman backscatter. The electron plasma wave (EPW) spectrum resulting from SRS and LDI is measured using collective Thomson scattering, and structure is observed in the spectra consistent with LDI cascade. At least two LDI cascade steps are inferred from the measurements presented. The data shows excellent agreement between the backscattered SRS, time-resolved Thomson, and time-integrated Thomson spectra.

In this chapter the theory of SRS and LDI is first presented so that a general understanding of these effects is gained prior to proceeding to presentation and interpretation of the experimental data. Next, the experimental results are presented and explained. Correlation between LDI and the saturation of SRS is discussed in relation to data illustrating these phenomena. LDI cascade was observed on only a handful of the ~75 energy-on-target shots. It is desirable to attempt to develop trends that would predict in what regimes the cascade would and would not be present. All of the data collected in the experiment was analyzed for general trends and these are outlined in a later section. Clear cut trends on where LDI cascade occurs could not be ascertained. In general, the single hot spot (SHS) experiments yield results that are closely approximated by nonlinear coupled mode theory. As such they are an excellent test bed for theory-to-practice experiments.

Now that LDI cascade has been established, a parameter study is necessary to understand the scaling of the number of cascades with plasma parameters, measure the energy in the cascade EPWs, and to investigate further the possible role of LDI in limiting the growth of SRS. All of this work is important but must be deferred to future experiments.

3.1 The Theory of SRS and LDI

Control of parametric laser-plasma interactions is essential to the success of inertial confinement fusion (ICF) [1,2]. Stimulated Raman scattering (SRS) [3,4]is one such interaction involving the resonant decay of an incident electromagnetic wave (EMW) into a scattered EMW and an electron plasma (or Langmuir) wave (EPW). SRS is undesirable not only because it can cause losses in drive energy and illumination symmetry but also because it can trap and accelerate electrons that could preheat the fusion capsule. The onset and scaling of SRS has been the subject of much investigation [5].

The dispersion relation for SRS is derived in Appendix A and it is reiterated here for a convenient reference

$$\boxed{D_L = \frac{1}{4}\mathrm{v}_o^2 k^2 \omega_{pe}^2 \left[\frac{\left(\hat{e}_o^* \bullet \hat{e}_+\right)^2}{D_{T+}} + \frac{\left(\hat{e}_o \bullet \hat{e}_-\right)^2}{D_{T-}}\right]}. \qquad \textbf{(16)}$$

Since the up-shifted, or Stokes, electromagnetic wave (EMW) governed by the dispersion relation D_{T+} does not satisfy the resonance matching condition, $\omega_o = \omega_T + \omega_L$, it is usually considered non-resonant and its contribution can be neglected. The dispersion relation for SRS is thus simplified to

$$D_L D_{T-} = \frac{1}{4} \mathrm{v}_o^2 k^2 \omega_{pe}^2 \left(\hat{e}_o \bullet \hat{e}_-\right)^2 . \qquad \textbf{(17)}$$

On the left-hand side is the product of the linear dispersion relations for the EPW and the scattered EMW. On the right-hand side is the coupling or growth term. The coupling term has a geometrical dependence on the polarization vectors of the incident laser and scattered EMW. In a plane containing both the pump and scattered EMW wave vectors, the dot product of their polarization vectors can be maximized for any arbitrary propagation direction (see Figure 21(a) where $\hat{e}_L \equiv \hat{e}_o$). However, when the two EMW wave vectors are propagating anti-parallel resonance matching dictates that the magnitude of the EPW wave vector is maximized, thus maximizing the growth rate for the SRS interaction. With respect to the direction of the laser pump propagation, the SRS EMW traveling in the directly backscattered direction will have the maximum growth. The maximized interaction is then one-dimensional and can be most easily visualized on a 1D ω vs. k matching diagram as shown in Figure 21(b). The maximized SRS interaction also happens to be the easiest measurement to perform experimentally. This is because the lens used to focus the incident interaction laser beam is also used to collect the backscattered light (see Figure 5).

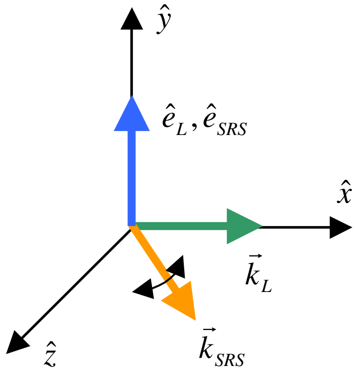

(a)

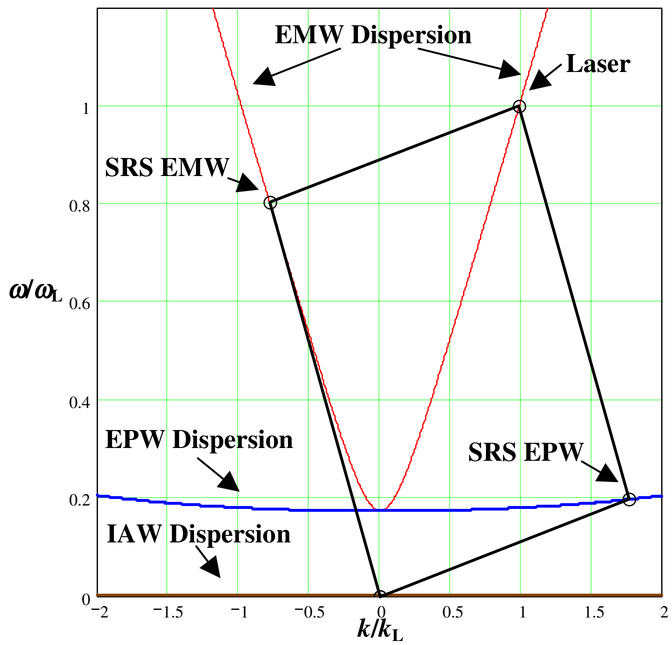

(b)

Figure 21. (a) Diagram showing polarizations of the pump and scattered EMWs for both propagating in the same plane, and (b) 1D frequency and wave vector matching diagram illustrating the maximized SRS interaction. Note that frequencies and wavenumbers are normalized to that of the laser.

Numerous instabilities, such as, SRS, stimulated Brillouin scattering (SBS), the two-plasmon interaction (TP), the plasmon-phonon interaction (PP), and filamentation can occur during the interaction of an intense laser with a plasma. These instabilities can occur simultaneously with SRS and LDI and scatter energy in all directions or in the case of filamentation focus down and intensify the incident laser. The experiment was only set up to monitor SRS in the direct backscatter direction and Thomson probe forward propagating EPWs resulting from SRS and LDI. Thus, based solely on an argument of total energy conservation, it is plausible that these other instabilities could have had some effect on the observed behavior of SRS and LDI cascade, especially if the growth rate for the particular instability exceeded its threshold which is proportional to the damping of the daughter waves involved in the interaction [65]. For parameters typical of the present SHS experiments, the growth rates and thresholds for some the above mentioned instabilities are collected in Table 2. For a more exhaustive stability analysis of these (and other) laser-plasma interactions and the definitions for the growth rates c.f. [4, and 65]. Table 2 is not meant to be a listing of all possible instabilities that could be present, but rather, is meant to show the possibility of other processes occurring simultaneously with SRS and LDI. It is seen that SRS, SBS, and LDI are all predicted to be above the convective threshold for the chosen parameters. The growth rates of SRS and SBS are even calculated to be above the absolute threshold. At this low value of n_e/n_c the threshold for the TP and PP interactions is not exceeded due to the large Landau damping of the daughter waves.

The spatial growth rates for thermal and pondermotive filamentation [51] were also evaluated and are listed in Table 2. The threshold for thermal filamentation is loosely defined here as providing one e-fold increase in the laser intensity which for a plasma of length L implies 2KL = 1. Taking the growth length as the length of the SHS (~75 μm) it is seen that using this simple analysis, both the thermal and pondermotive filamentation thresholds are expected to be exceeded. One element missing from the filamentation model in [51] is supersonic (Mach ~2) flow transverse to the direction of laser propagation. This supersonic transverse flow has been experimentally shown to stabilize filamentation [41] and is also present in the present SHS experiments. Thus even though the thresholds for thermal and pondermotive filamentation calculated using the simple models are exceeded, filamentation is not expected be significant in the present SHS experiments until very high intensities (~10^{16} W/cm^2).

Table 2: Nonlinear coupled mode growth rates for various laser plasma instabilities for the parameters 50/50 CH plasma, $n_e/n_c = 0.03$, $I_o = 2\times10^{15}$ W/cm^2, $\lambda_L = 527$ nm, T_e 350 eV, and $T_i = 100$ eV. The growth rates and thresholds are normalized to the laser frequency and the direction of maximum growth is with respect to the direction of the laser propagation. The convective and absolute thresholds are represented by γ_c and γ_a, respectively. If the growth rate for an interaction is $\gamma_c < \gamma_{max} < \gamma_a$, the spatial growth rate κ_{max} (normalized to the laser wavenumber) is given in parenthesis. Spatial growth rates for filamentation are given in μm^{-1} and for calculating the threshold (i.e. 2KL > 1) L = 75 μm was used.

Interaction	**γ_{max} (κ_{max})**	**γ_c**	**γ_a**	**Direction**
SRS: EMW → EMW+EPW	3.9×10^{-3}	4.73×10^{-4}	2.4×10^{-3}	Backscatter
SBS: EMW → EMW+IAW	1.04×10^{-3}	7.7×10^{-5}	4.6×10^{-4}	Backscatter
LDI: EPW → EPW+IAW	1.9×10^{-4} (5×10^{-3})	1.72×10^{-4}	2.4×10^{-4}	Backscatter
TP: EMW → EPW+EPW	1.2×10^{-3}	0.387	-	At 45° angles in the plane ⊥ to k_L
PP: EMW → EPW+IAW	0.016	0.087	-	Sidescatter
Filamentation	**K_{max} (μm^{-1})**	**$2K_{max}L$**		**Direction**
Thermal	0.077	11.5		NA
Pondermotive	0.021	3.2		NA

In quasi-homogeneous ignition-relevant plasmas, the EPW amplitude can be large for moderate SRS reflectivity so that saturation by nonlinear mechanisms is expected and observed [6,7,8,9]. One possible source of non-linearity is coupling of SRS to other parametric processes via wave-wave interactions. One such mechanism is the Langmuir decay instability (LDI) [3,10,11], where the daughter EPW from SRS grows to a significant amplitude and decays into an EPW and an ion acoustic wave (IAW). LDI occurs when the amplitude of the primary EPW exceeds a threshold that is proportional to the product of the damping rates for the secondary EPW and IAW [65]. The growth rate for LDI is maximized when the daughter EPW and IAW are propagating anti-parallel and parallel, respectively, to the primary EPW. Thus, the LDI interaction is maximized when the SRS interaction is maximized. Subsequent EPW decays due to LDI are possible if their amplitudes exceed the threshold. Here the terminology used is that an EPW generated by LDI is called an LDI cascade step and, collectively, more than one cascade step is called LDI cascade. The LDI cascade can saturate SRS since wave energy from the SRS EPW couples into secondary EPWs and IAWs that are non-resonant with the SRS process. The saturation effect is strongest when the daughter waves are strongly damped (but not so strongly damped that the threshold for the LDI interaction is not exceeded).

Backward (relative to the direction of the interaction laser) propagating EPWs presumed to be from LDI have been observed in laser-plasma experiments [12,13] and LDI has been observed in ionospheric plasma experiments [15,16]. Observation of Langmuir turbulence (i.e. the plasma was so strongly excited that a continuous spectrum of frequencies is present) in a laser-produced plasma has been reported recently [17]. However, it could not be established whether strong turbulence or weak LDI cascade was observed in those experiments due to inhomogeneity [18,19] and the experiment used a random phase plate (RPP) smoothed interaction beam so there were multiple interacting hot spots. The conclusions of Montgomery [18] would also apply to all previously published “LDI observation” experiments in which the plasma inhomogeneity was too large to observe the fine structure associated with LDI cascade.

The LDI and subsequent cascades are visualized on the 1D ω vs. k matching diagram as shown in Figure 22. Three cascade steps are shown in the diagram. Although the IAW phase velocity has been exaggerated in Figure 22 to illustrate the LDI cascade process, it is still seen that the frequency separation between cascade steps is small. The frequency separation can be estimated using the fluid dispersion relations for EPWs and IAWs and LDI kinematics. Starting with the dispersion relation for EPWs (8) and subtracting one EPW from the next subsequent cascade results in $\omega_{EPW1}^2 - \omega_{EPW2}^2 = 3V_{Te}^2(k_{EPW1}^2 - k_{EPW2}^2)$. Expanding the expressions on both sides of this equation gives $(\omega_{EPW1} + \omega_{EPW2})(\omega_{EPW1} - \omega_{EPW2}) = 3V_{Te}^2(k_{EPW1} + k_{EPW2})(k_{EPW1} - k_{EPW2})$. The difference between EPW frequencies is the IAW frequency and the sum of the EPW

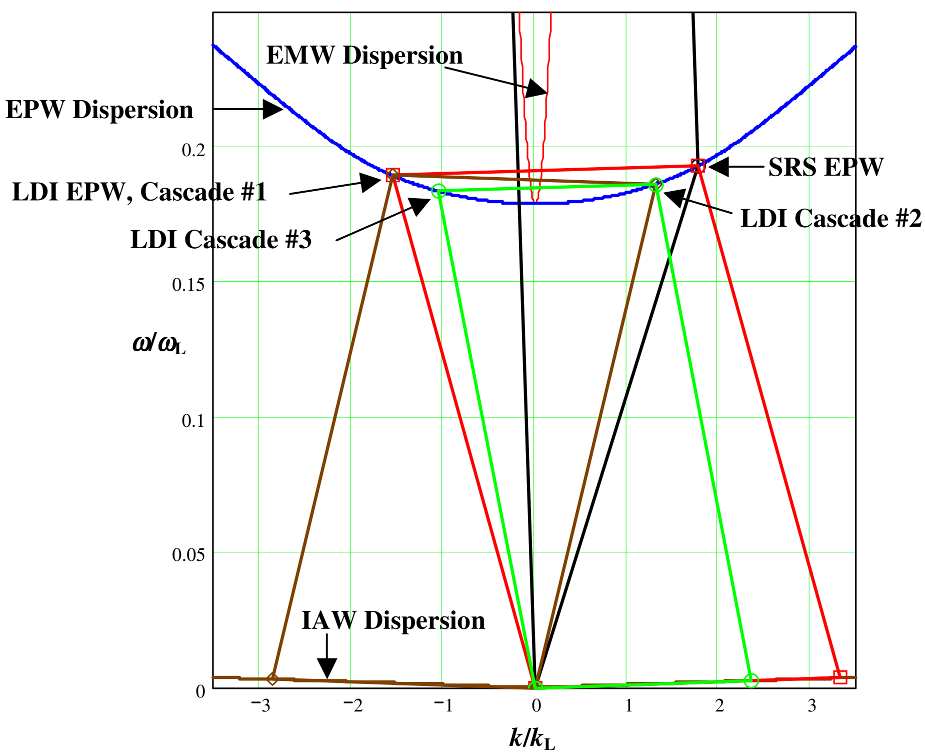

Figure 22. 1D frequency and wave vector matching diagram illustrating the maximized SRS, LDI and LDI cascade interaction. Note that frequencies and wavenumbers are normalized to that of the laser and for this figure, the IAW phase velocity has been exaggerated to illustrate the LDI cascade process.

wave numbers is the IAW wavenumber. Additionally, since the EPW frequency is much higher than that of the IAW, the sum of EPW frequencies is ~$2\omega_{pe}$. Using the above approximations and defining $\Delta k_{EPW} = (k_{EPW1} - k_{EPW2})$ results in $2\omega_{pe}\omega_{IAW} = 3V_{Te}^2 \Delta k_{EPW} k_{IAW}$. Since the IAW frequency is given by $\omega_{IAW} = c_s k_{IAW}$ and the Debye length is defined as $\lambda_{De} = V_{Te} / \omega_{pe}$ the previous result can be simplified to $\frac{2}{3}\frac{c_s}{V_{Te}} = \Delta k_{EPW} \lambda_{De}$. The wavenumber separation between two adjacent co-propagating or counter-propagating LDI cascade steps is twice this amount and is given by $\Delta k_{epw} \lambda_{De} \approx \frac{4}{3}\frac{c_s}{V_{Te}}$ which for the parameters of the present experiments translates into a scattered light wavelength separation on the order of $\Delta\lambda \approx 10$ Å. The plasma uniformity within the interaction volume must be $\Delta n/n_e << 1.5\%$ so that the fine spectral structure of the LDI cascade is not smeared out. This homogeneity requirement can be ascertained by using the calculation worksheet in Appendix E (Sections 1 and 16) and simply varying the density (n_e/n_c) to observe how much of a change in density gives a change in the LDI Thomson scattered wavelength of 10 Å. Note that for all subsequent cascade steps the EPW wavenumber decreases, and thus, so will $k\lambda_{De}$ for the EPW. As such, the Landau damping on all subsequent cascade EPWs decreases, thus lowering the convective threshold for the cascade step. What this means is that once the LDI cascade starts it is predicted that there will be numerous cascades until shut off by some other mechanism, i.e. either pump depletion or dephasing.

3.2 Observation of LDI Cascade and Interpretation of the Data

The experimental setup and plasma initial conditions were described in detail in Chapter 2. The plasma initial conditions are considered homogeneous on the scale of the laser focal spot volume where the interaction occurs, and enables the observation of fine spectral structure associated with LDI cascade. This removes any ambiguity due to inhomogeneity when interpreting the data. The initial conditions of these plasmas have been thoroughly characterized elsewhere [40]. Additionally, since the interaction beam is nearly diffraction-limited, there is no ambiguity in interpretation of the observations due to multiple interacting hot spots as would be the case with an RPP smoothed beam.

The location of the SHS was set at ~400 μm in front of the target, resulting in $n_e/n_c \approx 0.03$ as inferred from the backscattered SRS data shown later. Here, n_e is the electron density and $n_c \approx 4 \times 10^{21}$ cm^{-3} is the critical density above which 527 nm light does not propagate (see Chapter 2 for a more detailed description of the critical density). The Thomson scattering diagnostic was set up to diagnose only the forward propagating EPWs, i.e. those propagating in the same direction as the interaction laser. Although the backward propagating EPWs were not diagnosed, their presence is inferred from the resultant Thomson spectrum.

We use collective Thomson scattering [49,50] to observe the electrostatic waves driven by SRS and LDI in the plasma (see Chapter 2, Section 2.4). To calculate the probe and collection angles required, we use the linear dispersion relation for an EM wave in a plasma, a kinetic dispersion relation for EPWs, an analytic expression for IAWs that closely matches the kinetic one [52], and then match in frequency and wave vector the probe beam, scattered light, and the electrostatic wave. This calculation is performed using the calculation worksheet provided in Appendix E (Section 16). In this worksheet, parameters anticipated for the experiment are provided. Resonance matching the SRS and LDI interactions provides frequencies and wavenumbers at which the EPWs are expected to be observed. These frequencies and wavenumbers are then used to resonance match the Thomson probe interaction thus providing the expected scattered light wavelength and collection angle.

The f-number of the probe and collection optics allows for a finite range of wave vectors (and frequencies for the scattered light) to participate in the Thomson scattering (see Figure 12). Using calculations performed prior to the experiment, the Thomson probe was set up to investigate plasma densities near $n_e/n_c \approx 0.03$. The probe beam was focused into the plasma at 50±6.3 degrees and the scattered light was collected at 63±7.1 degrees, which allowed probing waves parallel to k_o (the free space wave number of the SHS interaction beam) from $1.34k_o$ to $1.76k_o$. Half of the Thomson scattered light was sent to a time-resolved diagnostic that integrated over the scattered wave vectors, and the other half was sent to a diagnostic that resolved the wavelength versus angle on the collection optic effectively providing ω vs. $\vec{k}$ (this calibration is described in more detail in Chapter 2, Section 2.4) and was time-integrated over the duration of the probe pulse. The latter was accomplished by imaging the optic plane of the collection lens, rather than its focal plane [48]. This diagnostic was useful for obtaining the dispersion properties of the LDI cascades, and in understanding any structure observed in the time-resolved (wave vector integrated) Thomson spectra.

The backscattered SRS spectrum from a typical shot in a regime where LDI cascade was observed is shown in Figure 23. When looking at the data one must remember that λ represents the free space wavelength of the measured scattered light, i.e. $\lambda=2\pi c/\omega$, where c is the speed of light. For this particular shot the laser peak intensity was $I\approx1.9\text{x}10^{15}$ W/cm^2 and the measured SRS reflectivity was R≈3.2%. The SRS spectrum begins at ~659 nm and has an intensity weighted centroid of ~657 nm. Using the measured SRS centroid wavelength and the measured mid-time T_e, we estimate $k_L\lambda_{De}\approx0.28$, where k_L is the wavenumber of the SRS Langmuir wave.

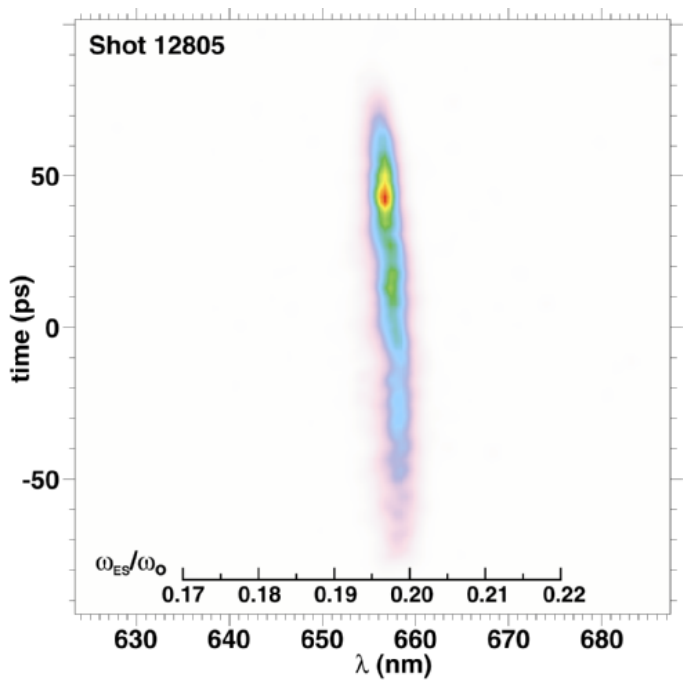

Figure 23. The SRS spectrum observed on shot number 12805. The normalized frequency scale ω_{ES}/ω_o (ω_o is the angular frequency of the SHS laser) shows the expected electrostatic wave frequency for a given wavelength.

A rough estimate of the Langmuir wave density fluctuation can be obtained from the SRS reflectivity, and compared to estimates of the LDI threshold as a consistency check [9,53] using the following formulas

$$(\delta n / n) = [4R_{\max}\Delta k / (n / n_{co})^2 k_o^2 L]^{1/2} \text{, and} \tag{18}$$

$$(\delta n / n)_{LDI} = 4k_L \lambda_D (\nu_{ia} / \omega_{ia})^{1/2} (\nu_L / \omega_p)^{1/2} . \tag{19}$$

In these equations, the variables and their assumed values (in parentheses) are: R_{max} (0.032) is the maximum reflectivity, Δk (45,125 m^{-1}) is the spectral width of the SRS (i.e. the observed spectral width ($\Delta\lambda_{SRS}\approx$3.55 nm) corrected in quadrature for the instrument resolution ($\Delta\lambda_I\approx$1.79 nm)), n (0.0303n_{co}) is the electron density, k_o (2π/527nm) and n_{co} (4.02x10^{21} cm^{-3}) are, respectively, the wave number and critical density of the incident beam, L (75 μm) is the interaction length, (ν_{ia}/ω_{ia}) (0.027) is the ratio of the IAW damping to its real frequency for our plasma conditions ($T_i\approx$100 eV), and (ν_L/ω_p) (0.007) is the ratio of the Langmuir wave damping to the plasma frequency. We calculate ($\delta n/n$)=0.024 is sufficient to exceed the LDI threshold of $(\delta n/n)_{LDI}$=0.015.

The SRS spectrum clearly shows curvature towards shorter wavelengths over the duration of the laser pulse and there is an abrupt change in the curvature at time t≈-10 ps. From the SRS spectrum and measured T_e the plasma density on this shot is n_e/n_c~0.0303. The decrease in the SRS wavelength with time is accounted for by the measured decrease in T_e. To ascertain this, the Mathcad worksheet in Appendix E (Section 9) was used to calculate the change in SRS wavelength assuming a constant n_e/n_c~0.0303 and a decrease in temperature from 480 eV to 300 eV (see Chapter 2 for details on the T_e measurement). The calculation shows that the SRS wavelength changes from ~662 nm to ~652 nm. The observed change in wavelength is not exactly this much. However, effects such as local heating of the plasma by the SHS and the exact T_e at the onset of SRS were not considered. Using the same Mathcad worksheet in Appendix E (Section 16), for these conditions the expected separation between the SRS EPW and the first forward propagating EPW from LDI cascade on the Thomson diagnostics would be ~11.5±0.8 Å, with the uncertainty being due to the temperature measurement.

The time-resolved Thomson spectrum corresponding to the SRS spectrum in Figure 23 unambiguously shows the signature of LDI cascade (see Figure 24(a)). A horizontal lineout of this image where the cascade separation is indicated is shown in Figure 24(b). From the SRS data and an ideal calculation (i.e. using nonlinear coupled mode theory and resonance matching) we would anticipate the SRS EPW to initially occur at a Thomson wavelength of ~406.1 nm and the observed data is in close agreement with this. The slight discrepancy in the Thomson wavelength for the SRS EPW ($\Delta\approx$0.5 nm) is within the uncertainties in the calibration of the SRS and Thomson diagnostic wavelength scales and the uncertainty in the T_e measurement. As indicated in Figure 24(b), the spacing between the SRS EPW and the second cascade is ~10.6 Å and is in excellent agreement with the ideal calculation. The curvature in the Thomson

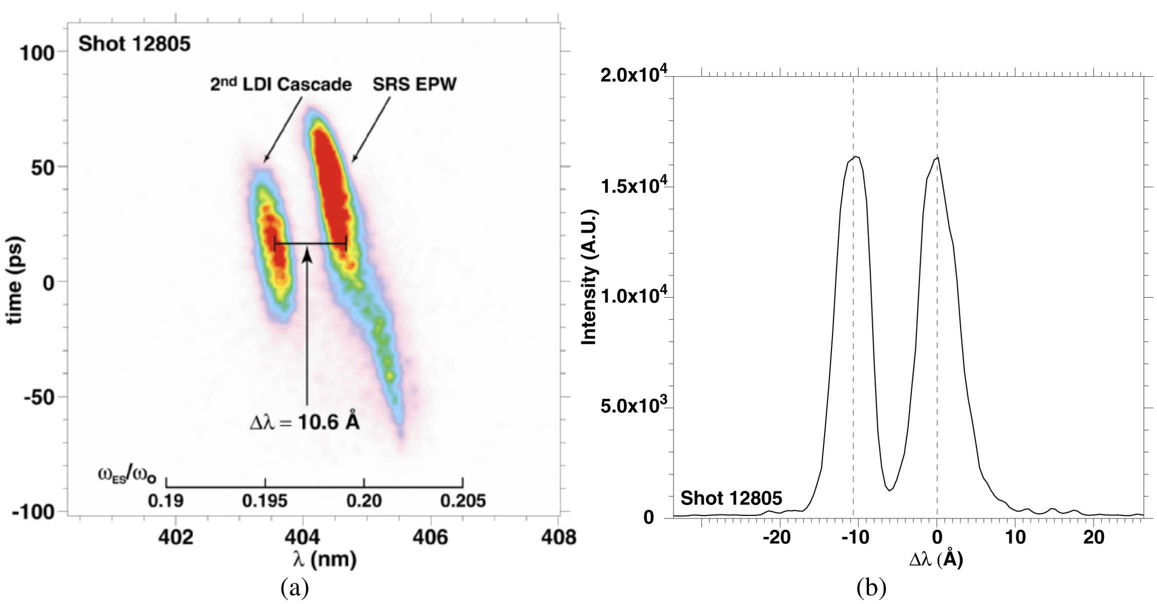

Figure 24. (a) Time-resolved Thomson spectrum from shot number 12805 showing the forward propagating EPW from SRS and the second LDI cascade. (b) A horizontal lineout taken where the cascade separation is indicated in (a).

spectrum closely follows that in the SRS spectrum. When comparing the SRS and Thomson data one must remember that the wavelength scales are drastically different. Although the calibration of the time axes in Figure 23 and Figure 24(a) are known individually, their zero reference is not directly comparable. The peak of the spectrum in each image has been placed at approximately time zero on the axis. One can still see that there is an abrupt change in the Thomson spectrum correlated with that in the SRS spectrum. The amount of change in wavelength is also not directly comparable as the scales are different and the EPW spectrum is from Thomson scattering. One must use the calculation worksheet in Appendix E (Section 16) to ascertain the expected behavior from the change in electron temperature.

The LDI does not start immediately with the SRS most likely due to being below threshold for the interaction, or due to detuning as indicated by the change in the SRS wavelength with time. Since the SRS process has a finite growth rate, it will take some time before the SRS EPW grows to sufficient amplitude to undergo Langmuir decay. Remember, the first backward propagating LDI cascade EPW is not shown in the image and it also needs time to grow to a sufficient amplitude in order to undergo Langmuir decay. Note that the observed magnitude of the LDI cascade is comparable to that of the SRS EPW. This is an important finding that is in stark disagreement with the results of recent numerical modeling [35] that predicts the effect of LDI daughter waves should be energetically negligible and not significantly affect the SRS process.

Note that LDI cascade #2 shuts off before the peak of the SRS EPW. This could be due to several reasons. Using the calculation worksheet in Appendix E (Section 9) shows that for a decreasing temperature and constant density the damping of the LDI daughter EPWs decreases. This is not only because the wave vector magnitude decrease but also because the Debye length decreases. Thus, $k\lambda_{De}$ decreases and so does the Landau damping for each LDI cascade EPW. Although the ion damping increases, the net effect is a decrease in the threshold for the LDI interaction. So, the change in damping due to the decrease in temperature is not predicted to be responsible for the shut off. One could also argue that the decrease in temperature detunes the interaction. This is not the case as the slow temperature decrease still allows for resonance matching the LDI interaction. As mentioned above and shown in Figure 24(a), the SRS and LDI EPW amplitudes are large. As such, one would anticipate significant particle trapping to be occurring. Nonlinear particle trapping effects have in theory been shown to produce a frequency (and wavenumber) shift of large amplitude EPWs [33]. The time-dependency of this frequency shift is outlined in [33] and its asymptotic value is $\sim\left(-1.87+\pi\gamma_L/\omega_B\right)$ [54] where Ω_o is given by

$$\Omega_o=\left(\frac{eE_o}{m_e k}\right)^{\frac{1}{2}}\left(\frac{\omega_{pe}}{k}\right)^2\left(\frac{\partial^2 f_o}{\partial \mathrm{v}^2}\right)\Bigg|_{\mathrm{v}_p}\left(\frac{\partial\varepsilon}{\partial\omega}\right)\Bigg|_{\omega_L}^{-1}, \quad \textbf{(20)}$$

and E_o is the amplitude of the plasma wave electric field, k is the EPW wavenumber, f_o is the initially homogeneous Maxwellian distribution, v_p is the phase velocity of the EPW, ε is the longitudinal permittivity function for the EPW, γ_L is the Landau damping of the EPW, and ω_L is the initial EPW frequency. More conveniently, the electric field can be written in terms of the bounce frequency $\omega_B\equiv\sqrt{eE_o k/m_e}$ and (20) can be recast as

$$\Omega_o=\frac{\omega_B}{k}\left(\frac{\omega_{pe}}{k}\right)^2\left(\frac{\partial^2 f_o}{\partial \mathrm{v}^2}\right)\Bigg|_{\mathrm{v}_p}\left(\frac{\partial\varepsilon}{\partial\omega}\right)\Bigg|_{\omega_L}^{-1}, \quad \textbf{(21)}$$

Numerical simulations (outlined in the next chapter) were performed to ascertain the value of the bounce frequency and (21) was coded into the calculation worksheet in Appendix E (Section 11) to evaluate the nonlinear frequency shift. Calculations show that for the parameters of shot 12805 the expected nonlinear shift in the EPW frequency and wavenumber are $\delta\omega/\omega_o \approx -6.05\text{x}10^{-4}$ and $\delta k/k_o \approx -0.03$, respectively, where ω_o and k_o are the SHS interaction laser frequency and wavenumber. The asymptotic nonlinear frequency and wavenumber shift is expected to occur on a time scale of $t = 2\pi/\omega_B$ which is on the order of ~0.1 ps. Note that the nonlinear frequency shift calculated is on the order of the growth rate for the LDI process (γ_{LDI}~$1.9\text{x}10^{-4}$ - see Table 2) and is most likely responsible for dephasing and effectively shutting off the LDI interaction. Also note that the frequency shift is *not* comparable to the SRS growth rate (γ_{SRS}~$3.9\text{x}10^{-3}$) and thus is not expected to completely dephase this interaction. There are at least three large amplitude EPWs participating in the LDI cascade process each of which will be subject to the nonlinear frequency and wavenumber shift described above. Thus there is dephasing on the SRS driven LDI interaction and on the LDI cascade interaction. It is expected that the shift in frequency and wavenumber of each subsequent LDI cascade EPW will be the sum of the shifts of the primary EPWs that decayed to form it. The interaction will hold on as long as resonance matching can be satisfied. When this is not the case it is expected that the interaction will abruptly terminate.

The LDI cascade has a unique signature in frequency and wavenumber due to the combination of the nonlinear shift discussed above and an effect that I introduce here as *thermal flattening*. The time-integrated Thomson spectrum corresponding to the SRS and time-resolved Thomson spectra shown in Figure 23 and Figure 24(a), respectively, show this distinct signature (see Figure 25). Two distinct waves are observed separated in both frequency (Thomson wavelength) and wave vector (position on the collection optic). The initial spacing in wavelength ($\Delta\lambda\approx$10.6 Å) and wave vector ($\Delta k/k_o\approx$-0.13) is consistent with the ideal calculation using the density estimated from the SRS spectrum and the mid-time measurement of T_e. The ω and k-space behavior of the spectrum can be

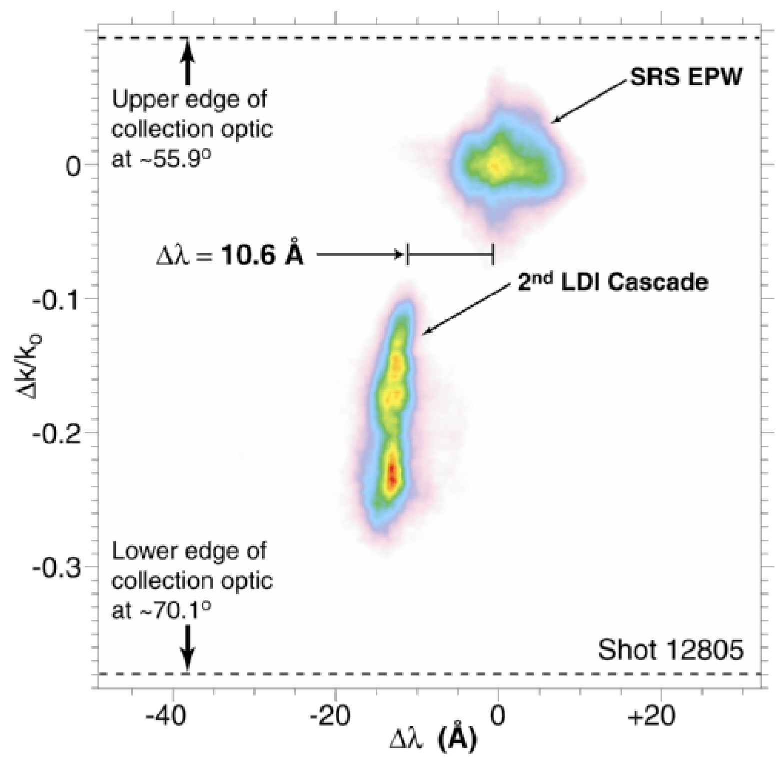

Figure 25. Time-integrated Thomson spectrum from shot number 12805 showing the forward propagating EPW from SRS and the second LDI cascade.

modeled using nonlinear coupled mode theory and resonance matching by assuming a fixed density and a decreasing temperature. The finite f-number of the SHS focusing lens allows for a range of wave vectors and frequencies to participate in the SRS interaction (see Figure 12). This will result in some fixed initial spread in both ω and k of the SRS EPW. As time progresses, T_e, and to a lesser degree, n_e/n_c decrease due to expansion of the plasma [46]. As T_e decreases, so does the curvature in the Langmuir wave dispersion. I propose that this be described succinctly as *thermal flattening* as it is a thermal cooling effect that leads to flattening of the EPW dispersion. For any subsequent EPWs generated by LDI, a small change in frequency will result in a large change in wave number due to this effect. Additionally, any change in frequency or wavenumber due to nonlinear particle trapping effects will be exaggerated due to thermal flattening.

In an underdense plasma, such as that in the present experiments, the frequency of the SHS interaction laser and SRS EM waves are much greater than that of the SRS EPW. To satisfy resonance matching as T_e decreases, the change in the SRS EPW wave number will be relatively small. However, the frequency does change slightly. This frequency change combined with the decrease in T_e is partly responsible for the spectrum shown in Figure 25. Calculations contrasting the effects of a constant temperature with decreasing density and constant density with decreasing temperature are plotted in Figure 26. For example, assuming a decrease in T_e of 100 eV (from 350 eV), the ideal calculation shows that the relative change in $\Delta\lambda$ and $\Delta k/k_o$ of the second LDI cascade to that of the SRS EPW are 0.94 and 7.1, respectively. What this means is that compared to the SRS EPW the LDI cascade EPW is expected to change about the same amount in frequency but much more in wavenumber. Thus, the narrow $\Delta\lambda$, broad $\Delta k/k_o$ time-integrated spectrum is characteristic of an EPW generated by LDI in a plasma exhibiting a decreasing electron temperature and not some other source of EPWs. The actual change in $\Delta\lambda$ and $\Delta k/k_o$ shown in Figure 25 do not exactly match the ideal calculation (assuming a decrease in T_e from 380 to 300 eV) most likely due to uncertainties in the actual T_e in the SHS and also due to the nonlinear frequency and wavenumber shift mentioned above. The LDI cascade signature shown in Figure 25 could possibly be used as a temperature diagnostic, at least in the SHS experiments, or also could be used to predict the EPW field amplitudes by measuring the nonlinear shift in wavenumber.

Another interesting shot showing LDI cascade is shown in Figure 27. This Spectrum corresponds to the SRS spectrum shown in Figure 8. This SRS spectrum is bifurcated most likely due to filamentation. It was originally thought that Figure 27 was

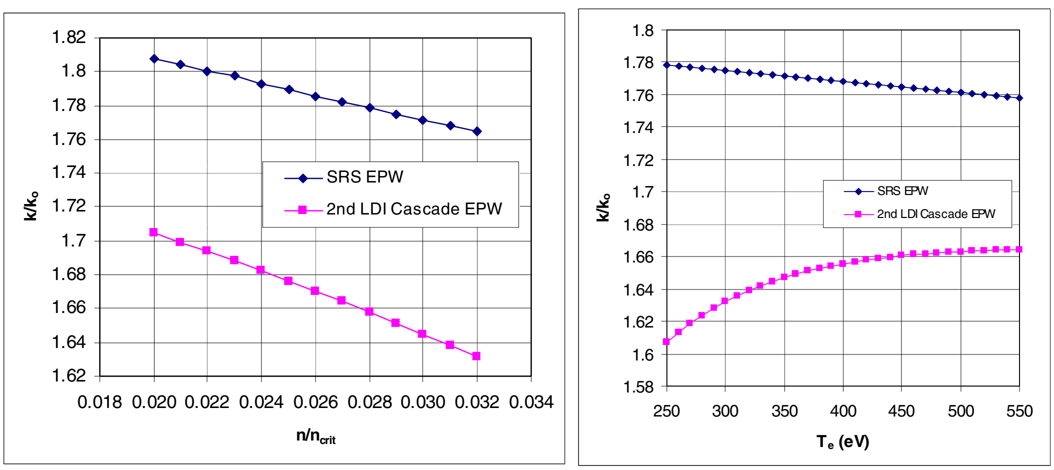

(a) (b)

Figure 26. SRS and 2nd LDI Langmuir wave behavior in *k*-space assuming (a) a constant temperature and decreasing density and (b) a constant density and decreasing temperature. Graphs were generated using linear theory dispersion relations and resonance matching calculation worksheet in Appendix E (Sections 9 and 18). The observed behavior is consistent with graph (b).

showing up to the sixth LDI cascade step. However, closer analysis of the spectrum revealed that there are two independent cascade processes due to the bifurcated SRS spectrum. Unfortunately, the gated Thomson diagnostic was grossly misaligned on this shot and offers no meaningful data.

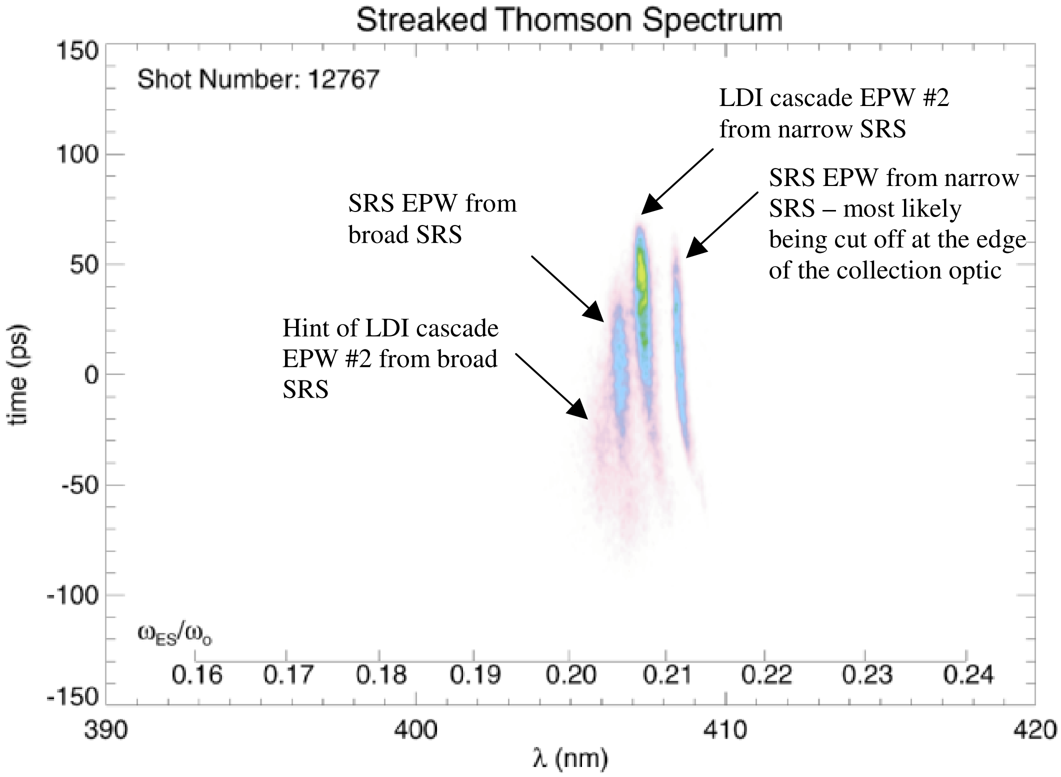

Figure 27. Streaked Thomson spectrum from shot 12767 showing two independent LDI cascade processes resulting from the bifurcated SRS spectrum shown in Figure 8. For this shot $I_o = 4.35\text{x}10^{15}$ W/cm^2, R = 4.46 %, $n_e/n_c = 0.035$, and $k\lambda_{De} = 0.245$.

The effect of the LDI cascade on the SRS amplitude can be gleaned from looking at the power in the SRS EMW, SRS EPW and the LDI cascade #2 EPW. The SRS and streaked Thomson CCD images provide a spectrum resolved in wavelength versus time. The pixel count (or intensity) on the CCD image is an indicator of the energy. Thus, if we integrate over all wavelengths in the spectrum and plot the CCD pixel counts versus time this is an indicator of the power in the particular wave. The power in the spectra of Figure 23 and Figure 24(a) is shown in Figure 28. All powers have been normalized to the maximum value in the spectrum, i.e. the LDI cascade #2 EPW has been normalized to the maximum amplitude of the SRS EPW. There is evidence that LDI is affecting SRS on this shot as indicated by the behavior of the power. What is not seen in Figure 28 is the power in LDI cascades #1 and #3 (if present) as the backward propagating EPWs were not diagnosed in the experiment. However, it is clear from Figure 28 that the growth rate of power in the SRS EMW and EPW decreases ($\gamma_2 < \gamma_1$) presumably when LDI cascade #1 becomes significant at t≈60 ps. When LDI cascade #2 drops off (most likely due to dephasing), the power in the SRS EPW is slowly decreasing and the power that was in the cascade(s) apparently shifts back to the SRS EMW. To understand the behavior here requires more than independent three-wave analyses as the SRS and LDI waves are coupled. A recent numerical study of the effect of multiple LDI (and SRS) cascades on SRS may provide more insight on the time-dependent behavior of the SRS and LDI daughter waves [55]. SRS quickly drops off while the laser intensity is still above threshold for the interaction. This is most likely also due to dephasing as the SRS EPW has grown to a large amplitude and particle trapping is expected to be significant. Unfortunately, it is impossible to extract the exact energies in the EPWs since no calibration for this was performed on the instrument. The relative power behavior does however at least qualitatively link LDI cascade to some saturation of SRS.

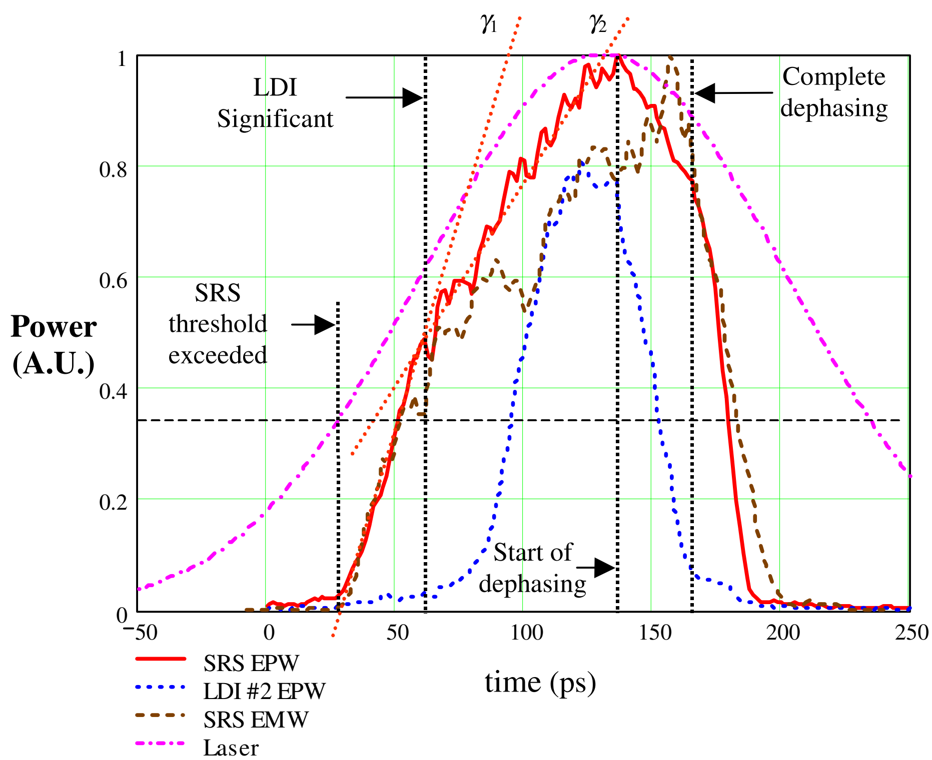

Figure 28. Power in the SRS EMW, SRS EPW and the LDI #2 cascade. The power is defined as the wavelength integrated counts on the CCD image for the particular wave per unit time. The LDI cascade EPW is normalized to the peak value of the SRS EPW.

3.3 Data Sorting and General Trends

In an effort to determine some general trends and regimes for LDI occurrence or non-occurrence, qualitative sorting was performed on the data collected in the present experiment. The qualitative data sorting categories and rating numbers are described in Table 3. Visualizations of typical streaked Thomson (ST) and gated Thomson (GT) data corresponding to these sorting categories are shown in Figure 29. Only generalized wavelength, time, and wavenumber axes are shown in the Figure 29 as only a qualitative analysis is being performed. Trends are found but they are subtle. These trends are shown graphically and described in the following paragraphs.

Table 3. Qualitative sorting category ratings and descriptions.

Rating	**Description**
0	GT, ST data are missing (can't determine the spectral quality), or the shot was used for a different purpose (e.g. EAW modes, IAW, low dispersion)
1	GT shows broad ω, narrow k, and ST shows broadening ω
1.5	GT shows broad ω, narrow k, but there's some frequency structure
2	GT and ST show definitive LDI cascade
2.5	There are indications of cascade, but also other structures visible
3	There is a lot of structure, but no definitive LDI cascade

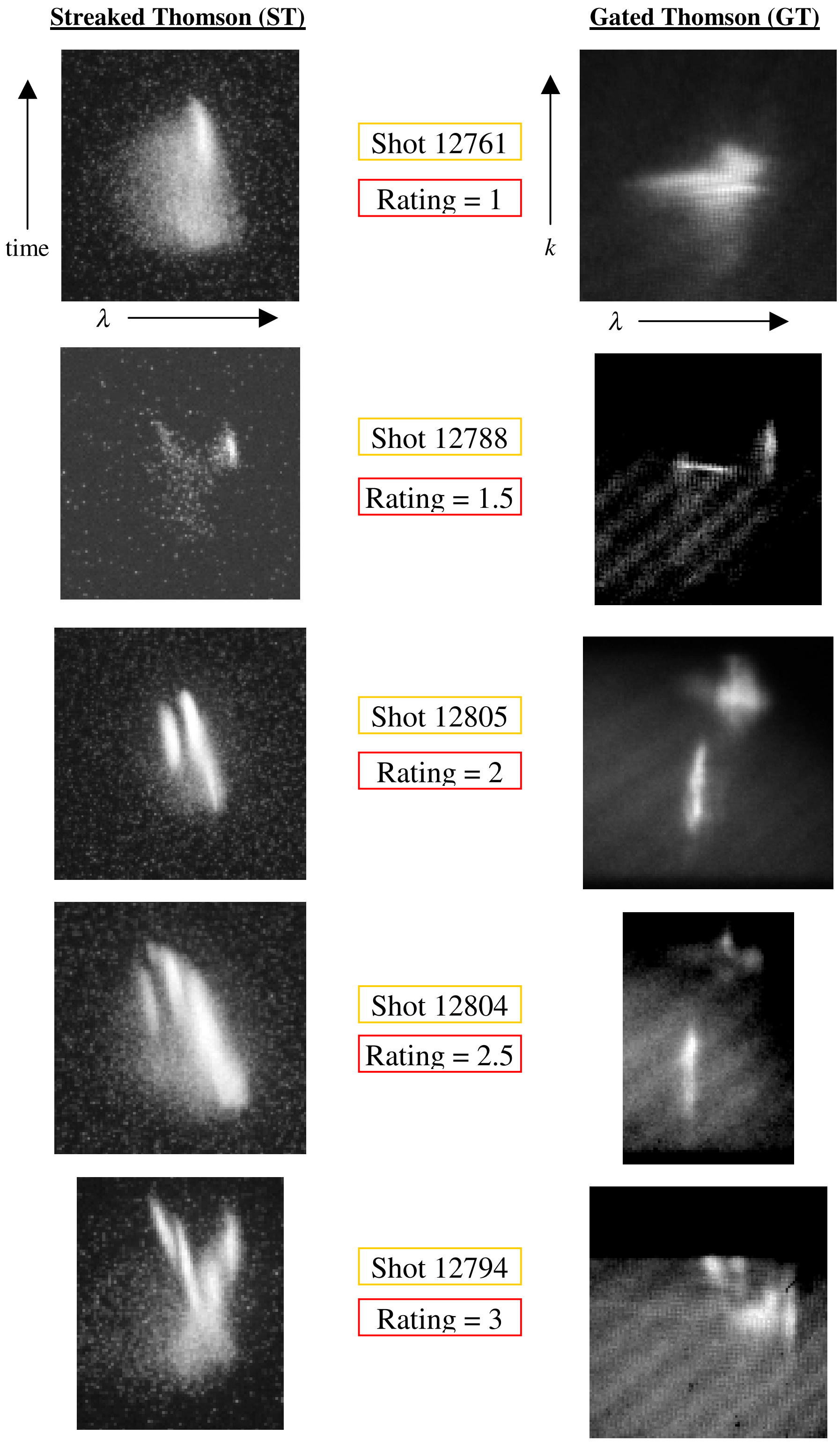

Figure 29. Visualizations of the qualitative data sorting categories and assigned ratings.

All of the data collected was analyzed and assigned a rating value as outlined above. For each shot certain other parameters are known from measurements, such as, the interaction beam intensity, the reflectivity, the value of n_e/n_c as determined from the backscattered SRS spectrum and measured T_e (or equivalently the value of $k\lambda_{De}$ calculated from these numbers). For the qualitative analysis, one is restricted to plotting the sorting category versus one of the aforementioned variables. Alternatively, combinations of the variables may be formed and plotted against if the quantity makes sense, e.g. the quantity $I_{o*}(n_e/n_c)$ in relation to the spatial growth rate for pondermotive filamentation [51]. Graphs of the data sorting categories versus the various parameters are shown in Figure 30 through Figure 33.

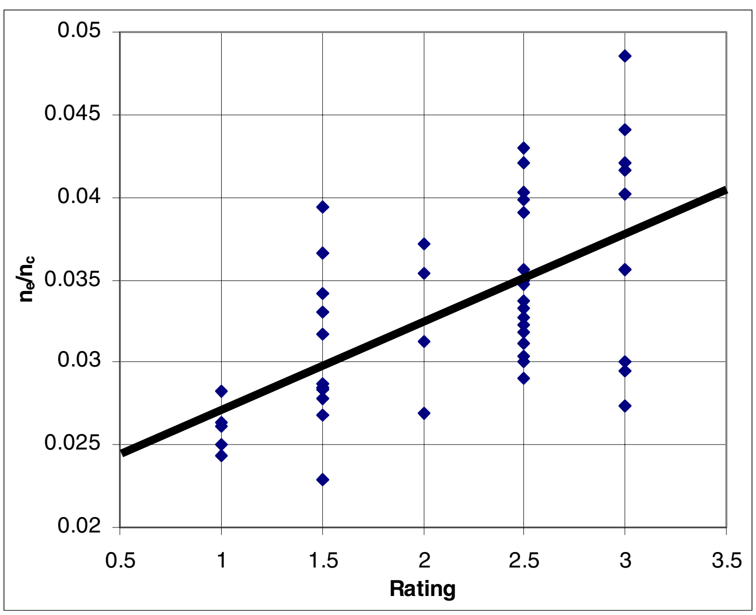

Figure 30. Qualitative data sorting – plot of the rating versus n_e/n_c.

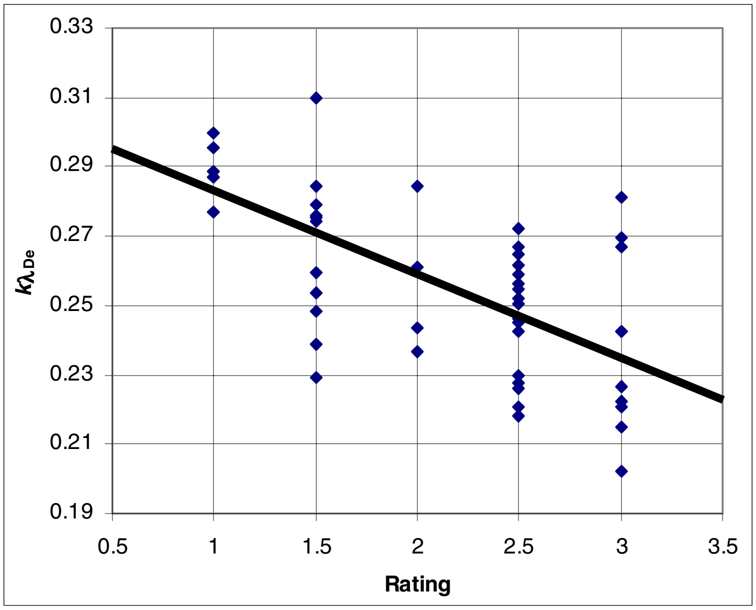

Figure 31. Qualitative data sorting – plot of the rating versus $k\lambda_{De}$.

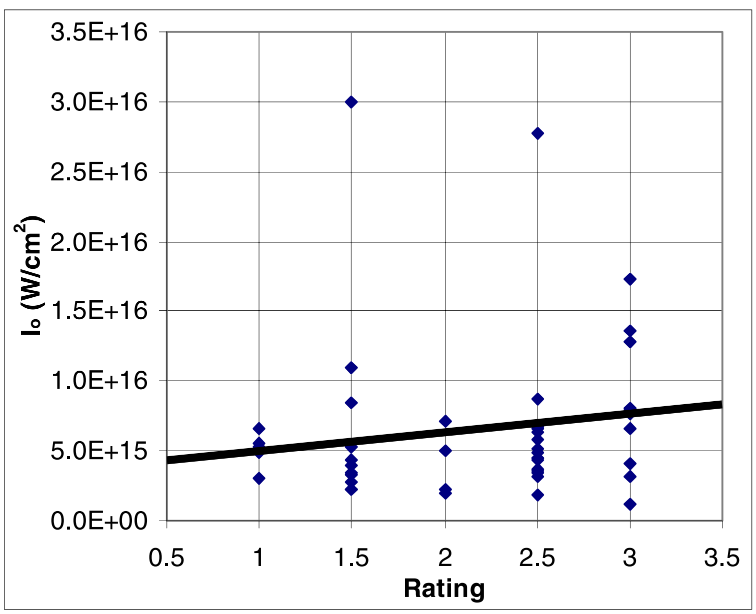

Figure 32. Qualitative data sorting – plot of the rating versus intensity.

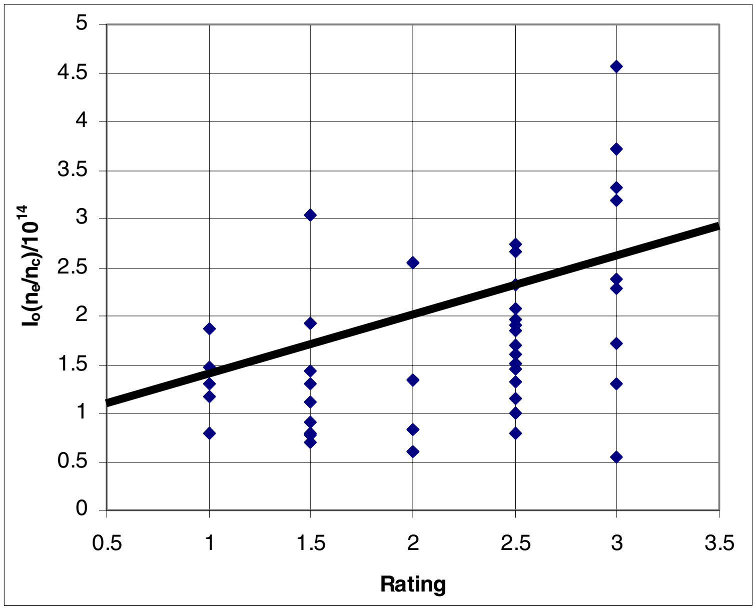

Figure 33. Qualitative data sorting – plot of the rating versus the product of Intensity and n_e/n_c normalized to 10^{14} W/cm^2.

Since the data does not represent what one would consider a large statistical group, there is little to be gained from the trend analysis. However, what one can glean from the trend analysis is the following.

- Data characterized by narrow k, broad ω (Rating=1) tend to be at the highest $k\lambda_{De}$. These spectral characteristics are what would qualitatively be expected for electron trapping [33].
- Data characterized by a bursty ω-spectra with k~constant (Rating=3) is what is qualitatively expected for SRS occurring is a filamented beam. Rating=3 data tend to occur at high densities (for lower intensities), or at "any density" given a "high enough" intensity.

- LDI, or LDI with filamented SRS, might only occur in a narrow range of $k\lambda_{De}$ for this experiment, being limited at high $k\lambda_{De}$ by trapping, and being limited at low $k\lambda_{De}$ by strong filamentation.

3.4 Conclusions on the Observation of LDI and Future Work Necessary

In summary, it is clear that LDI cascade was definitively observed in the experiment and this is claimed to be the first such observation. The LDI cascade was observed on only a handful of the ~75 energy on target shots. The amplitude of the LDI cascade EPW was comparable to that of the SRS EPW and there is evidence that significant particle trapping effects act to quickly dephase and shut off the LDI cascade completely before SRS terminates. A general trend analysis of the data did not reveal definitive regimes in which the cascade *did* and *did not* exist. However, the cascade process may have been observed in a limited range of $k\lambda_{De}$ being bordered on one side (low $k\lambda_{De}$) by filamentation and on the other (high $k\lambda_{De}$) by particle trapping effects. It is possible that since the electron temperature measured in the experiment was significantly less than that used in preparatory calculations, more than one forward propagating LDI cascade EPW existed. However, these LDI cascade EPWs may not have been detected due to the limited range of the probe and collection optics used for the Thomson diagnostic. Future experiments to further characterize the LDI cascade EPWs must therefore be conducted on hotter plasmas and use larger probe and collection optic apertures. It would also be very beneficial to simultaneously probe the forward and backward propagating EPWs from SRS and LDI and calibrate the streaked Thomson diagnostics so that the energy in the EPWs could be ascertained. If this is done, a clear picture of the effect that the LDI cascade has on SRS could be established.

Chapter 4: Observation of Stimulated Electron Acoustic Wave Scattering

This chapter presents observations of, numerical simulation of, and a theory for scattering off a new mode observed experimentally in a laser-produced plasma.[32] Scattering off of this new mode has been named *stimulated electron acoustic scattering* (SEAS) since the incident laser scatters off of an electron acoustic wave (EAW) to produce a scattered electromagnetic wave (EMW).

In the present single hot spot (SHS) experiments, stimulated scattering was observed at a frequency and phase velocity ($\omega \approx 0.4\omega_{pe}$, $v_\phi \approx 1.4v_e$) below that of the SRS driven electron plasma wave (EPW) and well above that of the ion acoustic wave (IAW). Although this mode has been observed previously [56,57] it was speculated to be a result of either stimulated Raman scattering (SRS) from an abnormally low density region in the plasma, increased levels of ion mode activity, or non-uniform laser heating of the plasma. However, no physical explanation, supporting theory, or calculations were provided to explain the observations. In the very homogeneous, well characterized plasmas used in the SHS experiments, a low density region near the SHS interaction volume and non-uniform laser heating of the plasma would be extremely difficult to create and there is no significant ion mode dynamics at or near this frequency.

A one-dimensional (1D), relativistic, finite-length, Eulerian-Vlasov code was used to investigate the nonlinear time evolution of the electron distribution function during SRS. It was found that as the potential of the plasma wave becomes large, beam-like structures (i.e. drifting structures having a thermal velocity less than that of the background plasma) develop in phase space above and below the phase velocity of the SRS EPW. As will be shown later, the electron distribution becomes non-Maxwellian as the electrons are redistributed in energy. This redistribution effectively forms a low density beam structure drifting at a velocity much less than the phase velocity of the SRS EPW. The beam structure persists for a time much greater than the growth time of SRS, thus allowing the laser to scatter off of new modes that are associated with this beam in the plasma.

Linear modeling of a Maxwellian background plasma containing a single Maxwellian beam (described in a later section of this chapter) shows that if the beam velocity is sufficiently separated from the phase velocity of the electron plasma wave ($v_{\phi EPW}$) generated by SRS, additional modes, which may be weakly damped, emerge and the SRS driven EPW mode is only slightly perturbed. It will be shown that these additional modes have acoustic dispersion, i.e. $\omega_r \approx k v_{ob}$, where v_{ob} is the beam velocity, and are thus called electron acoustic waves [58]. One possible explanation for SEAS which is put forth in this thesis is that the nonlinear evolution of the SRS-EPW results in effectively generating a weak (i.e. low density) electron beam (e-beam), with thermal spread, near the bulk of the original Maxwellian distribution. In addition to the electron plasma wave mode, this new distribution supports linear (weakly damped) modes having acoustic dispersion. An explanation for scattering off of this EAW mode, supported by a quasimode dispersion relation, is also presented in this chapter.

The experimental results are presented first as they are the motivation for the work that follows. Next, the results of numerical modeling of the experiment are provided that illustrate the time-evolution of the electron distribution function. A description of the equations solved and numerical procedures used in the code is provided in Appendix D. The code itself is also provided in Appendix D for a quick reference on implementation of the numerical methods. Additionally, for those interested a working version of the code is available on the CDROM attached to this thesis. A linear theory description of how the EAW mode may emerge is then presented using parameters gleaned from the numerical modeling as input to the model. Finally, a Vlasov description of scattering off of the new quasimode is outlined.

4.1 Experimental Observation of Stimulated Electron Acoustic Scattering

In the present single hot spot (SHS) experiments, stimulated scattering was observed at a frequency and phase velocity ($\omega \approx 0.4\omega_{pe}$, $v_\phi \approx 1.4 v_e$) below that of the SRS generated electron plasma wave (EPW) and well above that of the ion acoustic wave (IAW). The motivation for the work presented in this chapter was to understand the origins of and scattering off of this new electron acoustic wave (EAW) mode. As it turns out, scattering off of this or a similar mode was observed in past experiments [56,57] and although not understood it was explained as resulting from either stimulated Raman scattering (SRS) from an abnormally low density region in the plasma, increased levels of ion mode activity, or non-uniform laser heating of the plasma. In the very homogeneous, well characterized plasmas used in the SHS experiments, a low density region near the SHS interaction volume and non-uniform laser heating of the plasma would be extremely difficult to create and there is no possibility for an ion mode density fluctuation resulting in scattering at or even near this frequency.

In past experiments on TRIDENT [57] the energy scattered off of the EAW mode, henceforth called SEAS, represented a relatively small percentage of the total scattered energy. It was also observed that the time duration of SEAS was much less than the interaction laser pulse and the SRS. The French experiments [56] were conducted at low intensity (~10^{13}-10^{14} W/cm^2) and no backscattered electromagnetic wave (EMW) resulting from SEAS was ever observed. They found that the frequency of the mode was intensity-dependent and concluded that the emergence of this mode could not be explained by known theory. No physical explanation was offered in [56] and [57] for the presence of the EAW. They only provided speculation without any supporting calculations or theories. In the present SHS experiments, the mode is energetically insignificant when compared to the energy in the SRS EMW. This is shown by the time-integrated backscattered spectra shown in Figure 34. Due to the limited dynamic range of the streaked SRS spectrometer diagnostic, observation of both SRS and SEAS spectra on the same shot was not possible. Thus, Figure 34 is a composite of two separate shots having approximately the same laser and plasma conditions. The spectral resolution of the instrument is ~1.8 nm for the SRS spectra, and ~0.25 nm for the SEAS spectra. The spectrum shows a bright narrow peak at 654 nm (spectral width ~7 nm) corresponding to SRS scattering from an EPW with $k\lambda_{De} \approx 0.27$ ($T_e \approx 350 - 400$ eV). The SRS reflected energy was ~0.06 of the incident laser energy. Also shown is a spectrum recorded in the range from 540-600 nm on a separate shot with nearly identical laser and plasma conditions. A narrow peak was observed at 566.5 nm (spectral width ~5 nm), whose amplitude is ~3000x lower than the SRS peak – this is the EAW mode. The energy in the

SEAS mode was at most 2 x 10^{-5} of the incident laser energy. Note that the dispersion of the EAW mode was not established experimentally.

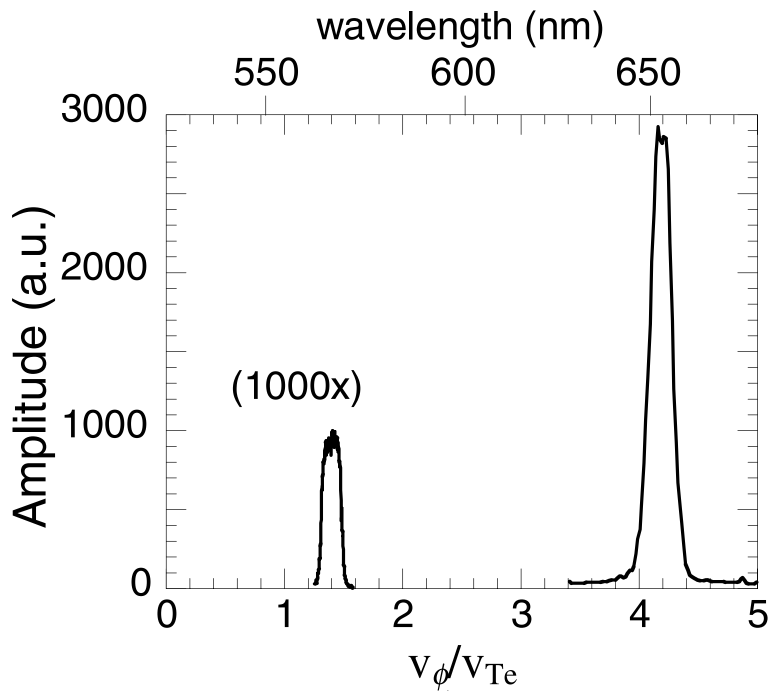

Figure 34. Composite image from two separate shots showing the time-integrated SRS and SEAS signals. The amplitude of the SEAS is seen to be approximately 3000x less than the SRS signal and occurs at a much lower phase velocity.

As characterization of SEAS was not the primary mission of the experiments, the only scaling performed was a variation of the interaction laser intensity. It was observed that at an intensity below I≈3x10^{15} W/cm^2, the SEAS mode dropped below the detection threshold of the instrument while SRS was still observed at the 0.005 level. Due to the experimental setup, no other scaling studies were feasible. Thus all that could be concluded is that there was a threshold for SEAS and that the frequency of the mode was known.

The phase velocity of the mode was estimated by assuming the scattering is a resonant process and *k*-matching the interaction. An example of resonance matching the

SEAS interaction is shown in Figure 35 along with the SRS interaction. It is seen that since the frequency of the EAW mode is much lower than the laser and SRS EMWs, the difference in the wavenumber of the SRS and SEAS EMWs is very small. What this means is that attempting to resolve these two EMWs in wavenumber will be more difficult than resolving them in frequency. This will be elaborated on in more detail in the analysis of the numerical simulation data shown in a later section of this chapter.

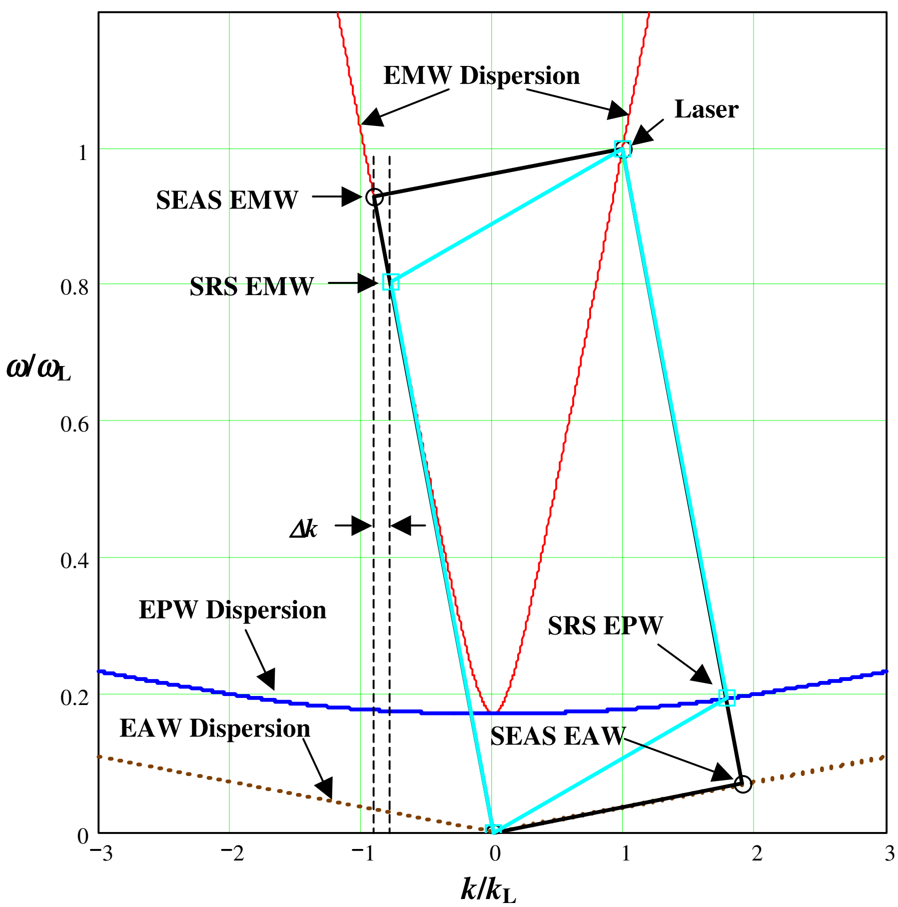

Figure 35. 1D resonance matching diagram showing the SRS and SEAS interactions. The phase velocity of the EAW dispersion has been set to that predicted by the experimental observation.

The results of data analysis on the SEAS observations are collected below in Table 4. To summarize, the past and present experimental observations of this mode show that

- The frequency and phase velocity of the mode lies in between that of the EPW and the IAW,
- The energy in the scattered mode is much less that that in SRS,
- In the French experiments, the frequency of the mode was observed to have a dependence on the interaction laser beam intensity,
- The present SHS experiments noted little deviation in the frequency versus interaction laser intensity which may be due to the fact that SRS was saturated,
- The SEAS interaction exhibited a threshold intensity, and
- The scattering does not last as long in time as the SRS.

Table 4: Summary of SEAS mode observations. Δt is the time duration of the observed spectrum.

SEAS Mode Shot Analysis:						
Calibration information:			1-1800/500 nm grating			
			nm/pix:	0.03		
			Reference:	557.03	at pixel	662
Shot Number	Energy (J)	I (W/cm^2)	$\Delta\lambda_{FWHM}$ (nm)	λ_{center} (nm)	R_{SRS} (%)	Δt (ps)
12807	0.35	4.185E+15	NA		NA	
12808	0.331	4.122E+15	4.71	565.925	6.61%	159.3
12809	0.244	3.831E+15	4.86	565.91	2.09%	157.5
12810	0.098	3.343E+15	NA		0.75%	
12826	0.152	3.524E+15	4.32	566.315	0.92%	168.2
12828	0.377	4.275E+15	NA		6.82%	
12829	0.51	4.719E+15	5.67	565.655	2.87%	134.5

On a few shots the Thomson diagnostic was set up to probe EPWs outside of the hot spot. The probe and collection geometry for these shots is shown in Figure 36. The spectra from these shots (c.f. Figure 37) show numerous spectro-temporal events possibly indicating that beaming electrons generated by SRS are interacting with the plasma outside the SHS and also give an approximate time duration of their interaction. The Thomson probe was carefully aligned to look outside of the interaction hot spot. However, it cannot be ruled out that the observed spectrum could have also been due to self-focusing and filamentation causing SRS past (i.e. in front of) the best focus position of the hot spot [41], but there is no hard evidence or experimental results to back this up. On shot 12831 the SRS spectrum (see Figure 37) is very broad and is not indicative of filamentation. On the other hand, distinct spectro-temporal events are noted in the streaked Thomson spectrum. An analysis of how far EPWs generated by SRS and electrons beaming at the EPW phase velocity could travel in the plasma was performed. These calculations are outlined in Appendix E (Section 10) and are illustrated in Figure 36. The calculations show that an EPW generated by SRS in the SHS would travel only ~2 μm before decaying in amplitude one e-folding due to Landau damping and thus

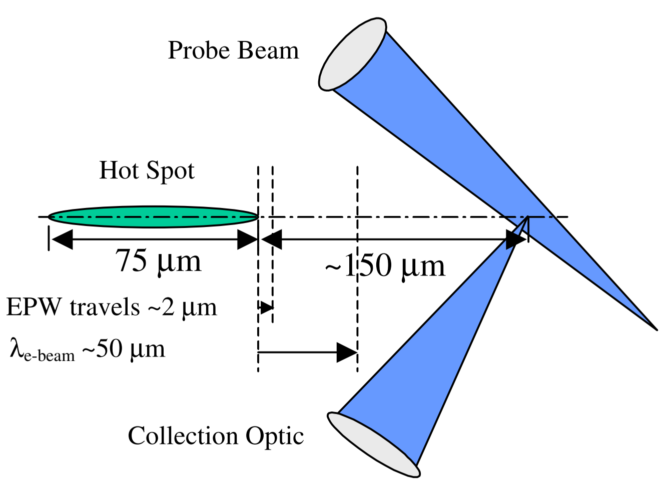

Figure 36. Hot spot and probe geometry for investigation of plasma waves outside of the SHS.

would not make it to the Thomson probe point. However, the mean free path of a beaming electron is on the order of ~50 μm and thus it is likely that these beaming electrons traveled several mean free paths and, via a beam-plasma interaction, could be the source of the EPWs observed outside of the SHS.

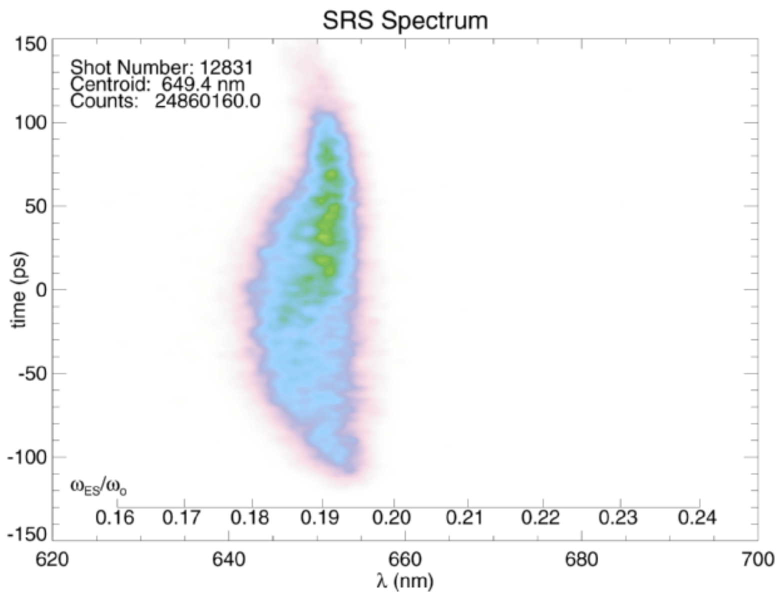

(a)

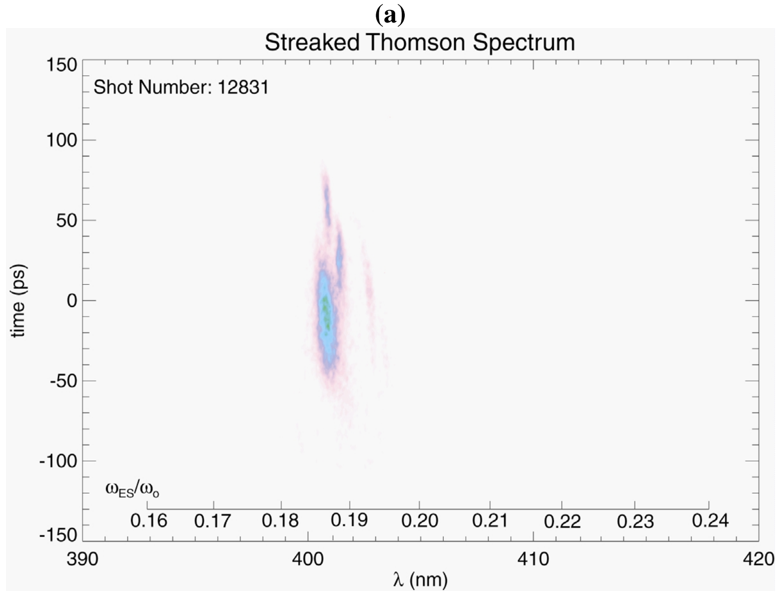

(b)

Figure 37. (a) SRS and (b) streaked Thomson spectra from shot 12831 where EPWs were probed outside of the SHS. The broad SRS spectrum does not directly correlate to the numerous spectro-temporal events observed in the streaked Thomson image. These EPWs could be the result of beaming electrons interacting with the plasma.

4.2 Numerical Simulation of SRS Using a 1D Vlasov Code

Numerical modeling using a relativistic, one-dimensional (1D), finite-length, Eulerian-Vlasov code with mobile electrons and a single species (also mobile) hydrogen ions was used to investigate the nonlinear time evolution of the electron distribution function during SRS. This code, with various boundary conditions and dimensionalities, has been used extensively in the past to simulate SRS and beat-wave phenomena [59, 60, 61, 62, 63, 64]. The equations solved and numerical methods employed are described in more detail in Appendix D. The code is only a numerical model for the physical system. As such, one must wonder if the elements of the model are adequate for simulating the physical problem of interest so that meaningful results are provided. We have justified the use of a 1D code with the following arguments.

A Vlasov code by definition neglects the effects of collisions. To determine if this is justified, one must compare the growth rates of the instabilities being studied, the evolution time of the electron distribution function of interest, and the simulation time to the characteristic collision time of the physical plasma system. The characteristic electron collision time τ_c is the inverse of the electron-ion collision frequency ν_{ei}. If the time between collisions is much greater than the simulation time, the plasma can be considered essentially collisionless and the Vlasov model is adequate for the simulation. The formula for ν_{ei} is [65]

$$\nu_{ei} \approx 2x10^{-6} \frac{Zn_e \ln(\Lambda)}{T_{eV}^{3/2}} (s^{-1}), \qquad \textbf{(22)}$$

where Z is the ion charge state, n_e is the electron density (in cm^{-3}), T_{eV} is the electron temperature in (in eV), and $\Lambda = 12\pi\lambda_{De}^2 n_e / Z$ is the plasma parameter defined as the ratio of the maximum to minimum impact parameters. Using parameters typical of the SHS plasmas the collision time $\tau_c=1/\nu_{ei}$ is on the order of ~1 ps. In the numerical simulations it is seen that SRS grows up from a small coherent excitation to significant levels even prior to the laser transiting one-half of the plasma region. Since the plasma is very underdense, the interaction laser wave front is traveling at essentially the speed of light. The length of the plasma region is chosen to model that of the SHS linear dimension (~75 μm). The time it would take the laser wave front to traverse the plasma region would be ~0.25 ps. Thus, significant SRS is developing in the numerical system prior to one transit of the system which takes much less than the collision time. Therefore, neglect of collisions in the numerical model is justified. Simulations performed for longer than ~1 ps would be unrealistic using the code as collisional effects would become important.

One might argue that transverse electromagnetic wave instabilities may develop due to temperature anisotropies in the physical plasma, i.e. a Weibel instability.[66] This instability could interfere with experimental observations if the unstable wavenumbers are in the range of the SRS wavenumbers, and if this were true it would need to be accounted for in the numerical model by increasing the dimensionality of the code. If the effect of this instability is not included in the numerical model, the results of any simulations might provide misleading information. A kinetic stability analysis of counter streaming and anisotropic temperature distributions predicts that the range of unstable wavenumbers is given by [67]

$$0 < k^2 < \sum_s \frac{\omega_{ps}^2}{c^2}\left(\frac{k_B T_{s\perp} + m_s \mathrm{v}_{so}^2}{k_B T_{s\|}} - 1\right), \quad \textbf{(23)}$$

where s represents a particular species in the plasma, $\omega_{ps} = \sqrt{n_s e_s^2 / \varepsilon_o m_s}$ is the plasma frequency for the species, k_B is Boltzmann's constant, $T_{s\perp}$ and $T_{s\|}$ are, respectively, the perpendicular and parallel temperatures of the species, m_s is the mass of the species, v_{so} is the drift velocity (if any) of the species component, and c is the speed of light. One can analyze all species in the plasma separately and get a feel for the range of unstable wavenumbers that it might contribute to. It is convenient to normalize the wavenumber to that of the free-space interaction laser beam, i.e. $kc/\omega_L \to k_n$. Multiplying both sides of (23) by the normalization factor c/ω_L and realizing that $\omega_{ps}/\omega_L = \sqrt{n_s/n_c}$, where n_c is the critical density for the given laser wavelength, gives

$$0 < k_n < \sum_s \sqrt{\frac{n_s}{n_c}}\left(\frac{k_B T_{s\perp} + m_s \mathrm{v}_{so}^2}{k_B T_{s\|}} - 1\right)^{\frac{1}{2}}. \quad \textbf{(24)}$$

Looking only at the non-drifting background plasma, one can estimate the temperature anisotropy necessary in order to obtain unstable wavenumbers near that of SRS. For parameters typical of the SHS experiments (n_e/n_c = 0.03, T_e = 400 eV, T_i = 100 eV, CH plasma) the normalized SRS wavenumber is expected to be k_n = 0.783. To obtain an unstable wavenumber at this magnitude would require a temperature anisotropy of ~21. This is totally unrealistic for the heater laser and plasmas generated in the SHS experiments since the heater beam is smoothed with a random phase plate (RPP) and there is no imposed drive for anisotropy in the experiment, e.g. magnetic field. For any realistically feasible temperature anisotropy, the range of unstable wavenumbers is far removed from the SRS wavenumbers. To date, no one has measured the temperature anisotropy in a laser-produced plasma driven by SRS. [68] However, the electron temperature both along the SHS and perpendicular to the target has been measured experimentally and was found to be approximately the same within the accuracy of the measurement.[68] The same arguments for any beaming species can also be applied. The beam density, as estimated from the Raman reflectivity levels [69], will be at most on the order of ~2% of the background plasma density. As such, the required anisotropy due to temperature alone would be ~2000. Assuming a beam temperature of roughly 1/10 that of the background plasma and a beam density of 1% of the background plasma would require that the beam velocity be $v_{so} \sim 14.3V_{Te}$. From Figure 34 it is seen that for these plasma parameters the EPW phase velocity is at roughly $4.2V_{Te}$. The numerical modeling predicts that the beam structures will develop near the phase velocity of the SRS EPW and thus it is unrealistic for those beams to provide unstable electromagnetic wavenumbers at those of the SRS. One can also look at the temporal growth rate for the Weibel instability due to temperature anisotropy alone. The maximum growth rate is given by

$$\omega_{i\max} = \frac{2}{3\sqrt{3\pi}} \frac{T_{e\parallel}}{T_{e\perp}} \left(\frac{T_{e\perp}}{T_{e\parallel}} - 1 \right)^{\frac{3}{2}} \frac{\omega_{pe} V_{Te}}{c} \tag{25}$$

and occurs when $k_n / \sqrt{\frac{n_e}{n_c} \left(\frac{T_{e\perp}}{T_{e\parallel}} - 1 \right)^{\frac{1}{2}}} \approx \frac{1}{\sqrt{3}}$. For the parameters typical of the SHS experiments, even assuming an unrealistic temperature anisotropy of 2, the maximum growth rate will be $\omega_{imax} \approx 0.002\ \omega_{pe}$, at a wavenumber $k_n \approx 0.1$. Normalizing this growth rate to the laser radial frequency for $n_e/n_c = 0.03$ gives $\omega_{imax}/\omega_L \approx 0.0004$ The SRS growth rate predicted by nonlinear coupled mode theory, normalized to the laser radial frequency, is γ_{SRS}~0.004. Thus, the maximum possible growth rate for the Weibel instability is approximately ten times less than that for SRS and occurs at a wavenumber nowhere near the SRS wavenumber. Thus, not accounting for temperature anisotropy and using a 1D code is justified, at least for the case of the Weibel instability.

If beam like structures, or bumps, in phase space are truly the source of the EAW mode one must wonder how long it will take for these bumps to flatten out. Since collisions are not modeled in the code, this flattening could most likely be due to quasilinear diffusion (see [70]). The quasilinear diffusion coefficient is given by

$$D_{QL}(w) \cong \frac{\pi}{\Delta k}\left(\frac{q}{m}\right)^2 \frac{\left\langle E^2 \right\rangle}{\left|\mathrm{v}_g - w\right|}, \tag{26}$$

where Δk, v_g, $\left\langle E^2 \right\rangle$ are, respectively, the spectral width, group velocity, and the mean-square electric field of the wave packet. In the context of this section, the wave packet is the EAW. In terms of the bounce frequency associated with a longitudinal electric field $\omega_B = \sqrt{eEk / m_e}$, (26) can be written approximately as

$$D_{QL}(w) \cong \frac{\pi}{\Delta k} \frac{\omega_B^4}{k^2\left|\mathrm{v}_g - w\right|}. \tag{27}$$

An estimate for the quasilinear diffusion time is then given by

$$\tau_{QL} \cong \frac{(\Delta \mathrm{v})^2}{D_{QL}}, \tag{28}$$

where Δv is the velocity spread of the bump. The simulation results predict that, for the parameters of the experiments $\omega_B \approx 0.1\omega_{pe}$. This can be used to estimate the longitudinal electric field amplitude produced by the SRS driven EPW. However, we are interested in the electric field amplitude of the EAW. The code solves for the longitudinal electric field and Fourier analyzing it can provide its spectral width. However, the wavenumber of the EAW is approximately equal to the wavenumber of the SRS driven EPW. Since the EAW amplitude is expected to be much smaller than the SRS driven EPW it may not be detectable in the resultant spectrum (and this was confirmed in the simulations). To estimate the quasilinear diffusion time the following approximations and assumptions are made. The spectral width of the EAW is obtained from the wavelength spread of the experimental observation and is $\Delta k \approx 1.96 \times 10^5$ m^{-1}. Also from the experimental observation, the ratio of energies in the EAW to SRS modes (see Figure 34) is used to estimate the EAW field amplitude given the SRS driven EPW amplitude from the simulation ($\omega_B \approx 0.1\omega_{pe}$). The wavenumber of the EAW mode is expressed in terms of $k\lambda_{De} \approx 0.28$ and the definition of λ_{De} is used to further simplify (27). The EAW mode is not in exact phase resonance with the beam that generates it (see Appendix E, Section 22) and thus gives $|\mathrm{v}_g - w| \approx 0.5\mathrm{V}_{Te}$. The velocity spread of the beam is estimated by assuming the beam temperature is 1/10 that of the background electron temperature thus giving $\Delta\mathrm{v} \approx \mathrm{V}_{Te} / \sqrt{10}$. Finally, the plasma frequency for the given conditions is $\omega_{pe} \approx 6.2 \times 10^{14}$ s^{-1}. Using the above assumptions, the quasilinear diffusion time is estimated to be $\tau_{QL} \approx 1.6 \times 10^{-13}$ s = 0.16 ps. What this means is that the beam-generated EAW is expected to be a transient process.

Additional time scales must be evaluated when one considers that in the SHS experiments a plasma flow transverse to the interaction beam is introducing fresh plasma into the system on a continuous basis and also that the streak camera diagnostic integrates over a small but finite period of time. These time scales must be considered because as the numerical plasma system evolves nonlinearly any phase space structure may be washed out due to quasilinear diffusion or some other effect. The transverse flow velocity at a distance of $z \approx 400\ \mu m$ ($n/n_c \approx 0.03$) from the target (see Figure 3) is $v_z \approx 6x10^7$ cm/s. Considering that the width of the single hot spot in the direction of the transverse flow is $w \approx 2.4\ \mu m$, the plasma will be completely swept out of the SHS in a time $t \approx 4$ ps. Additionally, fresh plasma is being swept into the SHS on a continuous basis. The SRS streak camera CCD had 1024x1024 pixels and the streak time for the EAW shots was 2 ns. Thus, each pixel actually gives a time-integrated picture over a period of ~2 ps. What the preceding analysis was meant to show is that LPI processes could be occurring in the plasma on a time scale much less than the integration time of the streak camera diagnostic CCD and they could never be resolved. If the LPI process is transient but is resurrected due to a continuous supply of fresh plasma, the time integration of the diagnostic will provide a picture that makes the process appear to be continuous.

4.3 Results of Numerical Modeling

Parameters typical of the regime where SEAS was observed are specified as inputs to the Vlasov code. Prior to the simulations, linear theory calculations based on these parameters are performed in order to determine the expected frequencies, wavenumbers, and phase velocities that would result from SRS. Although the code will evolve the system nonlinearly, these calculations serve as a good first order consistency check that the code is working properly. Parameters typical of the present experiment are: $I_o = 2x10^{15}\ W/cm^2$, $\lambda_L = 527$ nm, $L_{system} = 164.5$ (plasma region ~75 μm), $T_e = 350$

eV, T_i = 100 eV, n_e/n_c = 0.032, γ_{SRS}/ω_L = 0.004 (SRS growth rate), γ_{cSRS}/ω_L = 0.00023 (SRS convective threshold). Although the plasma in the experiment was 50/50 carbon-hydrogen (CH), the Vlasov code is limited to modeling only a hydrogen plasma. The effects of this limitation will primarily be manifested in the IAW damping which may affect SRS through LDI [55] but this is not considered here.

For convenience in the calculations, the code normalizes all parameters. These normalizations are explained as follows. Frequencies are normalized to the electron plasma frequency ω_{pe}. Thus, values listed for frequencies are multiples (or fractions) of ω_{pe}. Wavenumbers are normalized to the free space plasma wavenumber $k_{pe} = \omega_{pe} / c$, where c is the speed of light. Thus, wavenumber values are presented in multiples (or fractions) of k_{pe}. Electric and electromagnetic fields are normalized to $\omega_{pe} m_e c / e$ and are thus presented in multiples or fractions of this quantity. Time is normalized to the inverse of the electron plasma frequency and are thus presented in multiples of ω_{pe}^{-1}. And finally, momentum is normalized to $m_e c$ and are thus presented in multiples or fractions of this quantity.

For the above parameters, the results anticipated from the simulation (in normalized units) are: ω_o = 5.59, ω_{SRS} = 4.477, ω_{EPW} = 1.113, k_o = 5.5, $|k_{SRS}|$ = 4.364, k_{EPW} = 9.864, $P_{\phi EPW}$ = 0.114. Note that the backscattered SRS wavenumber will in actually be in the negative x direction, however, Fourier transforming the fields provides only magnitudes at a particular wavenumbers and not the wave vector directions.

Since the Vlasov code is essentially noiseless [60], it was necessary to add a small initial sinusoidal perturbation to the electron distribution in momentum space. This was an exact excitation at the expected spatial frequency of the SRS generated EPW, i.e.

$f(p) \sim \exp\left[-\frac{1}{2}\left(\frac{p}{p_{th}} - \varepsilon\cos(k_{EPW}x)\right)^2\right]$, where ε is the magnitude of the perturbation. As gleaned from the time-zero electron density diagnostic, in terms of a density fluctuation this perturbation was $\delta n/n \approx 6 \times 10^{-5}$. In fact, when conducting initial simulations using the Vlasov code it was found that without an initial perturbation there was no evolution of SRS during the simulation time period. Due to the way that the total charge in the system is divided equally and placed at the boundaries (see Appendix D) there is always some initial noise in the system. A spectral analysis of this noise revealed that it was in a very low frequency range. If this noise is in a range where the longitudinal oscillations are predicted for the SRS interaction then no initial perturbation need be added to the system. However, this was not the case for the present simulations.

To confirm that SRS is evolving in the numerical system, the longitudinal electric field and both forward and backward propagating transverse electromagnetic fields in the system are Fourier analyzed for their spectral content. For the present simulation at a time when the laser has propagated the simulation box ~1.2 times (i.e. $\tau \approx 197.4$ (ω_{pe}^{-1}), or in actual time t ≈ 0.32 ps) the spectral content of the fields is shown in Figure 38. The peaks for the laser, SRS EMW, and SRS EPW are at $k_o = 5.492$, $|k_{SRS}| = 4.362$, $k_{EPW} = 9.893$, respectively. This agrees closely with what resonance matching the SRS interaction predicted.

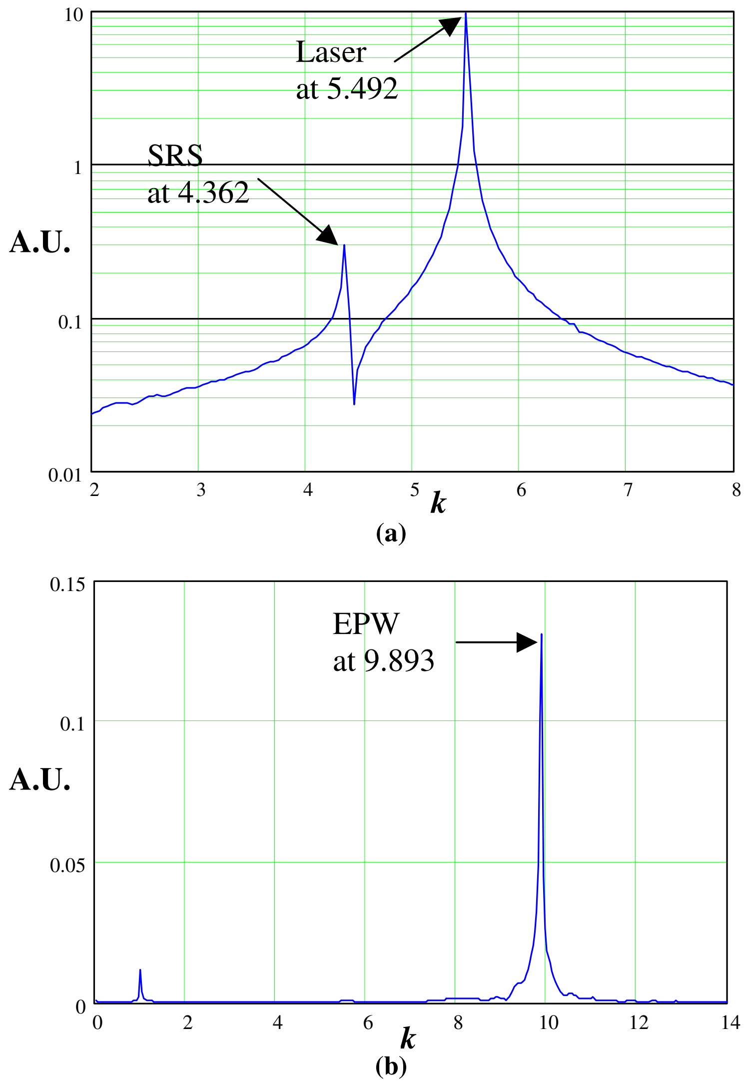

Figure 38. Spectral content of (a) the electromagnetic and (b) the electrostatic fields in the simulation box when the laser has propagated the simulation box ~1.2x.

As shown in Figure 39 the initial perturbation of the electron distribution function evolves to form vortices in phase space throughout the simulation box on a time scale of $\tau \approx 51.7$ (ω_{pe}^{-1}). At this time the laser has propagated to x = 51.7 (c/ω_{pe}). As the laser propagates through the plasma region, SRS amplifies the longitudinal field amplitude, and thus, the extents of the vortices grow in momentum space. The largest growth of the vortices occurs, of course, in the region where the laser has been present the longest, i.e.

near the left boundary of the simulation box where the laser enters the system. Particles not only become trapped in the vortices but also remain in the vicinity of the separatrix, i.e. the boundary between trapped and non-trapped particles. Thus, the particles can be characterized as either trapped, nearly trapped, or passing. To get an idea of how the electron distribution evolves in time, one region in phase space is followed as it is moving at the phase velocity of the SRS EPW.

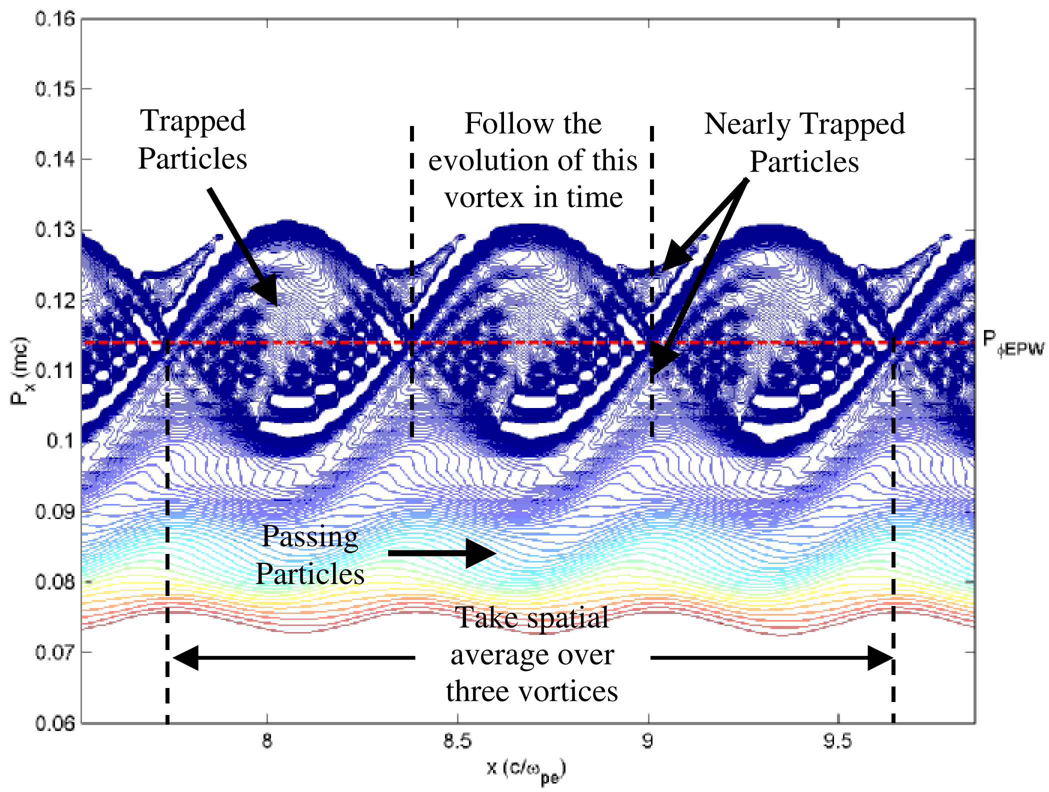

Figure 39. Snapshot at time $\tau \approx 51.7$ (ω_{pe}^{-1}) of a region in phase space showing the formation of vortices.

From the initial picture of phase space shown in Figure 39 the vortex centered at x ≈ 8.7 is followed in a frame moving at the phase velocity of the SRS EPW ($v_{\phi EPW} \approx 0.113$ c). In order to ascertain how the time-evolved electron distribution deviates from the initial Maxwellian, a spatial average is taken over approximately three plasma wave wavelengths (or vortices). Spatially averaging the time-evolved distribution function is necessary in order to analyze the distribution function in momentum space. As seen in Figure 40(a), the time-evolved distribution differs very slightly from the initial Maxwellian. Since this difference is so small, one cannot get a quantitative feel for it unless the initial Maxwellian is subtracted from the time-evolved distribution function. Figure 40(b) shows the deviation, or δf_e, of the time-evolved distribution function from the initial Maxwellian.

It is seen that a relatively small percentage of the bulk particles are being redistributed to higher energies. Thus, the time-evolved electron distribution may be effectively modeled by a Maxwellian with a lower density (compared to the initial Maxwellian) combined with a beam-like structure that is nearly Maxwellian. The behavior at this early stage in the evolution is a little noisy in momentum space. This will become more smoothed out as time progresses and the system evolves. To monitor the behavior of the electron distribution function, the vortex centered at x ≈ 8.7 (c/ω_{pe}) at time $\tau \approx 51.7$ (ω_{pe}^{-1}) is followed in time as SRS evolves.

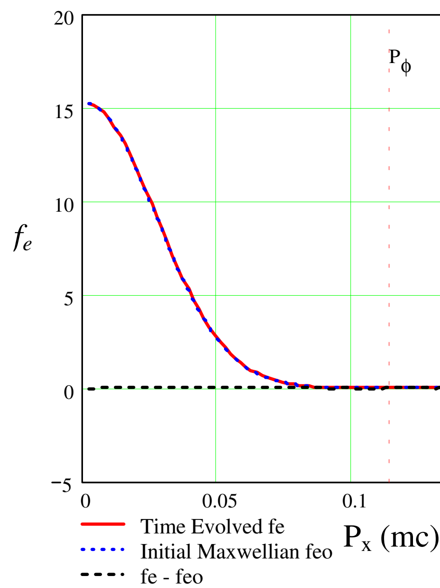

(a)

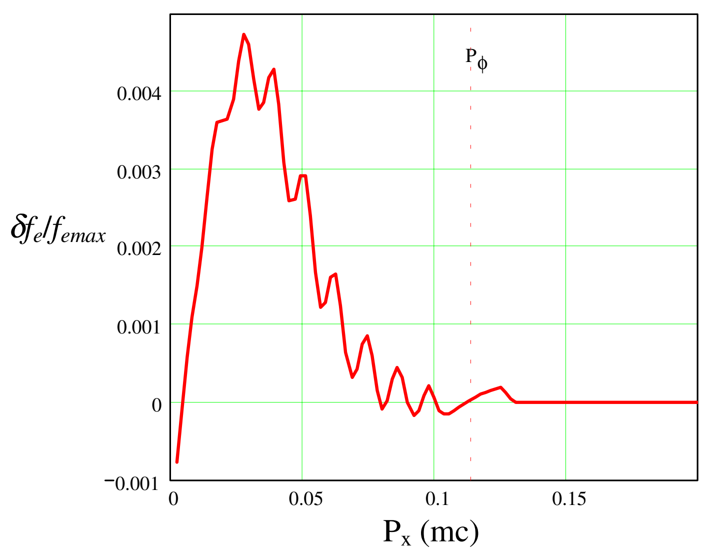

(b)

Figure 40. (a) Spatial average of the electron distribution over three vortices at $\tau \approx 51.7$ (ω_{pe}^{-1}) centered on $x \approx 8.7$ (c/ω_{pe}). (b) The deviation from the initial Maxwellian (normalized to the maximum of the time-evolved distribution) shows a redistribution of particles from lower energies to higher energies.

Taking a spatial average of the electron distribution over several vortices in phase space and subtracting the initial Maxwellian reveals that a very low density beam-like structure develops near the separatrix higher than the phase velocity of the EPW (see Figure 40(b)). Additionally, a beam-like structure with a relatively higher density develops below the phase velocity of the EPW. It is this lower velocity, higher density beam that is of interest in the SEAS observation. This is not to say that the higher velocity beam is of no importance. I believe there is also another weakly damped mode generated due to this beam. However, at the time of the experiments the theory (exposed in the following section) did not exist and no thought was ever given to diagnosing this other suspected mode. A future experiment should be performed to investigate this.

Plots of the phase space distribution at two points in time and spatial averages over three vortices (centered on the original vortex shown in Figure 39 at x = 8.7) are provided in Figure 41 and Figure 42. In these figures the laser wave front is at ~0.75x ($t \approx 0.19$ ps) and ~1.2x ($t \approx 0.3$ ps) the length of the simulation box. It is obvious that the vortices are growing in time and the field growth rate is close to that predicted by nonlinear coupled mode theory. From an analysis of the fields it is apparent that they are still growing, and thus, the interaction is not saturated. Figure 41 shows best the striking results of the simulations. That is, the time-evolved electron distribution is no longer Maxwellian but can be crudely approximated by a lower density Maxwellian (relative to the initial Maxwellian) and a low density beam-like structure with a velocity less than the phase velocity of the SRS driven EPW.

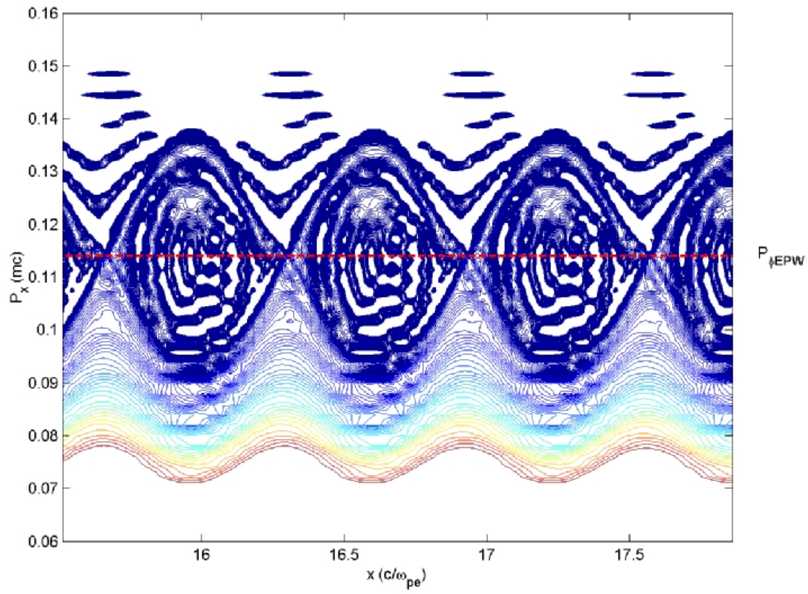

(a)

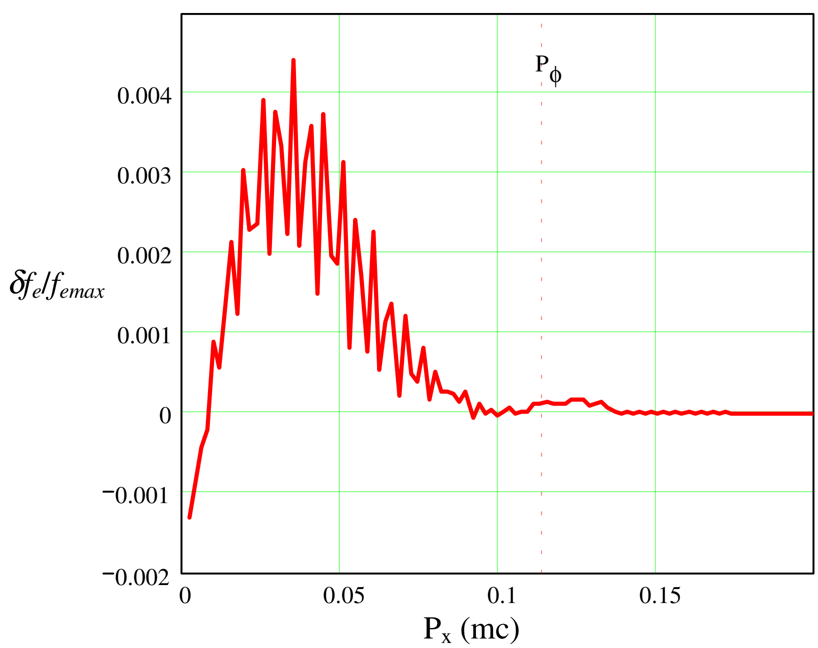

(b)

Figure 41. (a) Phase space window from Figure 39 at time $\tau \approx 122.2$ (ω_{pe}^{-1}). (b) Spatial average of the electron distribution over three vortices centered on the vortex at x ≈ 16.6 (c/ω_{pe}).

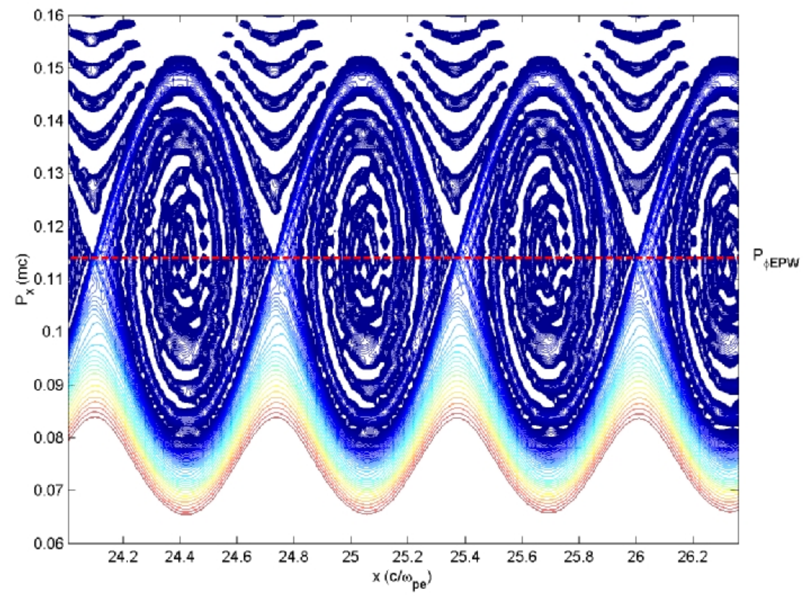

(a)

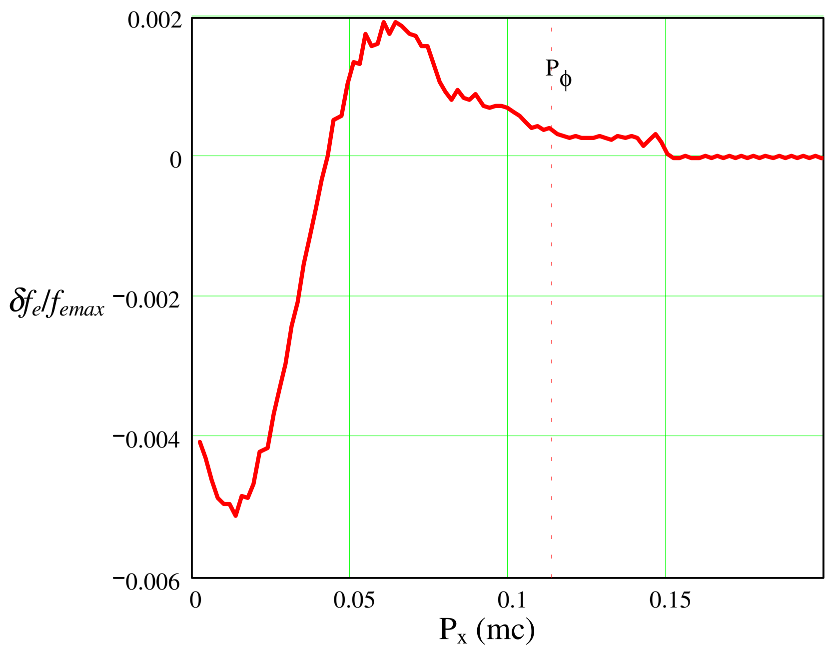

(b)

Figure 42. (a) Phase space window from Figure 39 at time $\tau \approx 197.4$ (ω_{pe}^{-1}). (b) Spatial average of the electron distribution over three vortices centered on the vortex at x ≈ 25.1 (c/ω_{pe}).

The 1D Vlasov code has the model elements necessary to predict scattering off of the EAW mode, should it exist. The *k*-space spectrum for the specified simulation parameters (see Figure 38) shows that SRS is occurring where expected. However, resonance matching predicts that the wavenumbers of the EMWs from SRS and SEAS will be very close in magnitude (see Figure 35). Additionally, the experimental observation shows that the amplitude of the SEAS mode is ~3 orders of magnitude less in intensity than that of SRS. Thus, looking at the *k*-space spectrum would most likely not reveal the mode. In order to ascertain whether or not the code will predict the SEAS mode self-consistently, the forward and backward propagating EMWs (see Appendix D) are saved at the boundaries of the plasma region at each time step. This data is Fourier analyzed to provide the frequency spectrum of the scattered light wave. Resonance matching predicts that the frequency difference between the SEAS and SRS modes should be discernable even for disparate amplitudes. Figure 43 shows the frequency spectrum of the backscattered EMWs at time $\tau = 128$ (ω_{pe}^{-1}) and there is structure in the region where the EAW mode is observed. The behavior of the spectral structure is bursty in time throughout the simulation and does not appear after a time $\tau \approx 160$ (ω_{pe}^{-1}). As will be shown in the next section, the damping of this mode is expected to be large compared to the SRS EPW (since it is a quasimode) and the growth rate for the SEAS interaction will be much less than SRS. It is believed that the Vlasov code is showing SEAS. However, it is difficult to observe this mode and future simulations must attempt to maximize its visibility, e.g. by making the ions more massive so as to eliminate SBS.

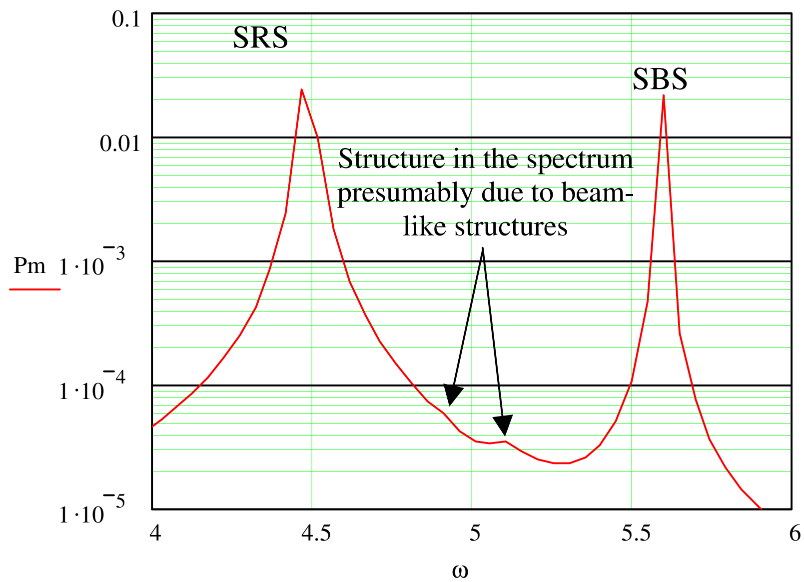

Figure 43. Fourier spectrum of the backward propagating EMW passing the left-hand boundary of the plasma region at time $\tau = 128$ (ω_{pe}^{-1}).

4.4 Description of SEAS Using Bi-Maxwellian Electron Distribution

Explanations for SEAS have been presented previously in the literature [32,71]. In this section, an alternate explanation for SEAS is presented. Starting from a plasma whose electron distribution is Maxwellian, solution of the Vlasov-Maxwell code shows that for the assumed initial perturbation, on a time scale of one laser transit of the plasma region the nonlinear evolution of SRS generates a quasi steady-state electron distribution which varies in space and time. Laser scattering off this distribution occurs on a time scale on which the distribution found from the nonlinear evolution of SRS can be taken as a new equilibrium distribution that exhibits low density, thermally spread, beam structures. One possible explanation for the EAW is that it is a linear, weakly damped mode of a plasma whose electron distribution function contains low density, thermally spread, beam structures. Thus, the observation of SEAS can be explained as a wave-wave (quasimode) interaction of the laser with a linear EAW whose existence depends on the non-linearly evolved electron distribution in SRS.

Intrigued by the results of previous numerical simulations showing that beam-like structures develop in the electron distribution function during SRS, a simple model was developed to investigate the effect of Maxwellian background plasma having a beam component. Only a single beam interacting with the background plasma is considered and thus the model is called a bi-Maxwellian. It is suggested that the EAW mode is generated by the interaction of low energy beam ($v_b < v_{\phi SRS\text{-}EPW}$) of electrons, produced by the nonlinear evolution of the electron distribution during SRS, with the background plasma. Using a bi-Maxwellian electron distribution function to model the beam-plasma system, it is found that, in addition to the usual linear beam-plasma mode, there exists another linear mode with characteristic features of an EAW. The weakly damped linear EAW, obtained from the dispersion relation with the complete plasma dispersion function, exists for parameters consistent with the experiments.

Using Maxwellian electron and ion distributions and a single Maxwellian beam, the fully kinetic dispersion relation governing the one-dimensional linear dynamics of this system is

$$D(k,\omega) = 1 - \frac{\omega_{pe}^2}{k^2 v_{the}^2} Z'\left(\frac{\omega}{|k| v_{the}}\right) - \frac{\omega_{pb}^2}{k^2 v_{thb}^2} Z'\left(\frac{\omega - k v_b}{|k| v_{thb}}\right) - \sum_i \frac{\omega_{pi}^2}{k^2 v_{thi}^2} Z'\left(\frac{\omega}{|k| v_{thi}}\right) = 0, \quad \textbf{(29)}$$

where $v_{the}^2 = 2T_e / m_e$, $v_{thb}^2 = 2T_b / m_e$, $v_{thi}^2 = 2T_i / m_i$, and $\omega_{ps}^2 = (Z n_s e^2 / m_s \varepsilon_o)$ are, respectively, the background electron thermal velocity, the electron beam (e-beam) thermal velocity, the ion thermal velocity, and the plasma frequency for the species (either electrons (Z=1) or ions (Z≥1). The drift velocity of the e-beam component is given by v_b, the temperatures are specified in electron volts (eV), and $Z^{'}(x)$ is the derivative of the plasma dispersion function (or Z-function) [44] with respect to its argument. Since the frequencies of interest are much greater than the ion plasma frequency, ignoring the ion dynamics is justified. Additionally, the analysis provided here normalizes frequencies to the background electron plasma frequency, ω_{pe}, and uses the conventions $v_{th}^2 = 2v_T^2$ and $\lambda_D^2 = v_T^2 / \omega_p^2$ thus reducing (29) to

$$D(k,\omega) = 1 - \frac{1}{2k^2\lambda_{De}^2} Z^{'}\left(\frac{\omega/\omega_{pe}}{\sqrt{2}|k|\lambda_{De}}\right) - \frac{1}{2k^2\lambda_{Db}^2} Z^{'}\left(\frac{\omega/\omega_{pb}}{\sqrt{2}|k|v_{Tb}}\omega_{pc} - \frac{v_b}{\sqrt{2}v_{Tb}}\right) = 0. \qquad \textbf{(30)}$$

Equation (30) can be further simplified by letting $\Omega = \omega/\omega_{pe}$, $K = |k|\lambda_{De}$, $V_b = v_b / v_{Tb}$ and rewriting λ_{Db} and v_{Tb} in terms of λ_{De} and v_{Te} by using ratios of the beaming and background electron densities and temperatures. Thus, (30) simplifies to

$$D(K,\Omega) = 1 - \frac{1}{2K^2} Z^{'}\left(\frac{\Omega}{\sqrt{2}K}\right) - \frac{1}{2K^2}\frac{n_b}{n_e}\frac{T_e}{T_b} Z^{'}\left(\frac{\Omega}{\sqrt{2}K}\sqrt{\frac{T_e}{T_b}} - \frac{V_b}{\sqrt{2}}\right) = 0. \qquad \textbf{(31)}$$

Solving for the roots of (30) (i.e. $D(K,\Omega) = 0$) the frequency (normalized to the background electron plasma frequency) versus $k\lambda_{De}$, the wave vector magnitude (or simply the wavenumber) times the background electron Debye length is obtained. It is convenient to specify the drift velocity of the e-beam component as a fraction (or multiple) of its thermal velocity. The beaming and background electron densities can be expressed as fractions of the total density as long as the total density adds up to one, i.e. $n_e + n_h = 1$.

Equation (31) was solved using Mathcad [45] and a Z-function solver created from IMSL routines. The results are compiled below. To verify that the model is working correctly, the e-beam component is turned off and the dispersion of the first and second Landau roots for the background electron plasma is solved for. The Mathcad worksheet used for this calculation is provided in Appendix E (Section 22) and the results of this calculation are shown in Figure 44. As expected, the first Landau root exhibits the weak damping and dispersion of the electron plasma wave mode. The second and all subsequent Landau roots have acoustic-like dispersions (i.e. $\omega \sim k$ as $k \to 0$) and are heavily damped.

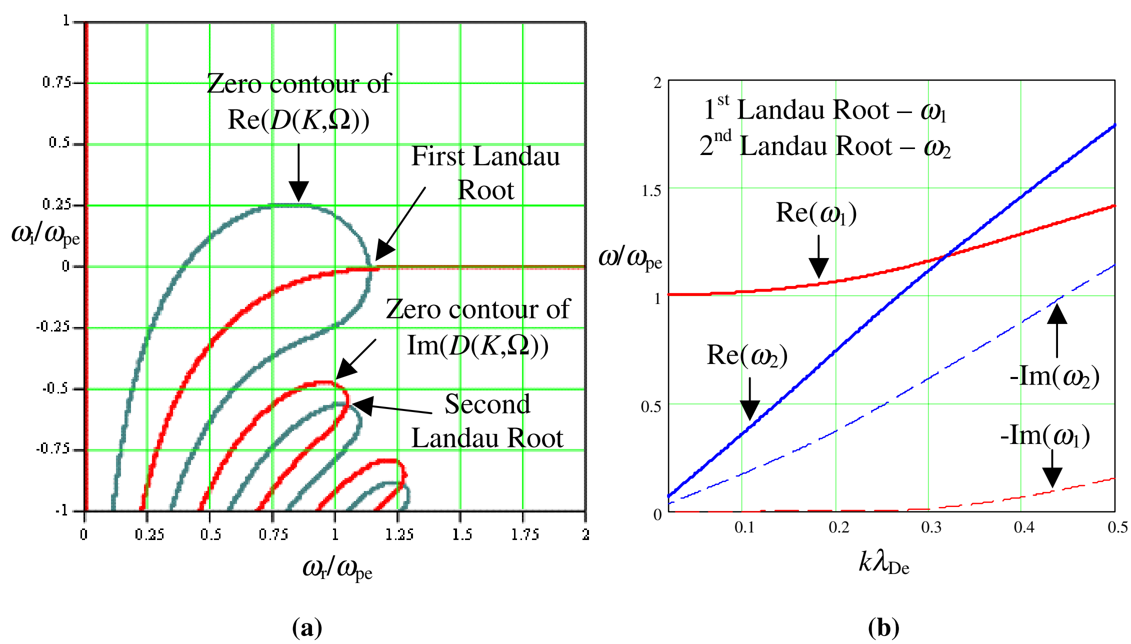

Figure 44. (a) Zero contours of the real and imaginary parts of (31) in the complex ω-plane for $k\lambda_{De}$ = 0.28. Where these contours intersect is a root of the dispersion relation. (b) dispersion of the first (EPW) and second (EAW) Landau roots for a range of $k\lambda_{De}$ values. Note that in (b) the $k\lambda_{De}$ values do not go to zero due to numerical problems following the EAW root in this region.

Next, parameters gleaned from experimental data from the SEAS shots of the present experiments were used to explore the effect on the damping and dispersion of the Landau roots. To reiterate, on these shots scattering, presumably stimulated, off of a mode having a normalized frequency Ω≈0.4 was observed. The measured electron temperature was T_e≈390 eV (this is the background electron temperature in our bi-

Maxwellian model). The plasma density is approximated from the SRS spectrum on similar shots and is found to be $n_e/n_{crit} \approx 0.03$. For the approximate plasma density and background electron temperature, the wavenumber times Debye length is $k\lambda_{De} \approx 0.28$. We do know the frequency of the SEAS mode but did not experimentally determine its dispersion. The parameters of the bi-Maxwellian model are then varied in order to obtain a weakly damped root that passes through the observed data point. The approximations we use to obtain these parameters are as follows.

1. The drift and thermal velocities of the beam component can be estimated by considering that the hot electrons are trapped by the SRS EPW and have an energy given by an electron traveling at the EPW phase velocity (i.e. $T_h \approx \frac{1}{2} m_e(\omega_{EPW}/k_{EPW})^2$). This would be a good estimate for the drift velocity. However, this may not be appropriate for estimating the temperature of the beam.
2. To find the beaming electron fraction, we measure the Raman reflectivity for the shot and use Manley-Rowe relations to estimate the energy in the EPW ($\frac{n_h m_e \mathrm{v}_\phi^3}{2} \approx RI_o \frac{\omega_{EPW}}{\omega_o}$ see [69]). Then we assume that as a high-end estimate all of this energy is being carried away by the kinetic energy of the beaming electrons.

Using these assumptions, we arrive at the parameters: $T_e = 390$ eV, $T_b = 3500$ eV, $n_e = 0.98$, $n_b = 0.02$, $V_b = 1.4$. Performing the same calculation used to generate Figure 44 it is found that the dispersion of the first and second Landau roots using these parameters is virtually unchanged from the previous result. These results are not shown graphically as they provide no new information. It is concluded that a beam having the parameters assumed above cannot responsible for the observed SEAS mode.

If the fraction of hot electrons is increased, the dispersion of what initially was the EPW root becomes acoustic-like and its frequency is lowered. Using other parameters assumed previously, the fraction of hot electrons required to get a weakly damped root near $\Omega \approx 0.4$ is $n_b = 0.87$ (i.e. 87% hot electrons). This large hot electron fraction is not plausible. Additionally, it is the first Landau root that develops the acoustic-like dispersion and the root corresponding to the usual EPW is no longer present in the system. A new root that exhibits EPW-like dispersion emerges, but it does so at $\Omega \approx 3$ (i.e. $\omega \approx 3\omega_{pe}$) for $K \rightarrow 0$ and this cannot be the usual EPW mode. Here again, it is concluded that a hot beam with an abnormally large electron density is not a plausible explanation for the observed SEAS mode.

The assumption that the temperature of the e-beam distribution is equal to its drift velocity is questionable. Electrons are being trapped from the cooler background distribution near the phase velocity of the SRS EPW. One would envisage that these electrons gain kinetic energy and maintain a relatively narrow width in temperature, i.e. the spread in energies differs little from the kinetic energy of the beam and their drift velocity differs little from the phase velocity of the EPW. Thus, the width of the distribution would be determined by the temperature range of the electrons trapped near the phase velocity of the SRS driven EPW. It is possible that the small number of electrons extracted near the phase velocity of the SRS driven EPW form a much colder beam rather than a much hotter drifting distribution. Interesting results emerge when we consider that the trapped electrons comprise a relatively cold beam. In this case it is possible to obtain two weakly damped roots at approximately the correct frequencies of the SRS driven EPW and the EAW observed in the experiments. Figure 45 shows the zero contours of (31) at K = 0.28 with parameters $T_e = 390$, $T_b = 20$, $n_e = .97$, $n_b = 0.03$, $V_b = 7.42$ ($\sim 0.4 v_{\phi EPW}$). What this shows is that a small percentage of electrons comprising a beam (i.e. an electron beam) with a small thermal spread can leave the SRS driven EPW root only slightly modified and also introduce a weakly damped electron acoustic mode. If the beam velocity is sufficiently separated from the phase velocity of the SRS driven EPW or if the beam density is very small, calculations have shown that the beam has little effect on the EPW mode. This is the major point of the section. The bi-Maxwellian model shows that electrons beaming through the background plasma are one possible explanation for the observed SEAS mode.

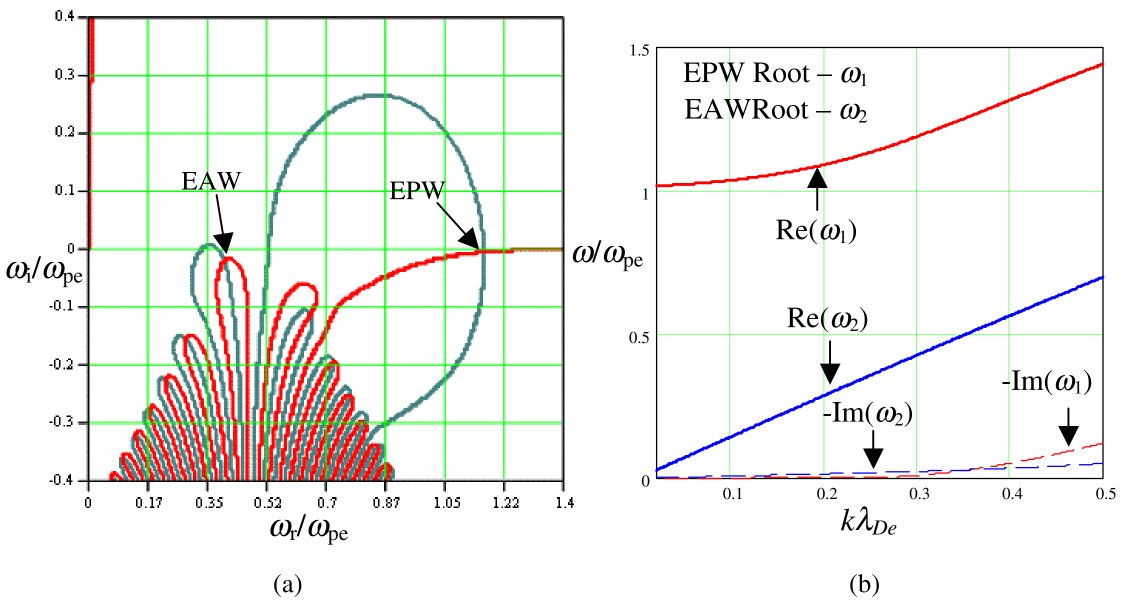

Figure 45. (a) Zero contours of (31) in the complex ω plane for a bi-Maxwellian plasma with parameters $T_e = 390$, $T_b = 20$, $n_e = .97$, $n_b = 0.03$, $V_b = 7.42$ ($\sim 0.4 v_{\phi EPW}$). (b) Dispersion of the electron plasma wave and weakest damped electron acoustic root.

Note that the beam parameters used to generate Figure 45(a) were chosen to produce a weakly damped EAW mode at the frequency observed in the experiments. Although the numerical modeling does not show a beam develop with these exact parameters, it does show the emergence of a low density beam-like structure at a velocity less that that of the SRS driven EPW and structure is exhibited in the backscattered EMW spectrum in the vicinity of the experimental observation (see Figure 40 through Figure 43). Note that if the beam parameters from the numerical simulations (e.g. from Figure 40) are used in the bi-Maxwellian model, the EAW frequency differs significantly from that shown in Figure 45 even though the backscattered EMW spectrum (see Figure 43) shows structure in the vicinity of the experimentally observed frequency.

The effect of the beam density on the frequency and damping of the EAW mode is shown in Figure 46. For the parameters used to generate Figure 45(a), it is seen that for larger beam density fractions the EAW mode becomes less damped. Even for very small beam density fractions the mode is not too heavily damped. Thus, the number of particles necessary to produce this mode is very small. For the experimental observation it is expected that only the weakest damped mode would be observed, and thus, this would correspond to the beam having the largest density fraction.

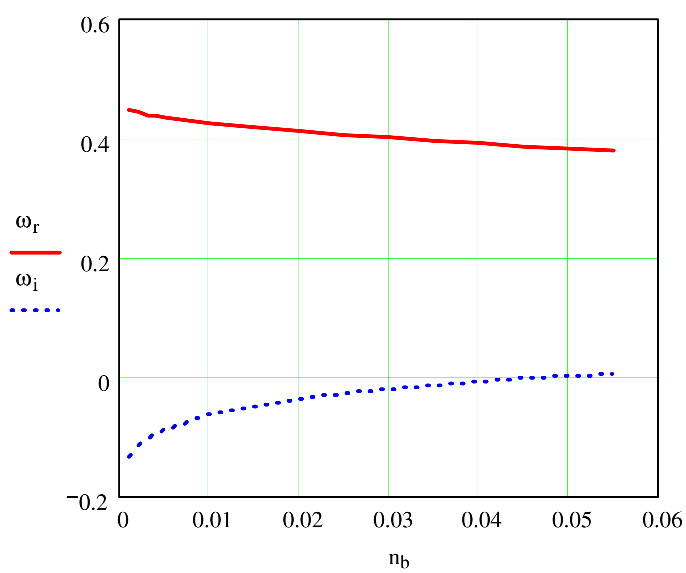

Figure 46. Plot of the frequency and damping of the EAW mode versus beam density fraction for the parameters $T_e = 390$, $T_b = 20$, $V_b = 7.42$ (~$0.4v_{\phi EPW}$), and $k\lambda_{De} = 0.28$.

4.5 Vlasov Description for Stimulated Scattering off of Electron Modes and Quasimodes in a Plasma

The dispersion relation describing the simultaneous stimulated scattering off of an arbitrary number of electrostatic electron modes in the plasma can be obtained using a kinetic, or Vlasov, description for the electron density fluctuations. A nonlinear pondermotive correction to the acceleration term is included in the Vlasov equation to allow coupling of the electron density fluctuations to the electromagnetic modes. The description, which allows for Landau damped modes, is termed a quasimode analysis of the nonlinear coupling of modes. The complete derivation of this dispersion relation is given in Appendix C and the resultant dispersion relation is reiterated here

$$\boxed{K_L = \frac{1}{4}k^2\mathbf{v}_o^2(-\chi_{Le})\left(\frac{1}{D_{T+}}+\frac{1}{D_{T-}}\right)}. \quad \textbf{(32)}$$

This model gives the nonlinear (to second order) coupling of linear modes. However, the EAW mode modeled in K_L is the result of a nonlinear effect, i.e. the trapping of particles in the large amplitude electrostatic wave generated by SRS. What we are attempting to do with the non-linear Vlasov-Maxwell code is to determine the SRS evolved electron distribution function whose linear normal modes exhibit EAWs and thus explains the observed laser scattering off of the EAW mode. Using this "new" initial distribution function, nonlinear quasimode coupling theory can be applied to describe scattering off of the mode contained in the general dispersion relation $K_L = 0$. The use of the nonlinear Vlasov code allows one to model the new equilibrium distribution function. This distribution function can then be modeled as a bi-Maxwellian and used to determine K_L and χ_{Le}. Using these values in (32) allows one to see where the modes are and predict what their growth rates will be. As an example, the results of this calculation are shown in Figure 47 for the bi-Maxwellian model using the parameters K = $k\lambda_{De}$ = 0.28, T_e = 390 eV, T_i = 100 eV, T_b = 20 eV, n_e = .97, n_b = 0.03, V_b = 7.6 (~0.4$v_{\phi EPW}$), and I_o=2x10^{15} W/cm^2. Solving for the most weakly damped roots of the dispersion relation, i.e. the normal modes and quasimodes present, one finds that the usual EPW is present and additionally, as a result of the to the electron beam, another mode emerges that exhibits acoustic-like dispersion (see Figure 45). Figure 47 can be directly compared to the experimental observation shown in Figure 34. Note that Figure 47 shows the response, or normal modes present in the plasma. The peaks represent zeros of the dispersion relation, i.e. K_L = 0. These peaks are not infinite in magnitude and have some width due to the modes being damped.

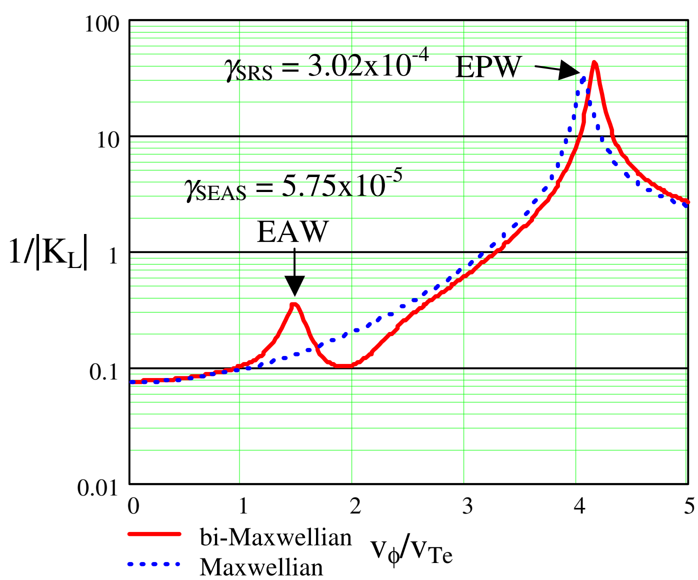

Figure 47. Plot of the inverse of the longitudinal permittivity function showing the difference between the Maxwellian and bi-Maxwellian models. For the parameters K = $k\lambda_{De}$ = 0.28, T_e = 390 eV, T_i = 100 eV, T_b = 20 eV, n_e = .97, n_b = 0.03, V_b = 7.6 (~0.4$v_{\phi EPW}$), and I_o = 2x10^{15} W/cm^2 the bi-Maxwellian model predicts the emergence of the EAW mode where observed experimentally. Growth rates are normalized to the laser frequency.

Chapter 5: Conclusions

It has been established that LDI cascade can be observed in the SHS laser-plasma interaction. In order to more completely understand the effects of LDI cascade on the saturation of SRS, more experiments must be performed. These experiments must be designed to look specifically at the energies in the LDI cascade daughter waves and will most likely involve the beating of a probe and interaction laser so that with known incident energies the energy transfer between beams can be evaluated. Since using larger optics in the Thomson scattering diagnostic is not feasible, future experiments should use hotter plasmas in order to reduce thermal effects on the IAW and EPW dispersion and thus allow more cascades to be observed with the existing optics. Additionally, in order to more fully understand the possible role of LDI in the saturation of SRS it is desirable to simultaneously monitor both the forward and backward propagating EPWs resulting from SRS and LDI.

Stimulated electron acoustic scattering (SEAS) has been experimentally observed and a sound basis for pursuing a more in depth theoretical understanding of this mode has been presented. It is believed that for the proper circumstances, many of these trapped and beaming particle modes exist in the plasma as a result of other processes such as SRS and SBS. An analytic model for scattering off these modes and quasimodes has also been presented. Again, experiments designed to look specifically at these new modes are required to completely understand and characterize them.

Although the 1D Vlasov-Maxwell model may be adequate, perhaps a better approximation for the time evolution of the electron distribution resulting from SRS would be obtained using a 1½ D Vlasov code, i.e. by adding an additional velocity component. Additionally, the Vlasov code used in this thesis only models a single ion species. A better model to approximate the physical plasmas would be obtained if it were multi-species in order to more correctly model the IAW damping. This is not difficult to implement but requires time and verification of the code. Since the code has mobile ions, it is possible to model the SRS-LDI interaction. This area was not explored in this thesis, but as alluded to the effect of LDI on SRS is an area ripe for study. The right-hand boundary of the plasma may affect long-time simulation results due to reflection of forward propagating waves, e.g. the laser or forward SRS. A future improvement to the code would be to remove these reflections by implementing a smooth or semi-infinite boundary condition on the right-hand side of the plasma. Lastly, the effect of the initial noise level on the saturation of the SRS interaction was not explored in this thesis. All of this must be left to future work.

Appendix A

Derivation of the Dispersion Relation Describing Stimulated Raman Scattering [72]

In this appendix, the dispersion relation that describes the stimulated Raman scattering (SRS) process is derived using a fluid description for the plasma and Maxwell's equations for the fields. All equations and quantities are in the International System of Units, i.e. *Systeme Internationale* (SI).

As usual, we start off with Maxwell's equations describing the electric and magnetic fields

$$\nabla \times \mathbf{E} + \frac{\partial \mathbf{B}}{\partial t} = 0, \tag{A1}$$

$$\nabla \times \mathbf{B} - \frac{1}{c^2}\frac{\partial \mathbf{E}}{\partial t} = \mu_o \mathbf{J}, \tag{A2}$$

$$\nabla \bullet \mathbf{E} = \frac{\rho}{\varepsilon_o}, \text{ and} \tag{A3}$$

$$\nabla \bullet \mathbf{B} = 0, \tag{A4}$$

where $\mathbf{E}$ is the electric field, $\mathbf{B}$ is the magnetic flux density, $\mathbf{J}$ is the current density, ρ is the charge density, μ_o and ε_o are, respectively, the permeability and permittivity of free space, and $c = 1/\sqrt{\mu_o \varepsilon_o}$ is the speed of light. In all equations, boldface letters indicate vector quantities.

Using the vector identity $\nabla \bullet (\nabla \times \mathbf{A}) = 0$, the magnetic flux density can be expressed as the curl of a vector potential, i.e. $\mathbf{B} = \nabla \times \mathbf{A}$. Using the Coulomb gauge with $\nabla \bullet \mathbf{A} = 0$, the electric field is defined by

$$\mathbf{E} = -\nabla \Phi - \frac{\partial \mathbf{A}}{\partial t}. \tag{A5}$$

Substituting these definitions for $\mathbf{E}$ and $\mathbf{B}$ into Ampere's equation (A2) gives

$$\nabla \times (\nabla \times \mathbf{A}) - \frac{1}{c^2}\frac{\partial}{\partial t}\left(-\nabla \Phi - \frac{\partial \mathbf{A}}{\partial t} \right) = \mu_o \mathbf{J}. \tag{A6}$$

Expanding the first term on the left-hand side of (A6) by using the vector identity $\nabla \times (\nabla \times \mathbf{A}) = \nabla(\nabla \bullet \mathbf{A}) - \nabla^2 \mathbf{A}$, using the Coulomb gauge, and grouping terms gives

$$\left(\frac{1}{c^2}\frac{\partial^2}{\partial t^2} - \nabla^2 \right)\mathbf{A} + \frac{1}{c^2}\frac{\partial}{\partial t}\nabla \Phi = \mu_o \mathbf{J}. \tag{A7}$$

The scalar potential Φ and the current density $\mathbf{J}$ must now be solved for in terms of the vector potential $\mathbf{A}$ and the electron density n_e. Substituting the charge density from Poisson's equation (A3)

$$\nabla^2\Phi = -\frac{\rho}{\varepsilon_o} \qquad \textbf{(A8)}$$

into the continuity equation

$$\frac{\partial\rho}{\partial t} + \nabla \bullet \mathbf{J} = 0 \qquad \textbf{(A9)}$$

results in

$$\varepsilon_o \frac{\partial}{\partial t}(-\nabla^2\Phi) + \nabla \bullet \mathbf{J} = 0. \qquad \textbf{(A10)}$$

Rearranging terms this can be rewritten as

$$\nabla \bullet \left(\varepsilon_o \frac{\partial}{\partial t}\nabla\Phi - \mathbf{J} \right) = 0. \qquad \textbf{(A11)}$$

The current density is comprised of both longitudinal and transverse parts, i.e. $\mathbf{J} = \mathbf{J}_L + \mathbf{J}_T$. For a transverse electromagnetic (TEM) mode, the charge density $\rho = 0$ and thus from the continuity equation $\nabla \bullet \mathbf{J}_T = 0$. Using this fact, (A11) can be rewritten as

$$\nabla \bullet \left(\varepsilon_o \frac{\partial}{\partial t}\nabla\Phi - (\mathbf{J}_T + \mathbf{J}_L) \right) = 0\text{, or} \qquad \textbf{(A12)}$$

$$\nabla \bullet \left(\varepsilon_o \frac{\partial}{\partial t}\nabla\Phi - \mathbf{J}_L \right) = 0 \Rightarrow \varepsilon_o \frac{\partial}{\partial t}\nabla\Phi = \mathbf{J}_L. \qquad \textbf{(A13)}$$

Using (A13) in (A7) gives

$$\left(\frac{1}{c^2}\frac{\partial^2}{\partial t^2} - \nabla^2 \right)\mathbf{A} = \mu_o \mathbf{J}_T. \qquad \textbf{(A14)}$$

The transverse current $\mathbf{J}_T$ must now be evaluated. To do so, we need to look at the electron dynamics using the force balance equation

$$m_e\left(\frac{\partial}{\partial t} + \mathbf{v}_e \bullet \nabla \right)\mathbf{v}_e = -e(\mathbf{E} + \mathbf{v}_e \times \mathbf{B}) \qquad \textbf{(A15)}$$

Looking at transverse components only, i.e. $(\mathbf{v}_e \bullet \nabla)\mathbf{v}_e = 0$, it is found that $m_e \frac{\partial \mathbf{v}_{eT}}{\partial t} = -e\mathbf{E}_T$. Substituting for **E** from (A5) and realizing that the scalar potential **Φ** represents the longitudinal component of the electric field gives

$$\frac{\partial \mathbf{v}_{eT}}{\partial t} = -\frac{e}{m_e}\mathbf{E}_T = \frac{e}{m_e}\frac{\partial \mathbf{A}}{\partial t} \Rightarrow \mathbf{v}_{eT} = \frac{e}{m_e}\mathbf{A}. \quad \textbf{(A16)}$$

The transverse current density, ignoring ion dynamics and assuming no initial drift velocity on the electrons, is $\mathbf{J}_T = -en_e\mathbf{v}_{eT}$. Substituting for the transverse electron velocity from (A16) yields

$$\mathbf{J}_T = -en_e\frac{e}{m_e}\mathbf{A} = -\varepsilon_o\omega_{pe}^2\frac{n_e}{n_o}\mathbf{A}, \quad \textbf{(A17)}$$

where $\omega_{pe} = \sqrt{\frac{n_o e^2}{\varepsilon_o m_e}}$ is the electron plasma frequency, and n_o is the background electron density. Substituting this definition for the transverse current density into (A14) gives

$$\left(\frac{1}{c^2}\frac{\partial^2}{\partial t^2} - \nabla^2\right)\mathbf{A} = -\mu_o\varepsilon_o\omega_{pe}^2\frac{n_e}{n_{eo}}\mathbf{A} = -\frac{\omega_{pe}^2}{c^2}\frac{n_e}{n_{eo}}\mathbf{A}, \quad \textbf{(A18)}$$

and multiplying both sides of the equation by c^2 gives

$$\left(\frac{\partial^2}{\partial t^2} - c^2\nabla^2\right)\mathbf{A} = -\omega_{pe}^2\frac{n_e}{n_{eo}}\mathbf{A}. \quad \textbf{(A19)}$$

The vector potential is comprised of the sum of two components

$$\mathbf{A} = \mathbf{A}_o + \mathbf{A}_1, \quad \textbf{(A20)}$$

where $\mathbf{A}_o$ is the pump EMW, $\mathbf{A}_1$ is the scattered EMW. The electron density also has two components

$$n = n_{eo} + n_1, \quad \textbf{(A21)}$$

where n_{eo} is the constant background electron density and n_1 is the low frequency, small-amplitude density fluctuation due to the electron plasma wave (EPW) such that $|n_1| << |n_{eo}|$ Substituting (A20) and (A21) into (A19) gives

$$\left(\frac{\partial^2}{\partial t^2} - c^2\nabla^2\right)(\mathbf{A}_o + \mathbf{A}_1) = -\omega_{pe}^2 \frac{(n_{eo} + n_1)}{n_{eo}}(\mathbf{A}_o + \mathbf{A}_1). \qquad \textbf{(A22)}$$

Substituting $\frac{n_1}{n_{eo}} = \frac{\delta n}{n}$ in (A22) and rearranging gives

$$\left(\frac{\partial^2}{\partial t^2} - c^2\nabla^2\right)(\mathbf{A}_o + \mathbf{A}_1) = -\omega_{pe}^2\left(1 + \frac{\delta n}{n}\right)(\mathbf{A}_o + \mathbf{A}_1). \qquad \textbf{(A23)}$$

Considering at only the resonant terms (i.e. the product of high and low frequency terms) and ignoring second order effects, i.e. making assumptions like $\frac{\delta n}{n}\mathbf{A}_0 >> \frac{\delta n}{n}\mathbf{A}_1$, (A23) can be massaged into a simpler form. The resultant equation is a very important result. It describes a scattered EMW driven by the beating of a pump EMW and an electron density fluctuation and is given by

$$\boxed{\left(\frac{\partial^2}{\partial t^2} - c^2\nabla^2 + \omega_{pe}^2\right)\mathbf{A}_1 = -\omega_{pe}^2 \frac{\delta n}{n}\mathbf{A}_o}. \qquad \textbf{(A24)}$$

Now, δn is the density fluctuation associated with the EPW and δn must be evaluated in terms of $\mathbf{A}_o$ and $\mathbf{A}_1$. To do so, we must again look at the electron dynamics. The electron velocity will be composed of longitudinal and transverse components, i.e. $\mathbf{v}_e = \mathbf{v}_{eL} + \mathbf{v}_{eT}$, and using the previous definition for the transverse velocity component gives

$$\mathbf{v}_e = \mathbf{v}_{eL} + \frac{e}{m_e}\mathbf{A}. \qquad \textbf{(A25)}$$

The electron dynamics are evaluated using the continuity and force balance equations which are, respectively,

$$\frac{\partial n_e}{\partial t} + \nabla \bullet (n_e \mathbf{v}_e) = 0 \qquad \textbf{(A26)}$$

$$n_e m_e\left(\frac{\partial}{\partial t} + \mathbf{v}_e \bullet \nabla\right)\mathbf{v}_e = -n_e e(\mathbf{E} + \mathbf{v}_e \times \mathbf{B}) - \nabla p_e, \qquad \textbf{(A27)}$$

where p_e is the pressure due to electrons. Rearranging (A27) gives

$$\left(\frac{\partial}{\partial t}+\mathbf{v}_e\bullet\nabla\right)\mathbf{v}_e+\frac{\nabla p_e}{n_e m_e}=-\frac{e}{m_e}(\mathbf{E}+\mathbf{v}_e\times\mathbf{B})\,. \qquad \mathbf{(A28)}$$

Substituting for the electron velocity in terms of its transverse and longitudinal components and for the electric field in terms of the scalar and vector potentials gives

$$\frac{\partial}{\partial t}\mathbf{v}_{eL}+\frac{e}{m_e}\frac{\partial}{\partial t}\mathbf{A}+(\mathbf{v}_e\bullet\nabla)\mathbf{v}_e+\frac{\nabla p_e}{n_e m_e}=-\frac{e}{m_e}(-\nabla\Phi-\frac{\partial\mathbf{A}}{\partial t}+\mathbf{v}_e\times(\nabla\times\mathbf{A})). \qquad \mathbf{(A29)}$$

Canceling like terms from both sides gives

$$\frac{\partial}{\partial t}\mathbf{v}_{eL}+(\mathbf{v}_e\bullet\nabla)\mathbf{v}_e+\frac{\nabla p_e}{n_e m_e}=-\frac{e}{m_e}(-\nabla\Phi+\mathbf{v}_e\times(\nabla\times\mathbf{A}))\,. \qquad \mathbf{(A30)}$$

Evaluating the curl of the electron velocity and realizing that $\nabla\times\mathbf{v}_{eL}=0$ allows substituting for the vector potential in terms of the electron velocity, i.e.

$$\nabla\times\mathbf{v}_e=\nabla\times\left(\mathbf{v}_{eL}+\frac{e}{m_e}\mathbf{A}\right)=\frac{e}{m_e}(\nabla\times\mathbf{A})\,. \qquad \mathbf{(A31)}$$

With this substitution (A30) becomes

$$\frac{\partial}{\partial t}\mathbf{v}_{eL}+(\mathbf{v}_e\bullet\nabla)\mathbf{v}_e+\frac{\nabla p_e}{n_e m_e}=\frac{e}{m_e}\nabla\Phi-\mathbf{v}_e\times(\nabla\times\mathbf{v}_e)\,. \qquad \mathbf{(A32)}$$

Rearranging terms and using the vector identity $(\mathbf{v}_e\bullet\nabla)\mathbf{v}_e+\mathbf{v}_e\times(\nabla\times\mathbf{v}_e)=\frac{1}{2}\nabla\mathbf{v}_e^2$ finally transforms (A30) to

$$\boxed{\frac{\partial}{\partial t}\mathbf{v}_{eL}+\frac{\nabla p_e}{n_e m_e}=\frac{e}{m_e}\nabla\Phi-\frac{1}{2}\nabla\mathbf{v}_e^2}\,. \qquad \mathbf{(A33)}$$

The continuity equation is now used to substitute for the longitudinal electron velocity in terms of the electron density fluctuation. This is derived in the following sequence. Starting with the continuity equation and expressing the electron density as a constant background component combined with a small amplitude perturbation gives

$$\frac{\partial\delta n_e}{\partial t}+\nabla\bullet\left[(n_{eo}+\delta n_e)(\mathbf{v}_{eL}+\frac{e}{m_e}\mathbf{A})\right]=0\,. \qquad \mathbf{(A34)}$$

Expanding the divergence term gives

$$\frac{\partial \delta n_e}{\partial t} + n_{eo} \nabla \bullet \mathbf{v}_{eL} + n_{eo} \frac{e}{m_e} \nabla \bullet \mathbf{A} + \nabla \bullet (\delta n_e \mathbf{v}_{eL}) + \nabla \bullet \left(\delta n_e \frac{e}{m_e} \mathbf{A} \right) = 0 . \quad \textbf{(A35)}$$

Realizing that $\mathbf{A}$ has only transverse components, i.e. $\nabla \bullet \mathbf{A} = 0$, and using the vector identity $\nabla \bullet (f\mathbf{T}) = \nabla f \bullet \mathbf{T} + f\nabla \bullet \mathbf{T}$ reduces (A35) to

$$\frac{\partial \delta n_e}{\partial t} + n_{eo} \nabla \bullet \mathbf{v}_{eL} + \delta n_e \nabla \bullet \mathbf{v}_{eL} + \nabla \delta n_e \bullet \mathbf{v}_{eL} + \nabla \delta n_e \bullet \frac{e}{m_e} \mathbf{A} = 0 . \quad \textbf{(A36)}$$

It was assumed that $\delta n_e << n_{eo}$ and since the density fluctuation is in the longitudinal direction, (A36) is simplified to

$$\frac{\partial \delta n_e}{\partial t} + n_{eo} \nabla \bullet \mathbf{v}_{eL} + \nabla \delta n_e \bullet \mathbf{v}_{eL} = 0 . \quad \textbf{(A37)}$$

Since both the density fluctuation and the longitudinal electron velocity will be at the same frequency, the last term on the left-hand side of (A37) provides only second-harmonic or zero frequency components. Thus, the continuity equation ultimately reduces to

$$\boxed{\frac{\partial \delta n_e}{\partial t} + n_{eo} \nabla \bullet \mathbf{v}_{eL} = 0} . \quad \textbf{(A38)}$$

The $\mathbf{v}_e^2$ term in (A33) can be evaluated in terms of the vector potential, i.e.

$$\mathbf{v}_e^2 = \left(\mathbf{v}_{eL} + \frac{e}{me} \mathbf{A} \right) \bullet \left(\mathbf{v}_{eL} + \frac{e}{me} \mathbf{A} \right) . \quad \textbf{(A39)}$$

Substituting $\mathbf{A} = \mathbf{A}_o + \mathbf{A}_1$ transforms this into

$$\mathbf{v}_e^2 = \mathbf{v}_{eL}^2 + 2\mathbf{v}_{eL} \bullet \frac{e}{m_e} (\mathbf{A}_o + \mathbf{A}_1) + \frac{e^2}{m_e^2} (\mathbf{A}_o^2 + 2\mathbf{A}_o \mathbf{A}_1 + \mathbf{A}_1^2) . \quad \textbf{(A40)}$$

Evaluating all terms on the right-hand side of (A40), one sees that $\mathbf{v}_{eL}^2$ is 2nd harmonic or zero frequency, $\mathbf{v}_{eL} \bullet (\mathbf{A}_o + \mathbf{A}_1) = 0$ since the components are transverse to each other, and that only one component of $(\mathbf{A}_o^2 + 2\mathbf{A}_o \mathbf{A}_1 + \mathbf{A}_1^2)$ is resonant with the density fluctuation. Thus, (A40) reduces to

$$\mathbf{v}_e^2 = 2 \frac{e^2}{m_e^2} \mathbf{A}_o \bullet \mathbf{A}_1 . \quad \textbf{(A41)}$$

The pressure gradient term is approximated by

$$\frac{\nabla p_e}{m_e n_e} = \frac{3\mathrm{T}_e \nabla n_e}{m_e n_e} = \frac{3k_B \mathrm{T}_e \nabla(n_{eo} + \delta n_e)}{m_e(n_{eo} + \delta n_e)} \approx \frac{3\mathrm{V}_{Te}^2 \nabla \delta n_e}{n_{eo}}, \tag{A42}$$

where k_B is Boltzmann's constant, $\mathrm{T_e}$ is the electron temperature, and $\mathrm{V}_{Te}^2 = k_B \mathrm{T}_e / m_e$ is the electron thermal velocity. Substituting (A41) and (A42) into (A33) reduces the force balance equation to

$$\boxed{\frac{\partial}{\partial t}\mathbf{v}_{eL} + 3\mathrm{V}_{Te}^2 \frac{\nabla \delta n_e}{n_{eo}} - \frac{e}{m_e}\nabla\Phi = -\nabla\left(\frac{e^2}{m_e^2}\mathbf{A}_o \bullet \mathbf{A}_1\right)}. \tag{A43}$$

The force balance equation and the continuity equation can be combined into one equation by taking the divergence of (A43) and the time derivative of (A38) and substituting for terms involving the longitudinal electron velocity in terms of the density fluctuation. This proceeds as follows

$$\frac{\partial}{\partial t}\nabla \bullet \mathbf{v}_{eL} + 3\mathrm{V}_{Te}^2 \nabla^2(\delta n_e / n_{eo}) - \frac{e}{m_e}\nabla^2\Phi = -\nabla^2\left(\frac{e^2}{m_e^2}\mathbf{A}_o \bullet \mathbf{A}_1\right) \tag{A44}$$

$$\frac{\partial}{\partial t}\nabla \bullet \mathbf{v}_{eL} = -\frac{\partial^2(\delta n_e / n_{eo})}{\partial t^2}. \tag{A45}$$

Using Poisson's equation $\nabla^2\Phi = -\rho/\varepsilon_o = -e\delta n_e/\varepsilon_o$ and substituting (A45) in (A44) gives

$$-\frac{\partial^2(\delta n_e / n_{eo})}{\partial t^2} + 3\mathrm{V}_{Te}^2 \nabla^2(\delta n_e / n_{eo}) - \frac{e^2 \delta n_e}{m_e \varepsilon_o} = -\nabla^2\left(\frac{e^2}{m_e^2}\mathbf{A}_o \bullet \mathbf{A}_1\right). \tag{A46}$$

Using the definition of the plasma frequency and grouping terms reduces this to

$$\boxed{\left(\frac{\partial^2}{\partial t^2} + \omega_{pe}^2 - 3\mathrm{V}_{Te}^2 \nabla^2\right)(\delta n_e / n_{eo}) = \frac{e^2}{m_e^2}\nabla^2(\mathbf{A}_o \bullet \mathbf{A}_1)}. \tag{A47}$$

This is another important result. It describes a density fluctuation arising from the beating of a pump and a scattered EMW. To summarize, the coupled equations describing SRS are

$$\boxed{\left(\frac{\partial^2}{\partial t^2} - c^2\nabla^2 + \omega_{pe}^2\right)\mathbf{A}_1 = -\omega_{pe}^2 \frac{\delta n}{n}\mathbf{A}_o}\text{, and}$$

$$\boxed{\left(\frac{\partial^2}{\partial t^2} + \omega_{pe}^2 - 3\mathrm{V}_{Te}^2\nabla^2\right)(\delta n_e / n_{eo}) = \frac{e^2}{m_e^2}\nabla^2\left(\mathbf{A}_o \bullet \mathbf{A}_1\right)}$$

To finalize the theory of SRS, frequencies are assigned to the pump $\mathbf{A}_o$ and the density fluctuation ($\delta n/n_{eo}$) and both are assumed to have a sinusoidal variation in space and time, i.e.

$$\mathbf{A}_o = \mathrm{Re}\left(\frac{1}{2}\mathbf{a}_o e^{i\vec{k}_o \bullet r - i\omega_o t}\right)\text{, and} \tag{A48}$$

$$\left(\frac{\delta n_e}{n_{eo}}\right) = \mathrm{Re}\left(\frac{1}{2}N_1 e^{i\vec{k}\bullet r - i\omega t}\right). \tag{A49}$$

The scattered EMW can be either up or down-shifted in frequency, i.e.

$$\left(\frac{\delta n_e}{n_{eo}}\right)\mathbf{A}_o = \mathrm{Re}\left(\frac{1}{2}N_1\mathbf{a}_o e^{i\vec{k}_+ \bullet r - i\omega_+ t}\right) + \mathrm{Re}\left(\frac{1}{2}N_1\mathbf{a}_o^* e^{i\vec{k}_- \bullet r - i\omega_- t}\right), \tag{A50}$$

where the star superscript, as usual, represents the complex conjugate of the quantity, $\omega_\pm = \omega \pm \omega_o$, and $k_\pm = k \pm k_o$. Using these definitions in the coupled equations results in

$$\left(\omega_\pm^2 - \omega_{pe}^2 - c^2k_\pm^2\right)\mathbf{A}_\pm = \omega_{pe}^2 \frac{1}{2}N_1\begin{pmatrix}\mathbf{a}_o \\ \mathbf{a}_o^*\end{pmatrix}\text{, and} \tag{A51}$$

$$\left(\omega^2 - \omega_{pe}^2 - 3\mathrm{V}_{Te}^2k^2\right)N_1 = \frac{1}{2}\frac{e^2}{m_e^2}k^2(\mathbf{a}_o^*\mathbf{A}_+ + \mathbf{a}_o\mathbf{A}_-). \tag{A52}$$

It is seen that the quantities in the parenthesis on the left-hand side of (A51) and (A52) are the linear dispersion relations for an EMW in a plasma and an electron plasma wave, respectively. If we represent these dispersion relations by

$$D_{T\pm} = \left(\omega_\pm^2 - \omega_{pe}^2 - c^2k_\pm^2\right)\text{, and} \tag{A53}$$

$$D_L = \left(\omega^2 - \omega_{pe}^2 - 3\mathrm{V}_{Te}^2 k^2\right) \qquad \textbf{(A54)}$$

(A51) and (A52) can be rewritten in the more compact form

$$D_{T\pm}\mathbf{A}_{\pm} = \omega_{pe}^2 \frac{1}{2} N_1 \begin{pmatrix} \mathbf{a}_o \\ \mathbf{a}_o^* \end{pmatrix}, \text{ and} \qquad \textbf{(A55)}$$

$$D_L N_1 = \frac{1}{2}\frac{e^2}{m_e^2} k^2 (\mathbf{a}_o^* \bullet \mathbf{A}_+ + \mathbf{a}_o \bullet \mathbf{A}_-). \qquad \textbf{(A56)}$$

Equation (A55) is really two equations representing the up and down-shifted scattered EMW. Expanding (A55) gives $D_{T+}\mathbf{A}_+ = \omega_{pe}^2 \frac{1}{2} N_1 \mathbf{a}_o$ and $D_{T-}\mathbf{A}_- = \omega_{pe}^2 \frac{1}{2} N_1 \mathbf{a}_o^*$. Solving for $\mathbf{A}_+$ and $\mathbf{A}_-$ and substituting these expressions into (A56) gives

$$D_L N_1 = \frac{1}{2}\frac{e^2}{m_e^2} k^2 \frac{\omega_{pe}^2}{2}\left[\frac{|\mathbf{a}_o|^2}{D_{T+}} + \frac{|\mathbf{a}_o|^2}{D_{T-}}\right], \qquad \textbf{(A57)}$$

and rearranging terms gives

$$D_L N_1 = \frac{1}{2}\left(\frac{e|\mathbf{a}_o|}{m_e}\right)^2 k^2 \frac{\omega_{pe}^2}{2}\left[\frac{1}{D_{T+}} + \frac{1}{D_{T-}}\right]. \qquad \textbf{(A58)}$$

The transverse electric field is defined in terms of the vector potential, i.e. $\mathbf{E}_T = -\frac{\partial}{\partial t}\mathbf{A}_o$. Assuming the definition for $\mathbf{A}_o$ given in (A48) and evaluating the derivative gives $\mathbf{E}_T = -i\omega_o \mathbf{a}_o$ which leads to $|\mathbf{a}_o|^2 = \left|\frac{\mathbf{E}_T}{\omega_o}\right|^2$. The quiver velocity of an electron in the transverse electric field is defined as

$$\mathrm{v}_o^2 = \left(\frac{e|\mathbf{a}_o|}{m_e}\right)^2 = \left|\frac{e\mathbf{E}_T}{m_e\omega_o}\right|^2. \qquad \textbf{(A59)}$$

Using this definition in (A58) and canceling like terms on both sides of the equation gives the dispersion relation for SRS

$$\boxed{D_L = \frac{1}{4} \mathrm{v}_o^2 k^2 \omega_{pe}^2 \left[\frac{1}{D_{T+}} + \frac{1}{D_{T-}} \right]}. \quad \textbf{(A60)}$$

Usually, the up-shifted scattered EMW is considered non-resonant and (A60) can ultimately be reduced to

$$\boxed{D_L D_{T-} = \frac{1}{4} \mathrm{v}_o^2 k^2 \omega_{pe}^2}. \quad \textbf{(A61)}$$

Note that the above derivation assumed that the pump and scattered EMW wave vectors, or equivalently their electric field vectors, were collinear. In general this may not be the case. If the EMW wave vectors are not collinear, a geometry factor will reduce the value of the growth rate for the interaction. To see how this is manifested one can split the fields, and thus the vector potentials, into a magnitude multiplying a polarization unit vector, e.g. for the pump field

$$\mathbf{E}_o = -i\omega_o \mathbf{a}_o \Rightarrow \mathrm{E}_o \hat{e}_o = -i\omega_o \mathrm{a}_o \hat{\mathrm{a}}_o. \quad \textbf{(A62)}$$

One can see that since the electric field and the vector potential are in the same direction so will be their unit vectors, i.e. $\hat{e}_o = \hat{\mathrm{a}}_o$. The scattered EMW can also be expressed in a similar manner and forming the dot product $(\mathbf{a}_o^* \bullet \mathbf{A}_+ + \mathbf{a}_o \bullet \mathbf{A}_-)$ will leave a geometry factor $\left[\frac{(\hat{e}_o^* \bullet \hat{e}_+)^2}{D_{T+}} + \frac{(\hat{e}_o \bullet \hat{e}_-)^2}{D_{T-}} \right]$ on the right-hand side of (A60). If we consider only the down-shifted scattered EMW to be resonant, the dot product of the two unit vectors can be simplified to $\hat{e}_o \bullet \hat{e}_- = \cos\theta$, where θ is the angle between the pump and scattered EMW polarization vectors. Thus, including geometry effects the generalized form of the SRS dispersion relation is given by

$$\boxed{D_L D_{T-} = \frac{1}{4} \mathrm{v}_o^2 k^2 \omega_{pe}^2 \cos^2\theta}. \quad \textbf{(A63)}$$

Appendix B

Derivation of the Dispersion Relation Describing the Langmuir Decay Instability [72]

In this appendix a derivation of the dispersion relation and the underlying physics of the Langmuir decay instability (LDI) are presented. In the context of this thesis, LDI is the result of the Langmuir wave generated by stimulated Raman scattering (SRS) growing to sufficient amplitude such that it decays into another counter propagating Langmuir wave and a co-propagating ion acoustic wave (IAW). The LDI process inherently involves the coupling of electron modes to ion modes in the plasma. All waves involved in the LDI process are electrostatic. This appendix takes a different approach than the former appendix in that a Zakharov fluid description is used [73]. This entails evaluating the high and low frequency dynamics of the fluid equations and selecting only those components that are resonant with the quantity of interest.

It is most easy to understand the Zakharov derivations by first providing an example of the products of high and low frequency quantities. All quantities are assumed to have a sinusoidal space-time variation. If we assign fast and slow variations to two complex quantities, e.g. **E** which represents an electric field with fast variation and n which represents a density fluctuation with slow variation, and look at their real parts these quantities are expressed as

$$\mathbf{E} = \frac{1}{2}\left(\mathbf{E}_o e^{i\mathbf{k}_o \bullet \mathbf{r} - i\omega_o t} + \mathbf{E}_o^* e^{-i\mathbf{k}_o \bullet \mathbf{r} + i\omega_o t}\right), \text{ and} \tag{B1}$$

$$n = \frac{1}{2}\left(n_s e^{i\mathbf{k}_s \bullet \mathbf{r} - i\omega_s t} + n_s^* e^{-i\mathbf{k}_s \bullet \mathbf{r} + i\omega_s t}\right). \tag{B2}$$

Forming the product of either the fast or slowly varying quantity with itself yields e.g.

$$n^2 = \frac{1}{4}\left(n_s^2 e^{i2\mathbf{k}_s \bullet \mathbf{r} - i2\omega_s t} + n_s^{*2} e^{-i2\mathbf{k}_s \bullet \mathbf{r} + i2\omega_s t} + 2\left|n_s\right|^2\right). \tag{B3}$$

It is seen that the components are either at the second harmonic or zero frequency. Forming the product of a fast and slow varying quantities yields a product which is at an intermediate frequency that is either up or down-shifted from a particular frequency, i.e. the product

$$n_s \mathbf{E} = \frac{1}{4}\begin{pmatrix} n_s \mathbf{E}_o e^{i(\mathbf{k}_s + \mathbf{k}_o)\bullet \mathbf{r} - i(\omega_s + \omega_o)t} + n_s^* \mathbf{E}_o^* e^{-i(\mathbf{k}_s + \mathbf{k}_o)\bullet \mathbf{r} + i(\omega_s + \omega_o)t} \\ + n_s^* \mathbf{E}_o e^{-i(\mathbf{k}_s - \mathbf{k}_o)\bullet \mathbf{r} + i(\omega_s - \omega_o)t} + n_s \mathbf{E}_o^* e^{i(\mathbf{k}_s - \mathbf{k}_o)\bullet \mathbf{r} - i(\omega_s - \omega_o)t} \end{pmatrix}, \tag{B4}$$

it is seen to have two pairs of quantities (up and down-shifted) that are complex conjugates.

The main point to remember is that the product of two quantities having the same frequencies provide second harmonic and zero frequency contributions. The product of two quantities one having a fast and the other a slow variation in space and time, is a quantity with up and down-shifted variations. This forms the basis of the following derivations. Additionally, when one looks at quantities that are at the same frequency, one must consider their amplitudes and neglect terms that are much lower in amplitude. These principles will be reiterated throughout the derivations where appropriate.

The derivation proceeds by first separating the high and low frequency dynamics. All quantities (except constant background densities) are assumed to have a space-time variation $\sim e^{i\vec{k}\bullet r - i\omega t}$. The high-frequency, or fast variations labeled using a subscript *f*, are at approximately the electron plasma frequency, i.e. $\omega \approx \omega_{pe} = \sqrt{n_{eo}e^2 / \varepsilon_o m_e}$ The low frequency, or slow variations labeled using a subscript *s*, are at a frequency much less than the ion plasma frequency, i.e. $\omega \ll \omega_{\mathrm{pi}} \ll \omega_{\mathrm{pe}}$. The field dynamics are electrostatic, i.e.

$$\mathbf{E} = \mathbf{E}_f + \mathbf{E}_s = -\nabla\Phi \qquad \textbf{(B5)}$$

and the perturbed magnetic field is negligible, i.e. $\mathbf{B}_1 = 0$. As in the previous appendix, bold-face type represents vector quantities. We consider a plasma consisting of electrons and a single ion species. There are no equilibrium drifts and the plasma is charge neutral, i.e.

$$n_e = n_{eo} + n_{es} + n_{ef} \, , \qquad \textbf{(B6)}$$

$$\mathbf{v}_e = \mathbf{v}_{es} + \mathbf{v}_{ef} \, , \qquad \textbf{(B7)}$$

$$n_i = n_{io} + n_{is} \, , \qquad \textbf{(B8)}$$

$$\mathbf{v}_i = \mathbf{v}_{is} \, , \qquad \textbf{(B9)}$$

$$Z_i n_{io} = n_{eo} = n_o \, , \qquad \textbf{(B10)}$$

where n is the density, **v** is the velocity, Z_i is the ion charge state, and the subscripts *e*, *i*, *o*, *s*, and *f* refer to, respectively, electrons, ions, equilibrium (or background), slow variation, and fast variation. In addition to fast variations, the electrons will also have slow variations due to their shielding effect on the ions. Note that the background densities are assumed constant and have no space-time variation. Also, the condition of low frequency quasi-neutrality is imposed, i.e.

$$Z_i n_{is} = n_{es} = n_s \tag{B11}$$

and collisions are ignored. Other approximations in the derivation are that $k\lambda_{De} << 1$ (i.e. weak damping) and $T_e >> T_i$.

For the high-frequency electron dynamics, the electron continuity and momentum balance equations must be evaluated. Ion dynamics are ignored in the high frequency derivations due to the previous assumption that $\omega_{is} << \omega_{pi} << \omega_{pe}$. Using the definitions for the electron density and velocity in (B6) and (B7) the electron continuity equation

$$\frac{\partial n_e}{\partial t} + \nabla \bullet (n_e \mathbf{v}_e) = 0 \tag{B12}$$

expands to

$$\begin{gathered} \frac{\partial}{\partial t}(n_{eo} + n_{es} + n_{ef}) + \\ \nabla \bullet (n_{eo}\mathbf{v}_{es} + n_{eo}\mathbf{v}_{ef} + n_{es}\mathbf{v}_{es} + n_{es}\mathbf{v}_{ef} + n_{ef}\mathbf{v}_{es} + n_{ef}\mathbf{v}_{ef}) = 0 \end{gathered} . \tag{B13}$$

Ignoring derivatives of constant terms, zero frequency, and second harmonic components and evaluating for the fast variations with coupling between fast and slow variations, (B13) reduces to

$$\frac{\partial n_{ef}}{\partial t} + n_{eo} \nabla \bullet \mathbf{v}_{ef} + \nabla \bullet (n_{es}\mathbf{v}_{ef}) + \nabla \bullet (n_{ef}\mathbf{v}_{es}) = 0 . \tag{B14}$$

It is seen that there are two additional second order terms that allow for coupling of the fast and slow electron dynamics, in other words, coupling of the electron and ion dynamics.

The momentum balance equation for electrons is

$$n_e m_e \left(\frac{\partial}{\partial t} + \mathbf{v}_e \bullet \nabla \right) \mathbf{v}_e = -n_e e(\mathbf{E} + \mathbf{v}_e \times \mathbf{B}) - \nabla p_e . \tag{B15}$$

Since there is no imposed magnetic field, the $\mathbf{v}_e \times \mathbf{B}$ term is neglected since it provides only second harmonic effects. Rearranging (B15) results in

$$\left(\frac{\partial}{\partial t} + \mathbf{v}_e \bullet \nabla \right) \mathbf{v}_e + \frac{\nabla p_e}{n_e m_e} = -\frac{e}{m_e}\mathbf{E} . \tag{B16}$$

The pressure term is approximated by

$$\frac{\nabla p_e}{m_e n_e} = \frac{\gamma_e k_B \mathrm{T}_e \nabla n_e}{m_e n_e} = \gamma_e \mathrm{V}_{Te}^2 \frac{\nabla(n_{eo} + n_{es} + n_{ef})}{(n_{eo} + n_{es} + n_{ef})}, \qquad \textbf{(B17)}$$

where $\gamma_e = 1$ for isothermal dynamics, or in adiabatic dynamics $\gamma_e = (d + 2)/d$ where d is the number of degrees of freedom in the dynamics, and k_B is Boltzmann's constant. For the fast variations the electrons are considered to be undergoing one-dimensional adiabatic expansion and $\gamma_e = 3$. Expanding (B16) and looking for fast variations only results in

$$\frac{\partial \mathbf{v}_{ef}}{\partial t} + (\mathbf{v}_{es} \bullet \nabla)\mathbf{v}_{ef} + (\mathbf{v}_{ef} \bullet \nabla)\mathbf{v}_{es} + 3\mathrm{V}_{Te}^2 \frac{\nabla n_{ef}}{n_{eo}} = -\frac{e}{m_e}\mathbf{E}_f . \qquad \textbf{(B18)}$$

The second and third terms on the left-hand side of can be ignored since their magnitudes are much less than the first term and thus the momentum equation for fast electron variations reduces to

$$\frac{\partial \mathbf{v}_{ef}}{\partial t} + 3\mathrm{V}_{Te}^2 \frac{\nabla n_{ef}}{n_{eo}} = -\frac{e}{m_e}\mathbf{E}_f . \qquad \textbf{(B19)}$$

Poisson's equation for the fast electron variations is given by

$$\nabla \bullet \mathbf{E}_f = \frac{\rho}{\varepsilon_o} = -\frac{e}{\varepsilon_o} n_{ef} \Rightarrow n_{ef} = -\frac{\varepsilon_o}{e} \nabla \bullet \mathbf{E}_f . \qquad \textbf{(B20)}$$

The fast electron dynamics can be expressed in terms of a single equation by combining (B14) and (B19) and using (B20) to express n_{ef} in terms of the electric field. This proceeds as follows. Taking the time derivative of (B14) gives

$$\frac{\partial^2 n_{ef}}{\partial t^2} + n_{eo} \nabla \bullet \frac{\partial \mathbf{v}_{ef}}{\partial t} + \nabla \bullet \frac{\partial}{\partial t}(n_{es}\mathbf{v}_{ef}) + \nabla \bullet \frac{\partial}{\partial t}(n_{ef}\mathbf{v}_{es}) = 0. \qquad \textbf{(B21)}$$

Expanding the time derivatives and grouping like terms gives

$$\frac{\partial^2 n_{ef}}{\partial t^2} + \nabla \bullet \left[(n_{eo} + n_{es}) \frac{\partial \mathbf{v}_{ef}}{\partial t} + \frac{\partial n_{es}}{\partial t}\mathbf{v}_{ef} + \frac{\partial n_{ef}}{\partial t}\mathbf{v}_{es} + n_{ef}\frac{\partial \mathbf{v}_{es}}{\partial t} \right] = 0. \qquad \textbf{(B22)}$$

With the assumed space-time variation, the time derivatives result in a multiplication by the respective frequency. The low frequency terms are ignored with respect to the high frequency terms resulting in

$$\frac{\partial^2 n_{ef}}{\partial t^2} + \nabla \bullet \left[(n_{eo} + n_{es}) \frac{\partial \mathbf{v}_{ef}}{\partial t} + \frac{\partial n_{ef}}{\partial t} \mathbf{v}_{es} \right] = 0. \quad \textbf{(B23)}$$

A final ordering of terms assuming $\left| (n_{eo} + n_{es}) \frac{\partial \mathbf{v}_{ef}}{\partial t} \right| >> \left| \frac{\partial n_{ef}}{\partial t} \mathbf{v}_{es} \right|$ results in

$$\frac{\partial^2 n_{ef}}{\partial t^2} + \nabla \bullet \left[(n_{eo} + n_{es}) \frac{\partial \mathbf{v}_{ef}}{\partial t} \right] = 0. \quad \textbf{(B24)}$$

Equation (B19) is used to solve for $\mathbf{v}_{ef}$ in terms of n_{ef} and substituting the result into the above equation results in

$$\frac{\partial^2 n_{ef}}{\partial t^2} - \nabla \bullet \left[(n_{eo} + n_{es}) \left(\frac{e}{m_e} \mathbf{E}_f + 3\mathrm{V}_{Te}^2 \frac{\nabla n_{ef}}{n_{eo}} \right) \right] = 0. \quad \textbf{(B25)}$$

Finally, using Poisson's equation to express n_{ef} in terms of the electric field results in

$$-\frac{\varepsilon_o}{e} \frac{\partial^2 \nabla \bullet \mathbf{E}_f}{\partial t^2} - \nabla \bullet \left[(n_{eo} + n_{es}) \left(\frac{e}{m_e} \mathbf{E}_f - 3\mathrm{V}_{Te}^2 \frac{\varepsilon_o}{e} \frac{\nabla \nabla \bullet \mathbf{E}_f}{n_{eo}} \right) \right] = 0. \quad \textbf{(B26)}$$

Factoring out and dividing both sides by $-(\varepsilon_o/e)$, rearranging terms, and grouping on the divergence operator results in

$$\nabla \bullet \left[\frac{\partial^2 \mathbf{E}_f}{\partial t^2} + \left(1 + \frac{n_{es}}{n_{eo}} \right) \frac{n_{eo} e^2}{\varepsilon_o m_e} \mathbf{E}_f - 3\mathrm{V}_{Te}^2 \left(1 + \frac{n_{es}}{n_{eo}} \right) \nabla \nabla \bullet \mathbf{E}_f \right] = 0. \quad \textbf{(B27)}$$

Using the definition of the plasma frequency gives

$$\nabla \bullet \left[\frac{\partial^2 \mathbf{E}_f}{\partial t^2} + \omega_{pe}^2 \left(1 + \frac{n_{es}}{n_{eo}} \right) \mathbf{E}_f - 3\mathrm{V}_{Te}^2 \left(1 + \frac{n_{es}}{n_{eo}} \right) \nabla \nabla \bullet \mathbf{E}_f \right] = 0. \quad \textbf{(B28)}$$

Evaluating the ratio of the two nonlinear terms on the left-hand side of the above equation results in $\frac{\left| 3\mathrm{V}_{Te}^2 \nabla \nabla \bullet \mathbf{E}_f \right|}{\left| \omega_{pe}^2 \mathbf{E}_f \right|} \sim \frac{3\mathrm{V}_{Te}^2 k_f^2}{\omega_{pe}^2} \sim k_f^2 \lambda_{De}^2 << 1$ and thus the last nonlinear term can be neglected due to its small amplitude. The nonlinear component of $\omega_{pe}^2 \left(1 + \frac{n_{es}}{n_{eo}} \right) \mathbf{E}_f$ is identified as a modulation of the electron density by the low frequency, slow variation mode. Finally, the resultant equation for the fast electron dynamics is

$$\boxed{\left[\frac{\partial^2 \mathbf{E}_f}{\partial t^2} + \omega_{pe}^2 \mathbf{E}_f - 3\mathrm{V}_{Te}^2 \nabla\nabla \bullet \mathbf{E}_f\right] = -\omega_{pe}^2 \frac{n_{es}}{n_{eo}} \mathbf{E}_f}. \qquad \textbf{(B29)}$$

The left-hand side of (B29) is identified as the linear partial differential equation for electron plasma waves (EPW) and the right-hand side is the nonlinear coupling of the low frequency density fluctuation and the high frequency electric field.

The low-frequency dynamics are now evaluated. The fast, mobile electrons are considered to be isothermal and thus $\gamma_e = 1$. The low frequency momentum balance equation, averaging over time the fast variations, is given by

$$\frac{\partial \mathbf{v}_{es}}{\partial t} + (\mathbf{v}_{es} \bullet \nabla)\mathbf{v}_{es} + \left\langle (\mathbf{v}_{ef} \bullet \nabla)\mathbf{v}_{ef} \right\rangle + \mathrm{V}_{Te}^2 \frac{\nabla n_{es}}{n_{eo}} = -\frac{e}{m_e}\mathbf{E}_s \,. \qquad \textbf{(B30)}$$

The term $(\mathbf{v}_{es} \bullet \nabla)\mathbf{v}_{es}$ provides only second harmonic or zero-frequency components and can be neglected. Using the low frequency continuity equation

$$\frac{\partial n_{es}}{\partial t} + n_{eo}\nabla \bullet \mathbf{v}_{es} = 0 \Rightarrow \left|\frac{\omega}{k}\right| = \left|\frac{n_{eo}\mathbf{v}_{es}}{n_{es}}\right| \qquad \textbf{(B31)}$$

and defining the sound velocity $c_s = \dfrac{\omega}{k}$, evaluating the ratio of the first and fourth terms on the left-hand side gives $\left|\dfrac{\omega \mathrm{v}_{es}}{\mathrm{V}_{Te}^2 k n_{es} / n_{eo}}\right| \sim \dfrac{c_s^2}{\mathrm{V}_{Te}^2} \approx \dfrac{m_e}{m_i} << 1$ and thus the first term can be neglected due to its small magnitude. The average over time of the fast variations is taken as follows. The standard definition of a time-average

$$\left\langle X \right\rangle = \frac{1}{\mathrm{T}} \int_{t_o}^{t_o+\mathrm{T}} \mathrm{X}\, dt \qquad \textbf{(B32)}$$

is used where T is the period of the time-varying quantity. Via vector algebra $(\mathbf{v}_{ef} \bullet \nabla)\mathbf{v}_{ef}$ reduces to

$$(\mathbf{v}_{ef} \bullet \nabla)\mathbf{v}_{ef} = (\nabla \mathbf{v}_{ef}) \bullet \mathbf{v}_{ef} - \mathbf{v}_{ef} \times (\nabla \times \mathbf{v}_{ef}) = \frac{1}{2}\nabla \left|\mathbf{v}_{ef}\right|^2 . \qquad \textbf{(B33)}$$

since the $\mathbf{v}_{ef} \times (\nabla \times \mathbf{v}_{ef})$ term is zero for purely longitudinal quantities. To find v_{ef} the momentum balance equation (B19), less the thermal correction, is used

$$\frac{\partial \mathbf{v}_{ef}}{\partial t} = -\frac{e}{m_e}\mathbf{E}_f . \qquad \textbf{(B34)}$$

The fast variations are assumed to have a time dependency $\sim e^{-i\omega_o t}$. Evaluating the fast continuity equation with this time dependency results in

$$\mathbf{v}_{ef} = -i\frac{e}{m_e\omega_o}\mathbf{E}_f \qquad \textbf{(B35)}$$

and

$$\frac{1}{2}(\mathbf{v}_{ef} \bullet \mathbf{v}^*_{ef}) = \frac{1}{2}\left|\mathrm{v_{ef}}^2\right| = \frac{1}{2}\left(\frac{e}{m_e\omega_o}\right)^2\left|\mathbf{E}_f\right|^2 . \qquad \textbf{(B36)}$$

Taking the time average of the right-hand side will result in an additional factor of ½ and thus ultimately we find

$$\frac{1}{2}\nabla\left\langle\left|\mathrm{v_{ef}}^2\right|\right\rangle = \frac{1}{4}\left(\frac{e}{m_e\omega_o}\right)^2\nabla\left|\mathbf{E}_f\right|^2 . \qquad \textbf{(B37)}$$

Using the above simplifying assumptions and substituting the above result into (B30) gives the dynamic equation for the low-frequency electrons

$$\boxed{\mathrm{V}_{Te}^2\frac{\nabla n_{es}}{n_{eo}} + \frac{e}{m_e}\mathbf{E}_s \approx -\frac{1}{4}\left(\frac{e}{m_e\omega_{pe}}\right)^2\nabla\left|\mathbf{E}_f\right|^2}, \qquad \textbf{(B38)}$$

where it has been assumed that the high frequency is approximately equal to the electron plasma frequency, i.e. $\omega_o \approx \omega_{pe}$.

One last aspect that must be evaluated is the low-frequency dynamics of the ions. On this time scale the ions are considered adiabatic and thus $\gamma_i = 3$. As with the fast dynamics, starting with the continuity equation (B12) and ignoring second harmonic and zero frequency components yields for the ions

$$\frac{\partial n_{is}}{\partial t} + n_{io}\nabla \bullet \mathbf{v}_{is} = 0 . \qquad \textbf{(B39)}$$

The momentum balance equation for the ion dynamics is

$$\frac{\partial \mathbf{v}_{is}}{\partial \mathrm{t}} + 3\mathrm{V}_{Ti}^2\frac{\nabla n_{is}}{n_{io}} = \frac{eZ_i}{m_i}\mathbf{E}_s . \qquad \textbf{(B40)}$$

Substituting for the slow field $\mathbf{E}_s$ in terms of the fast field using (B38) gives

$$\frac{\partial \mathbf{v}_{is}}{\partial \mathrm{t}} + 3\mathrm{V}_{Ti}^2 \frac{\nabla n_{is}}{n_{io}} \approx -\frac{1}{4} Z_i \frac{m_e}{m_i} \left(\frac{e}{m_e \omega_{pe}} \right)^2 \nabla \left| \mathbf{E}_f \right|^2 - Z_i \frac{m_e}{m_i} \mathrm{V}_{Te}^2 \frac{\nabla n_{es}}{n_{eo}} . \qquad \textbf{(B41)}$$

On the right-hand side of (B41), the definition of the electron plasma frequency is used to simplify it to

$$\frac{\partial \mathbf{v}_{is}}{\partial \mathrm{t}} + 3\mathrm{V}_{Ti}^2 \frac{\nabla n_{is}}{n_{io}} \approx -\frac{1}{4} \frac{\varepsilon_o Z_i}{m_i n_{eo}} \nabla \left| \mathbf{E}_f \right|^2 - Z_i \frac{m_e}{m_i} \mathrm{V}_{Te}^2 \frac{\nabla n_{es}}{n_{eo}} . \qquad \textbf{(B42)}$$

Grouping terms and using the neutrality and low frequency quasi-neutrality conditions given in (B10) and (B11), respectively, results in

$$\frac{\partial \mathbf{v}_{is}}{\partial \mathrm{t}} + c_s^2 \left(3 \frac{T_i}{Z_i T_e} + 1 \right) \frac{\nabla n_s}{n_o} \approx -\frac{1}{4} \frac{\varepsilon_o Z_i}{m_i n_o} \nabla \left| \mathbf{E}_f \right|^2 , \qquad \textbf{(B43)}$$

where $c_s^2 = Z_i T_e / m_i$ is the ion sound speed. Taking the divergence of the above equation, the time derivative of the low frequency continuity equation, substituting for the ion velocity in terms of the density, and using the substitution $\gamma_a = \left(3 \frac{T_i}{Z_i T_e} + 1 \right)$ simplifies this to

$$\boxed{\left(\frac{\partial^2}{\partial \mathrm{t}^2} - \gamma_a c_s^2 \nabla^2 \right) n_{es} \approx \frac{1}{4} \frac{\varepsilon_o Z_i}{m_i} \nabla^2 \left| \mathbf{E}_f \right|^2 .} \qquad \textbf{(B44)}$$

This is another important result. It describes the coupling of the high-frequency dynamics to the low-frequency dynamics via the pondermotive force created by the high frequency field. Thus, (B29) and (B44) are the coupled non-linear Zakharov equations describing the coupling the electron and ion dynamics.

As with the derivation of the dispersion relation for SRS in the previous appendix, the derivation here is completed by assigning frequencies to the fast field variation and slow density fluctuation, i.e.

$$\mathbf{E}_f = \mathrm{Re}\left(\mathbf{E}_o e^{i\vec{k}_o \bullet r - i\omega_o t} \right), \text{ and} \qquad \textbf{(B45)}$$

$$n_s = \mathrm{Re}\left(n_1 e^{i\vec{k} \bullet r - i\omega t} \right). \qquad \textbf{(B46)}$$

The non-linear drive term on the right-hand side of (B29) produces

$$n_s\mathbf{E}_f = \frac{1}{2}\left(n_1\mathbf{E}_o e^{i(\vec{k}+\vec{k}_o)\bullet r - i(\omega+\omega_o)t} + n_1\mathbf{E}_o^* e^{-i(\vec{k}+\vec{k}_o)\bullet r + i(\omega+\omega_o)t}\right) + \frac{1}{2}\left(n_1\mathbf{E}_o^* e^{i(\vec{k}-\vec{k}_o)\bullet r - i(\omega-\omega_o)t} + n_1\mathbf{E}_o e^{-i(\vec{k}-\vec{k}_o)\bullet r + i(\omega-\omega_o)t}\right), \qquad \textbf{(B47)}$$

and thus drives the a high-frequency field that is up and down-shifted from the pump frequency, i.e.

$$\mathbf{E}_\pm = \mathrm{Re}\left(\mathbf{E}_\pm e^{i(\vec{k}\pm\vec{k}_o)\bullet r - i(\omega\pm\omega_o)t}\right). \qquad \textbf{(B48)}$$

The star superscript, as usual, represents the complex conjugate of the quantity. Using the substitutions $\omega_\pm = \omega \pm \omega_o$ and $k_\pm = k \pm k_o$ (B29) can be written more compactly as

$$\left(\omega_\pm^2 - \omega_{pe}^2 - 3\mathrm{V}_{Te}^2 k_\pm^2\right)\mathbf{E}_\pm = \frac{\omega_{pe}^2}{n_o} n_1 \begin{pmatrix}\mathbf{E}_o \\ \mathbf{E}_o^*\end{pmatrix}. \qquad \textbf{(B49)}$$

The low frequency dynamics are thus described by

$$\left(\omega^2 - \gamma_a c_s^2 k^2\right)n_1 \approx \frac{1}{4}\frac{\varepsilon_o Z_i}{m_i} k^2 \left(\mathbf{E}_+ \bullet \mathbf{E}_o^* + \mathbf{E}_- \bullet \mathbf{E}_o\right). \qquad \textbf{(B50)}$$

It is seen that the quantities in the parenthesis on the left-hand side of (B49) and (B50) are the linear dispersion relations for an electron plasma wave (EPW) and an ion acoustic wave (IAW), respectively. As done previously in the SRS derivation, (B49) is used to solve for $\mathbf{E}_+$ and $\mathbf{E}_-$ which are then substituted into (B50) to yield one equation describing the dispersion relation for LDI, i.e.

$$\left(\omega^2 - \gamma_a c_s^2 k^2\right) \approx \frac{1}{4}\frac{\varepsilon_o Z_i}{m_i}\frac{\omega_{pe}^2}{n_o} k^2 \left|\mathbf{E}_o\right|^2 \left(\frac{\hat{e}_+ \bullet \hat{e}_o^*}{\omega_+^2 - \omega_{pe}^2 - 3\mathrm{V}_{Te}^2 k_+^2} + \frac{\hat{e}_-^* \bullet \hat{e}_o}{\omega_-^2 - \omega_{pe}^2 - 3\mathrm{V}_{Te}^2 k_-^2}\right). \qquad \textbf{(B51)}$$

This expression can be simplified by using the definition of the electron quiver velocity $\mathrm{v}_o^2 = \left|\frac{e\mathbf{E}_o}{m_e\omega_o}\right|^2$ and introducing the Debye length $\lambda_{De} = \mathrm{V}_{Te}/\omega_{pe}$ in the coupling term to finally arrive at

$$\boxed{\left(\omega^2 - \gamma_a c_s^2 k^2\right) \approx \frac{1}{4}\frac{\mathrm{v}_o^2}{\mathrm{V}_{Te}^2} k^2 \lambda_{De}^2 \omega_{pi}^2 \omega_o^2 \left(\frac{\hat{e}_+ \bullet \hat{e}_o^*}{\omega_+^2 - \omega_{pe}^2 - 3\mathrm{V}_{Te}^2 k_+^2} + \frac{\hat{e}_-^* \bullet \hat{e}_o}{\omega_-^2 - \omega_{pe}^2 - 3\mathrm{V}_{Te}^2 k_-^2}\right)}. \qquad \textbf{(B52)}$$

Appendix C

Vlasov Description for Stimulated Scattering off of Electrostatic Modes and Quasimodes in a Plasma [72]

In this Appendix, the general theory of stimulated scattering off of electrostatic modes in a plasma is developed. This work was motivated by the experimental observation of stimulated scattering off of an electron acoustic mode at a frequency $\omega \approx 0.44\omega_{pe}$ which is not necessarily a weakly damped mode, i.e. it may have appreciable Landau damping and is thus termed a *quasimode*. Since this scattering occurs via essentially the same process as stimulated Raman scattering (SRS), the theory presented here builds on that developed in Appendix A.

In the Vlasov scattering theory, the electron density fluctuation is derived using kinetic theory rather than fluid theory. Kinetic theory involves solving the Vlasov equation

$$\frac{\partial}{\partial t} f_e + \mathbf{v} \bullet \nabla_{\mathbf{r}} f_e + \mathbf{a} \bullet \nabla_{\mathbf{v}} f_e = 0, \qquad \textbf{(C1)}$$

to find the electron distribution function. In this equation, f_e is the electron distribution function, $\mathbf{v}$ is the velocity, $\nabla_{\mathbf{r}}$ is the spatial gradient, $\mathbf{a}$ is the acceleration due to the Lorentz force, which for electrons, is given by $\mathbf{a} = -\frac{e}{m_e}[\mathbf{E} + (\mathbf{v} \times \mathbf{B})]$, and $\nabla_{\mathbf{v}}$ is the velocity-space gradient. Once the distribution function is known, the density can be obtained from it by integrating f_e over velocity space. In the following, as in previous derivations, boldface letters represent vector quantities.

The derivation is simplified by representing the gradient in velocity-space by

$$\nabla_{\mathbf{v}} f_e = f_e^{'} = n_o \hat{f}_e^{'}, \qquad \textbf{(C2)}$$

where n_o is the constant background electron density and for electrostatic dynamics we neglect $\mathbf{B}$. Additionally, to allow coupling of the electron density fluctuation to the pump and scattered electromagnetic waves (EMW), a nonlinear pondermotive correction must be added to the linear electric field E in order to obtain the desired nonlinear Vlasov equation. Making the above substitutions into (C1) gives

$$\frac{\partial}{\partial t} f_e + \mathbf{v} \bullet \nabla_{\mathbf{r}} f_e - \frac{e}{m_e}[\mathbf{E} + \mathbf{E}_{NL}] \bullet n_o \hat{f}_e^{'} = 0. \qquad \textbf{(C3)}$$

The term $\mathbf{E}_{NL} = \mathbf{u} \times \nabla \times \mathbf{A}$ represents a second-order pondermotive correction to the electron force where $\mathbf{u}$ is the fluid velocity and $\mathbf{A}$ is the vector potential. Note that this vector potential is not a reintroduction of the magnetic field in the acceleration term of the electrostatic Vlasov equation, but rather, is obtained from the beating of two electromagnetic waves as in the case of stimulated Raman scattering. This second-order pondermotive correction term is evaluated using fluid theory and this derivation has already been performed in Appendix A. For convenience, the results are reiterated here substituting the fluid velocity **u** for **v** in the equations from Appendix A. From equation (A31) it was found that

$$\nabla \times \mathbf{u}_e = \frac{e}{m_e}(\nabla \times \mathbf{A}) \qquad \textbf{(C4)}$$

and thus,

$$-\frac{e}{m_e}\left[\mathbf{u}_e \times (\nabla \times \mathbf{A})\right] = -\left[\mathbf{u}_e \times (\nabla \times \mathbf{u}_e)\right]. \qquad \textbf{(C5)}$$

Following the derivation in Appendix A starting at (A31), the acceleration term including the nonlinear correction is given by the right-hand side of (A33), i.e.

$$\mathbf{a} = -\frac{e}{m_e}\mathbf{E} - \frac{1}{2}\nabla \mathbf{u}_e^2. \qquad \textbf{(C6)}$$

Further, following the derivation in Appendix A through (A41) where the term $\mathbf{u}_e^2$ is evaluated gives

$$\mathbf{a} = -\frac{e}{m_e}\mathbf{E} - \frac{e^2}{m_e^2}\nabla(\mathbf{A}_o \bullet \mathbf{A}_1). \qquad \textbf{(C7)}$$

Thus, the pondermotive correction to the acceleration can be defined as

$$\frac{e^2}{m_e^2}\nabla(\mathbf{A}_o \bullet \mathbf{A}_1) = \frac{\nabla \psi}{m_e}, \qquad \textbf{(C8)}$$

where

$$\psi = \frac{e^2}{m_e}(\mathbf{A}_o \bullet \mathbf{A}_1). \qquad \textbf{(C9)}$$

Substituting (C8) into the acceleration term reduces (C3) to

$$\boxed{\frac{\partial}{\partial t} f_e + \mathbf{v} \bullet \nabla_{\mathbf{r}} f_e - \left[\frac{e}{m_e}\mathbf{E} + \frac{\nabla \psi}{m_e}\right] \bullet n_o \hat{f}_e^{'} = 0}. \qquad \textbf{(C10)}$$

The electron distribution function can be obtained from (C10) in the usual manner by assuming a space-time behavior of $f_e \sim e^{i\mathbf{k}\bullet\mathbf{r}}e^{-i\omega\bullet t}$ so that the spatial gradient and time derivative become, respectively, $\nabla_{\mathbf{r}} \rightarrow i\mathbf{k}$ and $\frac{\partial}{\partial t} \rightarrow -i\omega$. Using the above operations in (C10) and rearranging terms gives

$$(-i\omega + i\mathbf{v}\bullet\mathbf{k})f_e = \left[\frac{e}{m_e}\mathbf{E} + \frac{\nabla\psi}{m_e}\right]\bullet n_o\hat{f}_e^{'}. \qquad \textbf{(C11)}$$

Solving for f_e yields

$$f_e = \left[\frac{e}{m_e}\mathbf{E} + \frac{\nabla\psi}{m_e}\right]\bullet n_o\frac{\hat{f}_e^{'}}{-i(\omega - \mathbf{v}\bullet\mathbf{k})}. \qquad \textbf{(C12)}$$

Integrating the electron distribution function over velocity space gives the electron density

$$n_e = \int f_e d\mathbf{v} = i\frac{en_o}{m_e}\left[\mathbf{E} + \frac{\nabla\psi}{e}\right]\bullet\int\frac{\hat{f}_e^{'}d\mathbf{v}}{(\omega - \mathbf{v}\bullet\mathbf{k})}. \qquad \textbf{(C13)}$$

The longitudinal susceptibility for a particular species is obtained by using the plasma dispersion function [44], i.e.

$$\chi_{Ls} = \frac{\omega_{ps}^2}{k}\int_{-\infty}^{\infty}\frac{\hat{f}_s^{'}d\mathbf{v}}{(\omega - \mathbf{v}\bullet\mathbf{k})}, \qquad \textbf{(C14)}$$

where $\omega_{ps} = \sqrt{\frac{n_{os}q_s^2}{\varepsilon_o m_s}}$ is the plasma frequency for the species. When more than one species is present, the total susceptibility is found by summing contributions due to all species, i.e. $\chi_L = \sum_s \chi_{Ls}$. Substituting for the electron plasma frequency in (C13), using (C14) to evaluate the integral, and evaluating the one-dimensional dynamics the electron density is given by

$$n_e(k,\omega) = i\frac{\varepsilon_o}{e}k\chi_{Le}\left[\mathrm{E} + \frac{|\nabla\psi|}{e}\right]. \qquad \textbf{(C15)}$$

The charge density is thus given by

$$\rho = -en_e \Rightarrow \rho(k,\omega) = -i\varepsilon_o k\chi_{Le}\left[\mathrm{E} + \frac{|\nabla\psi|}{e}\right]. \qquad \textbf{(C16)}$$

Poisson's equation (A3) gives

$$ik\mathrm{E} - \rho = 0 \tag{C17}$$

and using the above definition for the charge density gives

$$ik\varepsilon_o \mathrm{E} + i\varepsilon_o k\chi_{Le}\left[\mathrm{E} + \frac{|\nabla\psi|}{e}\right] = 0. \tag{C18}$$

Grouping terms, simplifying, and using the definition of the permittivity $K_L = 1 + \chi_L$ in (C18) gives

$$K_L \mathrm{E} = -\chi_{Le}\frac{|\nabla\psi|}{e}. \tag{C19}$$

Finally, operating on the right-hand side with the assumed spatial variation, the electric field due to electron density fluctuations is given by

$$\mathrm{E} = -ik\frac{\chi_{Le}}{K_L}\frac{\psi}{e}. \tag{C20}$$

Now, via Poisson's equation, the charge density will be due to an electron density fluctuation δn which can be defined in terms of the electric field given by (C20), i.e.

$$\boxed{\delta n = -\frac{ik\varepsilon_o \mathrm{E}}{e} = -\frac{ik\varepsilon_o}{e}\left[-ik\frac{\chi_{Le}}{K_L}\frac{\psi}{e}\right] = -\frac{k^2\varepsilon_o}{e^2}\frac{\chi_{Le}}{K_L}\psi}. \tag{C21}$$

Using definitions for $\mathbf{A}_o$ and $\mathbf{A}_1$ from Appendix A and evaluating (C9) for terms that are resonant with the density fluctuation gives

$$\psi = \frac{e^2}{m_e}\frac{1}{2}(\mathbf{a}_o^* \bullet \mathbf{A}_+ + \mathbf{a}_o \bullet \mathbf{A}_-). \tag{C22}$$

Thus, the electron density fluctuation is ultimately related to the pump and scattered electromagnetic fields by

$$\delta n = -\frac{k^2\varepsilon_o}{m_e}\frac{1}{2}\frac{\chi_{Le}}{K_L}(\mathbf{a}_o^* \bullet \mathbf{A}_+ + \mathbf{a}_o \bullet \mathbf{A}_-). \tag{C23}$$

Using the definition of the electron plasma frequency and substituting gives

$$\frac{\delta n}{n_o} = -\frac{\chi_{Le}}{K_L}\left(\frac{k^2 e^2}{m_e^2\omega_{pe}^2}\right)\frac{1}{2}(\mathbf{a}_o^* \bullet \mathbf{A}_+ + \mathbf{a}_o \bullet \mathbf{A}_-). \tag{C24}$$

From Appendix A, the definition for $\mathbf{A}_\pm$ is given by

$$\mathbf{A}_{\pm} = \omega_{pe}^2 \frac{1}{2}\frac{\delta n}{n_o}\frac{1}{D_{T\pm}}\begin{pmatrix}\mathbf{a}_o \\ \mathbf{a}_o^*\end{pmatrix}. \tag{C25}$$

This can be substituted into (C24) to give

$$\frac{\delta n}{n_o} = -\frac{\chi_{Le}}{K_L}\left(\frac{k^2 e^2}{m_e^2 \omega_{pe}^2}\right)\frac{\omega_{pe}^2}{4}\left|\mathbf{a}_o\right|^2 \frac{\delta n}{n_o}\left(\frac{1}{D_{T+}} + \frac{1}{D_{T-}}\right). \tag{C26}$$

Canceling like terms from both sides and in the numerator and denominator of (C26) and using the definition of the electron quiver velocity from (A59) gives

$$1 = -\frac{\chi_{Le}}{K_L}k^2 \frac{1}{4}\mathbf{v}_o^2\left(\frac{1}{D_{T+}} + \frac{1}{D_{T-}}\right). \tag{C27}$$

Finally, rearranging terms gives the Vlasov representation of scattering off of any electron modes, including quasimodes, that may be present in the plasma

$$\boxed{K_L = \frac{1}{4}k^2 \mathbf{v}_o^2(-\chi_{Le})\left(\frac{1}{D_{T+}} + \frac{1}{D_{T-}}\right)}. \tag{C28}$$

This is an important result. On the left-hand side is the kinetic permittivity, which when set equal to zero gives the dispersion relation for any longitudinal electron modes that may be present in the plasma. The term $\frac{1}{4}k^2\mathbf{v}_o^2(-\chi_{Le})$ represents the growth rate for the nonlinear interaction and D_{T+} and D_{T-} are the linear dispersion relations for the up and down-shifted scattered, transverse electromagnetic modes, respectively. Note that the derivation presented in this appendix considered only electron modes. It is straightforward to generalize this theory to allow for multiple electron distribution functions, e.g. a bi-Maxwellian consisting of a warm background and a colder beam-like component, and can include ion modes by including all species present in the definitions for the susceptibility and permittivity. Additionally, as with the derivation of the SRS dispersion relation in Appendix A, geometry effects can be considered for the case of the pump and scattered EMW electric field vectors not being collinear.

Appendix D

One-Dimensional (1D) Relativistic Vlasov Code Description

A numerical code was used to simulate the evolution of the electron distribution function during SRS. A general overview of the code is presented in the first part of this appendix. The latter part of the appendix contains the actual FORTRAN code showing implementation of the routines described in the first part. The actual code is packaged as a Compaq (formerly Digital) Visual FORTRN workspace and is available on the CDROM that accompanies this thesis.

The code is a relativistic, one-dimensional (1D) (in x) Euler-Vlasov with a "monokinetic" approximation used to obtain the velocities and current densities in the transverse direction (y). Both electrons and ions are mobile. The ion time step can differ from the electron time step, i.e. since the ions are less mobile, they can be moved less frequently. Currently, the code evolves the distribution functions for electrons and a single hydrogen ion species. However, it can be modified to simulate multiple ion species.

The generalized relativistic Vlasov equation in three dimensions is given by

$$\frac{\partial f}{\partial t}+\frac{\mathbf{p}}{m\gamma}\bullet\nabla_{\mathbf{r}} f+q(\mathbf{E}+\frac{\mathbf{p}}{m\gamma}\times\mathbf{B})\bullet\nabla_{\mathbf{p}} f=0. \qquad \textbf{(D1)}$$

Expanding the differentiation operators in (D1) results in

$$\begin{aligned}&\frac{\partial f}{\partial t}+\frac{1}{m\gamma}\left(p_x\frac{\partial f}{\partial x}+p_y\frac{\partial f}{\partial y}+p_z\frac{\partial f}{\partial z}\right)+q\left(E_x+\frac{1}{m\gamma}\left(p_yB_z-B_yp_z\right)\right)\frac{\partial f}{\partial p_x}\\&+q\left(E_y+\frac{1}{m\gamma}\left(p_zB_x-B_zp_x\right)\right)\frac{\partial f}{\partial p_y}+q\left(E_z+\frac{1}{m\gamma}\left(p_xB_y-B_xp_y\right)\right)\frac{\partial f}{\partial p_z}=0\end{aligned}. \qquad \textbf{(D2)}$$

For the code, the distribution function is considered to be a function of x, p_x, P_y, and t only, where P_y is the generalized or canonic momentum. Thus, the derivatives with respect to y, z, and p_z are all zero. Additionally, the following class of exact solution is considered

$$f=f(P_y,p_x,x,t)=\delta(p_y+qA_y)F(x,p_x,t), \qquad \textbf{(D3)}$$

What (D3) means that the longitudinal motion obeys the relativistic Vlasov equation for $F(x,p_x,t)$ which describes accurately the longitudinal motion of electrons in the two-dimensional x–p_x phase space. The effective transverse motion of particles is *"cold"* and simply described by a fluid macroscopic equation for the transverse mean velocity

$u_y = -qA/m$. This approximation is justified in the following section and has also been explored numerically [74].

Using a fluid approximation in the transverse direction is justified by considering the 1D propagation of an electromagnetic wave as shown in Figure 48. Since the propagation is 1D, the spatial derivatives in the transverse directions are zero, i.e. $\frac{\partial}{\partial y} = \frac{\partial}{\partial z} = 0$. In the y-direction, the generalized momentum balance equation in one dimension is

$$m\left(\frac{\partial \mathrm{u}_y}{\partial t} + \mathrm{v}_x \frac{\partial \mathrm{u}_y}{\partial x}\right) = qE_y - q\mathrm{u}_x B_z . \quad \textbf{(D4)}$$

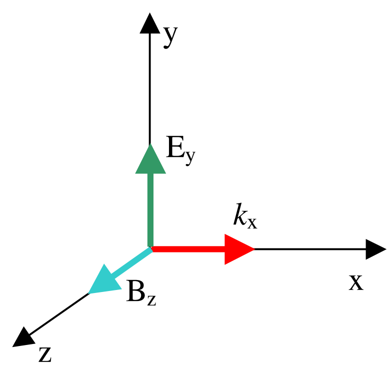

Figure 48. Geometry for justifying using the fluid approximation for the transverse velocity.

Using the vector identity $\nabla \bullet (\nabla \times \mathbf{A}) = 0$, the magnetic flux density can be expressed as the curl of a vector potential, i.e. $\mathbf{B} = \nabla \times \mathbf{A}$ and thus for the 1D case considered here $B_z = \frac{\partial A_y}{\partial x}$. Substituting this definition into the momentum balance equation gives

$$m\left(\frac{\partial \mathrm{u}_y}{\partial t} + \mathrm{v}_x \frac{\partial \mathrm{u}_y}{\partial x}\right) = qE_y - q\mathrm{u}_x \frac{\partial A_y}{\partial x} . \quad \textbf{(D5)}$$

Rearranging and grouping on the derivative in the x-direction gives

$$m\frac{\partial \mathrm{u}_y}{\partial t} = qE_y - \mathrm{u}_x \frac{\partial}{\partial x}\left(m\mathrm{u}_y + qA_y\right). \quad \textbf{(D6)}$$

The last term on the right-hand side is recognized as the generalized or canonic momentum $P_y = m\mathrm{u}_y + qA_y$ and thus (D6) can be rewritten as

$$m\frac{\partial \mathrm{u}_y}{\partial t} = qE_y - \mathrm{u}_x \frac{\partial}{\partial x} P_y . \qquad \textbf{(D7)}$$

Taking the time derivative of the spatial derivative with respect to x of the canonic momentum results in

$$\frac{\partial}{\partial t}\left(\frac{\partial P_y}{\partial x}\right) = \frac{\partial}{\partial t}\left[\frac{\partial}{\partial x}\left(m\mathrm{u}_y + qA_y\right)\right]. \qquad \textbf{(D8)}$$

Reversing the order of the linear differential operators on the right hand side results in

$$\frac{\partial}{\partial t}\left(\frac{\partial P_y}{\partial x}\right) = \frac{\partial}{\partial x}\left[m\frac{\partial \mathrm{u}_y}{\partial t} + q\frac{\partial A_y}{\partial t}\right]. \qquad \textbf{(D9)}$$

Using the Coulomb gauge the electric field can be written as $E_y = -\partial A_y / \partial t$. Using this definition for the electric field in (D7) and substituting for $m\partial \mathrm{u}_y / \partial t$ in (D9) results in

$$\frac{\partial}{\partial t}\left(\frac{\partial P_y}{\partial x}\right) = \frac{\partial}{\partial x}\left[-q\frac{\partial A_y}{\partial t} - \mathrm{u}_x\frac{\partial}{\partial x}P_y + q\frac{\partial A_y}{\partial t}\right] = \frac{\partial}{\partial x}\left[-\mathrm{u}_x\frac{\partial}{\partial x}P_y\right]. \qquad \textbf{(D10)}$$

Evaluating the spatial derivative, canceling like terms, and rearranging, (D10) can be rewritten as

$$\left(\frac{\partial}{\partial t} + \mathrm{u}_x\frac{\partial}{\partial x} + \frac{\partial \mathrm{u}_x}{\partial x}\right)\frac{\partial P_y}{\partial x} = 0 . \qquad \textbf{(D11)}$$

The important result is that if $\partial P_y / \partial x = 0$ initially, it will remain zero for all time. This is exactly the case for the 1D simulations and thus use of a fluid approximation for the transverse velocity is justified.

To resume with the derivation of the 1D Vlasov equations, for the problem considered here there is no magnetic field in the *y*-direction and the transverse velocity u_y is assumed to be much less than the speed of light (this is confirmed to be the case in the simulations) so that the relativistic mass correction factor is simplified to

$$\gamma_s = \sqrt{1 + \frac{p_{sx}^2 + p_{sy}^2}{m_s^2 c^2}} \approx \sqrt{1 + \frac{p_{sx}^2}{m_s^2 c^2}} , \qquad \textbf{(D12)}$$

With the above considerations and the assumed functional dependency (D3), equation (D2) reduces to

$$\frac{\partial f}{\partial t}+\frac{p_x}{m\gamma}\frac{\partial f}{\partial x}+q\left(E_x+\frac{p_yB_z}{m\gamma}\right)\frac{\partial f}{\partial p_x}+q\left(E_y-\frac{B_zp_x}{m\gamma}\right)\frac{\partial f}{\partial p_y}=0. \qquad \textbf{(D13)}$$

If one wishes to study the dynamics of a distribution function in a single dimension, the Vlasov equation is integrated over the space and momentum variables in the other dimensions that have variation in those dimensions. In our case, we wish to evaluate the dynamics in the *x*-direction and we need only integrate p_y. This leads to a new definition for the distribution function given by

$$F(x,p_x,t)=\int f dp_y\ . \qquad \textbf{(D14)}$$

Integrating the term $q\left(E_x+\frac{p_yB_z}{m\gamma}\right)\frac{\partial f}{\partial p_x}$ over p_y results in

$$\begin{aligned}&\int q\left(E_x+\frac{p_yB_z}{m\gamma}\right)\frac{\partial f}{\partial p_x}dp_y=\frac{\partial}{\partial p_x}\int q\left(E_x+\frac{p_yB_z}{m\gamma}\right)\delta(p_y-u_ym\gamma)f(x,p_x,t)dp_y= \\ &qE_x\frac{\partial F}{\partial p_x}+q\int\frac{p_yB_z}{m\gamma}\delta(p_y-u_ym\gamma)f(x,p_x,t)dp_y=q\left(E_x+u_yB_z\right)\frac{\partial F}{\partial p_x}\end{aligned}, \qquad \textbf{(D15)}$$

where it is seen that the delta function for the transverse velocity makes the integration trivial. Integration of the last term on the left-hand side of (D13) results in zero contribution because periodic conditions are assumed in this direction. Thus the resultant 1D Vlasov equation is

$$\frac{\partial F}{\partial t}+\frac{p_x}{m\gamma}\frac{\partial F}{\partial x}+q\left(E_x+u_yB_z\right)\frac{\partial F}{\partial p_x}=0. \qquad \textbf{(D16)}$$

In the code, the relativistic Vlasov equations for electrons and ions are solved self-consistently with Maxwell's equations. The Vlasov equations are given by

$$\frac{\partial F_e}{\partial t}+\frac{p_{ex}}{m_e\gamma_e}\frac{\partial F_e}{\partial x}-e(E_x+u_{ey}B_z)\frac{\partial F_e}{\partial p_x}=0 \qquad \textbf{(D17)}$$

$$\frac{\partial F_i}{\partial t}+\frac{p_{ix}}{m_i\gamma_i}\frac{\partial F_i}{\partial x}+e(E_x+u_{iy}B_z)\frac{\partial F_i}{\partial p_x}=0, \qquad \textbf{(D18)}$$

where the subscript s refers to the particular species (electrons or ions) and the transverse velocity is approximated by a fluid equation

$$\frac{\partial u_{sy}}{\partial t} = \frac{q_s}{m_s} E_y . \quad \textbf{(D19)}$$

The longitudinal self-consistent electric field is given by Poisson's equation $\nabla \bullet \mathbf{E} = \rho / \varepsilon_o$ with the electrostatic approximation

$$E_x = -\frac{\partial \phi}{\partial x} \quad \textbf{(D20)}$$

and thus,

$$\frac{\partial^2 \phi}{\partial x^2} + \frac{e}{\varepsilon_o}\left[n_i(x,t) - n_e(x,t)\right] = 0 \quad \textbf{(D21)}$$

The density for each species can be found by integrating its distribution function over momentum space, i.e.

$$n_s = \int F_s dp_{sx} . \quad \textbf{(D22)}$$

The transverse electromagnetic fields obey Maxwell's equations. Simplified for the geometry of the code these are given by

$$\frac{\partial B_z}{\partial t} = -\frac{\partial E_y}{\partial x}, \text{ and} \quad \textbf{(D23)}$$

$$\frac{\partial \mathrm{E}_y}{\partial t} = -c^2 \frac{\partial B_z}{\partial x} - \frac{1}{\varepsilon_o} J_y , \quad \textbf{(D24)}$$

where the current density is given by

$$J_y = e\left[n_i(x,t)u_{iy} - n_e(x,t)u_{ey}\right]. \quad \textbf{(D25)}$$

Defining $\mathrm{E}^{\pm} = \mathrm{E}_y \pm c\mathrm{B}_z$ Maxwell's equations can be rewritten as

$$\left(\frac{\partial}{\partial t} \pm c\frac{\partial}{\partial x}\right)\mathrm{E}^{\pm} = -\frac{1}{\varepsilon_o} J_y \quad \textbf{(D26)}$$

which enables solution of Maxwell's equations along their vacuum characteristics x ± ct = constant [75].

In the code, all differential equations are solved using the method of characteristics. The well-known fractional step or time splitting scheme [76,77] is implemented as follows. Times on the grid are defined as

$$t_n = n\Delta T , \quad \textbf{(D27)}$$

$$t_{n+1} = (n+1)\Delta T , \text{ and} \quad \textbf{(D28)}$$

$$t_{n+\frac{1}{2}} = (n+\tfrac{1}{2})\Delta T\,, \qquad \textbf{(D29)}$$

where ΔT is the time step. Momentum (p) space is divided into N_p cells between $-p_{max}$ and $+p_{max}$. The length L of the system is divided into N_x cells. The electron and ion distribution functions are initialized as Maxwellian for each grid point in x-space. Thus, the distribution function is known on N_pN_x grid points. The factional step method involves three steps:

(1) between t_n and $t_{n+½}$ shift the distribution function in x-space for a time ΔT/2

$$F_s^*(x, p_{sx}, t_{n+\frac{1}{2}}) = F_s\left[x-(p_{sx}/m_s\gamma_s)\Delta T/2, p_{sx}, t_n\right] \qquad \textbf{(D30)}$$

(2) Compute the fields at time $t_{n+½}$ and then shift in momentum space for a time ΔT

$$F_s^{**}(x, p_{sx}, t_{n+\frac{1}{2}}) = F_s^*\left[x, p_{sx} + e\Delta T(E_x + u_yB_z), t_{n+\frac{1}{2}}\right] \qquad \textbf{(D31)}$$

(3) between $t_{n+½}$ and t_{n+1} shift again in x-space for a time ΔT/2

$$F_s(x, p_{sx}, t_{n+1}) = F_s^{**}\left[x-(p_{sx}/m_s\gamma_s)\Delta T/2, p_{sx}, t_{n+\frac{1}{2}}\right] \qquad \textbf{(D32)}$$

The equation for the perpendicular motion is solved between t_n and t_{n+1} using a time-centered scheme, i.e.

$$u_y(x,t_{n+1}) = u_y(x,t_n) - \frac{e}{m}\Delta T\frac{E^+(x,t_{n+\frac{1}{2}}) + E^-(x,t_{n+\frac{1}{2}})}{2} \qquad \textbf{(D33)}$$

Maxwell's equations are solved using the time-centered advective scheme between $t_{n-½}$ and $t_{n+½}$

$$E^{\pm}(x\pm c\Delta T, t_{n+\frac{1}{2}}) = E^{\pm}(x, t_{n-\frac{1}{2}}) - \Delta T\varepsilon_o^{-1}J_y\left[x \pm c(\Delta T/2), t_n\right] \qquad \textbf{(D34)}$$

A cubic spline method is used for interpolation of. In general, expanding about some grid point to third order yields

$$y_i(x) = f_i + p_i(x-x_i) + \frac{1}{2}s_i(x-x_i)^2 + g_i(x-x_i)^3, \qquad \textbf{(D35)}$$

where

$$f_i = y_i(x_i) \qquad \textbf{(D36)}$$

$$p_i = y_i^{'}(x_i) \qquad \textbf{(D37)}$$

$$s_i = y_i^{''}(x_i)\text{, and} \qquad \textbf{(D38)}$$

$$g_i = \frac{1}{6} y_i'''(x_i) \quad \textbf{(D39)}$$

The following restrictions on the behavior of the function are imposed, i.e. the function and its first and second derivatives are continuous

$$y_{i-1}(x_i) = y_i(x_i) \quad \textbf{(D40)}$$

$$y_{i-1}'(x_i) = y_i'(x_i) \quad \textbf{(D41)}$$

$$y_{i-1}''(x_i) = y_i''(x_i) \quad \textbf{(D42)}$$

Taking successive derivatives of (D35) and using the above constraints lead to

$$f_{i-1} + p_{i-1} + \tfrac{1}{2} s_{i-1} + g_{i-1} = f_i \quad \textbf{(D43)}$$

$$p_{i-1} + s_{i-1} + 3g_{i-1} = p_i \quad \textbf{(D44)}$$

$$s_{i-1} + 6g_{i-1} = s_i \quad \textbf{(D45)}$$

These equations can be manipulated algebraically to solve for the derivatives in terms of the function at known grid points, i.e.

$$p_{i-1} + 4p_i + p_{i+1} = 3(f_{i+1} - f_{i-1}), \quad \textbf{(D46)}$$

$$s_{i-1} + 4s_i + s_{i+1} = 6(f_{i-1} - 2f_i + f_{i+1}), \text{ and} \quad \textbf{(D47)}$$

$$g_{i-1} + 4g_i + g_{i+1} = -f_{i-1} + 3f_i - 3f_{i+1} + f_{i+2}. \quad \textbf{(D48)}$$

A shift operator can be formed that depends only on the value of the function at known grid points and the amount that the function is to be shifted. For a shift in the forward direction, i.e. $y_i(x_i + \Delta) = \tilde{y}_i$

$$\tilde{y}_{i-1} + 4\tilde{y}_i + \tilde{y}_{i+1} = Af_{i-1} + Bf_i + Cf_{i+1} + Df_{i+2}, \text{ where} \quad \textbf{(D49)}$$

$$A = (1 - 3\Delta + 3\Delta^2 - \Delta^3), \quad \textbf{(D50)}$$

$$B = (4 - 6\Delta^2 + 3\Delta^3), \quad \textbf{(D51)}$$

$$C = (1 + 3\Delta + 3\Delta^2 - 3\Delta^3), \quad \textbf{(D52)}$$

$$D = \Delta^3, \text{ and} \quad \textbf{(D53)}$$

$$\Delta = |x_i - x| \quad \textbf{(D54)}$$

is the deviation from a known grid point x_i to the point x at which the function is to be evaluated. For a shift in the backward direction, i.e. $y_i(x_i - \Delta) = \tilde{y}_i$, (D49) is replaced by

$$\tilde{y}_{i-1} + 4\tilde{y}_i + \tilde{y}_{i+1} = Af_{i+1} + Bf_i + Cf_{i-1} + Df_{i-2}\,, \qquad \textbf{(D55)}$$

however, the definitions for A, B, C, and D remain the same.

The interior point equations (D49) and (D55) are solved using the Tridiagonal Algorithm which is a special case of Gaussian elimination, i.e.

$$-A_m W_{m+1} + B_m W_m - C_m W_{m-1} = D_m\,. \qquad \textbf{(D56)}$$

To do so, one postulates the existence of two vectors E and F such that

$$W_m = E_m W_{m+1} + F_m\,. \qquad \textbf{(D57)}$$

Indexing this equation down one in m yields

$$W_{m-1} = E_{m-1} W_m + F_{m-1}\,. \qquad \textbf{(D58)}$$

Substituting into the original equation (D57) and solving for W_m yields

$$W_m = \frac{A_m}{B_m - C_m E_{m-1}} W_{m+1} + \frac{D_m + C_m F_{m-1}}{B_m - C_m E_{m-1}} \qquad \textbf{(D59)}$$

and thus for $m \geq 2$ the recursion relations for E and F are

$$E_m = \frac{A_m}{B_m - C_m E_{m-1}}\text{, and} \qquad \textbf{(D60)}$$

$$F_m = \frac{D_m + C_m F_{m-1}}{B_m - C_m E_{m-1}}\,. \qquad \textbf{(D61)}$$

The left-hand boundary condition is used to determine E_1 and F_1 as follows. With m=2 (D58) gives

$$W_1 = E_1 W_2 + F_1 \qquad \textbf{(D62)}$$

For a Dirichlet condition $W_1 = a_1$, this relation must hold for all possible values of W_2. Thus, for $W_1 = a_1$

$$E_1 = 0; F_1 = a_1 \qquad \textbf{(D63)}$$

A Neumann boundary condition as in $\frac{\partial \psi}{\partial y} = s_1$ implies

$$\psi_2 - \psi_1 = s_1 \Delta y \qquad \textbf{(D64)}$$

or in other terms $W_1 = W_2 - s_1 \Delta y$. Comparing this with (D62) shows that for $\frac{\partial W}{\partial y} = s_1$, $E_1 = 1$ and $F_1 = -s_1\Delta y$. The right-hand boundary conditions are used to determine W_M as follows. For a Dirichlet condition obviously $W_M = a_M$. A Neumann boundary condition as in $\dfrac{\partial \psi}{\partial y} = s_M$ implies

$$W_{M-1} = W_M - s_1 \Delta y \qquad \textbf{(D65)}$$

Writing (D58) for m = M gives

$$W_{M-1} = E_{M-1} W_M + F_{M-1} \qquad \textbf{(D66)}$$

Equating the above two equations gives

$$W_M = \frac{F_{M-1} + s_M \Delta y}{1 - E_{M-1}} \qquad \textbf{(D67)}$$

So, the procedure for solving for E, F, and W is as follows. Set E_1 and F_1 from the left-hand boundary condition. March out and store the vectors E_m and F_m up to $m = M - 1$ according to the recursion relations (D60) and (D61). Set W_M from the right-hand boundary condition. Finally, use the relation (D59) with the known A, B, C, D, and calculated values for E and F to solve recursively for the solution vector W_m from W_{m+1} marching down from $m = M - 1$ to $m = 1$.

The initial and boundary conditions are now described. Both the electron and ion distribution functions are initialized as Maxwellian on each grid point in x-space. The electron and ion temperatures (and thus their thermal velocities) specified as inputs to the simulation. A variable-length vacuum region (i.e. zero density plasma) can be specified on both ends of the plasma. The bulk plasma length is specified in numbers of free-space laser wavelengths. A piecewise parabolic transition allows for a smooth transition from the vacuum to plasma region on both ends of the system. The total length of the simulation system is thus $L = 2(L_{Vac} + L_{Trans}) + L_{Plasma}$. The Maxwellian distribution functions are then multiplied by a profile modification to set the initial density. An early-time snapshot of the electron density in a particular simulation and close up of the parabolic transition region is shown in Figure 49.

The transverse electromagnetic field is composed of the sum of forward backward propagating waves. The forward propagating wave E^+ is comprised of the laser pump and possibly any forward scattered waves, e.g. from forward SRS. The boundary condition on E^+ is specified at the left-hand boundary and is given by

$$E^+(x = 0, t) = 2E_o \sin(\omega_o t) \qquad \textbf{(D68)}$$

The backward propagating wave E^- is comprised of the back-scattered waves and its boundary condition, specified at the right-hand boundary, is given by

$$E^-(x = L, t) = 0 \qquad \textbf{(D69)}$$

The boundary conditions for the longitudinal electric field are treated by assuming that the left (x = 0) and right-hand (x = L) boundaries are isolated capacitor plates. Thus, as energetic particles escape to the boundaries, the potential on the capacitor plates changes as they become charged. Thus, E_x must be specified at x = 0 and x = L and overall neutrality imposes the condition $E_x = 0$ at $x = \pm\infty$. When particles escape to the edges of the system, the plasma system becomes non-neutral and the electric field at the left and right-hand boundaries is given by

$$E_x(x = 0) - E_x(x = -\infty) = \frac{e}{\varepsilon_o}\int_{-\infty}^{0}\left[n_i(x) - n_e(x)\right]dx = \frac{eN_-}{\varepsilon_o} \text{ and} \qquad \textbf{(D70)}$$

$$E_x(x = +\infty) - E_x(x = L) = \frac{e}{\varepsilon_o}\int_{L}^{\infty}\left[n_i(x) - n_e(x)\right]dx = -\frac{eN_+}{\varepsilon_o}, \qquad \textbf{(D71)}$$

respectively. The code is set up to assume that the number of electrons escaping to the right boundary N_+ is equal to the number of electrons escaping to the left boundary N_- and thus the total charge in the plasma system (0<x<L) is divided equally between the boundaries, i.e.

$$E_x(x = L) = \frac{L\langle\rho\rangle}{2\varepsilon_o}, \text{ and} \qquad \textbf{(D72)}$$

$$E_x(x = 0) = -\frac{L\langle\rho\rangle}{2\varepsilon_o}, \qquad \textbf{(D73)}$$

where $\langle\rho\rangle$ is the mean charge density in the plasma.

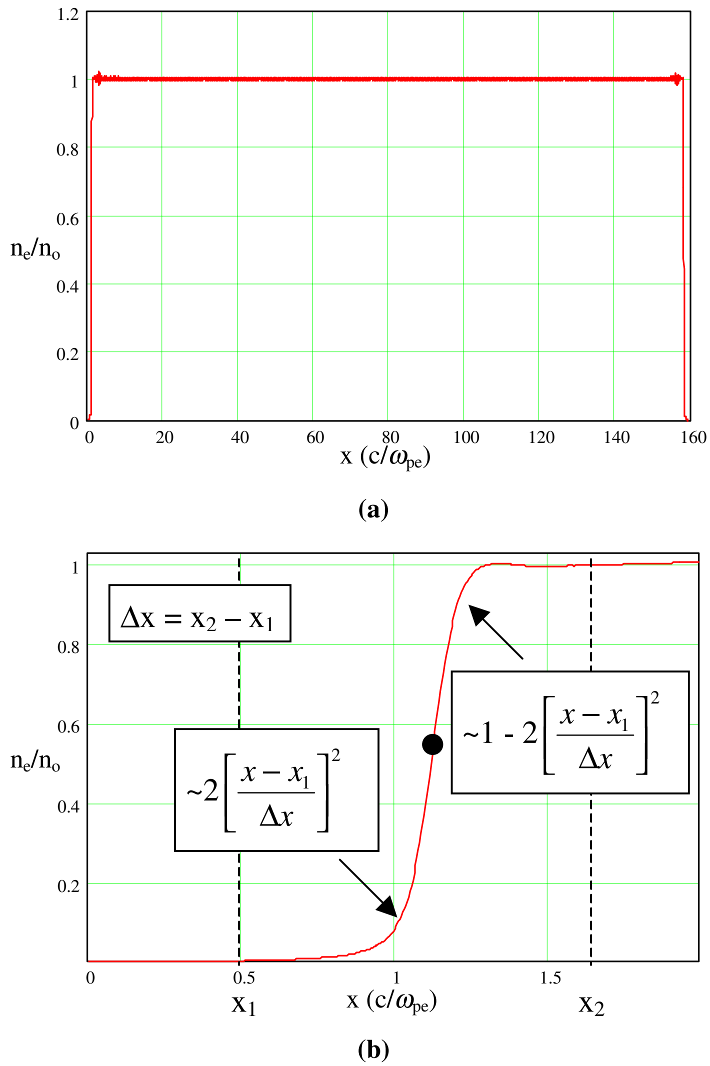

Figure 49. (a) Simulation electron density profile and (b) close up of the piecewise parabolic transition from the vacuum to plasma region.

The following is the actual FORTRAN code used for the numerical simulations.

```
C 1D Finite length Vlasov code for simulation of SRS
C
C Code obtained 8/10/01 from Dr. Magdi Shoucri of IREQ Canada
C and subsequently modified and commented by Ron Focia of MIT
C
C Declare variables as double precision
C

      IMPLICIT REAL*8 (A-H,O-Z)

C Declare external functions called
C
C  DFFTCB is an IMSL routine for computing the complex periodic
C   sequence from its Fourier coefficients - no longer used
C
      EXTERNAL DFFTCB

C PARAMETER statements set constants for the program unit they are
C  in.  The PARAMETER statements are split up into those that
C  specify parameters for the simulation and those that are derived
C  from them.
C
C M is for momentum space (Px), N is for x-space
C IZK is the length of the plasma in terms of the number of free space
C  laser wavelengths
C NSAUT and NSAUTI are the half-width of the boundary regions on either
C  end of the plasma region
C NA and NB can really be set arbitrarily to give the desired vacuum
C  region width on either end of the plasma. However, currently NA and
NB
C  have the same value and NA is determined by a formula.
C EPSI, EPS, IKI, and IKP are used to specify an initial perturbation
C  at the spatial frequency predicted by w/k matching.  This is
necessary
C  e.g. if the boundaries do not provide enough noise at the particular
C  frequency to get the simulation going.
C
      PARAMETER(M=256,MI=128,N=35000,IZK=142,NSAUT=48,NSAUTI=48)
      PARAMETER(EPSI=0.0,EPS=0.05,NVAC=1,IKP=255,IKI=24)

      PARAMETER(M2P1=2*M+1,M2=2*M,NP1=N+1,ND4P1=N/4+1)
      PARAMETER(MI2=2*MI,MI2P1=2*MI+1)
      PARAMETER(NM1=N-1,ND2=N/2,ND2P1=ND2+1,M2M1=M2-1,M2M2=M2-2)
      PARAMETER(NA=NVAC*N/(IZK+2*NVAC)+1)
      PARAMETER(I1=NA-NSAUT/2,I2=NA+NSAUT/2,NB=NP1-NA+1,I3=NB-NSAUT/2)
      PARAMETER(I4=NB+NSAUT/2,NCH=NB-NA+1)
      PARAMETER(II1=NA-NSAUTI/2,II2=NA+NSAUTI/2)
      PARAMETER(II3=NB-NSAUTI/2,II4=NB+NSAUTI/2)

      COMMON/ARRAY/F(NP1,M2P1),A(M2P1),B(M2P1),
     1C(M2P1),D(M2P1),P(NP1),E(NP1),G(NP1),
     2DSH(M2P1),EF(NP1),EEF(NP1),EK(NP1),X(M2P1),
```

```
     4T,XL,VMAX,DT,TMAX,Q,DV,DX,WK,VTH,VTH1,ALP
      COMMON/PARTIC/RHO(NP1),RHOI(NP1)
      COMMON/ARION/FI(NP1,MI2P1),AI(MI2P1),BI(MI2P1),
     1CI(MI2P1),DI(MI2P1),XI(MI2P1),DSHI(MI2P1),
     2VIMAX,DVI,DTI,XMEI,XTEI,TXI
      COMMON/WRKS/FZ(NP1,M2P1),YZ(NP1,M2P1)
      COMMON/PHO/EP(NP1),EM(NP1),VY(NP1),CJP(NP1),CJM(NP1),
     1VYI(NP1),DTT,XK0,OMK,PUMP
      COMMON/TRAC/HH,HS,C1,C3,C2,C5,EEN,C4,C6,VT
      COMMON/TRAC1/HH1,HH2,HH3,HH5,HH6,HH7,XKE,OMP,JS

      DIMENSION TRHO(NP1),HF(3000),HB(3000),XXX(N),VVX(M2),VVXI(MI2)
      DIMENSION FTEMP(M2)

      CHARACTER*24 filename

      REAL NENC,IO,LAMBDAL,TE,TI
C
C Open files for saving transverse field data at each time step
C
      OPEN(UNIT=166,FILE='Ept.dat')
      OPEN(UNIT=266,FILE='Emt.dat')

C Det IDEBUG to 1 to check file IO at each time step
C
      IDEBUG = 0

C Moving window parameters
C  These are gleaned from prior simulation results and w-k matching
C
C IXSTART is the grid point to start at
C ITSTART is the time iteration to start at
C IWINDOW is the width of the window for spatial averaging
C VPEPW is the phase velocity of the EPW normalized to speed of light
C
C These will change with the number of grid points used and must be
C  ascertained from the results of a simulation

      IXSTART = 800
      ITSTART = 1000
      IWINDOW = 380
      VPEPW = 0.11281
C
      NSAVEDATA = 1000
      NSTART = ITSTART

C  ITIME:INTEGRAL TIME COUNT-INCREASED BY 1 EVERY TIME STEP
C
      ITIME=0
C
C  NGRPH:EVERY NGRPH STEP TRACE IS CALLED
C
      NGRPH=128
C
C  NPRNT:EVERY NPRNT STEP ENERGY IS PRINTED
C
      NPRNT=64
```

```
C
C  NPLOT:F IS PLOTTED EVERY NPLOT STEP
C
      NPLOT=256

C New parameters for the simulation that other values are based on

C Electron and Ion temperatures in keV

      TE = 0.35
      TI = 0.1

C There is an option to start off with a bi-Maxwellian plasma
consisting
C  of the background and a hot electron component.  This parameter
C  specifies the hot electron temperature

      TEH = 10.0

C ne/ncrit

      NENC = 0.06

C Laser Intensity in 10^14 W/cm^2

      IO=20.0

C Laser wavelength in microns, 0.527 for the SHS laser

      LAMBDAL=0.527

C VTh specified in keV moralized to mc^2 (510.984 keV)
C They used a warm and hot distribution to get more particles
C  at the SRS phase velocity initially
C
C Warm electron distribution thermal velocity

      VMAX = 0.5
      VTH=DSQRT(TE/510.984D0)
      VT=VTH

C Hot electron distribution thermal velocity

      VTH1=DSQRT(TEH/510.984D0)

C Background electron fraction, the hot fraction is (1-ALP)
C  Used in INICON to construct a bi-Maxwellian distribution
C Turn off the hot component by setting ALP = 1.0

      ALP=1.0

C maximum time for the simulation

      TMAX=200.

C parameter specifying the pump quiver velocity normalized
C  to the speed of light
```

```
C
C  Q = (Eo*e/w_p*m_e)/c  or in terms of the quiver velocity
C  Q = (Vosc/c)/sqrt(n/nc)
C
C Typical values for 527 nm laser and n/nc = 0.032:
C
C  I = 1x10^15 w/CM^2    ; Q = 0.08
C  I = 1.92x10^15 w/CM^2 ; Q = 0.11
C  I = 2x10^15 w/CM^2    ; Q = 0.113
C  I = 3x10^15 w/CM^2    ; Q = 0.138
C  I = 4x10^15 w/CM^2    ; Q = 0.159
C  I = 5x10^15 w/CM^2    ; Q = 0.178
C  I = 6x10^15 w/CM^2    ; Q = 0.195
C
C Should really have as an input the value of n/nc and calculate
C  parameters that are based on this value

C Ron - New parameter-based expression for Q

      Q=(0.00854265*LAMBDAL*SQRT(IO))/SQRT(NENC)

C parameter specifying the normalized free space wave number of
C  the pump  XK0 = k_o*c/w_p.  Calculate by specifying the value
C  of n/nc by
C
C  XKO = k_o*w_p/c = sqrt(1/(n/nc) - 1)
C
C  So, it's probably better to have an input for n/nc and calculate
C  XKO using the formula above
C  For the SHS experiments n/nc ~ 0.032, XKO ~ 5.5

C Ron - New parameter-based expression for XK0

      XK0=SQRT(1/NENC - 1)

C electron to ion mass ratio.  Right now it's just a hydrogen
C  Plasma but later on we'll add another species and will have
C  to multiply by the atomic number

      XMEI=1./1836.

C electron to ion temperature ratio
C for SHS experiments use Te/Ti = 350/100 = 3.5

C Ron - New parameter-based expression for XTEI
      XTEI=TE/TI

C      XTEI=1.

C Max ion velocity expressed in terms of the electron thermal velocity

C Ron - New expression for VIMAX to make ion distribution roll
C  off to ~10^-16 based on electron thermal momentum

C      VIMAX=VMAX*VTH/DSQRT(XMEI*XTEI)
      VIMAX=24.0*VMAX*VTH/DSQRT(XMEI*XTEI)
```

```
C constant 2*pi

      PI2=4.0*DACOS(0.0D0)

C Plasma length - IZK is the length of the plasma in terms of
C  the number of free space laser wavelengths.  XK0 is the
C  laser wave number in terms of c/w_pe
C So, XL1 is the plasma length in terms of free space plasma
C  wavelengths

      XL1=IZK*PI2/XK0

C Vacuum length on each end

      XA=NVAC*PI2/XK0

C Total system length

      XL=XL1+2.0*XA

C 2pi divided by the system length in free space plasma wavelengths
C It's only used in INICON to calculate the normalized plasma wave
number

      WK=PI2/XL1

C deltaX - total system length divided by the number of grid
C points in x-space

      DX=XL/DBLE(N)

C Notes on deltaT = deltaX:
C
C  Should have about 20*DT in one cycle of the
C  fastest oscillation, i.e. the laser.  If the length is fixed,
C  the only way to decrease DT is to increase the number of
C  grid points in space N
C
C  The laser period normalized to the plasma period is
C   (w_p/w_L) = sqrt(n/nc). For the SHS experiments n/nc = 0.032
C   sqrt(0.032)/20 = .009.  If XL = 160 then the necessary N~18000

      DT=DX

C Ratio of electron time steps to ion time steps

      NSTEI=6

C deltaT for ions

      DTI=DBLE(NSTEI)*DT

C Ratio of ion to electron deltaTs

      TXI=DTI/DX
C
C UNIT 6 is the screen
```

```fortran
C
C Output initial data to the screen
C
C Ron - added writing simulation data to a text file so that
C  parameters for a particular simulation need not be
C  written down
C
      OPEN(UNIT=669,FILE='Readme.txt')

      WRITE(6,70)
      WRITE(669,70)
      WRITE(6,80)
      WRITE(669,80)
  80  FORMAT(14X,'VLASOV SIMULATION OF STIMULATED RAMAN SCATTERING')
      WRITE(6,70)
      WRITE(669,70)
  70  FORMAT(1H )
      WRITE(6,60)
      WRITE(669,60)
  60  FORMAT(10X,'XL',13X,'VMAX',11X,'DT',12X,'TMAX',12X,'EM0')
      WRITE(6,50) XL,VMAX,DT,TMAX,Q
      WRITE(669,50) XL,VMAX,DT,TMAX,Q
  50  FORMAT(5F15.5)
      WRITE(6,70)
      WRITE(669,70)
      WRITE(6,55)
      WRITE(669,55)
  55  FORMAT(10X,'N',11X,'M',10X,'NPRNT',7X,'NPLOT',9X,'V  ',8X,'K  ')
      WRITE(6,56) N,M,NPRNT,NPLOT,VTH,XK0
      WRITE(669,56) N,M,NPRNT,NPLOT,VTH,XK0
  56  FORMAT(4I12,F16.5,F11.5)
      WRITE(6,57)
      WRITE(669,57)
  57  FORMAT(1H )


      PUMP=0.0

C Set initial conditions

C Initialize electron and ion distributions and other variables
C  on the space and momentum grids

      CALL INICON
C
C Write all parameters for the simulation to the Readme file
C
      WRITE(669,70)
      WRITE(669,330)
      WRITE(669,331) MI,VIMAX,DVI,TI
 330  FORMAT(10X,'MI',10X,'Vimax',6X,'DVI',9X,'Ti')
 331  FORMAT(I12,F16.5,F12.5,F12.5)
      WRITE(669,70)
      WRITE(669,332)
      WRITE(669,333) IO,NENC,TE,DV,I2,I3
 332  FORMAT(10X,'Io',10X,'n',9X,'Te',8X,'DV',9X,'I2',7X,'I3')
 333  FORMAT(F16.4,3F10.4,2I10)
```

```
C Done with the parameter README file, close it
      CLOSE(669)

      WRITE(6,70)
      WRITE(6,1010)
 1010 FORMAT(1H ,'   TIME',2X,'Density',1X,' EKx Elec',1X,' EKy Elec',
     12X,'EK Total',2X,'E-Long',3X,' E-EM   ',2X,' E-Total ')
      WRITE(6,70)
C
C     CALL EZY(RHOI,NP1,'ION DENSITY$')

C Subroutine PREP calculates parameters used for shifting
C  in space and momentum

      CALL PREP

C Subroutine DENSI calculates the ion charge density
C  for each point in x-space

      CALL DENSI

C Subroutine ENGY calls TRACE which calculates all
C  energies

      CALL ENGY

C Subroutine DENS calculates the electron charge density
C  for each point in x-space

      CALL DENS

C Write x and Px to data files
C
C Ron - Modified to write raw data to individual files

C X-vector
      OPEN(UNIT=66,FILE='X.dat')
      WRITE(66,*) (FLOAT(I-1)*SNGL(DX),I=1,NP1)
      CLOSE(66)

C Px-vector for electrons
      DO J=1,M2
        VVX(J)=(J-1)*DV-VMAX
      ENDDO
      OPEN(UNIT=66,FILE='Pxe.dat')
      WRITE(66,*) (SNGL(VVX(J)),J=1,M2)
      CLOSE(66)
C Px-vector for ions
      DO J=1,MI2
        VVXI(J)=(J-1)*DVI-VIMAX
      ENDDO
      OPEN(UNIT=66,FILE='Pxi.dat')
      WRITE(66,*) (SNGL(VVXI(J)),J=1,MI2)
      CLOSE(66)

C Save initial transverse fields
```

```
C format specifier to write one data point per line
366   FORMAT(F8.6)
      WRITE(166,366) SNGL(EP(I3))
      WRITE(266,366) SNGL(EM(I2))

C Beginning of time step loop
C T is the actual time not the integer time step

    6 T=T+DT
C
C Increment the integer time step
C
      ITIME=ITIME+1
C
C Set the time-dependent pump amplitude (peak electric field)

      PUMP=2.*Q*DSIN(OMK*T)
C
C don't know what these were used for but they're obviously some
C  time-dependent shift in the pump frequency
C
C     PUMP=Q*DSIN(OMK*T*(1.-T/6000.D0))+Q*DSIN(1.562D0*T)
C     PUMP=2.*Q*DSIN(OMK*T*(1.-T/1500.))
C
C Only update ion information every NSTEI steps
C
      IF(MOD(ITIME,NSTEI).EQ.0) THEN
        DO 20 I=1,NP1
C Update ion Vy using half time step and the monokinetic fluid
approximation
          VYI(I)=VYI(I)+0.5*DTI*XMEI*(EP(I)+EM(I))
   20   CONTINUE
        CALL STRION
        CALL DENSI
      ENDIF

C Update electron Vy using half time step and the monokinetic fluid
approximation
      DO 10 I=1,NP1
        VY(I)=VY(I)-0.5*DT*(EP(I)+EM(I))
   10 CONTINUE
C
C Shift the electron distributions
      CALL STREAM

C Calculate the new longitudinal field
      CALL EFIELD

C Calculate the new transverse fields
      CALL SPHOTF

C Here the forward and backward propagating transverse fields
C  are saved at the boundaries for each time step
C
C     HB(ITIME)=EM(1)*EM(1)*0.25
C     HF(ITIME)=EP(NP1)*EP(NP1)*0.25
C
```

```
C Accelerate electrons and ions if necessary

      CALL ACC
      IF(MOD(ITIME,NSTEI).EQ.0) CALL ACCI
C
      IF(MOD(ITIME,NGRPH).EQ.0) THEN
C
        DO 77 I=1,NP1
          TRHO(I)=(EP(I)+EM(I))*0.5
   77   CONTINUE
C
        DO 78 I=1,NP1
          TRHO(I)=EF(I)
   78   CONTINUE
C
      ENDIF
C
C     IF(MOD(ITIME,NPLOT).EQ.0)CALL PLOTF
C
C Periodically save the spatially averaged electron distribution
function
C Must specify a window over which the distribution function will be
averaged.
C  Then sum all Fe on the same Px value and divide by the number of
points
C  summed over.
C
C Additionally, save all data on the last iteration

      IF(((MOD(ITIME,NSAVEDATA).EQ.0).AND.(ITIME.GE.NSTART))
     1.OR.(T.GE.TMAX).OR.(IDEBUG.GT.0))THEN

        WRITE(6,98)
  98    FORMAT(14X,'writing data files...')

C Spatially average the distribution function over a number of bins
C  moving at the phase velocity of the EPW

C Update the starting index for the moving window. This is only
meaningful
C  if we're not debugging

        IF(ITIME.GE.ITSTART)THEN
          IXSTART = IXSTART + INT(VPEPW*(ITIME-ITSTART))
        ENDIF

        NUMBINS=3

        DO 110 K=1,NUMBINS

          DO 112 J=1,M2
            S=0.0
            IS = (IXSTART + (K-2)*(IWINDOW+1))
            DO 111 I=IS,(IS+IWINDOW)
              S=S+F(I,J)
  111       CONTINUE
            FTEMP(J)=S/(IWINDOW+1)
```

```
  112      CONTINUE

           WRITE(filename,113) K,ITIME
  113      FORMAT('FeBin',I1,'T',I8,'.dat')
           OPEN(UNIT=66,FILE=filename)
           WRITE(66,*) (SNGL(FTEMP(J)), J=1,M2)
           CLOSE(66)

  110    CONTINUE

C Forward propagating field
         WRITE(filename,114) ITIME
  114    FORMAT('EP',I8,'.dat')
         OPEN(UNIT=66,FILE=filename)
         WRITE(66,*) (SNGL(EP(I)),I=1,NP1)
         CLOSE(66)

C Backward propagating field
         WRITE(filename,115) ITIME
  115    FORMAT('EM',I8,'.dat')
         OPEN(UNIT=66,FILE=filename)
         WRITE(66,*) (SNGL(EM(I)),I=1,NP1)
         CLOSE(66)

C Longitudinal field
         WRITE(filename,116) ITIME
  116    FORMAT('EF',I8,'.dat')
         OPEN(UNIT=66,FILE=filename)
         WRITE(66,*) (SNGL(EF(I)),I=1,NP1)
         CLOSE(66)

C Electron distribution
C Save the electron distribution in the plasma region and only in
positive
C  momentum space
         Nx = I3-I2+1
         Np = M2-(M-1)+1
         WRITE(filename,117) ITIME
 117     FORMAT('Fe',I8,'.dat')
         OPEN(UNIT=66,FILE=filename,ACTION='WRITE',FORM='BINARY',RECL=4)
         WRITE(66) Nx
         WRITE(66) Np
         WRITE(66) ((SNGL(F(I,J)),I=I2,I3),J=M,M2)
         CLOSE(66)

C Ion distribution
C Save the ion distribution in the plasma region and only in positive
C  momentum space
         Nx = I3-I2+1
         Npi = MI2-(MI-1)+1
         WRITE(filename,1171) ITIME
1171     FORMAT('Fi',I8,'.dat')
         OPEN(UNIT=66,FILE=filename,ACTION='WRITE',FORM='BINARY',RECL=4)
         WRITE(66) Nx
         WRITE(66) Npi
         WRITE(66) ((SNGL(FI(I,J)),I=I2,I3),J=MI,MI2)
         CLOSE(66)
```

```fortran
C Electron density
        DO I=1,N
          CINT=0.
          DO J=1,M2
            CINT=CINT+F(I,J)*DV
          ENDDO
          TRHO(I)=CINT
        ENDDO
        WRITE(filename,118) ITIME
  118   FORMAT('rhoe',I8,'.dat')
        OPEN(UNIT=66,FILE=filename)
        WRITE(66,*) (SNGL(TRHO(I)),I=1,N)
        CLOSE(66)

      ENDIF

      IF(MOD(ITIME,NPRNT).EQ.0)THEN
         CALL ENGY
      ENDIF
C
      IF(F(2,M2)*F(2,M2).GT.100.0) THEN
        WRITE(6,1007)
 1007   FORMAT(' TERMINATION DUE TO NUMERICAL INSTABILITY')
        IF(MOD(ITIME,NPRNT).NE.0)CALL ENGY
        STOP
      ELSE

C Save transverse fields
      WRITE(166,366) SNGL(EP(I3))
      WRITE(266,366) SNGL(EM(I2))

      IF(T.LT.TMAX) GO TO 6

C End of Main time loop
C
C     CALL EZY(HB,ITIME,'BACKWARD FLUX$')
C     CALL EZY(HF,ITIME,'FORWARD FLUX$')
C
      DO 79 I=1,NP1
        TRHO(I)=0.5*(EP(I)+EM(I))
  79  CONTINUE
C

      WRITE(6,99)
  99  FORMAT(14X,'Simulation complete')

C Close transverse field data files
      CLOSE(166)
      CLOSE(266)

      ENDIF
C
C Cancel calling PLOTF until I know whets going on in the routine
C     CALL PLOTF
C
      STOP
```

```
      END
C
C End of main program loop
C
C SUBROUTINE INICON sets initial conditions for the simulation
C
      SUBROUTINE INICON

      IMPLICIT REAL*8 (A-H,O-Z)

      PARAMETER(M=256,MI=128,N=35000,IZK=142,NSAUT=48,NSAUTI=48)
      PARAMETER(EPSI=0.0,EPS=0.05,NVAC=1,IKP=255,IKI=24)

      PARAMETER(M2P1=2*M+1,M2=2*M,NP1=N+1,ND4P1=N/4+1)
      PARAMETER(MI2=2*MI,MI2P1=2*MI+1)
      PARAMETER(NM1=N-1,ND2=N/2,ND2P1=ND2+1,M2M1=M2-1,M2M2=M2-2)
      PARAMETER(NA=NVAC*N/(IZK+2*NVAC)+1)
      PARAMETER(I1=NA-NSAUT/2,I2=NA+NSAUT/2,NB=NP1-NA+1,I3=NB-NSAUT/2)
      PARAMETER(I4=NB+NSAUT/2,NCH=NB-NA+1)
      PARAMETER(II1=NA-NSAUTI/2,II2=NA+NSAUTI/2)
      PARAMETER(II3=NB-NSAUTI/2,II4=NB+NSAUTI/2)

      COMMON/ARRAY/F(NP1,M2P1),A(M2P1),B(M2P1),
     1C(M2P1),D(M2P1),P(NP1),E(NP1),G(NP1),
     2DSH(M2P1),EF(NP1),EEF(NP1),EK(NP1),X(M2P1),
     4T,XL,VMAX,DT,TMAX,Q,DV,DX,WK,VTH,VTH1,ALP
      COMMON/ARION/FI(NP1,MI2P1),AI(MI2P1),BI(MI2P1),
     1CI(MI2P1),DI(MI2P1),XI(MI2P1),DSHI(MI2P1),
     2VIMAX,DVI,DTI,XMEI,XTEI,TXI
      COMMON/PHO/EP(NP1),EM(NP1),VY(NP1),CJP(NP1),CJM(NP1),
     1VYI(NP1),DTT,XK0,OMK,PUMP
      COMMON/TRAC1/HH1,HH2,HH3,HH5,HH6,HH7,XKE,OMP,JS
C
C    CALCULATE THE VALUES OF THE EQUILIBRIUM DISTRIBUTION
C
      PIE=2.0*DACOS(0.0D0)
      PIE2=2.0*PIE
C
      ARG=IZK*PIE2/DBLE(NB-NA)

C XKE is the normalized plasma wave number
      XKE=DBLE(IKP)*WK

      XKI=DBLE(IKI)*PIE2/XL
      ARGI=DBLE(IKI)*PIE2/DBLE(NB-NA)
      ARGP=IKP*PIE2/DBLE(NB-NA)
C
C laser frequency normalized to the plasma frequency
      OMK=DSQRT(1.0+XK0*XK0)

C Normalized plasma wave frequency
      OMP=DSQRT(1.0+3.0*XKE*XKE*VTH*VTH)

C Ion wave frequency...what's he doing here?
C  This is just a weird way to calculate OmI = k*Cs
C  OMI is first used to calculate Cs^2 and is then
C  corrected by the mass ratio and Vth
```

```
      OMI=(3.0/XTEI+1.0/(1.0+XKI*XKI*VTH*VTH))
      OMI=DSQRT(DABS(OMI*XMEI))*XKI*VTH
C
      WRITE(6,100) XMEI,XTEI,XKE,XKI,OMK,OMP,OMI,VIMAX
      WRITE(669,100) XMEI,XTEI,XKE,XKI,OMK,OMP,OMI,VIMAX
  100 FORMAT(2X,'XMEI=',E10.3,' XTEI=',E10.3,' XKE=',
     1E10.3,' XKI  =',E10.3,/,'  OMK =',E10.3,' OMP =',E10.3,
     2' OMI=',E10.3,' VIMAX=',E10.3,/)

C plasma wave phase velocity

      VPHI=OMP/XKE
C
C Le calcul suivant genere un underflow sqtr(-n)
C Following calculation generate an underflow-translation from
babblefish
C     PPHI=VPHI/DSQRT(1.D0-VPHI*VPHI)
C     JS=M+IDNINT(M*PPHI/VMAX)

C sqrt of 2pi - Fix: This should be a global constant

      S2PIE=DSQRT(PIE2)

C delta in momentum space.  variables are V but really they
C  hold Px

      DV=VMAX/(DBLE(M)-0.5)
      DVI=VIMAX/(DBLE(MI)-0.5)

      DTT=DT

      M2N=M2*N

      T=0.0

C     IF(T.GT.0.0)GOTO 22

C This loop initializes the hot electron distribution in momentum
C  space for each spatial grid point
C
C An initial perturbation can be specified with EPS or EPSI for
electron
C  plasma or ion acoustic waves, respectively.  I think this would
C  translate directly to dn/n.
C
      DO 97 J=1,M2
        V=(J-1)*DV-VMAX
        DO 97 I=1,NP1
          ARGPP=ARGP*FLOAT(I-1)
          ENER1=V-EPS*VTH1*DCOS(ARGPP)
          ENER1=1.-DSQRT(1.0D0+ENER1*ENER1)
          ENER1=ENER1/VTH1**2
          F(I,J)=DEXP (ENER1)
  97  CONTINUE
C
C don't know what this is for, looks like integrating the
```

```
C  hot distribution function and keeping track of the sum in H
C  Multiplying by DV gives the total area under F then dividing
C  by N gives the spatial average

      H=0.
      CTN=0.
C
      DO 51 I=1,N
        DO 51 J=1,M2
          H=H+F(I,J)
   51 CONTINUE
C
       CTN=H*DV/DBLE(N)

C     WRITE(6,108)CTN
C 108 FORMAT(2X,'C CTN DENSITY ',E20.10)
C
C This loop specifies the warm electron component in momentum space
C (on each grid point in x) and then adds it to the hot distribution
C calculated above

      DO 53 J=1,M2
        V=(J-1)*DV-VMAX
        V=V/VTH
        DO 53 I=1,NP1
          ARGPP=ARGP*FLOAT(I-1)
          ENER=0.5*(V-EPS*DCOS(ARGPP))**2
          FUNCT=ALP*DEXP(-ENER)/S2PIE/VTH
          F(I,J)=(1.-ALP)*F(I,J)/CTN+FUNCT
   53 CONTINUE

C Debug - Print out the electron distribution function
      OPEN(UNIT=66,FILE='FeInit.dat')
      WRITE(66,*) (SNGL(F(100,I)),I=1,M2)
      CLOSE(66)


C
C     ENER=0.5*(V-EPS*DCOS(ARGP*DREAL(I-1)))**2
C     F(I,J)=DEXP(-ENER)/S2PIE/VTH
C 20  CONTINUE

      XNS=NSAUT
C
C modify the electron distribution in space based on the specified
C  profile
C
      DO 27 J=1,M2
C
C In the vacuum region the distribution function is zero
        DO 21 I=1,I1
          F(I,J)=0.0
   21   CONTINUE
C
C The profile is then ramped up using piecewise parabolic
C  functions PRFE is simply a profile modification factor
        DO 22 I=I1+1,NA
```

```
          PRFE=2.0*(DBLE(I-I1)/XNS)**2
c      PRFE=DSIN(PIE*DBLE(I-I1)/(2.*XNS))
c      PRFE=PRFE*PRFE
          F(I,J)=F(I,J)*PRFE
   22   CONTINUE
C
        DO 23 I=NA+1,I2
          PRFE=1.-2.0*(DBLE(I-I2)/XNS)**2
c      PRFE=DSIN(PIE*DBLE(I-I1)/(2.*XNS))
c      PRFE=PRFE*PRFE
          F(I,J)=F(I,J)*PRFE
   23   CONTINUE
C
        DO 24 I=I3+1,NB
          PRFE=1.-2.0*(DBLE(I-I3)/XNS)**2
          F(I,J)=F(I,J)*PRFE
   24   CONTINUE
C
        DO 25 I=NB+1,I4
          PRFE=2.0*(DBLE(I-I4)/XNS)**2
          F(I,J)=F(I,J)*PRFE
   25   CONTINUE
C
C F is zero again in the right vacuum region
        DO 26 I=I4+1,NP1
          F(I,J)=0.0
   26   CONTINUE
C
   27 CONTINUE
C
C Initialize ion distribution, first in momentum space and then
C  in x-space modifying it with the profile as with the electron
C  distribution
C
C If we later allow multiple ion species, here is where they'll be
C  initialized
C
      CSTE=DSQRT(XMEI*XTEI)/S2PIE/VTH
C
      DO 40 J=1,MI2
        V=(J-1.)*DVI-VIMAX
        V=V*DSQRT(XMEI*XTEI)/VTH
        DO 40 I=1,NP1
          ARGII=ARGI*FLOAT(I-1)
          ENER=V-EPSI*DCOS(ARGII)
          ENER=0.5*ENER*ENER
          FI(I,J)=CSTE*DEXP(-ENER)
   40 CONTINUE
C
C Debug - Print out the ion distribution function
      OPEN(UNIT=66,FILE='FiInit.dat')
      WRITE(66,*) (SNGL(FI(100,I)),I=1,MI2)
      CLOSE(66)


      XNS=NSAUTI
C
```

```
      DO 38 J=1,MI2
        DO 31 I=1,II1
          FI(I,J)=0.0
   31 CONTINUE
C
      DO 32 I=II1+1,NA
        PRFI=2.0*(DBLE(I-II1)/XNS)**2
c     PRFI=DSIN(PIE*DBLE(I-II1)/(2.*XNS))
c     PRFI=PRFI*PRFI
        FI(I,J)=FI(I,J)*PRFI
   32 CONTINUE
C
      DO 33  I=NA+1,II2
        PRFI=1.-2.0*(DBLE(I-II2)/XNS)**2
c     PRFI=DSIN(PIE*DBLE(I-II1)/(2.*XNS))
c     PRFI=PRFI*PRFI
        FI(I,J)=FI(I,J)*PRFI
   33 CONTINUE
C
      DO 34 I=II2+1,II3
        PRFI=1.0
        FI(I,J)=FI(I,J)*PRFI
   34 CONTINUE
C
      DO 35 I=II3+1,NB
        PRFI=1.-2.0*(DBLE(I-II3)/XNS)**2
        FI(I,J)=FI(I,J)*PRFI
   35 CONTINUE
C
      DO 36 I=NB+1,II4
        PRFI=2.0*(DBLE(I-II4)/XNS)**2
        FI(I,J)=FI(I,J)*PRFI
   36 CONTINUE
C
      DO 37 I=II4+1,NP1
        FI(I,J)=0.0
   37 CONTINUE
C
   38 CONTINUE
C
C Looks like at one point they allowed reading in a distribution
C  from a file
C  22 READ(10)((F(I,J),J=1,M2),I=1,N)
C     REWIND(10)
C
C Initialize other parameters on the spatial grid

      DO 30 I=1,NP1
        VY(I)=0.0
        VYI(I)=0.0
        EM(I)=0.0
C Here we could specify a J1(x)/x profile for the laser
C  to simulate the SHS profile
        EP(I)=PUMP
   30 CONTINUE
C
      RETURN
```

```
      END
C
C  SUBROUTINE PREP
C
      SUBROUTINE PREP

      IMPLICIT REAL*8 (A-H,O-Z)

      PARAMETER(M=256,MI=128,N=35000,IZK=142,NSAUT=48,NSAUTI=48)
      PARAMETER(EPSI=0.0,EPS=0.05,NVAC=1,IKP=255,IKI=24)

      PARAMETER(M2P1=2*M+1,M2=2*M,NP1=N+1,ND4P1=N/4+1)
      PARAMETER(MI2=2*MI,MI2P1=2*MI+1)
      PARAMETER(NM1=N-1,ND2=N/2,ND2P1=ND2+1,M2M1=M2-1,M2M2=M2-2)
      PARAMETER(NA=NVAC*N/(IZK+2*NVAC)+1)
      PARAMETER(I1=NA-NSAUT/2,I2=NA+NSAUT/2,NB=NP1-NA+1,I3=NB-NSAUT/2)
      PARAMETER(I4=NB+NSAUT/2,NCH=NB-NA+1)
      PARAMETER(II1=NA-NSAUTI/2,II2=NA+NSAUTI/2)
      PARAMETER(II3=NB-NSAUTI/2,II4=NB+NSAUTI/2)

      COMMON/ARRAY/F(NP1,M2P1),A(M2P1),B(M2P1),
     1C(M2P1),D(M2P1),P(NP1),E(NP1),G(NP1),
     2DSH(M2P1),EF(NP1),EEF(NP1),EK(NP1),X(M2P1),
     4T,XL,VMAX,DT,TMAX,Q,DV,DX,WK,VTH,VTH1,ALP
      COMMON/ARION/FI(NP1,MI2P1),AI(MI2P1),BI(MI2P1),
     1CI(MI2P1),DI(MI2P1),XI(MI2P1),DSHI(MI2P1),
     2VIMAX,DVI,DTI,XMEI,XTEI,TXI
      DIMENSION DD(M2P1),DDI(MI2P1)

C FOR ELECTRONS

C starting off at an initial velocity of 1/2 the step
C This makes sense because the center velocity is zero

      V=0.5*DV

C Calculating the momentum in x relativistically

      DO 2 J=1,M
        PX=V/DSQRT(1.0D0+V*V)
        S=PX
        S=DMOD(S,1.D0)
C S holds the fractional part
C DSH holds momentum for + and - values
        DSH(M-J+1)=PX
        DSH(M+J)=PX
C DD holds the factional part
        DD(M-J+1)=S
        DD(M+J)=S
        V=V+DV
  2   CONTINUE

C FOR IONS
      V=0.5*DVI

CDIR$ IVDEP
```

```
      DO 3 J=1,MI
        PX=V*XMEI
        PX=PX/DSQRT(1.0D0+PX*PX)
        S=PX*TXI
        S=DMOD(S,1.D0)
        DSHI(MI-J+1)=PX*TXI
        DSHI(MI+J)=PX*TXI
        DDI(MI-J+1)=S
        DDI(MI+J)=S
        V=V+DVI
    3 CONTINUE

C FOR ELECTRONS
      X(1)=-0.25

      DO 10 J=2,M2
        X(J)=-1.0/(4.0+X(J-1))
  10  CONTINUE

C FOR IONS
      XI(1)=-0.25

      DO 11 J=2,MI2
        XI(J)=-1.0/(4.0+XI(J-1))
   11 CONTINUE

C    CALCULATE THE SHIFT COEFFICIENTS
      E(1)=-0.25
      G(1)=-0.25

      DO 21 I=2,NM1
        E(I)=-1.0/(4.0+E(I-1))
C As far as I can tell, G is not used anywhere
        G(I)=+G(I-1)*E(I)
  21  CONTINUE

C FOR ELECTRONS
      DO 9 J=1,M2
        AD=DD(J)
        A(J)=(1.-AD)**3
        B(J)=4.0-3.0*AD*AD*(1.0+(1.0-AD))
        C(J)=4.0-3.0*((1.0-AD)**2)*(1.0+AD)
        D(J)=AD*AD*AD
  9   CONTINUE

C FOR IONS
      DO 8 J=1,MI2
        AD=DDI(J)
        AI(J)=(1.-AD)**3
        BI(J)=4.0-3.0*AD*AD*(1.0+(1.0-AD))
        CI(J)=4.0-3.0*((1.0-AD)**2)*(1.0+AD)
        DI(J)=AD*AD*AD
    8 CONTINUE

      RETURN
      END
C
```

```
C  SUBROUTINE NONPERIODIC
C
      SUBROUTINE NONPERIODIC (F,V,N)
      PARAMETER (NM=256)
      IMPLICIT REAL*8 (A-H,O-Z)
      INTEGER N
C
C       COMMON/SHFT/X(NM),E(NM),G(NM),EE(NM)
      DIMENSION X(NM),E(NM),G(NM),EE(NM)
C
      DIMENSION  F(N),V(N)
      DIMENSION FL(N),H(N),ALPHA(N),BETA(N),S(0:N+1),OLD_F(0:N+1)
C       REAL A,B,C,D,XJ
C
      INTEGER I,J
C
C     ---------------------------------------------
C     Copy F to OLD_F & periodic boundary conditions
C     ---------------------------------------------
      OLD_F(N+1)  = F(N)
      DO I = 1,N
         OLD_F(I)  = F(I)
      F(I)=0.
      ENDDO
      OLD_F(0)    =0.
CC      OLD_F(N+1)  = F(N)
C     ---------------------------------------------
C     Calculate L_i
C     ---------------------------------------------
      DO I = 1,N
         FL(I)=3.0*(OLD_F(I-1)-2.*OLD_F(I)+OLD_F(I+1))
      ENDDO
C     ---------------------------------------------
C     Calculate H_i
C     ---------------------------------------------
      H(1)  = FL(1)/4.0
      H(1)=0.
      DO I = 2,N
         H(I)  = EE(I)*(H(I-1)-FL(I))
      ENDDO
C     ---------------------------------------------
C     ---------------------------------------------
C     Calculate S_i
C     ---------------------------------------------
C      S(N)  = (FL(N)-BETA(1)-BETA(N-1))/(ALPHA(1)+ALPHA(N-1)+4.0)
      S(N+1)=H(N)/(1.-EE(N))
      DO I = 0,N-1
C         S(I)  = ALPHA(I)*S(N)+BETA(I)
         S(N-I) =EE(N-I)*S(N-I+1)+H(N-I)

      ENDDO
C      S(0)    = S(N)
      S(0)=0.
C      S(N+1)  = S(1)
C
C     =============================================
C     Begin of interpolation loop over i
```

```
C     ==============================================
      DO I = 1,N
C     ----------------------------------------------
C     Calculate "origin" index j for index i
C     ----------------------------------------------
CM         XJ = MODULO(FLOAT(I)-V(I)-1.0,FLOAT(N))+1.0
         XJ = FLOAT(I)-V(I)
      IF(XJ.LT.0.0) XJ=0.
      IF(XJ.GT.N) XJ=FLOAT(N)
C     ----------------------------------------------
C     Calculate A,B,C and D. ( B = delta )
cc      FIELD=V(I)
cc      SS=DMOD(DABS(FIELD),1.0D0)
cc      IF(FIELD.LE.0.0) THEN
cc      ISGNF=-1
cc      ELSE
cc      ISGNF=+1
cc      ENDIF

         B =DMOD(XJ,1.0D0)
cc      B=SS

         A = 1.0 - B
         C = A*(A-1)*(A+1)/3.0
         D = B*(B-1)*(B+1)/3.0
C     ----------------------------------------------
C     Calculate J
C     ----------------------------------------------
         J = INT(XJ)
C     ----------------------------------------------
C     Calculate F(I)
C     ----------------------------------------------
         F(I) = A*OLD_F(J)+B*OLD_F(J+1)+C*S(J)+D*S(J+1)
cc         F(I+INT(ABS(FIELD))*ISGNF) =
cc     1 A*OLD_F(I)+B*OLD_F(I-ISGNF)+C*S(I)+D*S(I-ISGNF)
C
      ENDDO
C     ==============================================
C     End of loop over i
C     ==============================================
C
      RETURN
      END
C
C  SUBROUTINE PLOTF
C
C  This routine appears to be the only place where external
C    FFT routines are called
C
C  Create phase space plots of the distribution functions to
C    see the vortices
C
C  Ron - This has now been replaced by my Matlab post processing
C
      SUBROUTINE PLOTF

C  Declare variables as double precision
```

```fortran
      IMPLICIT REAL*8 (A-H,O-Z)

      PARAMETER(M=256,MI=128,N=35000,IZK=142,NSAUT=48,NSAUTI=48)
      PARAMETER(EPSI=0.0,EPS=0.05,NVAC=1,IKP=255,IKI=24)

      PARAMETER(M2P1=2*M+1,M2=2*M,NP1=N+1,ND4P1=N/4+1)
      PARAMETER(MI2=2*MI,MI2P1=2*MI+1)
      PARAMETER(NM1=N-1,ND2=N/2,ND2P1=ND2+1,M2M1=M2-1,M2M2=M2-2)
      PARAMETER(NA=NVAC*N/(IZK+2*NVAC)+1)
      PARAMETER(I1=NA-NSAUT/2,I2=NA+NSAUT/2,NB=NP1-NA+1,I3=NB-NSAUT/2)
      PARAMETER(I4=NB+NSAUT/2,NCH=NB-NA+1)
      PARAMETER(II1=NA-NSAUTI/2,II2=NA+NSAUTI/2)
      PARAMETER(II3=NB-NSAUTI/2,II4=NB+NSAUTI/2)

      PARAMETER(LL=9,LL1=LL+1,VAR=200.,NCHS2=(NCH-1)/2)

      COMMON/ARRAY/F(NP1,M2P1),A(M2P1),B(M2P1),
     1C(M2P1),D(M2P1),P(NP1),E(NP1),G(NP1),
     2DSH(M2P1),EF(NP1),EEF(NP1),EK(NP1),X(M2P1),
     4T,XL,VMAX,DT,TMAX,Q,DV,DX,WK,VTH,VTH1,ALP
C  variable TRHO becomes complex the other remainders

C     DIMENSION FPL(192,64),WORK(2,128),TRHO(2,M2P1-1),LWK(LL1),IWK(8)
      DIMENSION FPL(NCH-1,256)
C it looks like the line below is used for the IMSL routine
      COMPLEX*16 TRHO(M2P1-1),GG(M2P1-1),WORK(128),GGW(128)
c      DIMENSION F1(96,64),F2(96,64)
C     REAL*8 AR(0:M2-1),AI(0:M2-1)
      DIMENSION F1((NCH-1)/2,256),F2((NCH-1)/2,256)
      IFAIL=0.
      NDI=(NCH-1)/192
      MDI=M2/64
      NDI=2
      DO 102 I=NDI,NCH-1,NDI
C
        DO 120 J=1,M2
C
C Transform to COMPLEX
C use one or the other but not both
C     TRHO(2,J)=0.
C     TRHO(1,J)=0.0
        TRHO(J)=DCMPLX(0.0D0,0.0D0)
C     AR(J-1)=0.
C     AI(J-1)=0.

        DO 200 IM=-NDI,-1
          SF=F(I+NA+IM,J)
C Transform to COMPLEX
C     TRHO(1,J)=TRHO(1,J)+SF
          TRHO(J)=DCMPLX(DREAL(TRHO(J))+SF,DIMAG(TRHO(J)))
C     AR(J-1)=AR(J-1)+SF

  200   CONTINUE
C     AR(J-1)=AR(J-1)/FLOAT(NDI)
C     IF(J.LT.M/2.OR.J.GT.3*M/2) AR(J-1)=0.

C Transform to COMPLEX
```

```
C     TRHO(1,J)=TRHO(1,J)/DBLE(NDI)
      TRHO(J)=DCMPLX(DREAL(TRHO(J))/DBLE(NDI),DIMAG(TRHO(J)))

  120  CONTINUE

c Fourier Transform version 9.2  A REMPLACER PAR VERSION 10
c     CALL FFT2C(TRHO,LL,LWK)
C DFFTCB is a double precision IMSL routine
      CALL DFFTCB(2**LL,TRHO,GG)
C C06EAF NAG routine
C  Single one-dimensional real discrete Fourier transform, no extra
workspace
C     CALL C06EAF(AR,M2,IFAIL)
      DO NI=1,M2P1-1
        TRHO(NI)=GG(NI)
      END DO

CCCCCCCCCCCCCCCCCCCCCCCCCCCCCCCCCCCCCCCCCCCCCCCCCCCCCCCCCCCCCCCC

cc      DO 103 K=1,33
      DO 103 K=2,256
      SMOOTH=DBLE(K-1)**2/VAR
cc      SMOOTH=DEXP(-SMOOTH)/DBLE(M2-1)
      SMOOTH=DEXP(-SMOOTH)
C     AR(K-1)=AR(K-1)*SMOOTH
C     AR(512-K+1)=AR(512-K+1)*SMOOTH
C Transform to COMPLEX
C     WORK(1,K)=TRHO(1,K)*SMOOTH
C 103 WORK(2,K)=-TRHO(2,K)*SMOOTH
      WORK(K)=DCMPLX(DREAL(TRHO(K))*SMOOTH,-DIMAG(TRHO(K))*SMOOTH)
  103 CONTINUE
cc      DO 104 K=2,32
      DO 104 K=2,256
C Transform to COMPLEX
C     WORK(1,130-K)=WORK(1,K)
C 104 WORK(2,130-K)=-WORK(2,K)
      WORK(130-K)=DCMPLX(DREAL(WORK(K)),-DIMAG(WORK(K)))
  104 CONTINUE

      DO 112 K=34,97
C Transform to COMPLEX
C     WORK(1,K)=0.
C 112 WORK(2,K)=0.
      WORK(K)=DCMPLX(0.0D0,0.0D0)
  112 CONTINUE
C C06GBF NAG routine - Complex conjugate of Hermitian sequence
C      CALL C06GBF(AR,512,IFAIL)
C C06EBF NAG routine
C  Single one-dimensional Hermitian discrete Fourier transform, no
extra workspace
C      CALL C06EBF(AR,512,IFAIL)
cc    DO 107 J=257,385
      DO 107 J=257,257+170
C  107 FPL(I/NDI,J-256)=AR(J)

c transf de Fourier version 9.2
c      CALL FFT2C(WORK,7,IWK)
```

```
      CALL DFFTCB(2**7,WORK,GGW)
C
      DO NI=1,128
        WORK(NI)=GGW(NI)
      END DO
C
cc      DO 107 J=65,128
C Transform to COMPLEX
C 107 FPL(I/NDI,J-64)=WORK(1,J)
  107 FPL(I/NDI,J-64)=DREAL(WORK(J))

CCCCCCCCCCCCCCCCCCCCCCCCCCCCCCCCCCCCCCCCCCCCCCCCCCCCCCCCCCCCCCCC


  102 CONTINUE
c      DO 300 J=1,128
      DO 300 J=1,170
cc      DO 310 I=1,96
      DO 310 I=1,(NCH-1)/(2*NDI)
      F1(I,J)=FPL(I,J)
 310  CONTINUE
cc      DO 300 I=97,192
      DO 300 I=(NCH-1)/(2*NDI)+1,(NCH-1)/NDI
cc      F2(I-96,J)=FPL(I,J)
      F2(I-(NCH-1)/(2*NDI),J)=FPL(I,J)
 300  CONTINUE
      OPEN(UNIT=3,FILE='contour3.dat')
      WRITE(3,*) 1
ccc   WRITE(3,*) 96,64
cc      WRITE(3,*) (NCH-1)/(2*NDI),128
      WRITE(3,*) (NCH-1)/(2*NDI),170
ccc   WRITE(3,*) (SNGL((I-1)*DX),I=1,96)
      WRITE(3,*) (SNGL((I-1)*NDI*DX),I=1,(NCH-1)/(2*NDI))
cc      WRITE(3,*) (SNGL((J-1)*DV),J=1,128)
      WRITE(3,*) (SNGL((J-1)*DV),J=1,170)
C     WRITE(3,*) (SNGL((J-1)*DV),J=1,128)
ccc      WRITE(3,*) ((F1(I,J),I=1,96),J=1,256)
      WRITE(3,*) ((F1(I,J),I=1,(NCH-1)/(2*NDI)),J=1,170)
      WRITE(3,*) 0
      REWIND 3
      CLOSE(3)
      OPEN(UNIT=4,FILE='contour4.dat')
      WRITE(4,*) 1
ccc   WRITE(4,*) 96,64
      WRITE(4,*) (NCH-1)/(2*NDI),170
      WRITE(4,*) (SNGL((I-1)*NDI*DX),I=1,(NCH-1)/(2*NDI))
ccc   WRITE(4,*) (SNGL((I-1)*DX),I=1,96)
      WRITE(4,*) (SNGL((J-1)*DV),J=1,170)
cc    WRITE(4,*) (SNGL((J-1)*DV),J=1,128)
ccc      WRITE(4,*) ((F2(I,J),I=1,96),J=1,256)
c      WRITE(4,*) ((F2(I,J),I=1,96),J=1,128)
      WRITE(4,*) ((F2(I,J),I=1,(NCH-1)/(2*NDI)),J=1,170)
      WRITE(4,*) 0
      CLOSE(4)
      OPEN(UNIT=5,FILE='contour5.dat')
      WRITE(5,*) 1
ccc   WRITE(5,*) 96,64
```

```
c        WRITE(5,*) (NCH-1)/(2*NDI),128
      WRITE(5,*) 201,170
      WRITE(5,*) (SNGL((I-1)*NDI*DX),I=(NCH-1)/(2*NDI)-500,
     1(NCH-1)/(2*NDI)-300)
      WRITE(5,*) (SNGL((J-1)*DV),J=1,170)
      WRITE(5,*) ((F1(I,J),I=(NCH-1)/(2*NDI)-500,
     1(NCH-1)/(2*NDI)-300),J=1,170)
      WRITE(5,*) 0
      REWIND 5
      CLOSE(5)

CCC   CALL CONREC(F1,96,96,64,0.0001,0.0041,0.001,0,-1,0)
CCC   CALL FRAME
CCC   CALL CONREC(F2,96,96,64,0.0001,0.0041,0.001,0,-1,0)
CCC   CALL FRAME
      RETURN
      END
C
C  SUBROUTINE ENGY - computes energies for print out
C
C  Subroutine TRACE really does all the computations
C   so what's the use of this function?
C
      SUBROUTINE ENGY

      IMPLICIT REAL*8 (A-H,O-Z)

      PARAMETER(M=256,MI=128,N=35000,IZK=142,NSAUT=48,NSAUTI=48)
      PARAMETER(EPSI=0.0,EPS=0.05,NVAC=1,IKP=255,IKI=24)

      PARAMETER(M2P1=2*M+1,M2=2*M,NP1=N+1,ND4P1=N/4+1)
      PARAMETER(MI2=2*MI,MI2P1=2*MI+1)
      PARAMETER(NM1=N-1,ND2=N/2,ND2P1=ND2+1,M2M1=M2-1,M2M2=M2-2)

      COMMON/ARRAY/F(NP1,M2P1),A(M2P1),B(M2P1),
     1C(M2P1),D(M2P1),P(NP1),E(NP1),G(NP1),
     2DSH(M2P1),EF(NP1),EEF(NP1),EK(NP1),X(M2P1),
     4T,XL,VMAX,DT,TMAX,Q,DV,DX,WK,VTH,VTH1,ALP
      COMMON/PARTIC/RHO(NP1),RHOI(NP1)
      COMMON/PHO/EP(NP1),EM(NP1),VY(NP1),CJP(NP1),CJM(NP1),
     1VYI(NP1),DTT,XK0,OMK,PUMP
      COMMON/TRAC/HH,HS,C1,C3,C2,C5,EEN,C4,C6,VT

      CALL TRACE

      WRITE(6,1002) T,C1,C3,C2,C5,EEN,C4,C6
 1002 FORMAT(F8.2,E9.1,6F10.6)

      RETURN
      END
C
C  SUBROUTINE STREAM - move electrons in space along characteristic
C
      SUBROUTINE STREAM

      IMPLICIT REAL*8 (A-H,O-Z)
```

```
      PARAMETER(M=256,MI=128,N=35000,IZK=142,NSAUT=48,NSAUTI=48)
      PARAMETER(EPSI=0.0,EPS=0.05,NVAC=1,IKP=255,IKI=24)

      PARAMETER(M2P1=2*M+1,M2=2*M,NP1=N+1)
      PARAMETER(NM1=N-1,ND2=N/2,ND2P1=ND2+1,M2M1=M2-1,M2M2=M2-2)


      COMMON/ARRAY/F(NP1,M2P1),A(M2P1),B(M2P1),
     1C(M2P1),D(M2P1),P(NP1),E(NP1),G(NP1),
     2DSH(M2P1),EF(NP1),EEF(NP1),EK(NP1),X(M2P1),
     4T,XL,VMAX,DT,TMAX,Q,DV,DX,WK,VTH,VTH1,ALP
      DIMENSION FF(NP1),Y(NP1)

C     SHIFT THE ELECTRON DISTRIBUTION FUNCTION
C
C The shift is done differently depending on the positive or
C  negative velocity space. So, it's split up into two similar
C  blocks of code
C

      NM2=N-2

      DO 6 J=1,M
        A1=A(J)
        B1=B(J)
        C1=C(J)
        D1=D(J)
        DO 1 I=2,NM2
    1     FF(I)=A1*F(I-1,J)+B1*F(I,J)+C1*F(I+1,J)+D1*F(I+2,J)
        FF(1)=B1*F(1,J)+C1*F(2,J)+D1*F(3,J)
        FF(N-1)=A1*F(N-2,J)+B1*F(N-1,J)+C1*F(N,J)
        FF(N)=A1*F(N-1,J)+B1*F(N,J)
        FF(1)=.25*FF(1)
        DO 2 I=2,N
          FFIM1=FF(I-1)
          FFI=FF(I)
    2     FF(I)=(FFIM1-FFI)*E(I)
        Y(N)=FF(N)
C
C Tridiagonal algorithm is used to solve for the new value
C  of the distribution function
C
C It is possible that the shift is over more than one grid
C  spacing. The value K accounts for this.
C
        DO 3 I=NM1,1,-1
          YIP1=Y(I+1)
    3     Y(I)=YIP1*E(I)+FF(I)
        K=DSH(J)
        DO 4 I=N-K+1,N
    4     F(I,J)=0.0
        DO 5 I=1,N-K
    5     F(I,J)=Y(I+K)
    6 CONTINUE

      DO 16 J=M+1,M2
        A1=A(J)
```

```
        B1=B(J)
        C1=C(J)
        D1=D(J)
        DO 11 I=3,NM1
 11       FF(I)=A1*F(I+1,J)+B1*F(I,J)+C1*F(I-1,J)+D1*F(I-2,J)
        FF(1)=A1*F(2,J)+B1*F(1,J)
        FF(2)=A1*F(3,J)+B1*F(2,J)+C1*F(1,J)
        FF(N)=B1*F(N,J)+C1*F(N-1,J)+D1*F(N-2,J)
        FF(1)=.25*FF(1)
        DO 12 I=2,N
          FFIM1=FF(I-1)
          FFI=FF(I)
 12       FF(I)=(FFIM1-FFI)*E(I)
        Y(N)=FF(N)
        DO 13 I=NM1,1,-1
          YIP1=Y(I+1)
 13       Y(I)=YIP1*E(I)+FF(I)
        K=DSH(J)
        DO 14 I=1,K
 14       F(I,J)=0.0
        DO 15 I=K+1,N
 15       F(I,J)=Y(I-K)
 16   CONTINUE

      RETURN
      END
C
C  SUBROUTINE STRION - move ions in space along characteristic
C
      SUBROUTINE STRION

      IMPLICIT REAL*8 (A-H,O-Z)

      PARAMETER(M=256,MI=128,N=35000,IZK=142,NSAUT=48,NSAUTI=48)
      PARAMETER(EPSI=0.0,EPS=0.05,NVAC=1,IKP=255,IKI=24)

      PARAMETER(MI2P1=2*MI+1,MI2=2*MI,NP1=N+1,M2P1=2*M+1)
      PARAMETER(NM1=N-1,ND2=N/2,ND2P1=ND2+1,MI2M1=MI2-1,MI2M2=MI2-2)

      COMMON/ARRAY/F(NP1,M2P1),A(M2P1),B(M2P1),
     1C(M2P1),D(M2P1),P(NP1),E(NP1),G(NP1),
     2DSH(M2P1),EF(NP1),EEF(NP1),EK(NP1),X(M2P1),
     4T,XL,VMAX,DT,TMAX,Q,DV,DX,WK,VTH,VTH1,ALP
      COMMON/ARION/FI(NP1,MI2P1),AI(MI2P1),BI(MI2P1),
     1CI(MI2P1),DI(MI2P1),XI(MI2P1),DSHI(MI2P1),
     2VIMAX,DVI,DTI,XMEI,XTEI,TXI
      DIMENSION FF(NP1),Y(NP1)

C    SHIFT THE ION DISTRIBUTION FUNCTION
C
C The shift is done differently depending on the positive or
C  negative velocity space. So, it's split up into two similar
C  blocks of code
C
      NM2=N-2

      DO 6 J=1,MI
```

```
        A1=AI(J)
        B1=BI(J)
        C1=CI(J)
        D1=DI(J)
        DO 1 I=2,NM2
    1     FF(I)=A1*FI(I-1,J)+B1*FI(I,J)+C1*FI(I+1,J)+D1*FI(I+2,J)
        FF(1)=B1*FI(1,J)+C1*FI(2,J)+D1*FI(3,J)
        FF(N-1)=A1*FI(N-2,J)+B1*FI(N-1,J)+C1*FI(N,J)
        FF(N)=A1*FI(N-1,J)+B1*FI(N,J)
        FF(1)=.25*FF(1)
        DO 2 I=2,N
          FFIM1=FF(I-1)
          FFI=FF(I)
    2     FF(I)=(FFIM1-FFI)*E(I)
        Y(N)=FF(N)
C
C Tridiagonal algorithm is used to solve for the new value
C  of the distribution function
C
C It is possible that the shift is over more than one grid
C  spacing. The value K accounts for this.
C
        DO 3 I=NM1,1,-1
          YIP1=Y(I+1)
    3     Y(I)=YIP1*E(I)+FF(I)
        K=DSHI(J)
        DO 4 I=N-K+1,N
    4     FI(I,J)=0.0
        DO 5 I=1,N-K
    5     FI(I,J)=Y(I+K)
    6 CONTINUE

      DO 16 J=MI+1,MI2
        A1=AI(J)
        B1=BI(J)
        C1=CI(J)
        D1=DI(J)
        DO 11 I=3,NM1
   11     FF(I)=A1*FI(I+1,J)+B1*FI(I,J)+C1*FI(I-1,J)+D1*FI(I-2,J)
        FF(1)=A1*FI(2,J)+B1*FI(1,J)
        FF(2)=A1*FI(3,J)+B1*FI(2,J)+C1*FI(1,J)
        FF(N)=B1*FI(N,J)+C1*FI(N-1,J)+D1*FI(N-2,J)
        FF(1)=.25*FF(1)
        DO 12 I=2,N
          FFIM1=FF(I-1)
          FFI=FF(I)
   12     FF(I)=(FFIM1-FFI)*E(I)
        Y(N)=FF(N)
        DO 13 I=NM1,1,-1
          YIP1=Y(I+1)
   13     Y(I)=YIP1*E(I)+FF(I)
        K=DSHI(J)
        DO 14 I=1,K
   14     FI(I,J)=0.0
        DO 15 I=K+1,N
   15     FI(I,J)=Y(I-K)
   16 CONTINUE
```

```
      RETURN
      END
C
C  SUBROUTINE ACC - accelerate electrons along characteristic
C
      SUBROUTINE ACC

      IMPLICIT REAL*8 (A-H,O-Z)

      PARAMETER(M=256,MI=128,N=35000,IZK=142,NSAUT=48,NSAUTI=48)
      PARAMETER(EPSI=0.0,EPS=0.05,NVAC=1,IKP=255,IKI=24)

      PARAMETER(M2P1=2*M+1,M2=2*M,NP1=N+1)
      PARAMETER(NM1=N-1,ND2=N/2,ND2P1=ND2+1,M2M1=M2-1,M2M2=M2-2)

      COMMON/ARRAY/F(NP1,M2P1),A(M2P1),B(M2P1),
     1C(M2P1),D(M2P1),P(NP1),E(NP1),G(NP1),
     2DSH(M2P1),EF(NP1),EEF(NP1),EK(NP1),X(M2P1),
     4T,XL,VMAX,DT,TMAX,Q,DV,DX,WK,VTH,VTH1,ALP
      COMMON/PHO/EP(NP1),EM(NP1),VY(NP1),CJP(NP1),CJM(NP1),
     1VYI(NP1),DTT,XK0,OMK,PUMP
      DIMENSION FF(M2P1),VF(M2P1),R(NP1)
      DIMENSION Y(M2P1)

      DTSDV=DT/DV

      DO 1 I=1,NP1
        EMF=(VY(I)-0.25*DT*(EP(I)+EM(I)))*(EP(I)-EM(I))*0.5
C       EMF=0.0
    1   R(I)=-(EF(I)+EMF)*DTSDV

      DO 12 I=1,N
        DO 2 J=1,M2
    2     FF(J)=F(I,J)
        S=DMOD(DABS(R(I)),1.D0)

C Calculate shift operator coefficients

        SS=1.0-S
        WS=S*S
        WSS=SS*SS
        W1=WSS*SS
        W2=4.0-3.0*WS*(1.0+SS)
        W3=4.0-3.0*WSS*(1.0+S)
        W4=WS*S

        IF(R(I).LE.0.0) THEN
          VF(1)=W2*FF(1)+W3*FF(2)+W4*FF(3)
          DO 3 J=2,M2M2
    3       VF(J)=W1*FF(J-1)+W2*FF(J)+W3*FF(J+1)+W4*FF(J+2)
          VF(M2M1)=W1*FF(M2M2)+W2*FF(M2M1)+W3*FF(M2)
          VF(M2)=W1*FF(M2M1)+W2*FF(M2)
        ELSE
          VF(1)=W1*FF(2)+W2*FF(1)
          VF(2)=W1*FF(3)+W2*FF(2)+W3*FF(1)
          DO 4 J=3,M2M1
```

```
   4        VF(J)=W1*FF(J+1)+W2*FF(J)+W3*FF(J-1)+W4*FF(J-2)
          VF(M2)=W2*FF(M2)+W3*FF(M2M1)+W4*FF(M2M2)
        ENDIF

C Tridiagonal Algorithm used to solve for Y

        Y(1)=0.25*VF(1)
        DO 5 J=2,M2
   5      Y(J)=(Y(J-1)-VF(J))*X(J)
          VF(M2)=Y(M2)
        DO 6 J=M2M1,1,-1
          VWK=VF(J+1)
    6     VF(J)=X(J)*VWK+Y(J)

C K tells if we shifted past one grid point

        IF(R(I).GT.0.0) THEN
          K=R(I)
          DO 7 J=1,K
   7        Y(J)=0.0
          KK=M2-K
          DO 8 J=1,KK
   8        Y(J+K)=VF(J)
        ELSE
          K=DABS(R(I))
          MK=M2-K+1
          DO 9 J=MK,M2
   9        Y(J)=0.0
          KK=1+K
          DO 10 J=KK,M2
  10      Y(J-K)=VF(J)
        ENDIF

        DO 11 J=1,M2
  11      F(I,J)=Y(J)
  12  CONTINUE

      RETURN
      END
C
C  SUBROUTINE ACCI - accelerate ions along characteristic
C
      SUBROUTINE ACCI

      IMPLICIT REAL*8 (A-H,O-Z)

      PARAMETER(M=256,MI=128,N=35000,IZK=142,NSAUT=48,NSAUTI=48)
      PARAMETER(EPSI=0.0,EPS=0.05,NVAC=1,IKP=255,IKI=24)

      PARAMETER(MI2=2*MI,MI2P1=2*MI+1,NP1=N+1,M2P1=2*M+1)
      PARAMETER(NM1=N-1,ND2=N/2,ND2P1=ND2+1,MI2M1=MI2-1,MI2M2=MI2-2)

      COMMON/ARRAY/F(NP1,M2P1),A(M2P1),B(M2P1),
     1C(M2P1),D(M2P1),P(NP1),E(NP1),G(NP1),
     2DSH(M2P1),EF(NP1),EEF(NP1),EK(NP1),X(M2P1),
     4T,XL,VMAX,DT,TMAX,Q,DV,DX,WK,VTH,VTH1,ALP
      COMMON/ARION/FI(NP1,MI2P1),AI(MI2P1),BI(MI2P1),
```

```
     1CI(MI2P1),DI(MI2P1),XI(MI2P1),DSHI(MI2P1),
     2VIMAX,DVI,DTI,XMEI,XTEI,TXI
      COMMON/PHO/EP(NP1),EM(NP1),VY(NP1),CJP(NP1),CJM(NP1),
     1VYI(NP1),DTT,XK0,OMK,PUMP
      DIMENSION  FF(MI2P1),VF(MI2P1),R(NP1)
      DIMENSION Y(MI2P1)

      DTSDV=DTI/DVI

      DO 1 I=1,NP1
        EMF=(EP(I)+EM(I))*0.25*DTI*XMEI
        EMF=(VYI(I)+EMF)*(EP(I)-EM(I))*0.5
 1        R(I)=(EF(I)+EMF)*DTSDV

      DO 12 I=1,N
        DO 2 J=1,MI2
 2        FF(J)=FI(I,J)
        S=DMOD(DABS(R(I)),1.D0)

C Calculate shift operator coefficients

        SS=1.0-S
        WS=S*S
        WSS=SS*SS
        W1=WSS*SS
        W2=4.0-3.0*WS*(1.0+SS)
        W3=4.0-3.0*WSS*(1.0+S)
        W4=WS*S

        IF(R(I).LE.0.0) THEN
          VF(1)=W2*FF(1)+W3*FF(2)+W4*FF(3)
          DO 3 J=2,MI2M2
3           VF(J)=W1*FF(J-1)+W2*FF(J)+W3*FF(J+1)+W4*FF(J+2)
          VF(MI2M1)=W1*FF(MI2M2)+W2*FF(MI2M1)+W3*FF(MI2)
          VF(MI2)=W1*FF(MI2M1)+W2*FF(MI2)
        ELSE
          VF(1)=W1*FF(2)+W2*FF(1)
          VF(2)=W1*FF(3)+W2*FF(2)+W3*FF(1)
          DO 4 J=3,MI2M1
4           VF(J)=W1*FF(J+1)+W2*FF(J)+W3*FF(J-1)+W4*FF(J-2)
          VF(MI2)=W2*FF(MI2)+W3*FF(MI2M1)+W4*FF(MI2M2)
        ENDIF

C Tridiagonal Algorithm used to solve for Y and VF

        Y(1)=0.25*VF(1)
        DO 5 J=2,MI2
5         Y(J)=(Y(J-1)-VF(J))*XI(J)
        VF(MI2)=Y(MI2)
        DO 6 J=MI2M1,1,-1
          VWK=VF(J+1)
 6        VF(J)=XI(J)*VWK+Y(J)

C K tells if we shifted past one grid point

        IF(R(I).GT.0.0) THEN
          K=R(I)
```

```fortran
          DO 7 J=1,K
    7       Y(J)=0.0
          KK=MI2-K
          DO 8 J=1,KK
    8       Y(J+K)=VF(J)
        ELSE
          K=DABS(R(I))
          MK=MI2-K+1
          DO 9 J=MK,MI2
    9       Y(J)=0.0
          KK=1+K
          DO 10 J=KK,MI2
   10       Y(J-K)=VF(J)
        ENDIF

        DO 11 J=1,MI2
   11     FI(I,J)=Y(J)

   12 CONTINUE

      RETURN
      END
C
C  SUBROUTINE EFIELD - calculate the new E-field
C
      SUBROUTINE EFIELD

      IMPLICIT REAL*8 (A-H,O-Z)

      PARAMETER(M=256,MI=128,N=35000,IZK=142,NSAUT=48,NSAUTI=48)
      PARAMETER(EPSI=0.0,EPS=0.05,NVAC=1,IKP=255,IKI=24)

      PARAMETER(M2P1=2*M+1,M2=2*M,NP1=N+1)
      PARAMETER(NM1=N-1,ND2=N/2,ND2P1=ND2+1,M2M1=M2-1,M2M2=M2-2)

      COMMON/ARRAY/F(NP1,M2P1),A(M2P1),B(M2P1),
     1C(M2P1),D(M2P1),P(NP1),E(NP1),G(NP1),
     2DSH(M2P1),EF(NP1),EEF(NP1),EK(NP1),X(M2P1),
     4T,XL,VMAX,DT,TMAX,Q,DV,DX,WK,VTH,VTH1,ALP
      COMMON/PARTIC/RHO(NP1),RHOI(NP1)
      COMMON/PHO/EP(NP1),EM(NP1),VY(NP1),CJP(NP1),CJM(NP1),
     1VYI(NP1),DTT,XK0,OMK,PUMP
      DIMENSION GE(NP1),GF(NP1),PHI(NP1),TRHO(NP1)

C PARTICLE DENSITY AND CURRENT DENSITY

      RHOM=0.0

      DO 1 I=2,N
        DRHO=0.
        DO 2 J=1,M2
    2     DRHO=DRHO+F(I,J)
        DRHO=DRHO*DV
        CJP(I)=0.5*(DRHO*VY(I)+RHO(I-1)*VY(I-1))
        CJM(I)=0.5*(DRHO*VY(I)+RHO(I+1)*VY(I+1))
        TRHO(I)=DRHO-RHOI(I)
        RHOM=RHOM+TRHO(I)
```

```
    1 CONTINUE

C CAS I=1

      DRHO=0.

      DO 3 J=1,M2
 3      DRHO=DRHO+F(1,J)

      DRHO=DRHO*DV
      CJM(1)=0.5*(DRHO*VY(1)+RHO(2)*VY(2))
      TRHO(1)=DRHO-RHOI(1)
      RHOM=(RHOM+TRHO(1))*DX
C CAS I=N+1
      CJP(NP1)=0.5*(DRHO*VY(NP1)+RHO(N)*VY(N))

      DO 8 I=1,N
 8      RHO(I)=TRHO(I)+RHOI(I)

      RHO(NP1)=RHO(1)
      TRHO(NP1)=TRHO(1)
      EF(1)=-0.5*RHOM
      EF(NP1)=+0.5*RHOM
      GF(1)=DX*DX*(TRHO(3)-6.0*TRHO(2)-7.0*TRHO(1))/24.0-EF(1)*DX

      DO 10 J=2,N
        W=GF(J-1)
        GF(J)=-(TRHO(J-1)+10.0*TRHO(J)+TRHO(J+1))*DX*DX/12.0+W
 10   CONTINUE

      PHI(1)=0.0

      DO 20 J=2,NP1
        W=PHI(J-1)
        PHI(J)=W-GF(J-1)
 20   CONTINUE

      GE(1)=-1.0
      GF(1)=2.0*(PHI(2)-PHI(1))/DX+DX*(TRHO(2)-TRHO(1))/6.

      DO 30 J=2,N
        DNN=4.0+GE(J-1)
        GE(J)=-1.0/DNN
        W=GF(J-1)
        GF(J)=(3.0*(PHI(J+1)-PHI(J-1))/DX-W)/DNN
 30   CONTINUE

      DO 40 J=N,2,-1
        W=EF(J+1)
        EF(J)=GE(J)*W+GF(J)
 40   CONTINUE

C This was a hack fix for the electron sign change
      DO J=1,NP1
        EF(J)=-EF(J)
      ENDDO
```

```
      RETURN
      END
C
C  SUBROUTINE SPHOTF
C
      SUBROUTINE SPHOTF

      IMPLICIT REAL*8 (A-H,O-Z)

      PARAMETER(M=256,MI=128,N=35000,IZK=142,NSAUT=48,NSAUTI=48)
      PARAMETER(EPSI=0.0,EPS=0.05,NVAC=1,IKP=255,IKI=24)

      PARAMETER(M2P1=2*M+1,M2=2*M,NP1=N+1)

      COMMON/PHO/EP(NP1),EM(NP1),VY(NP1),CJP(NP1),CJM(NP1),
     1VYI(NP1),DTT,XK0,OMK,PUMP
      DIMENSION WKP(NP1),WKM(NP1)

      DO 10 I=2,NP1
 10     WKP(I)=EP(I-1)+DTT*CJP(I)

C CAS PERIODIQUE, SINON WKP(1)=PUMP
C     WKP(1)=WKP(NP1)

      WKP(1)=PUMP

      DO 30  I=1,N
 30     WKM(I)=EM(I+1)+DTT*CJM(I)

C CAS PERIODIQUE, SINON WKM(NP1)=0.

      WKM(NP1)=0.0

      DO 50 I=1,NP1
        EP(I)=WKP(I)
 50     EM(I)=WKM(I)

      RETURN
      END
C
C  SUBROUTINE DENS -
C
      SUBROUTINE DENS

      IMPLICIT REAL*8 (A-H,O-Z)

      PARAMETER(M=256,MI=128,N=35000,IZK=142,NSAUT=48,NSAUTI=48)
      PARAMETER(EPSI=0.0,EPS=0.05,NVAC=1,IKP=255,IKI=24)

      PARAMETER(M2P1=2*M+1,M2=2*M,NP1=N+1)

      COMMON/ARRAY/F(NP1,M2P1),A(M2P1),B(M2P1),
     1C(M2P1),D(M2P1),P(NP1),E(NP1),G(NP1),
     2DSH(M2P1),EF(NP1),EEF(NP1),EK(NP1),X(M2P1),
     4T,XL,VMAX,DT,TMAX,Q,DV,DX,WK,VTH,VTH1,ALP
      COMMON/PARTIC/RHO(NP1),RHOI(NP1)
```

```
C Integrate the electron distribution function in momentum space
C  for each grid point in x-space

      DO 1 I=1,NP1
        DRHO=0.
        DO 2 J=1,M2
          DRHO=DRHO+F(I,J)
   2    CONTINUE
        RHO(I)=DRHO*DV
   1  CONTINUE

      RETURN
      END
C
C  SUBROUTINE DENSI -
C
      SUBROUTINE DENSI

      IMPLICIT REAL*8 (A-H,O-Z)

      PARAMETER(M=256,MI=128,N=35000,IZK=142,NSAUT=48,NSAUTI=48)
      PARAMETER(EPSI=0.0,EPS=0.05,NVAC=1,IKP=255,IKI=24)

      PARAMETER(NP1=N+1,MI2=2*MI,MI2P1=2*MI+1)

      COMMON/ARION/FI(NP1,MI2P1),AI(MI2P1),BI(MI2P1),
     1CI(MI2P1),DI(MI2P1),XI(MI2P1),DSHI(MI2P1),
     2VIMAX,DVI,DTI,XMEI,XTEI,TXI
      COMMON/PARTIC/RHO(NP1),RHOI(NP1)

C Integrate the ion distribution function in momentum space
C  for each grid point in x-space

      DO 1 I=1,NP1
        DRHO=0.
        DO 2 J=1,MI2
    2     DRHO=DRHO+FI(I,J)
    1   RHOI(I)=DRHO*DVI

      RETURN
      END
C
C  SUBROUTINE TRACE
C
      SUBROUTINE TRACE

      IMPLICIT REAL*8 (A-H,O-Z)

      PARAMETER(M=256,MI=128,N=35000,IZK=142,NSAUT=48,NSAUTI=48)
      PARAMETER(EPSI=0.0,EPS=0.05,NVAC=1,IKP=255,IKI=24)

      PARAMETER(M2P1=2*M+1,M2=2*M,NP1=N+1)
      PARAMETER(NM1=N-1,ND2=N/2,ND2P1=ND2+1,M2M1=M2-1,M2M2=M2-2)

      COMMON/ARRAY/F(NP1,M2P1),A(M2P1),B(M2P1),
     1C(M2P1),D(M2P1),P(NP1),E(NP1),G(NP1),
     2DSH(M2P1),EF(NP1),EEF(NP1),EK(NP1),X(M2P1),
```

```
     4T,XL,VMAX,DT,TMAX,Q,DV,DX,WK,VTH,VTH1,ALP
      COMMON/PARTIC/RHO(NP1),RHOI(NP1)
      COMMON/TRAC/HH,HS,C1,C3,C2,C5,EEN,C4,C6,VT
      COMMON/TRAC1/HH1,HH2,HH3,HH5,HH6,HH7,XKE,OMP,JS
      COMMON/PHO/EP(NP1),EM(NP1),VY(NP1),CJP(NP1),CJM(NP1),
     1VYI(NP1),DTT,XK0,OMK,PUMP
      DIMENSION TRHO(2,NP1)

      USN=1.0/DBLE(N)

      MP1=M+1

      DO 11 I=1,N
        HH=0.0
        H=0.0
        DO 12 J=1,M
          V=(DBLE(J)-.5)*DV
C H holds the first moment - Momentum
          H=H+V*(F(I,M+J)-F(I,MP1-J))
C HH holds the second moment - Energy
          HH=HH+(DSQRT(V**2+1.0D0)-1.0D0)*(F(I,M+J)+F(I,MP1-J))
  12    CONTINUE
C Multiplying by the spacing in momentum space gives the integral
C  this is stored on every spatial grid point
        EK(I)=HH*DV
        P(I)=H*DV
  11  CONTINUE

C This is calculating the electron density or charge density
C This is done in Sub DENS so I don't know why it's done here and
C  then DENS is called afterwards

      DO 1 I=1,N
        H=0.0
        DO 5 J=1,M2
          H=H+F(I,J)*DV
   5    CONTINUE
        RHO(I)=H
   1  CONTINUE

      EEN=0.0
      C1=0.
      C2=0.
      C3=0.
      C4=0.

C Summing quantities for all spatial grid points
      DO 4 I=1,N
C EF - longitudinal field
        EEN=EEN+EF(I)*EF(I)
C Charge density
        C1=C1+RHO(I)-RHOI(I)
C Transverse Kinetic energy in electrons
        C2=C2+RHO(I)*VY(I)*VY(I)
C more field energies - transverse pump plus scattered
        C4=C4+EP(I)*EP(I)+EM(I)*EM(I)
C electron kinetic energy in x
```

```
          C3=C3+EK(I)
    4   CONTINUE

C compute spatial averages and RMS values
        EEN=0.5*EEN/DBLE(N)
        C1=C1/DBLE(N)
        C2=0.5*C2/DBLE(N)
        C3=C3/DBLE(N)
        C4=0.25*C4/DBLE(N)

C Total electron kinetic energy
        C5=C3+C2

C Total energy
        C6=C5+EEN+C4

        RETURN
        END
```

Appendix E

Mathcad Worksheets Used for Various Calculations Cited in the Thesis

This appendix provides the Mathcad worksheets used to perform various calculations cited throughout the thesis. Presented first is the worksheet used to perform the resonance matching calculations, the Thomson scattering probe and collection angles calculation, calculate the anticipated growth rates and thresholds, and numerous other calculations related to the single hot spot laser-plasma experiments. Presented next is the worksheet used to perform the Thomson scattering form factor fit to the experimental data and determine the electron temperature. Finally, the worksheet used to calculate the roots of the bi-Maxwellian dispersion relation is presented.

The Mathcad worksheets are thoroughly commented in hopes that it is obvious what is going on in the calculations. The original Mathcad worksheets are live math, i.e. changing parameters at the beginning of the worksheet update all calculations that depend on those parameters. Thus, the worksheets included in this appendix are only snapshots of a particular calculation. For the interested reader, the actual Mathcad worksheet files are available on the CDROM that accompanies this thesis.

References

[1] J. D. Lindl, "Development of the indirect-drive approach to inertial confinement fusion and the target physics basis for ignition and gain," Phys. Plasmas **2**, 3933 (1995).

[2] J. D. Lindl, *Inertial Confinement Fusion: The Quest for Ignition and Energy Gain Using Indirect Drive*, (Springer-Verlag, New York, 1997).

[3] D. F. DuBois and M. V. Goldman, "Radiation-Induced Instability of Electron Plasma Oscillations," Phys. Rev. Lett. **14**, p. 544 (1965).

[4] F. W. Chambers, *Space-Time Evolution of Instabilities in Laser-Plasma Interactions*, Ph.D. Thesis, Massachusetts Institute of Technology, Cambridge, MA (1975).

[5] H. A. Baldis, E. M. Campbell, and W. L. Kruer, in *Physics of Laser Plasma*, Handbook of Plasma Physics (North-Holland, Amsterdam, 1991), Vol. 3, Chap. 9.

[6] J. C. Fernández et al., "Observed Dependence of Stimulated Raman Scattering on Ion-Acoustic Damping in Hohlraum Plasmas," Phys. Rev. Lett. **77**, p. 2702 (1996).

[7] J. C. Fernández et al., "Measurements of laser-plasma instability relevant to ignition hohlraums," Phys. Plasmas **4**, p. 1849 (1997).

[8] J. C. Fernández, J. A. Cobble, D. S. Montgomery, M. D. Wilke, and B. B. Afeyan, "Observed insensitivity of stimulated Raman scattering on electron density," Phys. Plasmas **7**, p. 3743 (2000).

[9] R. K. Kirkwood et al., "Effect of Ion-Wave Damping on Stimulated Raman Scattering in High-Z Laser-Produced Plasmas," Phys. Rev. Lett. **77**, p. 2706 (1996).

[10] V. N. Oraevskii and R. Z. Sagdeev, "Stability of Steady-State Longitudinal Plasma Oscillations," Sov. Phys. Tech. Phys. **7**,955 (1963).

[11] D. F. DuBois and M. V. Goldman, "Parametrically Excited Plasma Fluctuations," Phys. Rev. **164**, p. 207 (1967).

[12] K. S. Baker et al., "Thomson Scattering Measurements of the Langmuir Wave Spectra Resulting from Stimulated Raman Scattering," Phys. Rev. Lett. **77**, p. 67 (1996).

[13] K. S. Baker et al., "Observation of the Langmuir decay instability driven by stimulated Raman scattering," Phys. Plasmas **4**, p. 3012 (1997).

[14] K. S. Baker, *Saturation of Langmuir Waves in Laser-Produced Plasmas*, Ph.D. Thesis, University of California, Davis (1996).

[15] D. F. DuBois, D. A. Russell, P. Y. Cheung, and M. P. Sulzer, "High-power high-frequency-induced Langmuir turbulence in the smooth ionosphere at Arecibo. I. Theoretical predictions for altitude-resolved plasma line radar spectra," Phys. Plasmas **8**, p. 791 (2001).

[16] P. Y. Cheung, M. P. Sulzer, D. F. DuBois, and D. A. Russell, "High-power high-frequency-induced Langmuir turbulence in the smooth ionosphere at Arecibo. II. Low duty cycle, altitude-resolved, observations," Phys. Plasmas **8**, p. 802 (2001).

[17] S. Depierreux et al., "First Observation of Ion Acoustic Waves Produced by the Langmuir Decay Instability," Phys. Rev. Lett. **84**, p. 2869 (2000).

[18] D. S. Montgomery, Comment on "First Observation of Ion Acoustic Waves Produced by the Langmuir Decay Instability," Phys. Rev. Lett. **86**, 3686 (2001).

[19] D. Pesme, et al., Reply Phys. Rev. Lett. **86**, 3687 (2001).

[20] R. J. Focia, D. S. Montgomery, J. C. Fernández, and R. P. Johnson, "Observation of Multiple Cascade Steps of the Langmuir Decay Instability in a Laser Plasma," Phys. Rev. Lett. Submitted (2001).

[21] D. Bohm and E. P. Gross, “Theory of Plasma Oscillations. A. Origin of Medium-Like Behavior,” Phys. Rev. **75**, 1851 (1949).

[22] B. D. Fried and R. W. Gould, “Longitudinal Ion Oscillations in a Hot Plasma,” Phys. Fluids **4**, 139 (1961).

[23] J. F. Drake *et al*., “Parametric instabilities of electromagnetic waves in plasmas," Phys. Fluids **17**, 778 (1974).

[24] T. H. Stix, *The Theory of Plasma Waves* (McGraw-Hill, New York, 1962), p. 218.

[25] D. C. Montgomery, *Theory of Unmagnetized Plasma* (Gordon and Breach, New York, 1971), p. 69.

[26] I. B. Bernstein, J. M. Greene, and M. D. Kruskal, “Exact Nonlinear Plasma Oscillations,” Phys. Rev. **108**, 546 (1957).

[27] H. Schamel, “Role of Trapped Particles and Waves in Plasma Solitons – Theory and Application,” Phys. Scr. **20**, 306 (1979).

[28] H. Schamel, “Hole equilibria in Vlasov–Poisson systems: A challenge to wave theories of ideal plasmas,” Phys. Plasmas **7**, 4831 (2000), and references therein.

[29] J. P. Holloway and J.J. Dorning, “Undamped Longitudinal Plasma Waves,” Phys. Lett. A **138**, 279 (1989).

[30] J. P. Holloway and J. J. Dorning, “Undamped plasma waves,” Phys. Rev. A **44**, 3856 (1991).

[31] V. B. Krapchev and A. K. Ram, “Adiabatic theory for a single nonlinear wave in a Vlasov plasma,” Phys. Rev. A **22**, 1229 (1980).

[32] D. S. Montgomery, R. J. Focia, H. A. Rose, D. A. Russel, J. A. Cobble, J. C. Fernández, and R. P. Johnson, "First Observation of Stimulated Electron Acoustic Wave Scattering," Phys. Rev. Lett. **87**, 155001 (2001).

[33] G. J. Morales and T. M. O'Neil, "Nonlinear Frequency Shift of an Electron Plasma Wave," Phys. Rev. Lett. **28**, 417 (1972).

[34] B. I. Cohen and A. N. Kaufman, "Nonlinear plasma waves excited near resonance," Phys. Fluids **20**, 1113 (1977).

[35] H. X. Vu, D. F. DuBois, and B. Bezzerides, "Transient Enhancement and Detuning of Laser-Driven Parametric Instabilities by Particle Trapping," Phys. Rev. Lett. **86**, 4306 (2001).

[36] K.G. Estabrook, W. L. Kruer, and B. F. Lasinski, "Heating by Raman Backscatter and Forward Scatter," Phys. Rev. Lett. **45**, 1399 (1980).

[37] R. J. Briggs, *Electron Stream Interactions with Plasmas* (MIT Press, Cambridge, MA 1964).

[38] A. Bers, *Linear Waves and Instabilities*, in *Plasma Physics* (Les Houches, 1972 - Gordon and Breach, London, 1974).

[39] N. K. Moncur, R. P. Johnson, R. G. Watt, and R. B. Gibson, "Trident: a versatile high-power Nd:glass laser facility for inertial confinement fusion experiments," App. Opt. **34**, p. 4274 (1995).

[40] D. S. Montgomery, R. P. Johnson, J. A. Cobble, J.C. Fernández, E. L. Lindman, H. A. Rose, and K. G. Estabrook, "Characterization of plasma and laser conditions for single hot spot experiments," Laser and Particle Beams **17**, p. 349 (1999).

[41] D. S. Montgomery, R. P. Johnson, H. A. Rose, J. A. Cobble, and J. C. Fernández, "Flow-Induced Beam Steering in an Single Laser Hot Spot," Phys. Rev. Lett. **84**, 678 (2000)

[42] G. Zimmerman and W. Kruer, “Numerical Simulation of Laser-Initiated Fusion,” Comments Plasma Phys. Controlled Fusion **2**, 51 (1975).

[43] Max Born and Emil Wolf, *Principles of Optics: Electromagnetic Theory of Propagation, Interference and Diffraction of Light*, 7th Edition (Cambridge University Press, New York, 1999), Sections 8.5.2 and 8.8.

[44] B. D. Fried and S. D. Conte, *The Plasma Dispersion Function, The Hilbert Transform of the Gaussian* (Academic Press, New York, 1961).

[45] Mathcad is developed by MathSoft Engineering & Education, Inc. 101 Main Street, Cambridge, MA 02142. www.mathcad.com.

[46] R. A. London and M. D. Rosen, “Hydrodynamics of exploding foil x-ray lasers,” Phys. Fluids **29**, 3813 (1986).

[47] J. H. Hunter, Jr. and R. A. London, “Multidimensional similarity models for exploding foils,” Phys. Fluids **31**, 3102 (1988).

[48] D. M. Villeneuve, H. A. Baldis, J. E. Bernard, and R. Benesch “Collective Thomson scattering in a laser-produced plasma resolved in time, space, frequency, or wave number,” J. Opt. Soc. Am. B **8**,895 (1991).

[49] J. Sheffield, *Plasma Scattering of Electromagnetic Radiation* (Academic Press, New York, 1975).

[50] I. H. Hutchinson, *Principles of Plasma Diagnostics* (Cambridge University Press, New York, 1990).

[51] E. M. Epperlein, “Kinetic Theory of Laser Filamentation in Plasmas,” Phys. Rev. Lett. **65**, 2145 (1990))

[52] D. Besnard, G. Bonnaud, and G. Schurtz, in *La Fusion Thermonucléaire Intertielle par Laser*, Part 3, eds. R. Dautray and J.-P. Watteau, Eyrolles, Paris, France (1993), Chapter XIII, pp. 1105-1114.

[53] S. J. Karttunen, “Ion fluctuation effects on the two-plasmon decay and stimulated Raman scattering,” Phys. Rev. A **23**, 2006 (1981).

[54] G. J. Morales, Comments on “Nonlinear frequency shift of a plasma mode,” Phys. Fluids **18**,1220 (1975).

[55] Ante Salcedo, *Coupled Modes Analysis of SRS Backscattering, with Langmuir Decay and Possible Cascadings*, Ph.D. Thesis, Massachusetts Institute of Technology, Cambridge, MA (2002).

[56] C. Labaune et al., “Large-Amplitude Ion Acoustic Waves in a Laser-Produced Plasma,” Phys. Rev. Lett. **75**, 248 (1995).

[57] J. A. Cobble et al., Phys. Plasmas, “The spatial location of laser-driven, forward-propagating waves in a National-Ignition-Facility-relevant plasma,” Phys. Plasmas **7**, 323 (2000).

[58] S. P. Gary, “Electrostatic Instabilities in Plasmas With Two Electron Components,” J. Geophys. Res. **90**, 8213 (1985).

[59] A. Ghizzo et al., “A Vlasov Code for the Numerical Simulation of Stimulated Raman Scattering,” J. Comput. Phys. **90**,431 (1990).

[60] P. Bertrand et al., “A nonperiodic Euler-Vlasov code for the numerical simulation of laser-plasma beat wave acceleration and Raman scattering,” Phys. Fluids B **2**, 1028 (1990).

[61] A. Ghizzo et al., “Comparison between 1D and 1 ½ D Eulerian Vlasov Codes for the Numerical Simulation of Simulated Raman Scattering,” J. Comput. Phys. **102**, 417 (1992).

[62] P. Bertrand et al., “Two-stage electron acceleration by simultaneous stimulated Raman backward and forward scattering,” Phys. Plasmas **2**, 3115 (1995).

[63] M. L. Bégué, A. Ghizzo, and P. Bertrand, “Two-Dimensional Vlasov Simulation of Raman Scattering and Plasma Beatwave Acceleration on Parallel Computers,” J. Comput. Phys. **151**, 458 (1999).

[64] A. Ghizzo et al., “Trajectories of Trapped Particles in the Field of a Plasma Wave Excited by a Stimulated Raman Scattering,” J. Comput. Phys. **108**, 373 (1993).

[65] W. L. Kruer, *The Physics of Laser Plasma Interactions*, (Addison-Wesley, 1988).

[66] E. S. Weibel, “Spontaneously Growing Transverse Waves in a Plasma Due to an Anisotropic Velocity Distribution,” Phys. Rev. Lett. **2**, 83 (1959).

[67] A. Bers, “Kinetic Theory of Instabilities in Unmagnetized Plasmas,” in Chapter 11 of the Course Notes for Introduction to Plasma Physics II taught at MIT (1999).

[68] Private communications with David Montgomery of the Los Alamos National Laboratory.

[69] R.P. Drake, et al., “Efficient Raman Sidescatter and Hot-Electron Production in Laser-Plasma Interaction Experiments,” Phys. Rev. Lett. **53,** 1739 (1984)

[70] A. Bers, “Kinetic (Vlasov-Landau) Theory,” in Chapter 10 of the Course Notes for Introduction to Plasma Physics II taught at MIT (1999).

[71] H. A. Rose, “A self-consistent trapping model of driven electron plasma waves and limits on stimulated Raman scatter,” Phys. Plasmas **8**, 4784 (2001).

[72] A. Bers, in Notes for Courses 6.652J, 8.614J, and 22.612J, “Introduction to Plasma Physics - II,” Massachusetts Institute of Technology (2001).

[73] V. E. Zakharov, S. L. Musher, and A. M. Rubenchik, "Hamiltonian Approach to the Description of Non-Linear Plasma Phenomena," Physics Reports (Review section of Physics Letters) **129**, 285-366 (1985).

[74] A. Ghizzo, P. Bertrand, J. Lebas, M. Shoucri, T. Johnston, E. Fijalkow, and M. R. Feix, "Comparison between 1D and 1 ½ D Eulerian Vlasov Codes for the Numerical Simulation of Stimulated Raman Scattering," J. Comput. Phys. **102**, 417 (1992).

[75] B. Cohen, M. Mostrom, D. Nicholson, A. Kaufman, and B. Langdon, "Simulation of laser beat heating of a plasma," Phys. Fluids **18**,470 (1975).

[76] C. G. Cheng and G. Knorr, "The integration of the Vlasov equation in configuration space," J. Comput. Phys. **22**, 330 (1976).

[77] M. Shoucri and R. J. Gagné, "Splitting Schemes for the Numerical Solution of a Two-Dimensional Vlasov Equation," J. Comput. Phys. **27**, 315 (1978)